Analysis of Prestressed Sandwich Panels with Ultra-High Performance Concrete Facings

Von der Fakultät für Bauingenieurwesen
der Rheinisch-Westfälischen Technischen Hochschule Aachen
zur Erlangung des akademischen Grades eines Doktors der Ingenieurwissenschaften
genehmigte Dissertation

vorgelegt von

Alexander Peter Bastian Stark

Berichter: Univ.-Prof. Dr.-Ing. Josef Hegger
Univ.-Prof. Dr.-Ing. habil. Peter Mark

Tag der mündlichen Prüfung: 23.08.2017

Kurzfassung

Sandwichelemente sind besonders geeignet, um effiziente Gebäudehüllen bereitzustellen, die gleichzeitig mehrere Anforderungen erfüllen. Neben niedrigem Eigengewicht bei gleichzeitig hoher Tragfähigkeit, bieten Sandwichbauteile zum Beispiel ausreichende bauphysikalische Eigenschaften, wie Wärme- und Schalldämmung. Im Allgemeinen werden Sandwichelemente im Bauwesen mit dünnen, ebenen oder profilierten Metalldeckschichten oder mit dicken Betondeckschichten hergestellt. Bauteile ohne zusätzliche Unterkonstruktionen sind jedoch auf kurze Spannweiten begrenzt. Im Gegensatz dazu, bieten räumliche Betonkonstruktionen, wie gefaltete oder gekrümmte Querschnitte, auch bei geringen Bauteildicken hohe Steifigkeiten und Tragfähigkeiten.

Die Anwendung von gefalteten oder gekrümmten Schalenträgern auf die Sandwichbauweise vereint die Vorteile beider Konstruktionsmethoden, sodass leichte Bauteile mit großen Spannweiten und hohen Tragfähigkeiten ermöglicht werden. Um dünne Betondeckschichten mit verschiedenen Geometrien zu realisieren, sind Hochleistungsbetone vorteilhaft. Ultra-hochfester Faserbeton (UHPFRC) bietet gleichzeitig hohe Druck- und Zugfestigkeiten sowie eine ausreichende Verformungsfähigkeit. Die Verwendung von nicht-korrodierender Bewehrung aus carbonfaserverstärktem Kunststoff (CFK) ermöglicht es, filigrane Betonelemente mit geringen Betondeckungen herzustellen, die nur die Verbundanforderungen erfüllen müssen. Bei Sandwichelementen mit gefalteten oder gekrümmten Deckschichten sind neue Fertigungsverfahren erforderlich, um beliebige Querschnitte zu ermöglichen und hohe Verbundfestigkeiten zwischen den Deckschichten und dem Kernmaterial sicherzustellen.

In dieser Arbeit wird die Entwicklung innovativer Sandwichbauteile schrittweise beschrieben. Die Materialien und die daraus zusammengesetzten Kompositbauteile werden mit experimentellen und numerischen Untersuchungen analysiert. Unterstützt werden diese Untersuchungen durch theoretische Modelle. Unter anderem wird die Zugfestigkeit des UHPFRC aus Biegeversuchen mit Hilfe von abgeleiteten Momenten-Krümmungsbeziehungen bestimmt und anschließend UHPFRC-Bauteile mit CFK-Vorspannung näher betrachtet. Zur Ermittlung von Verbundfestigkeiten, Übertragungslängen und Mindestabmessungen von dünnen UHPFRC-Elementen werden Verbunduntersuchungen an vorgespannter CFK-Bewehrung durchgeführt. Hieraus leiten sich die erforderlichen Dicken der gefalteten und doppelt-gekrümmten UHPFRC-Deckschichten ab. Aus Untersuchungen an kleinformatigen Sandwichquerschnitten unter Zug- und Schubbelastung werden Steifigkeiten und Festigkeiten des Kernmaterials sowie der Verbindungsmittel für theoretische Modelle und numerische Simulationen abgeleitet. Aufbauend auf diesen Ergebnissen wird das Trag- und Verformungsverhalten von gefalteten und doppelt-gekrümmten Sandwichbauteilen untersucht. Anschließend wird ein analytisches Modell auf Basis der Sandwichtheorie abgeleitet, das die Rissbildung von mit CFK vorgespannten UHPFRC-Deckschichten berücksichtigt.

Abstract

Sandwich-structured composites represent an efficient method to establish building envelopes which concurrently satisfy several demands. Besides low self-weight with high load-bearing capacity, sandwich panels provide sufficient physical properties, such as heat and sound insulation. In general, sandwich panels for applications in building industry are made of flat or thin profiled metal sheets or thick concrete facings. However, standard elements without additional bearing structures are limited to short spans. In contrast, spatially shaped concrete structures with folded plate or curved geometry provide high stiffness and load-carrying capacity even for thin elements.

The application of folded plate and curved concrete structures to sandwich panels combines the advantages of both construction methods enabling light elements with long spans and high load-carrying capacities. To realise thin facings in various shapes, high performance cementitious composites are advantageous. Ultra-high performance fibre reinforced concrete (UHPFRC) provides high compressive and tensile strengths with ductile material behaviour. The application of non-corrosive reinforcement, e.g. carbon fibre reinforced polymer (CFRP), allows for filigree concrete elements with a thin concrete cover to only fulfil bond requirements. For sandwich panels with folded plate or curved facings, new production methods are necessary to account for cross-sections in various shapes as well as high bond strengths between UHPFRC facings and core material.

This thesis introduces the stepwise development of innovative sandwich panels. Materials and interactions of different components are investigated by experimental testing and numerical modelling. Theoretical considerations are conducted to determine the tensile strength of UHPFRC from flexural testing. Additionally, approaches to calculate moment-curvature relationships of UHPFRC sections with CFRP reinforcement are derived and applied to further theoretical investigations. Subsequently, input parameters for non-linear numerical simulations are deduced. To determine bond strengths, transfer lengths and minimum dimensions of thin UHPFRC elements, investigations on the bond behaviour of prestressed elements with CFRP reinforcement are conducted. Thus, dimensions of folded plate and doubly curved UHPFRC elements are identified. Investigations on small-scale sandwich sections under tensile and shear loading are performed to specify stiffness and strength of the core material and shear connectors. This serves as a basis for further theoretical approaches and numerical modelling. Based on the previous findings, the flexural behaviour of folded plate and doubly curved sandwich panels is investigated. Finally, an analytical model for sandwich panels is proposed which accounts for cracking of prestressed UHPRC facings with CFRP tendons.

Preface and Acknowledgements

This dissertation was written during my time as a research associate at the Institute of Structural Concrete of RWTH Aachen University. Essential parts of the dissertation are based on projects funded by the German Research Foundation (Deutsche Forschungsgemeinschaft: DFG) within the priority programme 1542 “Concrete light. Future concrete structures using bionic, mathematical and engineering formfinding principles”. The discussions with the members of the priority programme were a great help during the last six years.

First and foremost, I want to thank the supervisor of my doctoral thesis, Univ.-Prof. Dr.-Ing. Josef Hegger, head of the Institute of Structural Concrete at RWTH Aachen University, for the opportunity to be part of his research team. His encouragement, advice and confidence during the last years motivated me to conclude my work. I am also extremely grateful to Univ.-Prof. Dr.-Ing. habil. Peter Mark from the Institute of Structural Concrete of the University of Bochum for his advice and critical review of my thesis.

I want to thank all my colleagues at the Institute of Structural Concrete at RWTH Aachen University for their support and critical discussion of my work. Especially, the long discussions at day and night are part of the success of my thesis. I am sure that the gained friendships will remain after my time at the institute. Additionally, I want to acknowledge the support of the laboratory staff and their friendly cooperation during the experimental investigations. I am also very grateful to my student assistants as well as bachelor and master students, who supported me during the experimental investigations and helped me managing the day-to-day business.

I would like to express my deep gratitude to my family, especially to my parents and my sister, for supporting me so much all my life. I also want to thank my friends for showing me the real important things in life over and over again.

Special thanks go to Viviane, who always supported me and greatly contributed to the success of my work.

Aachen, May 2017 Alexander Stark

Contents

Nomenclature

Nomenclature

In the following list the most relevant units and symbols, which were used within this thesis, are summarised. Symbols, which are not contained in this list, are explained in the section where they were used.

Units:

Force:	kN, MN
Bending moment:	kNm, MNm
Stresses:	MPa, kPa
Strain:	‰
Length:	mm, cm, m
Cross-sectional area:	mm², cm², m²
Angle:	°, rad
Density:	kg/m³
Temperature:	°C

Lower-case Latin symbols

a	Distance between centroid of top and bottom facing
$a_{\mathrm{top/bot}}$	Distance between the x-axis and centroid of top/bottom facing
c	Concrete cover
d_{f}	Diameter of fibres
d_{p}	Bending length of pin connector
e	Distance between support and point load
f_{cm}	Mean concrete compression strength
f_{ctm}	Mean concrete tensile strength
g	Fibre efficiency
h	Height of cross-section
h_{c}	Core height of sandwich panel
i	Control variable
k	Spring stiffness
l_{f}	Length of fibres
n_{F}	Number of increments of applied load F
p	Uniformly distributed transverse loading; hydrostatic stress; pressure
q	Arbitrary transverse loading / deviatoric stress
r	Radius
s	Spacing of prestressing tendons
t	Thickness

t_p	Embedment length of pin-connector
t_R	Embedment length of roving (shear grid)
$t_\mathrm{top/bot}$	Thickness of top/bottom facing of sandwich panel
$u_\mathrm{top/bot}$	Axial displacement of top/bottom facing of sandwich panel
v	Core compression / displacement
w	Deflection / crack width of UHPFRC
w_1	Ratio of fracture energy G_f and tensile strength f_ctm
x	Control variable (distance from support)
x_0	Height of compressive zone
x_1	Height of linear elastic tensile zone
x_2	Height of cracked zone of fibre concrete
x_e	Fixation depth of pin connector

Capital Latin symbols

A	Cross-section / Shear stiffness of core material
B	Flexural rigidity of sandwich panel
B_s	Flexural rigidity from sandwich action
$B_\mathrm{top/bot}$	Flexural rigidity of top/bottom facing
C_i	Integration constants
D	Axial stiffness of sandwich panel
$D_\mathrm{top/bot}$	Axial stiffness of top/bottom facing
E_c	Young's modulus of core material
E_cm	Mean Young's modulus of concrete
E_pin	Young's modulus of pin-connector
$E_{\mathrm{R},0^\circ}$	Young's modulus of roving in 0°-direction
EA	Axial stiffness
EI	Flexural stiffness
F_c	Resulting force of concrete in compression
F_f	Resulting force of cracked fibre concrete
F_p	Resulting force of prestressing reinforcement
F_t	Resulting force of concrete in tension (elastic)
G_c	Shear modulus of core material
G_f	Fracture energy
I_pin	Second moment of area of pin-connector
$I_\mathrm{top/bot}$	Second moment of area of top/bottom facing
L_f	Length of single roving
M	Bending moment

M_s	Bending moment from composite (sandwich) action
$M_{top/bot}$	Bending moment of top/bottom facing
N	Axial force
$N_{top/bot}$	Axial force in top/bottom facing
R	Radius
T	Shear flow
V	Shear force
V_s	Shear force in core material
$V_{top/bot}$	Shear force in top/bottom facing

Greek symbols

α	Angle
γ	Transverse strain
γ_1	Shear strain from beam deflection
Δu	Relative displacement of concrete facings in axial direction
Δv	Relative displacement of concrete facings in transverse direction
ε	Strain
ε_c	Concrete compression strain
ε_{ct}	Elastic tensile concrete strain
$\varepsilon_{top/bot}$	Axial strain in top/bottom facing / strain at top/bottom of concrete member
η	Fibre orientation
ξ	Ratios of control variable x and length of the beam
κ	Curvature
σ	Stress
σ_p	Jacking stress of prestressing reinforcement
σ_r	Stresses in radial direction
σ_t	Stresses in circumferential direction
τ	Bond strength
τ_c	Shear strength of core material

Subsripts

bot	Bottom
c	Core / Compression
f	Fibre
m	Mean value
pin	Pin-connector
R	Roving
SG	Shear grid
t	Tension / Tensile
top	Top

Symbols

Ø	Diameter
||	Parallel

1 Introduction

1.1 Background and Motivation

In current building practice, standard load-bearing elements are mostly of rectangular shape. Exceptions are large shell structures, such as cupolas of domes or cooling towers of power plants. In contrast, shells made of RC were widely applied for building construction in the last century. For this purpose, large structures were usually cast in situ. Additionally, long-span precast elements, with limited width were produced. These folded plate or doubly curved elements were realised with a thickness of less than 10 cm and usually prestressed with steel tendons. Concerns regarding the corrosion resistance might have been a reason that such constructions are not built regularly today.

The development of ultra-high performance fibre reinforced concrete (UHPFRC) and reinforcement made of fibre reinforced polymer (FRP) are major innovations of construction materials of the last decades. FRP reinforcement is either applied as bar, strand, plate or mesh material. Hence, all fields of application from standard RC or PC members can be covered. The corrosion resistance and high tensile strength of carbon fibre reinforced polymer (CFRP) makes thin and durable concrete elements possible, since only bond requirements need to be fulfilled. These developments allow for a new design flexibility, which leads to the wish of applying UHPFRC and CFRP reinforcement to shell structures.

A major field of application of high performance concrete in combination with FRP as mesh reinforcement, so-called textile reinforced concrete (TRC), is the utilisation for innovative sandwich panels. This construction method combines the advantages of light-weight sandwich panels with metal facings and load-bearing elements with thick RC facings. Hence, a new construction method for modern building envelopes is provided. The most common applications are curtain walls, but first developments of axially load-bearing wall elements were made in the last years. Nevertheless, in general sandwich panels are often limited in span without any support constructions.

The main motivation of this thesis is the development of sandwich panels with thin, spatially shaped cross-sections, which unify advantages of both construction principles. With this method, light elements with high load-bearing capacities can be established, which provide effective precast solutions for long-span roof constructions. Furthermore, sufficient physical properties, such as heat or sound insulation can be fulfilled. To establish a framework for production processes and analysis procedures, the interaction of innovative materials and construction methods has to be investigated step by step.

1.2 Problem Definition

Sandwich panels with concrete facings are generally produced by using prefabricated slabstock foams. This production method is not suitable for sandwich panels with folded plate or curved facings, since the prefabricated core materials can only be brought into shape with high effort. Additionally, standard production methods do not provide high and reliable bond strength between concrete facings and core material. This is caused by fine dust from cutting slabstock foam material and air inclusions, which occur during the setting of the core material into fresh concrete. Even with an elaborate procedure, the bond quality cannot be controlled and predicted in advance /Sha15b/. For the design of standard sandwich panels with RC facings, the contribution of sandwich action of the core material is usually neglected and assumed to be controlled only by shear connectors.

A new production method, which enhances the bond strength between core material and concrete, can enable a high load-bearing capacity. Besides the contribution of core material and bond zone, the load-bearing capacity of facings needs to be predictable. The application of CFRP reinforcement in UHPFRC is rarely investigated. Especially, for pre-tensioned concrete structures, the bond behaviour and the interaction of fibre contribution and strain-controlled CFRP reinforcement is not investigated. This interaction is essential for an accurate prediction of the contribution of the facings.

So far, sandwich panels with folded plate or curved UHPFRC facings are not investigated. The additional stiffness of these facings needs to be considered in the analysis. For the core material, a production method has to be applied, which provides high and reliable bond strength and is suitable for non-flat sections.

1.3 Objectives and Applied Methodology

This thesis aims at providing the background for the development of long-span sandwich panels for roof structures (Fig. 1.1). In order to achieve this aim, experimental, numerical and theoretical investigations are conducted to provide folded plate and doubly curved sandwich panels with prestressed facings made of UHPFRC and CFRP reinforcement.

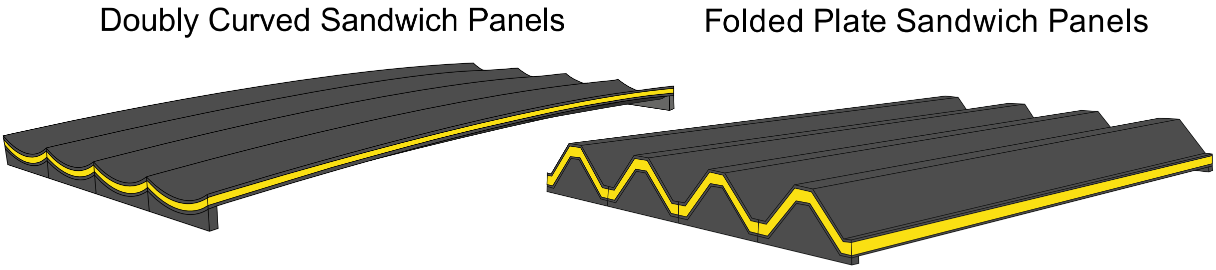

Fig. 1.1 **Doubly curved and folded plate sandwich panels for roof construction**

Step-by-step, production methods and material properties are investigated in tests on small-scale specimens and theoretical approaches are derived. Based on these findings, folded plate and doubly curved sandwich panels are established and examined.

In particular, the following steps are applied during the development:

- Identification of material properties of UHPFRC for theoretical and numerical models;
- Derivation of theoretical moment-curvature relationships of UHPFRC members with pre-tensioned CFRP reinforcement under combined axial and flexural loading;
- Development of an anchorage system for CFRP reinforcement;
- Identification of bond properties, transfer lengths and minimum thicknesses of UHPFRC elements prestressed with CFRP reinforcement;
- Providing a production technique for folded plate and doubly curved concrete sections, which accounts for UHPFRC usage and pre-tensioned CFRP reinforcement;
- Development and application of a suitable production technique for spatially shaped sandwich elements, which provides a reliable and high bond strength of the interface zone;
- Identification of material properties of the core material and the interface zone;
- Experimental and numerical investigations on folded plate and doubly curved sandwich panels with prestressed facings made of UHPFRC and CFRP reinforcement;
- Derivation of a calculative approach for sandwich panels by combining sandwich theory and theoretically derived moment-curvature relationships of prestressed UHPFRC with CFRP reinforcement.

This thesis is composed of eight chapters. After a short summary of the state-of-the-art (chapter 2), the background of experimental and numerical investigations is described in chapter 3. Therefor the applied materials as well as production methods of test specimens are summarised and material models for non-linear finite element simulations described.

In chapter 4, an approach for the determination of the tensile strength of UHPFRC based on the flexural behaviour is shown. Additionally, a calculative approach to predict the flexural behaviour of UHPFRC members prestressed with CFRP reinforcement is derived. Both approaches are based on theoretical moment-curvature relationships.

The bond behaviour of pre-tensioned CFRP reinforcement in UHPFRC is closely investigated in chapter 5. For this purpose, experimental investigations in terms of pull-out tests and tests on the transfer lengths are presented, to determine the bond strengths, minimum dimension for a crack-free transmission zone as well as the transfer lengths. With aid of numerical simulations as well as semi-empirical and analytical approaches, the bond behaviour is additionally analysed.

In chapter 6, the production technique of the sandwich panels is evaluated in tensile and shear tests on small-scale specimens. From these tests, input parameters for non-linear finite element simulations and theoretical models are derived.

Based on the findings of the chapter 2-6, prestressed UHPFRC single layers as well as sandwich panels with different cross-sections are investigated in chapter 7. With derived non-linear finite element models and a calculative approach based on the sandwich theory, the load behaviour of sandwich panels with UHPFRC facings is analysed closely.

This thesis is summarised in chapter 8.

2 Background and Previous Research

2.1 Preface

In this chapter, the background for the development and investigation of spatially shaped sandwich panels made of high-performance cementitious composites is shortly summarised. The basic ideas of sandwich technology and thin-walled structural members are discussed. Also, the materials to be applied for sandwich facings and core layer are described.

2.2 Sandwich Technology

Sandwich structures are made of several layers, i.e. materials with different properties. This structural type can be found in nature in many different assemblies. For example, bone structures of mammals are composed of hard and soft material to provide a high tensile and compressive strength with relatively low weight at the same time /Her05/. Nowadays, sandwich constructions are widely used in different fields, such as automotive, aviation or building industries (e.g. /Dav01/, /Fai49/, /Her05/, /Noo96/).

The primary reason for the application of sandwich structures is the combination of low weight and high stiffness of structural members. To demonstrate the sandwich effect, the following example is often shown (Fig. 2.1), which is based on consideration conducted by /Zen95/. A beam element made of a homogenous, stiff material of thickness *t* is subjected to bending. Weight, flexural rigidity and bending strength of the homogenous beam element are set to 1 as control values. Dividing the beam of thickness *t* into two layers of thickness *t*/2 and separating them by a light, less stiff core material leads to only little increase in weight, but to substantial gains in rigidity and strength (for a linear elastic behaviour of layers and full composite action).

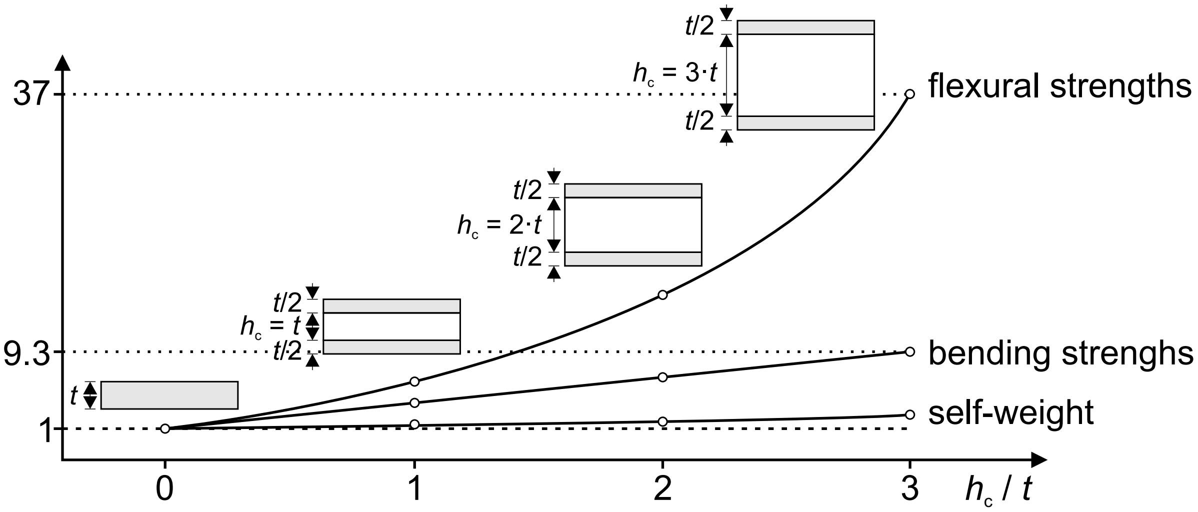

Fig. 2.1 **Ratios of flexural rigidity and bending strength of sandwich cross-sections in comparison to homogenous layer**

Sandwich panels for the application in building industry are usually made of metal or concrete facings. The main field of application is for roof or wall elements, including curtain walls. For sandwich panels with metal facings, either flat or profiled cross-sections are used. To establish long-span roof elements, usually, a support structure needs to be provided /Dav01/. Sandwich panels with concrete facings are produced as flat elements and mostly applied for walls.

2.2.1 Precast Concrete Sandwich Panels (PCSP)

In building industry, sandwich sections with two outer facings made of metal or concrete are primarily used. The concrete facings are generally reinforced with steel rebars. Different examples of sandwich panels with prestressed (steel tendon) concrete facings were investigated (e.g. /Bus94/, /Sal94/, /Pes03/). To provide sufficient concrete covering to ensure corrosion resistance (e.g. /DIN04/, /ACI05/), thick facings are necessary. The connection between the concrete facings is usually provided by the application of shear connectors (Fig. 2.2).

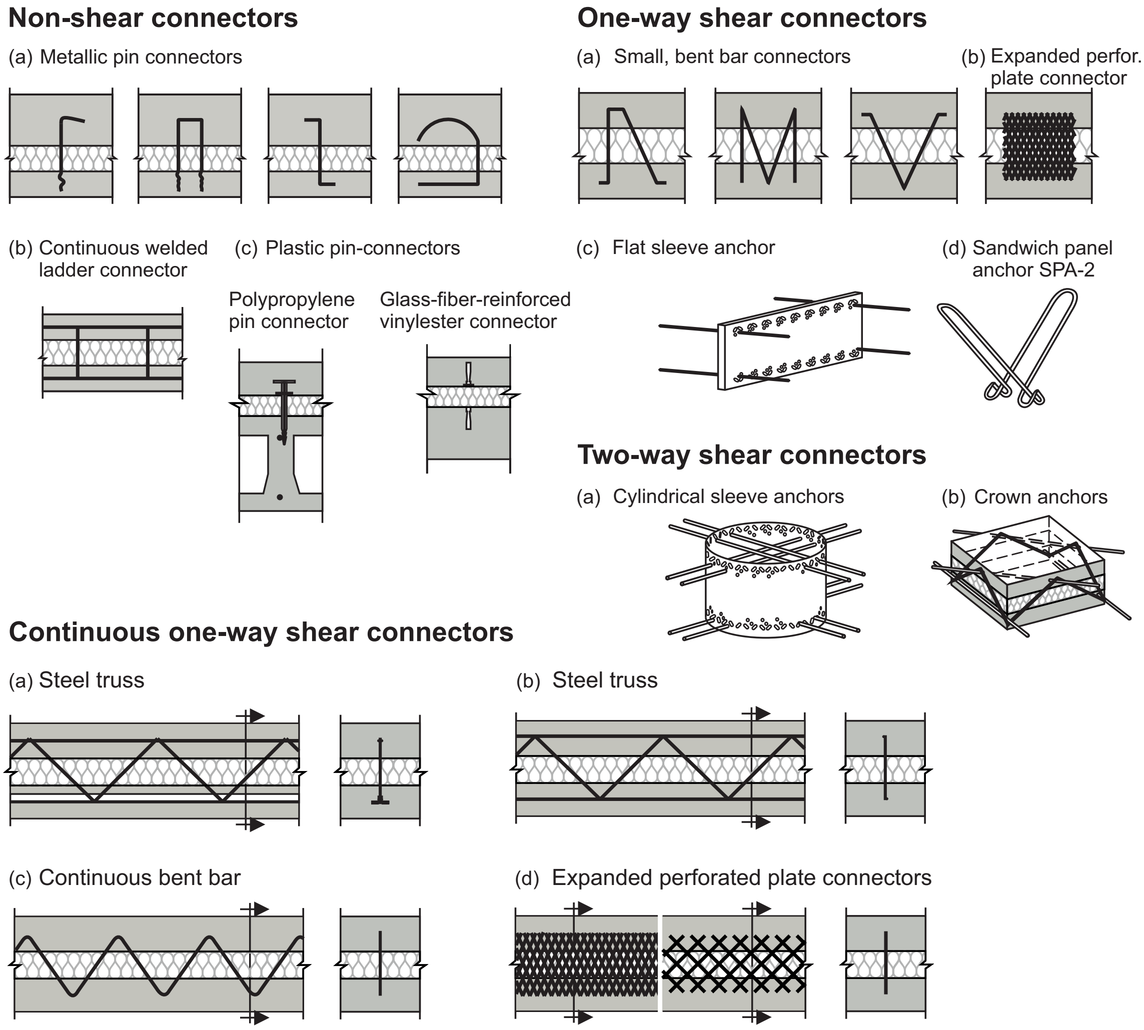

Fig. 2.2 **Shear connectors according to shear resistance (reproduced from /Hor10/, in dependence on /See97/ and product descriptions from Aslan Pacific Ltd, Halfen Group, Peikko)**

These connectors are usually classified by their shear stiffness. Typical pin connectors are less stiff than continuous shear connectors. Even though, most connectors are made of steel or stain-less steel, achievements have been made applying FRP to reduce thermal bridges.

Besides the load-bearing capacity, the thickness of concrete facings is determined by a minimum concrete cover to provide corrosion protection for steel reinforcement. To realise light-weight sandwich panels with thin, load-carrying concrete facings, developments using reinforcement made of fibre reinforced polymers (FRP) were made. Investigations on sandwich elements using reinforcement made of alkali resistant (AR) glass fibres (GFRP) and carbon fibres (CFRP) were conducted recently (e.g. /Hor10/, /Mül15/, /Sha15b/, /Zan13/).

Sandwich elements, either steel or FRP reinforced, are usually produced using pre-fabricated slabstock foam. Hence, one facing is cast, the pre-fabricated core material is placed into the fresh concrete and the other facing is concreted on top. In general, two different production methods are used. For wall elements, usually one thick load-bearing and one thin facing layer are installed. For the production of precast concrete sandwich panels, two different methods can be classified. The FACE-DOWN METHOD is applied to establish a smooth finish of external, visible facings from the formwork. With this method, the warping due to time-dependent differential shrinkage occurs in addition to the warping from structurally-dependent differential shrinkage, since the thin layer does not provide sufficient stiffness. This results in pronounced deformations (Fig. 2.3 a)) and cracking may occur. On the other hand, using the FACE-UP METHOD, the thick load-bearing layer is concreted first. The thick layer remains nearly flat and warping deformations of the facing layer are restrained by the thick layer. Hence, cracking on the concrete surfaces is not likely, since large deformations do not result (Fig. 2.3 b)), but architectural concrete requirements cannot be fulfilled with standard concrete mixtures. With these production methods, usually strong and reproducible bond zones between concrete and core material cannot be obtained. On the one hand, air inclusions may occur when placing the pre-fabricated slabstock foam and fine dust from cutting the core material cannot be removed. Either harm the bond strength, which is essential for load-bearing elements /Sha15a/. Additionally, only planar sandwich sections can be produced efficiently, since for folded plate or curved elements, aligned core materials would be necessary.

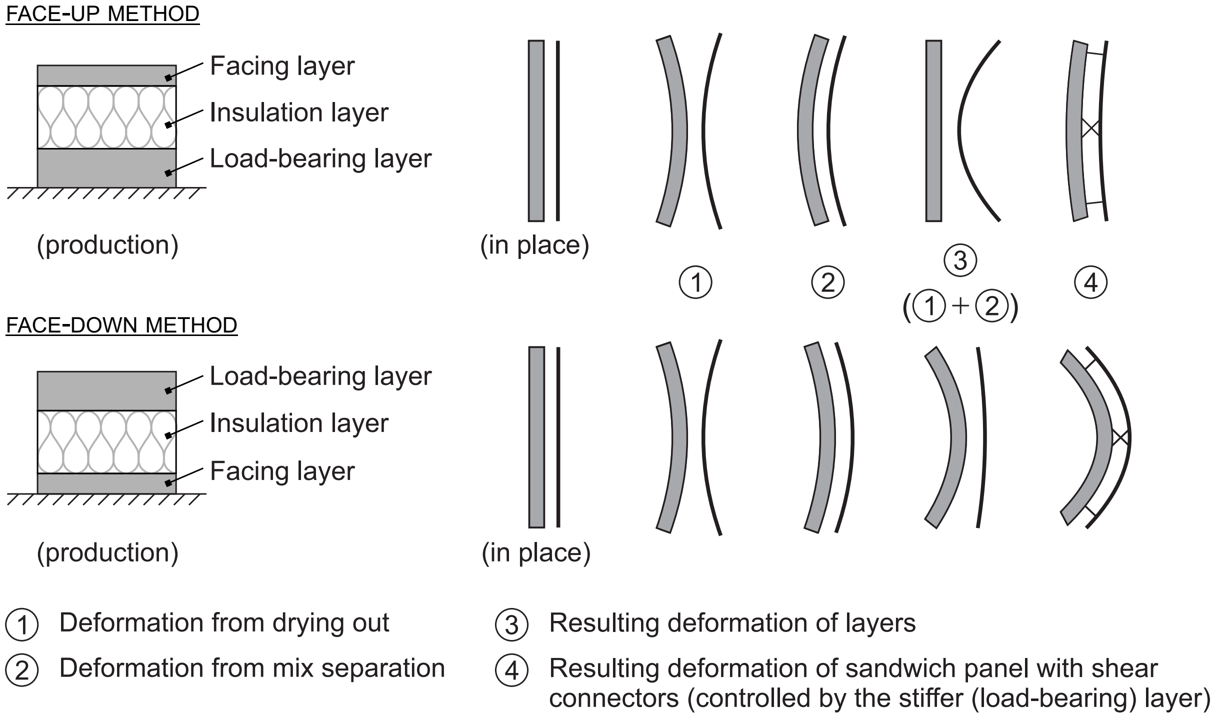

Fig. 2.3 Deformations from shrinkage for FACE-UP METHOD and FACE-DOWN METHOD

SHAMS /Sha15a/, /Sha15b/ applied a method by foaming in pack to produce sandwich panels with concrete facings. A reaction mixture of polyurethane (PU) is poured between two hardened concrete layers (Fig. 2.4).

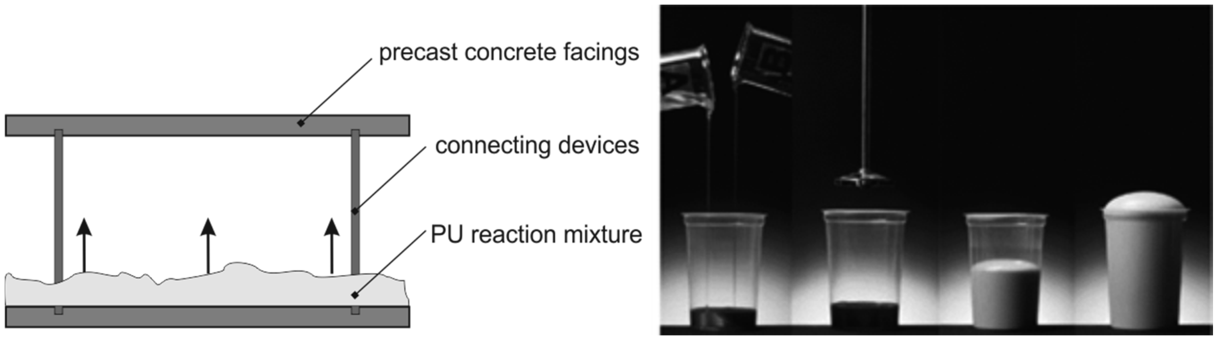

Fig. 2.4 Production method for sandwich panels with hardened concrete layers by foaming in pack of PU mixture (left) and expansion of PU mixture (right) (photo: BASF) /Sha15a/, /Sha15b/

SHAMS used this method, i.e. simply pouring the liquid mixture, only for small-scale elements, such as tensile or shear test specimens. For flat sandwich panels with TRC facings, two methods of PU injection were investigated by SHAMS. On the one hand, in horizontal position with only provisional bracing of the elements. Hence, the pressure loads had to be carried mainly by FRP pin-connectors. Due to the high pressure, cracking occurred in the outer concrete layers. Therefore, a braced steel frame (Fig. 2.5) was applied to inject the reaction mixture in either horizontal or vertical position between the hardened concrete layers.

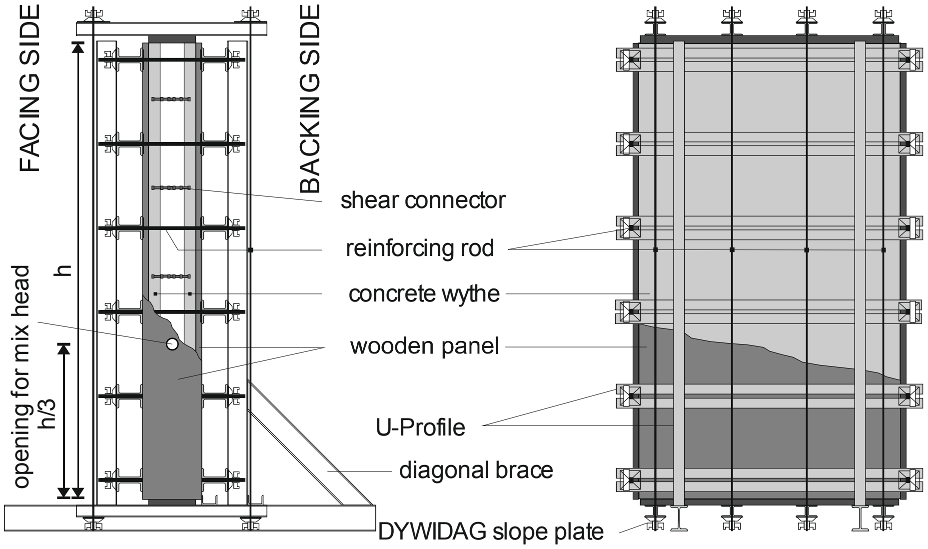

Fig. 2.5 **Strengthening and production method for large-scale sandwich elements by foaming in pack (reproduced from /Sha15b/)**

With this method, sandwich wall elements investigated in /Sha15b/ were produced with homogenous foam quality and without cracking of the TRC layers.

2.2.2 Flexural Behaviour of Sandwich Panels

For the composite action of sandwich panels, shear and tensile forces must be transmitted between the different layers. As for every composite cross-section, the external forces are divided into internal forces of each composite part. This is dependent on the stiffness of each part and the bond strength between the parts /Hor10/. The load-carrying action of sandwich panels with two outer layers and a less stiffness core is mainly dependent on the ratio of thickness t of the outer layers compared to the thickness of the core h_c and the shear stiffness of the core material. Sandwich elements with thin outer layers (cp. Table 2.1) mainly carry flexural loads by membrane stresses in the outer layers. Shear forces can be assumed to be carried by the core material only (Fig. 2.6 a))).

Table 2.1: **Definition of flexural stiffness of outer layers according to /All69/**

Designation of thickness	condition	Shear stiffness of core material	Flexural stiffness of outer layers
very thin	$a/t > 100$	$S = b \cdot a$	~0
thin	$100 > a/t > 5.77$	$S = (b \cdot a^2)/h_c$	~0
thick	$a/t < 5.77$	$S = (b \cdot a^2)/h_c$	$b \cdot t^3/12$

Hence, for statically determined systems, the internal forces can be directly determined from external loading.

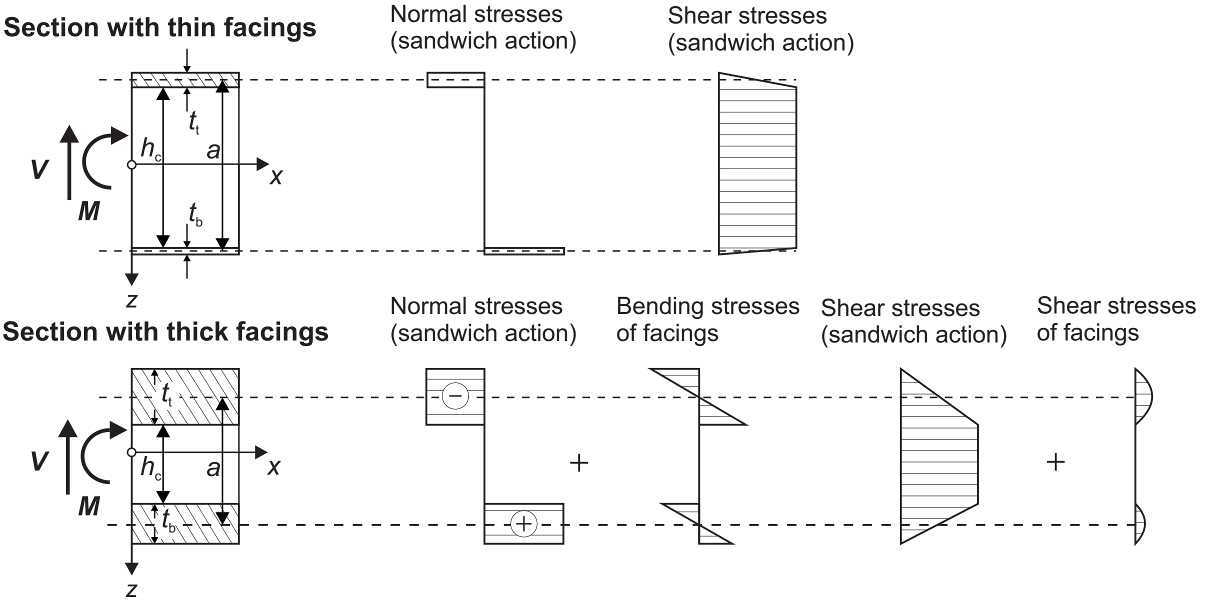

Fig. 2.6 **Stress distribution of sandwich elements with thin (top) and thick (bottom) facings (reproduced from /Aic87/, /Sta74/)**

For sandwich elements with thick outer layers, a considerable proportion of flexural and shear forces is carried by the outer layers, additionally to the membrane action from composite action. Since the three layers are statically indeterminate, internal forces cannot be calculated directly. Examples are sandwich elements with profiled metal or planar concrete layers. The calculation procedure and assumptions are summarised in sections 2.2.3 and 7.4.2.

For sandwich elements with small shear stiffness, the load-carrying action is mainly dependent on the outer layers. Hence, BERNOULLI hypothesis is not valid. For increasing shear stiffness, composite action is increased. Depending on the shear strength, the composite action is classified as NON-COMPOSITE ACTION (NCA), PARTIALLY-COMPOSITE ACTION (PCA) or FULLY-COMPOSITE ACTION (FCA) /Sal97/, /See97/ (Fig. 2.7).

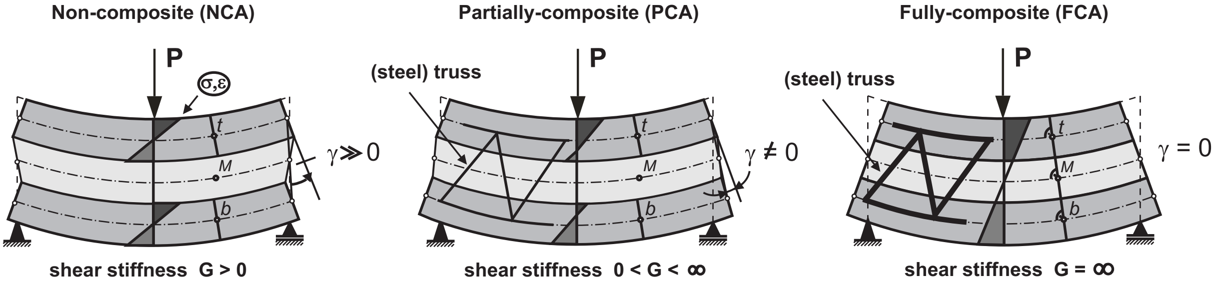

Fig. 2.7 **Influence of the core stiffness and connecting devices on the sandwich action /Ber98/, /Sal97/, /Sta74/ (reproduced from /Hor10/)**

In building practice, using standard core materials, the NCA or PCA sandwich panels are most common. However, FCA panels can be obtained by the application of steel lattice girders as continuous shear connectors /Hor10/.

2.2.3 Analytical Models for Sandwich Elements

Analytical models for sandwich elements are based on elasticity theory for the elastic-orthotropic continuum. The arising system of differential equations cannot be solved in closed form, even though, often only small deformations are assumed /Sta74/. By means of simplifications, linear sandwich theory and theory of bond slip deliver solutions for the differential equations.

Linear sandwich theory is based on deflection w and transverse strain γ, whereas theory of bond slip uses deflection w and relative slip δ. Either theories are based on the following assumptions:

a) The resulting deformation of a beam is composed of a flexural and a shear part;
b) Materials of facings and core are linear elastic (homogeneous and isotropic);
c) Small deformations: linear relationships between deflection and transverse strain/relative slip);
d) Only in-plane stresses in facings (neglecting out-of-plane stresses);
e) Facings are plane and parallel; flexural stiffness of facings has to be taken into account; axial stresses are uniformly distributed;

Thick facings affect the flexural and shear stiffness of sandwich elements. The investigated sandwich beams (chapter 7) have thick facings according to /All69/, since ratios a / t (inner lever arm / thickness of facings) are smaller than 5.77. For thick facings the following assumptions are made:

f) EA~0 for core; hence, shear stresses and shear angle are constant over core height
g) Core height keeps constant;
h) One dimensional beam element; hence, all static parameters are only dependent on the longitudinal control variable x;
i) Loading is transverse; ordinary differential equations (ODE's) are derived with linear static analysis; loading is assumed to act on neutral axis;
j) BERNOULLI HYPOTHESIS is valid for each layer, but not for the cross-section of the sandwich elements.

In contrast to sandwich theory, theory of bond slip assumes a priori rigid facings. Models using theory of bond slip have been widely applied and developed (e.g. /Stü47/, /Hol65/, /Möh56/, /Aic87/. Since the investigated construction method of sandwich elements with UHPFRC facings is assumed to allow excessive cracking in the outer layers, theory of bond slip is not discussed further.

The sandwich theory has been developed on the basis of /Rei45/, /Hof50/, /Tim51/ and /Min51/. The basics of sandwich theory can be found in /Pla66/ and /All69/. One of the most detailed reference dealing with sandwich constructions is the book by STAMM and WITTE /Sta74/. The derivation of the arising equations is shown in chapter 7 and appendix E. Due to the versatility, HORSTMANN /Hor10/ and SHAMS /Sha15b/ applied and extended the approaches by cracking of the concrete facings and additional load cases.

2.3 Thin-Walled Concrete Structures

Thin-walled concrete members are applied for architectural and structural reasons. A distinction is usually made between self-supporting and load-bearing elements. The development of non-corroding FRP reinforcement, either as meshes or bars, makes it possible to produce concrete elements with thicknesses of only a few centimetres, since only bond requirements have to be fulfilled. Self-supporting elements, such as façade cladding made of textile reinforced concrete (TRC), provide a durable and attractive choice to apply innovative and thin-walled concrete elements for building envelopes. Besides carrying self-weight, the elements transfer wind loads to structural members. In contrast, load-bearing thin-walled concrete elements are part of the bearing structure itself. The most common applications of thin-walled concrete elements are shell structures. Even though, in combination with FRP reinforcement, nowadays, even small bridges are built with only a few centimetres thickness of webs and plates (e.g. /Hel16/). Shell structures carry external loads partly by membrane action. Examples of rotational symmetric shell structures are cupolas (spherical shells) of halls or cooling towers of power plants (parabolic hyperboloid). Segments of shells, such as hyperbolic paraboloids, were built by many architects and structural engineers, e.g. by MÜLLER, MÜTHER, ISLER and CANDELA, to establish long-span roof elements with low weight compared to their bearing capacity.

For beam elements made of RC or PC, which are subjected to flexural loading, the cross-section is basically determined by span and loading. For shell elements, the stiffness and bearing capacity mainly result from spatial load-carrying action of thin-walled cross-sections. For the same section height *h*, resulting stresses are generally smaller in shell elements compared to beams due to the spatial load-carrying action.

Long-span curved or folded plate elements are usually produced as precast or semi-precast elements. Examples of curved structures are cylindrical or butterfly elements or hyperbolic paraboloids (Fig. 2.8). These elements were produced with spans of up to 50 m and thicknesses of 100 mm (e.g. /Rüh70/). Since these cross-sections usually do not provide space for a relatively large amount of reinforcement, these elements are often prestressed to increase load-bearing capacity and reduce deformations from cracking and shrinkage. For these constructions, prestressing steel tendons and steel reinforcement meshes were used. Folded plate elements carry loads mainly by in-plane action to supporting members, such as walls or columns. Besides global in plane load-carrying action, out-of-plane action occurs, since the loading direction is usually perpendicular to the elements. Examples are folded plate elements with V, A or VT shape. Results of investigations on prestressed VT folded plate elements can be found in /Küh68/. The thin NSC (normal strength concrete) elements (length: 18 m, width:

2.4 m) were prestressed with steel strands in the bottom flanges and reinforced with steel wire meshes.

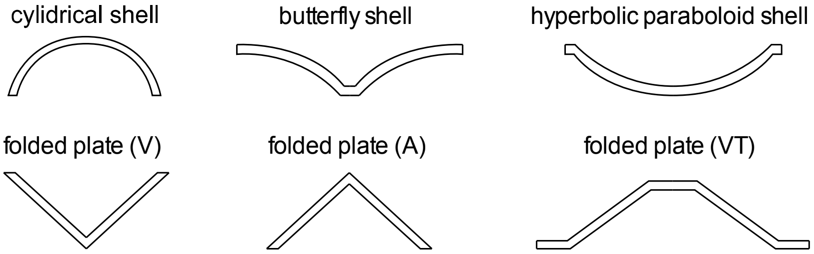

Fig. 2.8 **Examples of curved (top) and folded plate (bottom) cross-sections (reproduced from /Rüh70/).**

In the 1960's and 1970's, SILBERKUHL and NORMKO (association for standardised construction and structural engineering calculations) established different design principles and patents in Germany. For example, standardised doubly curved elements (hyperbolic paraboloids) with spans up to 25 m and width of about 2.5 m were applied for roofing elements. Since hyperbolic paraboloids mathematically consist of a family of straight lines (cp. section 2.4), these doubly curved elements were produced as pre-tensioned concrete members. In Fig. 2.9, a schematic example of the arrangement of tendons is shown. For large spans, more than 50 tendons were used. To further increase the load-bearing capacity, a beam was often placed underneath the doubly curved elements in longitudinal direction.

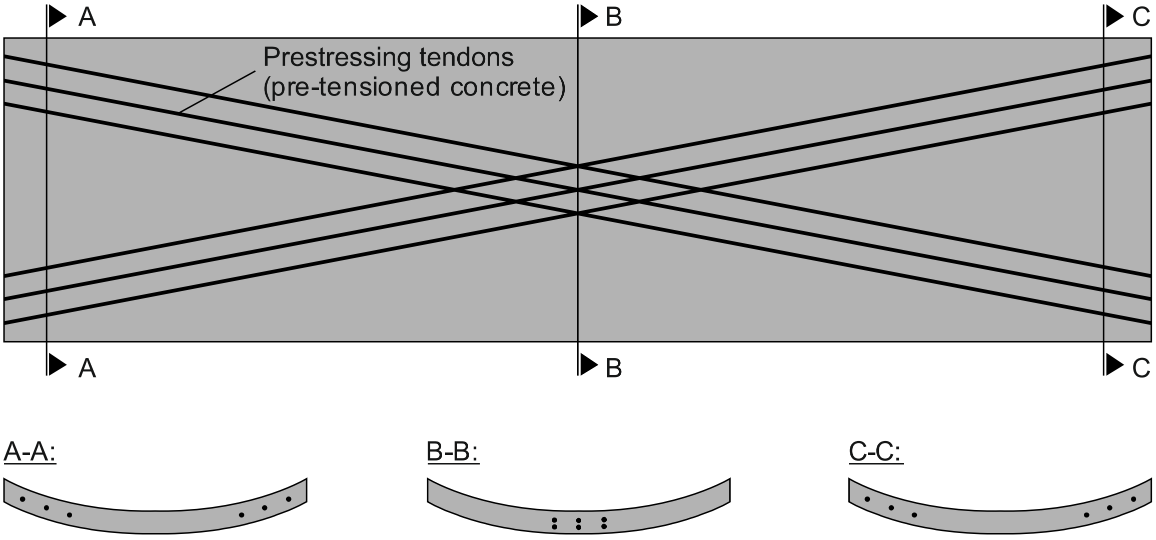

Fig. 2.9 **Arrangement of prestressing tendons in doubly curved concrete elements (based on /Sta13/)**

For the production of elements made of NSC, curved formwork and straight, but skew prestressing steel tendons were used. Usually, stiff concrete was used and vibrating beams were applied for compacting. For folded plate elements a foldable formwork often was employed.

The analysis procedure for thin, spatially shaped concrete elements is usually based on shell theory (e.g. /Bil82/, /Mik70/). In the last decades, numerical models are often applied to predict cracking and failure loads (e.g. /Pol93/).

2.4 Hyperbolic Paraboloid

Mathematically, a *hyperbolic paraboloid* (HP) represents a differentiable area as a unification of a family of straight lines. In Fig. 2.10, an example of a HP with corresponding coordinate system is shown.

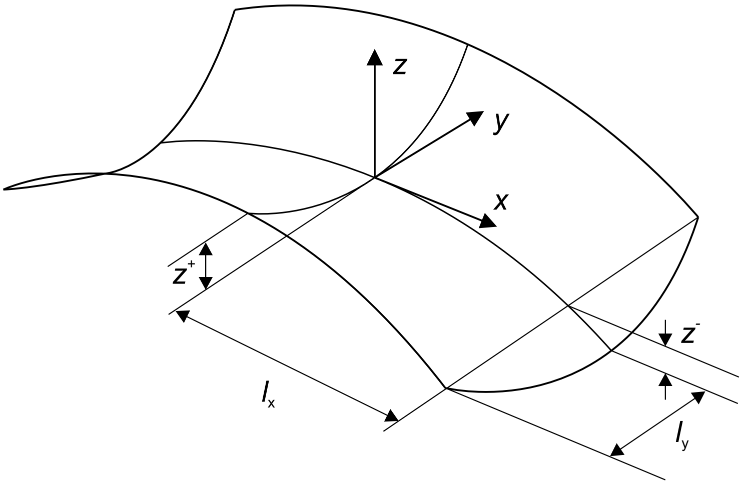

Fig. 2.10 Example of a hyperbolic paraboloid shape and mathematic nomenclature

The doubly curved area may be defined by the following expression:

$$\begin{aligned} z &= \frac{y^2}{b} - \frac{x^2}{a} \\ a &= \frac{L_x^2}{z^-}, \qquad b = \frac{L_y^2}{z^+} \end{aligned} \tag{2.1}$$

The scale factors *a* and *b* are dependent on the respective lengths and the *z*-coordinates (Fig. 2.10). For given scale factors *a* and *b* lines within the doubly curved area can be found. E.g., linear equations are used as follows:

$$x = x_0 + \alpha \cdot t, \quad y = y_0 + \alpha \cdot t, \quad z = z_0 + \alpha \cdot t, \quad t \in \Re \tag{2.2}$$

By applying equation (2.2) to equation (2.1) and setting parts of t^2 to zero, one obtains lines within the doubly curved shape. At the position of these lines, prestressing tendons or reinforcement can be placed in straight lines (cp. Fig. 2.9).

2.5 Ultra-High Performance Concrete

ULTRA-HIGH PERFORMANCE CONCRETE (UHPC) was established as further development of REACTIVE POWDER CONCRETE (RPC), which was designed and investigated in the late 1980's (e.g. /Che95/, /Ric95/). The basic idea of RPC was the minimisation of pores and micro cracks in the concrete matrix. Reactive and chemically inert additives lead to a dense concrete matrix with low water requirements. The maximum grain size d_g is much smaller than 1.0 mm. Superplasticizers guarantee the workability of concrete with water-binder-ratios of less than 0.35 (e.g. /Leu08/). Based on the investigations on RPC, different mixtures, also with coarse grains, were developed in the 1990's. These developments were finally leading to today's UHPC mixtures with uniaxial compression strengths of over 150 MPa. For these mixtures aggregates (quartz or basalt sand or chips), quartz powder, Portland cement or blast furnace cement, silica fumes, super-plasticizers and water are used. Usually, one differentiates between fine-grained ($d_g \leq 1.0$ mm) and coarse-grained ($1.0 \leq d_g \leq 16.0$ mm) UHPC /DAfStb08/. Within the priority programme 1182 of the German research foundation, different types of fine-grained UHPC (M1Q-M3Q) and coarse-grained UHPC (B1Q-B5Q) were developed. For details of these mixtures it is referred to /Feh05/. Due to brittle material behaviour of UHPC, usually short fibres are added, mainly made of high-strength steel. Steel fibres are rather applied than non-metallic fibres, since a wide range of investigations and applications exists and only corrosion of the fibres at the concrete surfaces occurs, which does not affect the durability of the structure significantly /Sch08/. For standard mixtures of ULTRA-HIGH PERFORMANCE FIBRE REINFORCED CONCRETE (UHPFRC), mainly flat steel fibres with lengths between 9 mm and 20 mm are applied. Fibre contents between 0.5 Vol.-% and 2.5 Vol.-% lead to increased ductility. Nevertheless, with short, flat fibres, a pronounced load increase under tensile loading is usually not achieved after first cracking.

State-of-the-art of UHPC and fibre concrete regarding production, design and durability is summarised in different guidelines (e.g. /AFGC13/, /DAfStb08/, /FHWA06b/, /FHWA06a/). In the last years, different designs and applications of structural elements for building or bridge constructions using UHPFRC have been made (e.g. /Hon16/, /Lau14/, /Lee13/, /Voo14/).

Material properties of UHPFRC vary significantly depending on mixture, fibre content and curing procedure. Usually, uniaxial compressive, tensile and flexural strength are determined in a similar manner compared to normal strength concrete or fibre-reinforced normal strength concrete. Depending on the country and code, different dimensions of test specimens are used. In general, cubes or cylinders are applied to determine the compression strength and Young's Modulus. For the determination of tensile strength, two different approaches are common. On the one hand, the tensile strength is determined by direct, uniaxial tensile tests. For these tests, often specimen with an a priori known failure zone, in terms of notching /RILEM01/ or varying widths over the specimen length /Feh05/ are used. Since these tests are difficult to conduct and the results tend to scatter, on the other hand, often flexural testing on prisms or small beams is applied. Beams in four-point bending /DAfStb10/, /DBV01/ or notched beams in three point bending /RILEM02/ are used to determine flexural strength and crack-mouth opening displacement (CMOD). With small prisms (e.g. 40x40x160 mm³), usually only the flexural strength is derived. The tensile strength f_{ct} can be determined from flexural tensile strength $f_{\mathrm{ct,fl}}$ (e.g. /AFGC13/). UHPFRC usually shows a high tensile strength already after one day, i.e. a high bond strength, which makes applications to pre-tensioned concrete members efficient (e.g. /Ber12/).

2.6 Core Materials for Sandwich Sections

The core material plays a key role for the structural performance of sandwich panels. Without sufficient material characteristics, the load transfer between the different layers is harmed and sandwich action cannot be developed, especially in case of flexible shear connectors or without shear connectors. The most important requirements are low weight, sufficient stiffness and strength as well as physical properties, such as heat or sound insulation. Especially the stiffness perpendicular to the outer facings as well as shear stiffness and strength control the load carrying mechanisms. In comparison to the outer layers made of concrete or steel, core materials show small stiffness and strength. These stiffnesses and strengths are controlled by the composition of materials used for the core layer. On the one hand, homogenous foam cores and on the other hand textured cores, e.g. honeycomb structures, are applied. Since textured cores do not play a key role for sandwich panels applied in building industry /Hor10/, subsequently, only homogeneous core material is shortly discussed.

For sandwich panels in building industries, usually synthetic foam (organic) or mineral rock wool (inorganic) are applied. As synthetic foams, usually polystyrene and polyurethane (PU) are applied. Polystyrene is either expanded by moulding (EPS) or extruded (XPS). The density of EPS is usually in the range of 15-30 kg/m³ and of XPS about 25-50 kg/m³. EPS and XPS show a heat transmission value of roughly 0.030-0.040 W/(m·K). In contrast, PU holds a density in the range of 30-100 kg/m³ and a heat transmission value of 0.024-0.030 W/(m·K) /Pfu07/.

For sandwich panels with concrete facings, usually the FACE-DOWN-METHOD or FACE-UP-METHOD using pre-fabricated slabstock foams are applied (cp. section 2.2.1). In this study, the production method was changed to foaming in pack of hardened concrete layers (cp. sections 2.2.1 and 3.5). For this purpose, polyurethane was applied, since it can be handled without moulding or extrusion process in a precast plant.

PU usually consist of polyol, isocyanate as well as blowing agent and activators to control the chemical reaction. Different properties can be achieved by different mixing ratios of the components. Generally, PU is either produced by moulding, spraying or pouring. The reaction, i.e. expansion, of the components starts shortly after mixture of the components. Thick PU elements can heat up to 150°C during the foaming process

/Dav01/, /Sha15b/ since the chemical reaction is exothermic. Depending on the production process, the materials show anisotropic material behaviour. PU decomposes at temperatures of 250°C. To increase the heat resistance of up to 350°C, polyisocyanurate modified foams (PIR) were developed. The production process is more complex, since the chemical reaction requires 40-45°C /Sha15b/. The structure of the hardened foam shows closed cells filled with blowing agent. This leads to excellent insulation properties /Dav01/.

A detailed summary of production techniques, composition and material behaviour of PU, EPS, XPS and mineral rock wool can be found for example in /Dav01/, /Pfu07/, /Hor10/ or /Sha15b/.

2.7 Reinforcement Made of Fibre Reinforced Polymers

In the last decades, FIBRE REINFORCED POLYMER (FRP) has been developed for a wide range of applications in different fields, such as automotive, aerospace, sports or structural engineering /Jia08/. FRP consists of either carbon, glass or aramid fibres and a resin for impregnation. Usually, thermosetting resins, e.g. polyester, epoxy or vinylester, are used /ACI04/. The properties and characteristics of resins can be controlled only with little limitation. Hence, a generalisation of properties of FRP is practically not possible /ACI04/. CARBON FIBRE REINFORCED POLYMER (CFRP) provides advantages for many applications compared to other FRP materials. It usually holds usually higher strength and Young’s modulus as well as better durability properties compared to FRP using glass or aramid /ACI04/. Subsequently, the basic characteristics and properties of reinforcement and prestressing tendons made of CFRP are described.

CFRP reinforcement provides a high uniaxial strength, light weight and is non-corrosive, among others. It is available as bars, grids, plates or tendons /ACI04/. Tendons are also made as seven-wire strands, as known from steel prestressing members.

CFRP reinforcement and tendons have been investigated in terms of material testing, development of anchorage systems (cp. section 2.8), bond to concrete and structural performance (e.g. /Lu00/, /Mah99/, /Nan96/, /Riz12/, /Sou97/, /Ter13/). Typical material properties of the final product are uniaxial tensile strengths of about 2.000-3.500 MPa, corresponding ultimate strain of 15-20 ‰, Young’s moduli of 150,000 MPa and density of about 1.5 g/cm^3 /ACI04/, /CEB07/. Usually, the carbon fibre content is about 65 %. Under tensile loading, CFRP reinforcement shows a linear elastic material behaviour, without pronounced yielding. The failure is usually rather abrupt, only signalised by cracking noise. Generally, it can be stated that the application of CFRP prestressing tendons reduces the transfer length up to 50 % compared to steel strands due to the relatively rough surface of CFRP (e.g. /Sou97/, /Lu00/, /Ter13/, /Sta13/). Relaxation loses at room temperature are usually less than 1 % (100 h).

According to /ACI04/, the jacking stresses should be kept below 65 % of ultimate strength of the CFRP tendons to avoid creep rupture.

Since the 1990's, different design guidelines for FRP-reinforced or prestressed concrete members have been released, e.g. /JSCE97/, /ACI04/, /CEB07/, /CAN12/. In these guidelines recommendations regarding material selection, testing, flexural and shear design in ultimate limit state well as requirements in serviceability limit state are proposed. Since there is no standardisation of production methods and final products, considerable engineering effort is required /ACI04/. CFRP is not yielding in the well-known manner of steel reinforcement and thus the design is strain-controlled.

2.8 Anchorage Systems for FRP reinforcement

The high uniaxial tensile strength of CFRP is accompanied by a pronounced sensitivity to lateral pressure perpendicular to the longitudinal direction. Hence, the goal of anchorage systems is to reduce the lateral pressure, while providing sufficient anchorage action. Generally, three different types of anchorage systems are used. For building practice in a precast plant, the reusability of anchorage systems is relevant. Thus, systems using resin to provide the anchorage (Fig. 2.11, bottom) are not discussed further. Other systems use clamping or wedge action (Fig. 2.11, top). Reusable clamping anchorages are usually difficult to assemble and often do not provide sufficient counteraction for lateral pressure.

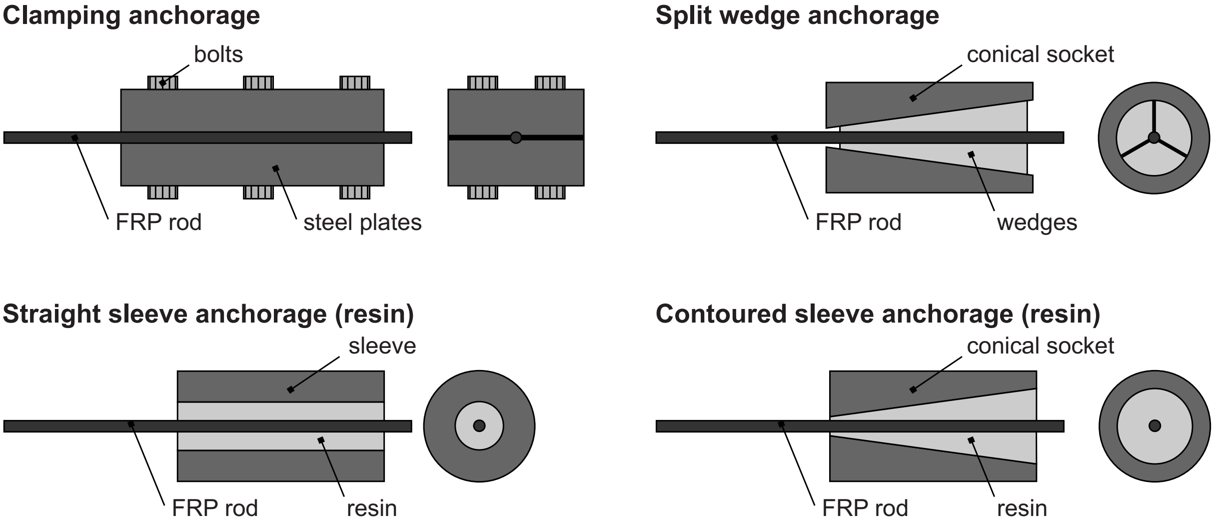

Fig. 2.11 Different types of anchorages in dependence on /ACI04/

Wedge anchorages consist of a barrel and two or three wedges. To reduce the lateral pressure, different approaches can be used. The inner surface of the wedge is usually rather smooth compared to wedge anchorages for steel tendons. The wedges are often made of aluminium, which provides less hardness (e.g. BRINELL) compared to steel wedges. Approaches using different gradients or curvatures for wedges and outer barrels have been investigated (e.g. /Al01/).

2.9 Conclusions

Innovations and developments of high performance materials provide the basis for design flexibility of modern building envelopes. In combination with the well-known principle of sandwich construction, light cross-sections with thin UHPFRC facings are possible. The slenderness of constructions is limited by deflection, cracking of the concrete layers and performance until maximum loading. To increase the stiffness and load-bearing capacity, it seems reasonable to apply folded plate or doubly curved elements made of high-performance materials to sandwich panels. These innovative structural panels can provide efficient precast elements which fulfil several properties at the same time. Besides high stiffness and bearing capacity, these elements provide heat and sound insulation. Additionally, large elements can be easily mounted due the relatively light weight. To provide the background for the development of long-span sandwich panels, in the following chapters, the materials and interaction of materials were analysed by experimental and theoretical investigations.

3 Background of Experimental and Numerical Investigations

3.1 Preface

In the following chapters, experimental and numerical investigations have been performed to develop and analyse spatially shaped load-bearing sandwich elements. The experimental studies have been conducted consistently with the same material combinations and production methods for prestressed sandwich panels (section 3.2-3.5). In the same manner, numerical simulations have been performed using the same solution techniques and assumptions for material models (section 3.6) consistently for all investigations.

3.2 Applied Materials

3.2.1 Concrete

All concrete specimens were fabricated with the same fine-grained mixture of UHPFRC (in dependence on M3Q, cp. section 2.5), developed within the priority programme 1182 of the German Research Foundation /SPP05/. In Table 3.1 the composition of the applied UHPFRC mixture is summarised.

Table 3.1: Mixture of UHPFRC

Material	Quantity [kg/m³]
Cement Cem I 52,5 R HS-NA	825.0
Silica fume	175.0
Quartz powder W12	200.0
Sand 0.125 – 0.5 mm	975.0
Steel fibres (0.9 Vol.-%)	70.7
Water	175.0
Superplasticizer	27.5

The maximum grain size of this mixture is 0.5 mm, which accounts for pouring of UHPFRC for thin elements. High strength steel fibres ($f_y > 2200$ MPa) with a length of 9 mm and a diameter of 0.15-0.17 mm (tolerances) were added to the mixture. The steel fibre ratio was chosen to 0.9 Vol.-% leading to an enhanced ductile behaviour and good pouring quality. Higher ratios do not necessarily result in significantly better ductility and bond behaviour of strands /Ber12/, but to ineffective pouring, since local conglomerations of fibres often take place without proper bond to the concrete matrix. For the application in sandwich panels, steel fibres were used rather than non-metallic fibres, since a wide range of experience exists and only corrosion of the concrete surface occurs, without significant effect of the durability of the structure /Sch08/. For future investigations and applications, the applicability and workability of non-metallic fibres should be considered.

All specimens were cast without external vibrators. The slump flow /DIN09/, /DIN10b/ of the mixture was about 800-900 mm. Further investigations on the fresh concrete have not been conducted. The properties of the hardened concrete were determined in accordance with /DIN00/ and /DIN05/. The uniaxial compression strength (cube, 150x150x150 mm³ was about 170 MPa and the Young's Modulus (cylinder, Ø150 mm, height: 300 mm) was about 45,000 MPa after 28 days. After one day of concrete hardening, a uniaxial compression strength of about 65 MPa and a Young's modulus of about 32,000 MPa were observed. The flexural tensile strength (prism, 40x40x160 mm³) was approximately 6-7 MPa after one day and 18-20 MPa after 28 days.

3.2.2 Reinforcement and Shear Connectors

The aim to provide thin concrete facings for sandwich panels excluded the usage of steel reinforcement at this point of the investigations. Due to the high tensile strength and corrosion resistance, CARBON FIBRE REINFORCED POLYMER (CFRP) was applied in the investigations for rebars or prestressing tendons as well as for shear connectors between the outer concrete facings.

A CFRP single bar and a CFRP seven-wire strand were investigated as prestressing tendons (Fig. 3.1 a) and b), CFCC (carbon fibre composite cable) from Tokyo Rope Ltd.). In the production process, PAN-based carbon fibres (polyacrylonitrile) and epoxy resin are used. From multiple pieces of prepeg, i.e. pre-impregnated fibres as semi-hardened tows, are bundled. Afterwards, these bundles are coated and formed into rods /ACI04/. For multiple-wire strands, these rods are stranded and formed into a tendon /ACI04/. In the last step, the bars or multiple-wire strands are heated and cured. The coating enhances the bond strength to concrete and protects the reinforcement bars and tendons from UV radiation and mechanical damage /ACI04/.

For the investigated bar and seven-wire strand, the maximum tensile strength and Young's moduli were determined by experimental testing. Further investigations on material properties have not been performed.

The general material properties, given by the manufacturer (Tokyo Rope Ltd.) are listed in Table 3.2.

Table 3.2: Material properties of CFRP reinforcement given by the manufacturer

Designation [-]	Diameter [mm]	Eff. cross-sectional area [mm²]	Guaranteed capacity [kN]	Young's Modulus [GPa]
● U 5.0∅	5.0	15.2	38	167
✿ 1x7 7.5∅	7.5	31.1	76	155

From guaranteed capacities, calculated stresses are about 2,500 MPa for the bar (Ø5 mm) and 2,440 MPa for the seven-wire strand (Ø7.5 mm). In conducted tensile tests, the CFRP bar and seven-wire strand reached maximum stresses of 3,200 MPa and 2,650 MPa using the developed wedge anchorage (cp. section 3.3). The Young's moduli of both types of CFRP were determined to 165 GPa and 150 GPa for bar and strand, respectively.

The Poisson's ratio of CFRP usually varies between 0.02 and 0.27 /CEB07/. The thermal expansion in transverse direction is about 10 to 40 times higher than in longitudinal direction /ACI04/, /CEB07/. Experiments at 100°C (212°F) showed a reduction in ultimate limit strength of 20 to 40 % /CEB07/. For the application of CFRP in buildings or bridges, these facts have to be considered. Relaxation losses from jacking stresses are about 0.5 to 1.0 % at 102 h for seven-wire strand /ACI04/. This value is about three to five times smaller compared to steel stands.

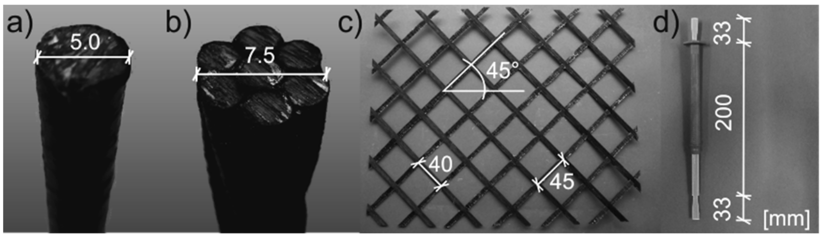

Fig. 3.1 **a) CFRP bar, b) CFRP strand, c) CFRP shear grid (C-Grid®) cut under 45°, d) GFRP pin connector (Thermomass®)**

In general, shear connectors between concrete facings increase the load-bearing capacity of sandwich panels. The application of non-metallic shear connectors causes less thermal bridges in the cross-section than commonly used metal connectors. Furthermore, the connectors can be used for different purposes. The main reason for an application is to bear shear loads, induced by shrinkage of the facings, thermal expansions or bending of the elements. SHAMS /Sha15b/ used shear connectors also as spacers between the inner and outer concrete facings before the panels were foamed with PU mixture (cp. section 3.5). These connectors can partly carry tensile forces during the foaming process /Sha15b/. In the current investigations, mainly continuous shear connectors were applied. Testing of the material characteristics of shear connectors was not carried out, since a wide range of experiences exists (e.g. /Hor10/, /Sha15b/).

For the application in small-scale test specimen and flexural tests on flat elements, an epoxy coated mesh-like textile was cut under 45° to sustain shear loads (Fig. 3.1, c)). The grid spacing is 45 mm in 0°-direction and 40°mm in 90°-direction. The corresponding cross-sectional areas are 40.4 mm²/m and 45.4 mm²/m. The Young's modulus is about 200 GPa with a tensile strength of about 2,300 MPa to 2,600 MPa, in 0°-direction and 90°-direction, respectively. Glass-fibre reinforced polymer (GFRP) pin-connectors (Fig. 3.1, d)) were applied for test purposes in small-scale specimen. These connectors have a tensile strength of 950 MPa and elastic modulus of about 40 GPa under tensile loading and 30 GPa under flexural loading. The cross-sectional area in the anchorage zone is about 25 mm².

3.2.3 Core Material

The PU core used in the experimental studies is a mixture of two components, which exhibits a density of about 90 kg/m³. The mechanical properties of the PU foam were determined by tensile, compressive, and shear tests, according to /DIN13b/, /DIN13c/, /DIN13d/ (Fig. 3.2).

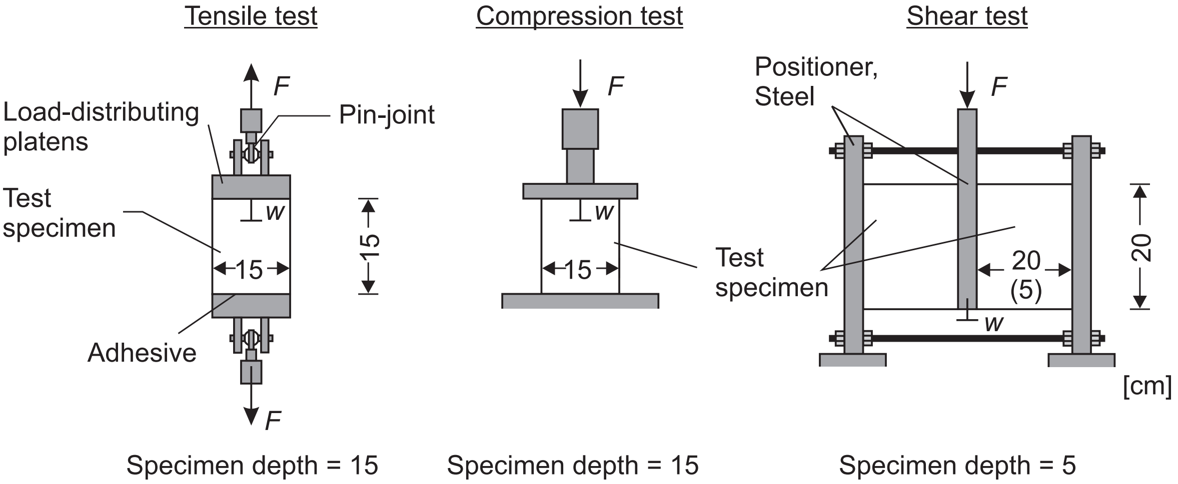

Fig. 3.2 Tests on PU to determine material characteristics

The compressive strength was approximately 950 kPa with a Young's modulus of 32,000 kPa. The tensile strength was measured to 580 kPa with a Young's modulus of 42,000 kPa. Under shear load, the strength was determined to 570 kPa with a shear modulus of 11,500 kPa. All material properties had relatively low standard deviations of less than 15 %.

3.3 Developed Anchorage for CFRP Reinforcement

In section 2.8, examples of anchorages for CFRP reinforcement were exemplarily presented. Based on these findings, a reusable anchor technique was developed to provide an easy way of pre-tensioning CFRP reinforcement in the laboratory. Since a bar and a seven-wire strand were applied, a solution was preferable, which fulfilled the demands of both shapes. The CFRP bar has a relatively smooth surface with a circular cross-section, whereas the seven-wire strand shows a geometrically non-smooth surface.

For simplicity of preparation, a wedge anchor was used rather than clamping anchor, consisting of three aluminium wedges in a steel barrel. To increase friction between the CFRP tendons and the aluminium wedges and to provide a circular and smooth cross-section, especially for the seven-wire strand, a resin was applied on the CFRP reinforcement. The resin consisting of two components (polymerisation catalyst: methyl methacrylate and monomer: methyl acrylic ester) was cured, i.e. hardened, before placing the wedges. The finals design is depicted in Fig. 3.3. The only difference in the anchorages for bar and seven-wire strand were the inner diameters of the steel barrels. The outer diameter of the barrel was 35 mm.

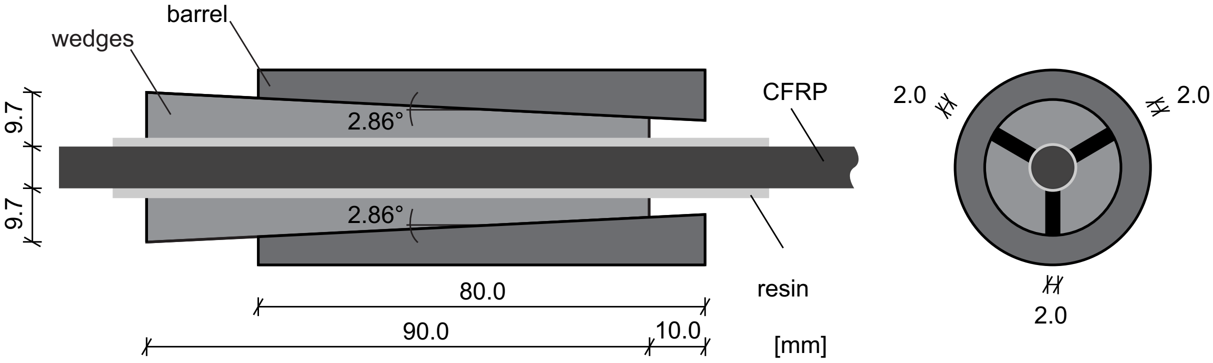

Fig. 3.3 **Developed wedge anchor**

With the developed anchors, stresses of 3,200 MPa and 2,650 MPa could be applied in tensile tests on CFRP bars and seven-wire strands, respectively.

3.4 Prestressing and Casting of Thin UHPFRC Facings

For all UHPFRC members with CFRP reinforcement orientated parallel to the longitudinal axis of the members, i.e. tests on the transfer length (cp. chapter 5) and flat as well as folded plate facings (cp. chapter 7), the standard configuration of prestressing bed in the laboratory was used in combination with developed anchorages (cp. section 3.3) and adjustment screws. In section 2.4 it was discussed that for given hyperbolic paraboloid shapes, straight lines can be found. These lines are straight, but skew to each other. Hence, for investigated doubly curved elements the standard prestressing bed could not be used. Instead, a stiff frame was set up to allow for skew, but linear configuration of reinforcement (Fig. 3.4). Hollow piston cylinders were applied for jacking at each CFRP tendon. Additionally, adjusting screws were used to ensure correct positions of tendons. The tendons were placed about half the diameter up for one diagonal direction and down for the other diagonal direction. With this method it was ensured that the tendons did not bend at the crossing points. In case of elements without prestressing, wedge anchors and adjusting screws were applied for straight alignment of the coiled CFRP rebars.

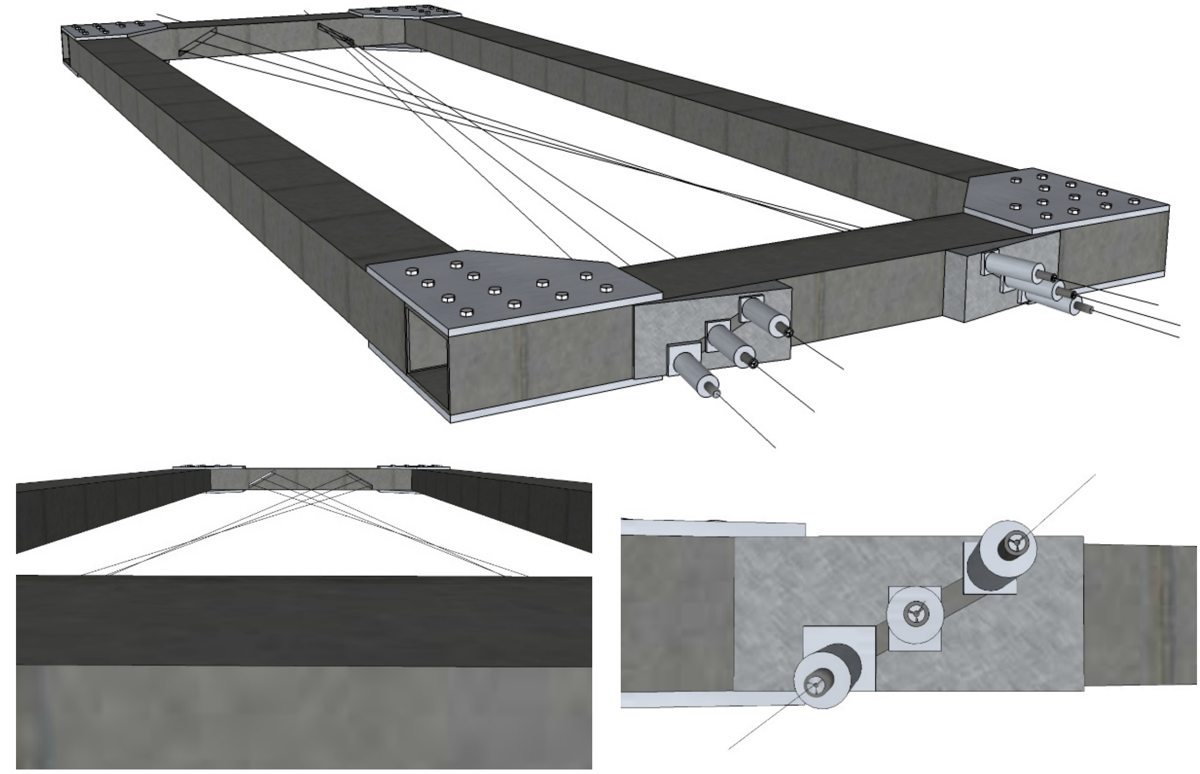

Fig. 3.4 **Developed prestressing frame for doubly curved elements: Illustration of frame with prestressing tendons (top), details of skew, but straight tendons (bottom left) and inclination of hollow piston cylinders (bottom right)**

For all elements with area by area straight edges, the formwork was placed in a standard way. Folded plate elements were cast from top flange in a closed formwork. For doubly curved elements, a closed formwork was set up using the principle of straight but skew lines. A thin medium density fibreboard (MDF) was placed in strips of 50 mm width on wooden frames (Fig. 3.5, left). These frames were shaped like the corresponding top or bottom surface at the particular position. Afterwards, a filler was applied on top of the MDF to provide a smooth surface (Fig. 3.5, right), which is impermeable to water. The elements were cast upside down to avoid discontinuities from casting at midspan (highest position) of the elements. Therefore, at both ends openings were provided to cast in the UHPFRC. Thus, the resulting discontinuities were placed close to the supports, which did not negatively affect structural performance. The UHPFRC mixture was cast from only one side until the formwork was filled up. Hence, ventilation was guaranteed and smooth surfaces with only small air inclusions were producible.

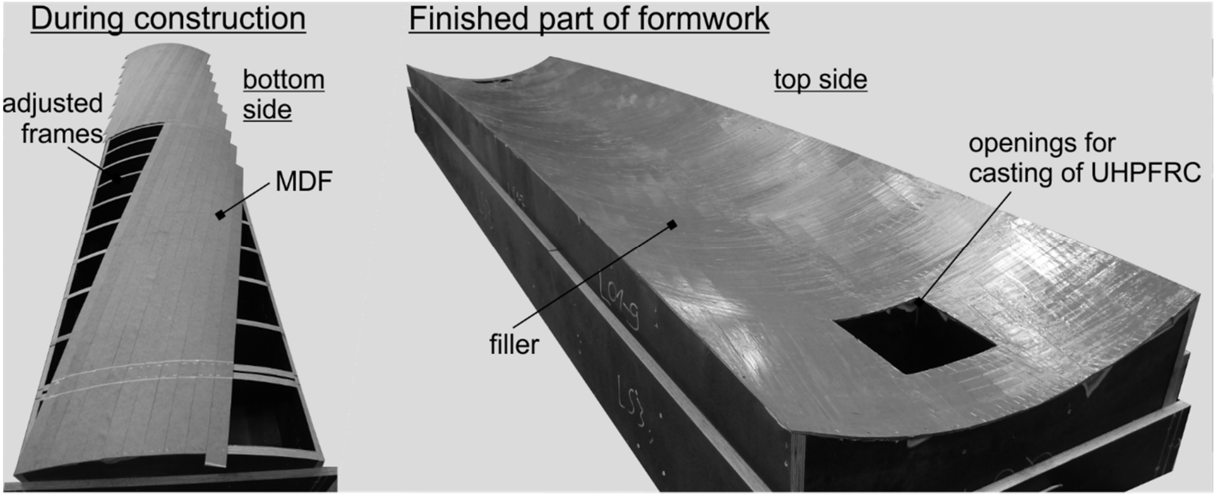

Fig. 3.5 **Formwork for doubly curved elements**

After one day of concrete hardening and stripping of the top side of the formwork, the prestressing forces were released. Afterwards, the elements were turned into final position.

3.5 Production Method for Sandwich Elements

The production method of sandwich sections has a remarkable influence on the quality of the bond zone and consequently on the load-carrying behaviour. Commonly, for sandwich sections with rigid layers, such as concrete facings, multistage processes are applied. In general, one concrete layer is cast and a prefabricated slabstock foam is pressed into the fresh concrete. Afterwards, the second layer is concreted on top. Besides deformations from shrinkage of the concrete layers under different drying conditions, a repeatable high bond quality cannot be achieved and curved or folded plate cross-sections are only to be enabled with high effort (cp. chapter 2).

In order to address these issues, a new production method based on investigations conducted in /Sha15b/ and /Sha15a/ was applied for all test specimens. Adapted from steel sandwich sections, a polyurethane (PU) mixture was foamed in pack between two hardened concrete layers. With this method, various shapes of cross-sections can be generated and a repeatable high bond quality was aimed.

The production process was carried out in the following steps (Fig. 3.6):

a) Casting of UHPFRC for prestressed or reinforced (CFRP) facings;

b) Stripping formwork and fixing of hardened concrete facings in a special wooden formwork (covered with foil);

c) Mixing of PU components and pouring between both UHPFRC facings;

d) Closing the wooden formwork; the mixture expands within a few seconds.

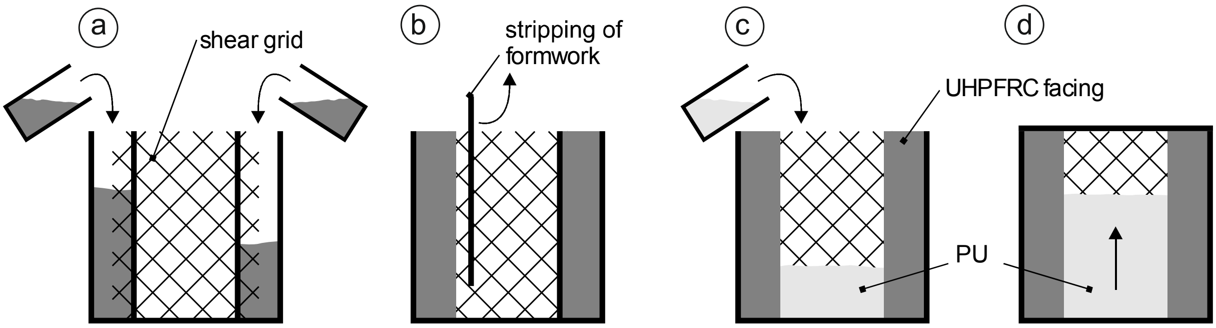

Fig. 3.6 **Schematic illustration of the production procedure of sandwich elements**

Afterwards, the formwork can be removed.

In contrast to investigations conducted in /Sha15b/ (cp. Fig. 2.4 and Fig. 2.5), the mixture was also poured in for large-scale elements. In Fig. 3.7, the production procedure for doubly curved sandwich panels is exemplarily shown. After weighing the two components for the reaction mixture of PU and preparing of formwork with hardened UHPFRC facings, the PU mixture was poured in. The braced wooden formwork was closed and a counterweight was applied to withstand the pressure from expansion of the PU mixture.

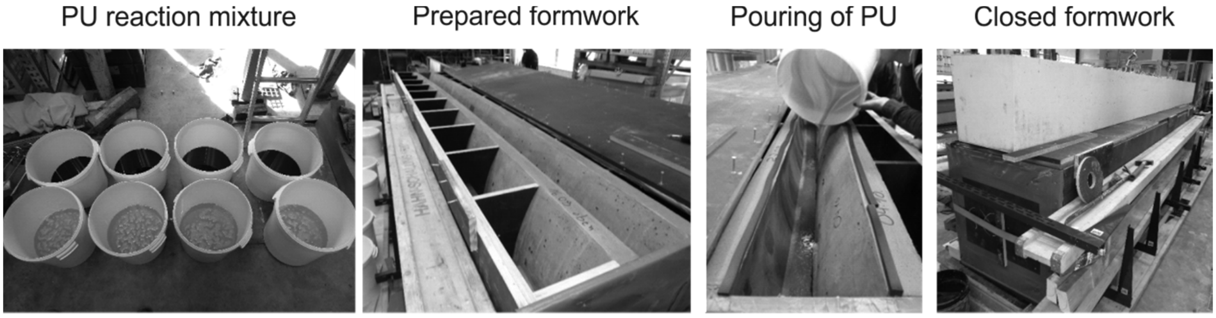

Fig. 3.7 **Production procedure for large-scale sandwich elements**

For the production of the elements, no special treatment of the UHPFRC surfaces was applied.

3.6 Finite Element Modelling

3.6.1 Preface

Non-linear numerical investigations were performed during the development of sandwich panels with UHPFRC facings. The numerical investigations have been performed with the finite element environment ABAQUS /Aba14/ using non-linear models for materials. For each investigation step, the test specimens have been modelled and the results of the calculations were validated with experimental data to evaluate the applicability of the provided material laws for the materials.

3.6.2 Modelling

The numerical investigations were performed using 3D models. When applicable, symmetry of geometry and loading was utilised, i.e. only half or a quarter of the test specimen was modelled using appropriate support conditions. In all cases, 8-node volume elements with reduced integration were applied for concrete, loading plates and PU foam. The reinforcement was idealised as truss members with rigid bond to the surrounding concrete. Only in case of bond investigations, the reinforcement was modelled discretely using volume elements.

All models were simulated using the implicit solution technique of NEWTON RAPHSON procedure. The element size was adapted in dependence on the size of investigated member. General solution controls were set for brittle material behaviour, i.e. $R_n^\alpha = 0.01$ (residual control), $C_n^\alpha = 1.0$ (solution correction control) and $I_0 = 8$ as well as $I_R = 10$ (discontinuous analysis).

For load applications and supports, linear elastic steel plates were modelled for flat test specimens and adjusted elastic UHPFRC elements were assembled continuously over the width for the folded plate and curved elements. The single UHPFRC facings of the were prestressed in a separate simulation and the resulting stresses were imported in a second simulation to investigate the flexural behaviour.

3.6.3 Material Model for Concrete

3.6.3.1 Damage Plasticity Model

Concrete shows a non-linear behaviour under tensile and compressive loading conditions. Different approaches to account for the non-linear material behaviour are widely used. Especially for bending stress states, the DAMAGE PLASTICITY MODEL fulfils the demands to predict the material behaviour of concrete members /Aba14/. Within the model, a smeared cracking approach in combination with scalar damage is used. This model is incorporated in the non-linear finite element software ABAQUS /Aba14/.

The model uses uniaxial stress-strain relationship for tensile and compressive behaviour (Fig. 3.8). Exceeding the linear-elastic capacity, strain softening occurs under tensile loading, while under compression at first strain hardening can be observed, followed by strain softening. Releasing the load results in different stiffness, i.e. Young's Modulus, which is covered by scalar damage parameters d_t and d_c.

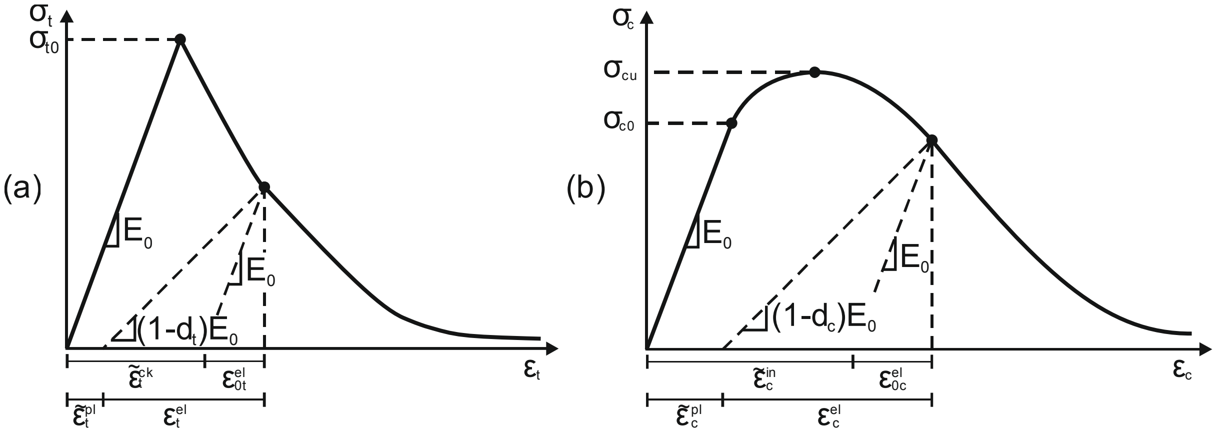

Fig. 3.8 **Schematic stress-strain relationships: tensile (a) and compressive (b) stress with strain softening and hardening (reproduced from /Aba14/)**

Linear and plastic behaviour is described by the yield criterion /Lub89/, /Lee98/, which represents an area in the principal coordinate system. This area is dependent on the ratio of biaxial and uniaxial compressive strength f_{b0}/f_{c0} and the shape factor K_c, which describes the deviator plane (Fig. 3.9 (a)). After reaching the maximum tensile strength, the yield surface is reduced due to softening. Under compressive loads, strain hardening increases the yield surface, which is followed by a reduction of the yield surface at high stresses. The damage parameters control the equivalent plastic strains and hence, the change in yield surface. The direction of the strain vector is described by the yield criterion (Fig. 3.9 (b)). The incorporated damage model uses non-associated plastic flow, i.e. the flow potential is independent of the yield criterion. This results in a non-symmetric material stiffness matrix. The direction of strain increments is perpendicular to the surface of the flow potential. The invariants p and q describe the direction of hydrostatic and deviator stresses (Fig. 3.9 (c)). The eccentricity ε characterises the convergence of the potential function to the asymptote in the vicinity of low hydrostatic pressure. In case the eccentricity tends to zero, the potential function correlates to a straight line with the gradient Ψ, as for the typical Drucker-Prager function. At high hydrostatic pressures, the potential function approaches a straight line with gradient Ψ. In general, the dilatancy (shear thickening) describes the increase in volume under shear loads.

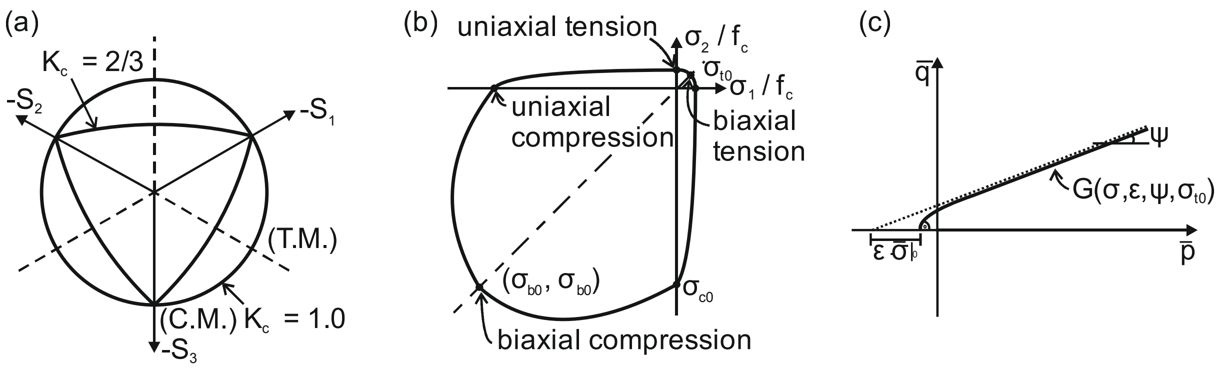

Fig. 3.9 **Yield surface (a) in deviator plane corresponding to different values of K_c, (b) in plane stress and (c) potential function in meridional plane (in dependence on /Aba14/ and /Kue15/)**

3.6.3.2 Determination of Parameters for Damage Plasticity Model

The input values for uniaxial tensile and compressive behaviour were determined by theoretical approaches considering the material properties. For tensile behaviour a stress-displacement (crack-width) relationship was used rather than a stress-strain relationship, since validated theoretical approaches exist and mesh-size dependencies are decreased /Aba14/. Approaches by HILLERBORG /Hil76/, BEHLOUL /Beh96b/ and LEUTBECHER /Leu08/ have been examined for the applied UHPFRC mixture with 0.9 Vol.-% steel fibres. Since only flexural material testing on UHPFRC was carried out, further investigations were performed to determine the uniaxial tensile strength and fracture energy (cp. chapter 4). From this, the approach by HILLERBORG with exponential softening was used (Fig. 3.10, cp. chapter 4). The uniaxial tensile strength was determined to $f_{ct} = 5.0$ MPa and fracture energy $G_f = 2.5$ N/mm. The damage parameter d_t was derived as the normalised reciprocal relationship of the tensile stress-displacement relationship (Fig. 3.10).

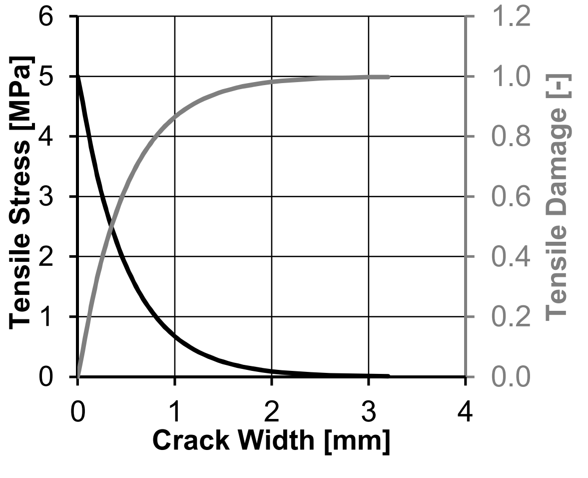

Fig. 3.10 **Tensile stress and tensile damage parameter over the crack width**

Theoretical relationships for the uniaxial compressive stress-strain relationship of concrete are often based on /Sar71/. The formula is simplified in /CEB90/ (equation (3.1)), with the ductility parameter set to zero.

$$\begin{aligned} \sigma_c &= f_{cm} \cdot \frac{k \cdot \eta + \eta^2}{1 + (k-2) \cdot \eta} \\ \eta &= \frac{\varepsilon_c}{\varepsilon_{c1}} \\ k &= n \cdot \frac{E_{c0} \cdot \varepsilon_{c1}}{f_{cm}} \end{aligned} \tag{3.1}$$

According to /Feh05/, it is proposed to apply ε_{c1} =4.0 ‰ and $n = 1.0$ to account for the different material behaviour of UHPRC compared to NSC or HSC. Other models can be found in literature (e.g. in /Maj03/ or /Bal97/) and are not discussed further.

The applied compression stress-strain relationship is shown in Fig. 3.11 and was determined according to /Sar71/ with modification by /Feh05/ (cp. equation (3.1)). The compressive strength $f_{c,cyl}$ and Young's modulus E_c were derived from material testing to $f_{c,cyl}$ = 150 MPa and E_c = 45,000 MPa. Poisson ratio was set to $\nu = 0.2$.

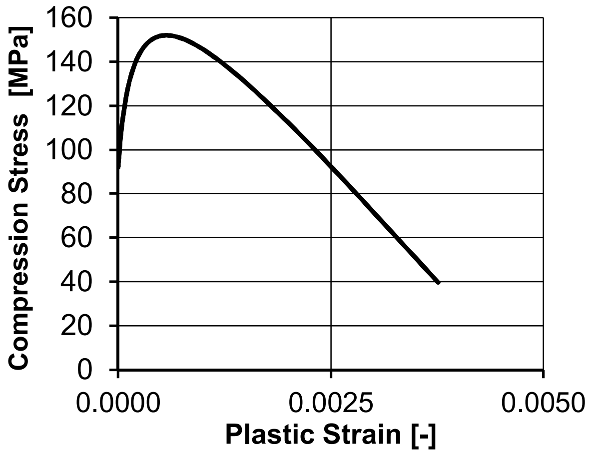

Fig. 3.11 Compression stress-strain relationships

Tests on UHPFRC cubes under multiaxial compression and tension have been conducted by SPECK /Spe07/. It was shown that the average ratios of biaxial to uniaxial compressive strength σ_{b0}/σ_{c0} are about 1.0 (coarse-grained) to 1.08 (fine-grained). In contrast, for NSC usually 1.16 is taken into account.

In Table 3.3 the applied parameters of the DAMAGE PLASTICITY MODEL (cp. chapter 3.6.3.1) used for fine-grained UHPFRC (M3Q) are shown.

Table 3.3: Parameters for the Damage Plasticity Model

Dilatation ψ [°]	Eccentricity ε [-]	σ_{b0}/σ_{c0} [-]	K_c [-]
30	0.10	1.08	0.67

In /Kue15/ the applicability of a DAMAGE PLASTICITY MODEL for UHPFRC material samples was shown for different stress states, i.e. tensile, bi-axial compressive and flexural loading.

3.6.4 Material Model for CFRP

Pre-tensioned bars and strands as well as rovings of the shear grid are mainly subjected to pure tension. To minimise the complexity of numerical models, the anisotropic material behaviour of all CFRP components was neglected. In accordance with HORSTMANN /Hor10/, an isotropic linear-elastic material behaviour with failure at maximum tensile strength was assumed. For the bar, strand and shear grid, the maximum strength and Young's moduli were applied in accordance with information given in section 3.2.2. Poisson's ratio was set constantly to 0.2 /ACI04/, /CEB07/.

3.6.5 Material Model for PU-foam

The bearing behaviour of sandwich panels is greatly affected by the core material. The anisotropic material behaviour of foam, such as polyurethane (PU), cannot be neglected in general. Within the finite element environment Abaqus /Aba14/ this material behaviour can be simplified by the material law CRUSHABLE FOAM in combination with an isotropic and elastic material behaviour. In /Hor10/ it was shown, that results using this approach were in agreement with test results from flexural tests on sandwich sections with TRC-facings.

The elastic part follows the general assumption of HOOKE's law, i.e. the shear modulus can be determined from Young's Modulus and Poisson's ratio, even though Poisson's ratio of foam materials is sometimes outside the range of $0 \leq \nu \leq 0.5$ /Hor10/. In the case of PU in /Hor10/ values of ν in the range of 0.33 up to 2.0 were shown, depending on the density of the core material. For the own investigations, Poisson's ratio was set to 0.41 to account for the relationship of Young's modulus and shear modulus. For the plastic state the CRUSHABLE FOAM material law was applied. The volumetric hardening approach presumes that the yield stress is mainly dependent on compressive stresses. The plastic behaviour is represented by a MISES-circle and an ellipse in meridian direction (Fig. 3.12). Key parameters are the yield points under uniaxial compression stress, hydrostatic compression stress and hydrostatic tensile stress. For the applied PU foam, no test results under hydrostatic stresses exist. Hence, the recommendations from HORSTMANN /Hor10/ were applied, using a compression yield stress ratio of 2.0 and the hydrostatic stress ratio of 1.0.

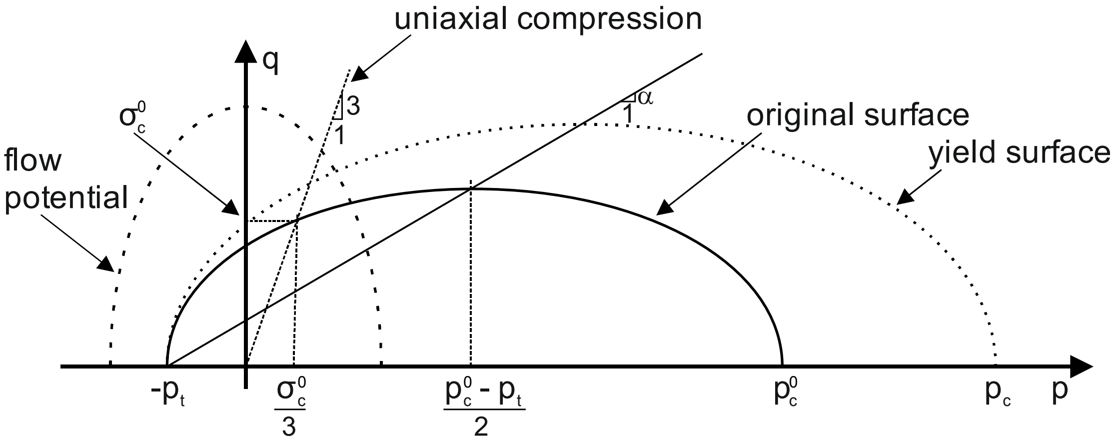

Fig. 3.12 Yield surface and flow potential of CRUSHABLE FOAM material law (reproduced from /Aba14/)

The stress-strain relationship of yield stress under compression was derived from material testing (cp. section 6.4).

HORSTMANN additionally applied the material model SHEAR DAMAGE to further account for a shear failure of the core material. For this model the fracture strain, shear stress rate and strain rate, which is a time-dependent variable, have to be provided. For time-independent analysis, the criterion reduces to the shear stress rate, which is the ratio of Mises-stress q and maximum shear stress $\tau_{\max}$. In the investigations conducted by HORSTMANN, the approach led to a premature compressive failure of the core in the vicinity of the supports. In the own investigations, the core material showed a relatively high density, compared to foams investigated by HORSTMANN. For the own investigations in this thesis, the criterion was applied for test purposes and did not have any influence on the results.

3.6.6 Modelling of Interface UHPFRC-PU

The quality of the interface between facing and core material mainly controls the bearing behaviour of sandwich sections, especially for cases without any additional shear connectors. Hence, an appropriate modelling of the interface zone between UHPFRC and PU core material is a necessary condition. Generally, approaches using springs, cohesive interface or rigid bond are available to model the bond zone.

Rigid bond assumptions usually result in an overestimation of the maximum load and an underestimation of the deflection, since the load-deflection response is only governed by cracking of concrete, failure of reinforcement and deformation or failure of the core material. Spring models are usually a basic approach to model a yielding bond zone. However, extensive calibration is necessary, since non-linear spring stiffnesses cannot directly be determined from small-scale tests. By means of a cohesive interface, the complex delamination process of the interface zone can be modelled. This approach was successfully used in /Hor10/ to characterise the interface of sandwich elements with TRC layers.

Since the non-linear finite element simulations were intended to model the load-deflection response of prestressed sandwich panels, a cohesive interface was applied to account for possible failure of the bond zone. For this purpose a traction-separation relationship was used, which is shown schematically in Fig. 3.13. The nominal traction stresses **t** are dependent on the separation δ.

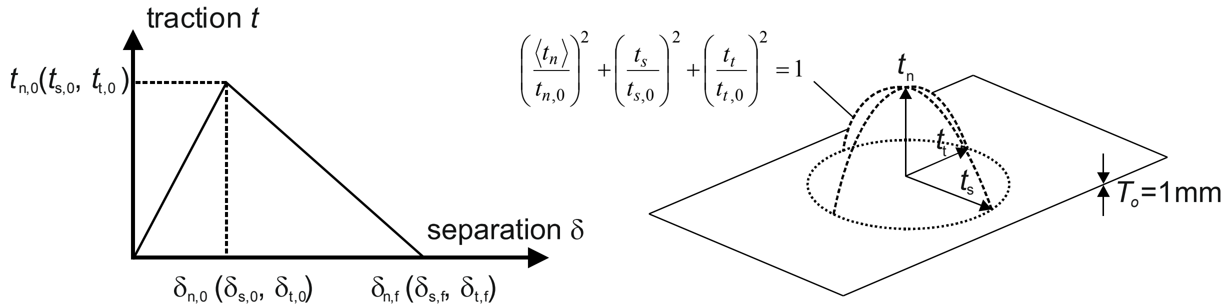

Fig. 3.13 **Traction-separation relationship (left) and quadratic failure criterion (right) (reproduced from /Aba14/ and /Hor10/)**

The failure criterion was assumed as a quadratic relationship (sphere) of bond strengths t_i^0 in different directions (n: normal, s and t: shear). The failure criterion is defined in equation (3.2) and Fig. 3.13. The MACAULAY bracket indicates, that compressive stresses do not contribute to the damage criterion.

$$\left(\frac{\langle t_n \rangle}{t_{n,0}}\right)^2+\left(\frac{t_s}{t_{s,0}}\right)^2+\left(\frac{t_t}{t_{t,0}}\right)^2=1 \tag{3.2}$$

The stiffness reductions after exceeding maximum bond strengths was modelled by “damage evolution”. After failure of elements, it is possible to provide a friction law for the transmission of bond stresses. The bond strengths were derived from tests on small-scale specimens under tensile and shear loading (compare chapter 6.3).

4 Development of Simplified Approaches for UHPFRC Members under Flexural Loading

4.1 Preface

The maximum flexural capacity of conventional RC members is usually determined by neglecting concrete tensile stresses and assuming a stress block over the height of the compression zone. Generally, yielding of steel reinforcement is assumed and from equilibrium of axial forces, the height of the compression zone and thus the flexural capacity are determined. For fibre reinforced concrete, often a stress block over the height of the tension zone is additionally introduced as an estimate to account for crack-bridging effects of fibres (e.g. /DAfStb10/). This smeared approach of fibre contribution is usually sufficiently accurate in the ultimate limit state. Nevertheless, all of these assumptions result in insufficient accuracy when it comes to the determination of moment-curvature or load-deflection relationships. In case of ultra-high performance fibre reinforced concrete (UHPFRC), even short fibres lead to a pronounced post-peak behaviour, which varies over the height of a member for increasing load.

In this chapter, based on existing, theoretical approaches for concrete under tensile loading, general solutions for UHPFRC under flexural loading are derived in terms of moment-curvature and load-deflection relationships. With the aid of these solutions, the tensile strength and the fracture energy of UHPFRC were determined from material samples under flexural loading. Additionally, solutions for moment-curvature relationships of UHPFRC members with pre-tensioned CFRP reinforcement are presented.

4.2 Approaches for Concrete under Tensile Loading

For theoretical and numerical investigations on concrete members, knowledge about the material behaviour is essential. Especially for UHPFRC, the behaviour under tensile loading has to be described accurately since even short fibres lead to crack-bridging effects. Hence, tensile stresses can still be carried even for crack widths of a few millimetres.

Theoretical relationships for the uniaxial tensile behaviour or determination of fracture energy of concrete have been introduced by different researchers, e.g. HILLERBORG /Hil76/, BEHLOUL /Beh96a/, /Beh96b/, FEENSTRA /Fee96/, WANG /Wan01/ and LEUTBECHER /LEU12/, or can be found in guidelines, e.g. MODEL CODE 1990 /CEB90/ or MODEL CODE 2010 /CEB12/. These models vary in complexity, accuracy and easiness of application. The most convenient way is to describe the tensile stresses as a function of crack widths in a smeared cracking approach. Subsequently, two models are shown in particular.

In 1976, HILLERBORG proposed the *fictitious crack model* /Hil76/, a fracture model for concrete using fracture energy. He distinguishes two crack regions. On the one hand the *physical crack region*, where cracking process is completed, hence, stresses cannot be propagated anymore. In this region, *crack opening displacement* (COD) is high, but constant, and stress and displacement show discontinuities. On the other hand, the *fracture process zone* (FPZ), which is located in the physical crack region, where cracks are initiated and propagating. The peak stress at crack tip corresponds to the uniaxial tensile strength. Stresses are continuous and displacements are discontinuous. The cracks are propagated in FPZ in case stresses reach the uniaxial tensile strength. While propagating, the stresses do not become zero. Hence, stress at any point can be calculated.

The model assumes a linear elastic material behaviour until maximum tensile strength is reached. In case the deformations are related to the widths of the FPZ, the tensile behaviour can be expressed by a stress-displacement relationship. The deformations are represented by the crack width of a fictional crack /Hil76/. The relationship of tensile stress σ_{ct} and crack width w is controlled by the tensile strength of concrete f_{ctm} and fracture energy G_f, which is the integral of the σ_{ct}-w relationship. Hence, G_f is the energy needed for a complete separation of a structural member. HILLERBORG proposed different tensile stress-displacement relationships /Hil76/. For these approaches the tensile strength f_{ctm} has to be known a priori. A common assumption is an exponential relationship, similarly shown by /Fee96/:

$$\sigma_{ct} = f_{ctm} \cdot e^{-w/w_1} \tag{4.1}$$

The constant parameter w_1 is always the ratio of fracture energy G_f and tensile strength f_{ctm} as shown in equation (4.2).

$$\begin{aligned} G_f &= \int_0^\infty \sigma_{ct}(w)dw = f_{ctm}\int_0^\infty e^{-w/w_1}dw = f_{ctm} \cdot w_1 \\ &\Rightarrow w_1 = \frac{G_f}{f_{ctm}} \end{aligned} \tag{4.2}$$

For normal strength concrete (NSC), fracture energy G_f is usually determined in dependence on maximum grain size and compression strength f_{cm}, e.g. according to MODEL CODE 1990 /CEB90/.

$$\begin{aligned} G_f &= G_{f0} \cdot \left(\frac{f_{cm}}{10\text{MPa}}\right)^{0.7} \\ G_{f0} &= 0.025 - 0.058 \text{ Nmm/mm}^2 \text{ (NSC)} \end{aligned} \tag{4.3}$$

For example, for concrete class C30 with maximum grain size $d_{\max}$ of 8 mm, equation (4.3) yields $G_f = 0.065$ Nmm/mm² and for $d_{\max}$ of 32 mm $G_f = 0.095$ Nmm/mm². For class C80 fracture energy is roughly doubled for either grain sizes. In MODEL CODE 2010 /CEB12/, fracture energy G_f is simplified to $G_f = 73 \cdot (f_{cm})^{0.18}$, which leads to roughly 80 to 110 % higher values compared to fracture energy determined according to equation (4.3).

In /Feh05/, fracture energy of cured (90°C for three days) UHPFRC with 2.5 Vol.-% fibres was determined from direct tensile tests to about 17 Nmm/mm². On the other hand, fracture energy determined in splitting tests by MA /Ma09/ on coarse- and fine-grained UHPC without fibres was observed smaller than for NSC. Besides tensile strength, fracture energy is dependent on the maximum grain size /Leu08/, /Ma09/. For coarse grain UHPC ($d_g = 5$ mm) without fibres, MA determined the fracture energy to 90 Nmm/mm², whereas for fine grained UHPC, values of about 60 Nmm/mm² were investigated. MA explained this behaviour by a smaller fracture process zone of UHPC without fibres compared to NSC.

In UHPC, usually short flat steel fibres are applied. These short fibres usually pull-out of the concrete, rather than rupture after cracking of concrete. BORNEMANN and FABER /Bor04/ investigated the bond behaviour of flat steel fibres (Ø: 0.15 mm) in fine-grained UHPFRC (mixture M1Q). Bond length of 10 mm and 15 mm resulted in a rupture of the fibres at 2200 – 2700 MPa fibre stress. In contrast, with bond length of 5 mm, the fibres pulled out at 8.7-13.6 MPa (mean value 11 MPa) bond strength. BEHLOUL observed similar bond stresses of 11.5 MPa for the mixture BPR (DUCTAL®) /Beh96b/. VOO and FOSTER /Voo03/ conducted a study on the pull-out behaviour of single fibres from NSC and HSC and derived relationships in dependence on the tensile strength (Table 4.1). For the mixture M1Q LEUTBECHER /Leu08/ reports a uniaxial tensile strength of 9-10 MPa, which leads to a bond strength of 9-10 MPa for straight fibres. This calculated values are in good accordance with results observed by BORNEMANN and FABER /Bor04/.

Table 4.1: Relationship between bond strength and tensile strength of the fibre concrete matrix according to /Voo03/

Fibre Type	Matrix	Bond Strength τ_b
End-hooked	Concrete	$2.5 \cdot f_{ct}$
	Mortar	$2.0 \cdot f_{ct}$
Straight	Concrete	$1.2 \cdot f_{ct}$
	Mortar	$1.0 \cdot f_{ct}$

The maximum stress in fibre concrete σ_{cf0} is mainly dependent on fibre geometry (length l_f and diameter d_f), bond strength τ_f of fibres in concrete, fibre ratio ρ_f and fibre orientation η.

In case, all fibres are exclusively orientated perpendicular to the crack, σ_{cf0} can be derived as follows /Beh96a/, /Beh96b/, /Pfy03/, /Leu08/:

$$\sigma_{cf0} = \rho_f \cdot \tau_f \cdot \frac{l_f}{d_f} \tag{4.4}$$

In equation (4.4) the embedment length varies between zero and $l_f/2$. When the fibre is fully activated over the length of $l_f/2$, σ_{cf0} is reached. The crack width w_0, at which the fibre pull-out regime begins, can be derived as follows:

$$w_0 = \frac{\tau_f \cdot l_f^2}{E_f \cdot d_f} \tag{4.5}$$

The fibre orientation is strongly dependent on the casting process, since fibres orientate in flow direction. Hence, a coefficient of fibre orientation is usually introduced. Different approaches can be found to determine a geometric parameter (e.g. /Lin96/, /Mar06, /Pfy03/). Amongst others, LIN /Lin96/ used a ratio of fibre length projected in tensile direction and the true fibre length as a mean value.

$$\eta = \frac{1}{N} \cdot \sum_{1}^{N} \cos \alpha_i \tag{4.6}$$

N Number of fibres in a considered area

α Angle between fibres

If all fibres are perpendicular to the crack, i.e. a one-dimensional fibre orientation, η equals 1.0. For two- and three dimensional orientated fibres, one can determine the coefficient of fibre orientation analytically. A perfect two-dimensional orientation yields $\eta_{2D} = 2/\pi$, whereas a three-dimensional orientation adds up to $\eta_{3D} = 0.5$. Due to the flow direction of fresh concrete and influences of formwork, varying coefficients of fibre orientations can be observed. Therefore, simplified approaches have been introduced to account for different orientations. Usually, these approaches account for fibres in the vicinity of the formwork with a two-dimensional fibre orientation (e.g. /AFGC13/, /Beh96b/) or empirically found mean values of homogeneous three-dimensional orientation /Voo03/. MARKOVIC /Mar06/ investigated the fibre orientation in beam elements and hourglass-shaped cylinders by counting and an optical (photogrammetric) measurement technique. For flat steel fibres, coefficients of fibre orientation of 0.596 to 0.927 were found, depending on the length and diameter of the fibres. Since for each mixture, fibres of two lengths were used, fibres may have influenced each other. Usually short fibres are less influenced by formwork and flow direction than long fibres /Leu08/, /Mar06/.

Equation (4.4) can be extended by coefficients of fibre orientation η and fibre efficiency g as follows:

$$\sigma_{cf0} = \eta \cdot g \cdot \rho_f \cdot \tau_f \cdot \frac{l_f}{d_f} \tag{4.7}$$

Fibres, which are inclined to a crack, experience an additional deviation force, which can either lead to fibre rupture, flanking of surrounding concrete or even to an enhancement in pull-out force due to friction /Leu08/, /Leu12/. To keep the coefficient of fibre orientation in the same manner as shown before, a coefficient of fibre efficiency g was introduced (e.g. /Beh96b/, /Leu08/, /Mar06/). Depending on the type of concrete, values of g vary greatly. For UHPC (BPR from DUCTAL®) Behloul /Beh96a/ reports values between 1.0 and 1.2. In contrast FOSTER /Fos01/ proposed to neglect the enhanced fibre contribution for fibres inclined more than 60° to the tensile direction. Based on this idea, JUNGWIRTH /Jun06/ derived coefficients of fibre efficiency to $g_{2D} = \sqrt{(0.75)}$ and $g_{3D} = 0.75$. PFYL /Pfy03/ assumes no influence of the inclination angle, i.e. $g = 1.0$. Due to this discrepancy, LEUTBECHER /Leu08/ performed tensile tests on UHPFRC specimens with varying fibre geometry and content. Assuming all parameters of equation (4.7) are known besides g, LEUTBECHER /Leu08/ calculated values of g from experimental results for the two cases of three and two-dimensional orientation. Table 4.2 shows the results for fibre lengths of 9 mm and 17 mm for different fibre ratios ρ_f. It was found that the shorter the fibre and the smaller the fibre ratio, the higher the fibre efficiency.

Table 4.2: Calculated coefficients of fibre orientation η and fibre efficiency g for flat fibre Ø0.15 mm and bond strength τ_f = 11 MPa /Leu08/

	Fibre length l_f [mm]	9		17		
	Fibre ratio ρ_f [Vol.-%]	0.9	2.5	0.9	1.45	2.0
	$\eta \cdot g$	1.23	0.78	0.84	0.56	0.52
Ideal 3D	η_{3D}	0.5	0.5	0.5	0.5	0.5
	g_{3D}	2.46	1.56	1.68	1.12	1.06
Predominant 2D	η_{2D}	0.72	0.72	0.79	0.79	0.79
	g_{2D}	1.71	1.08	1.06	0.71	0.66

Based on the differential equation of bond-slip, stress-crack opening relationships can be derived /Beh96a/, /Pfy03/, /Jun06/, /Leu08/. For simplicity, the contribution to the deformation of concrete matrix as well as fibre stress at the fibre's end are often neglected /Pfy03/. In doing so, the stress-crack opening relationships can be formulated for the fibre activation regime (equation (4.8)) and the fibre pull-out regime (equation (4.9)) /Leu08/, /Pfy03/.

$$\sigma(w) = \left(2 \cdot \sqrt{\frac{w}{w_0}} - \frac{w}{w_0}\right) \cdot \sigma_{cf0} \tag{4.8}$$

$$\sigma(w) = \left(1 - 2 \cdot \frac{w}{l_f \cdot \eta}\right)^2 \cdot \sigma_{cf0} \tag{4.9}$$

Equation (4.9) is often simplified to a linear function (e.g. /Leu08/). Based on equations (4.1), (4.7) and (4.9), two different relationships of tensile strengths and crack widths were investigated. The maximum crack width is limited to ($l_f \cdot \eta$) / 2. As, for example, LEUTBECHER /Leu08/ showed, the formwork influences the fibre orientation significantly, which results mainly in a two-dimensional alignment. Hence, following the assumptions made above, the mean fibre orientation η reaches values of about 0.72 to 0.79. LEUTBECHER /Leu08/ experimentally determined the values g greater than 1.2 for a fine-grained UHPC M2Q with 0.9 Vol.-% short steel fibres (length: 9 mm, Ø: 0.15 mm) as shown in Table 4.2 leading to the top curve in Fig. 4.1. Standard values of η and g /Beh96a/, /Beh96b/, /Leu08/ would lead to $\eta = 0.5$ to 0.72 and $g = 1.2$. Fig. 4.1 shows the clear influence of the fibre efficiency g and fibre orientation η, since all other parameters of equation (4.7) are assumed to be sufficiently determined. Hence, it seems problematic to determine the tensile strength only from geometric and material parameters in the manner of equation (4.7). Besides the tensile strength, the fracture energy is influenced greatly.

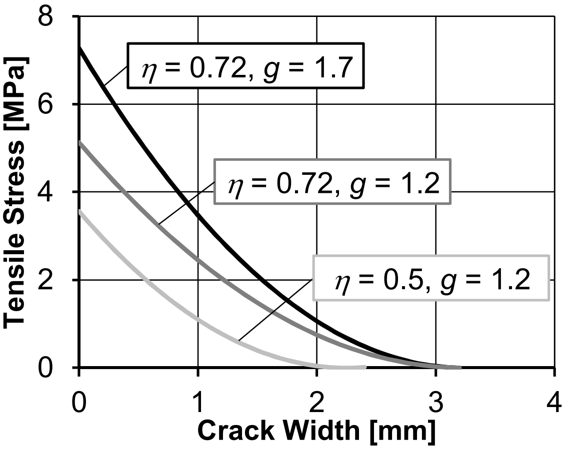

Fig. 4.1 Tensile stress over crack width for different fibre orientations η and efficiencies *g* according to equations (4.7) and (4.9)

By integrating σ(w) (equation (4.9)), the fracture energy G_f can be determined as follows:

$$
\begin{aligned}
G_f &= \int_0^{w_{\max}} \sigma(w) dw = \int_0^{w_{\max}} \left(1 - 2 \cdot \frac{w}{l_f \cdot \eta}\right)^2 \cdot \sigma_{cf0} dw \\
&= \left[-\frac{1}{6} \cdot l_f \cdot \eta \cdot \left(1 - 2 \cdot \frac{w}{l_f \cdot \eta}\right)^3 \cdot \sigma_{cf0} \right]_0^{w_{\max}}, \quad w_{\max} = \frac{l_f \cdot \eta}{2} \\
&= \frac{1}{6} \cdot l_f \cdot \eta \cdot \sigma_{cf0}
\end{aligned}
\tag{4.10}
$$

Applying $\eta = 0.72$ and $g = 1.2$ to equation (4.7) leads to $G_f = 5.5$ Nmm/mm², which is about 34 to 80 times higher than for NSC ($f_{cm} = 50$ MPa) according to equation (4.3). Depending on the fibre length and content, the quadratic approach may result in an overestimation of fracture energy, since the typical softening behaviour of UHPFRC with short steel fibres may be overestimated.

4.3 Derivation of the Tensile Strength from Flexural Testing

The tensile strength of concrete or UHPFRC in particular can generally be determined by experimental testing. Usually, tensile tests on notched prisms /RILEM01/ or hourglass shaped specimen /Feh05/ are conducted. However, tensile tests are complex and the results tend to scatter. Hence, often flexural testing on small prisms /AFGC13/ or small beams (notched in three-point bending /RILEM02/ or un-notched in four-point bending /DBV01/, /DAfStb10/) is applied. The flexural strength has to be transformed into a uniaxial tensile strength. For this purpose, usually an empirical relationship is applied accounting for size effects (height of specimen: h). For UHPFRC, equation (4.11) is often applied (e.g. /AFGC13/ and /DAfStb08/).

$$
f_{ctm} = f_{ct,fl} \cdot \frac{2 \cdot \left(\frac{h}{h_0}\right)^{0.7}}{1 + 2 \cdot \left(\frac{h}{h_0}\right)^{0.7}}, \quad h_0 = 100\,\text{mm}
\tag{4.11}
$$

From material testing on the applied UHPC mixture M3Q with 0.9 Vol.-% steel fibres (cp. Table 3.1), mean values of flexural strength were determined to 18-20 MPa with prisms (40x40x160 mm³) and 9 MPa with beams in four-point bending (150x150x600 mm³) /DAfStb10, DBV01/ (Fig. 4.2).

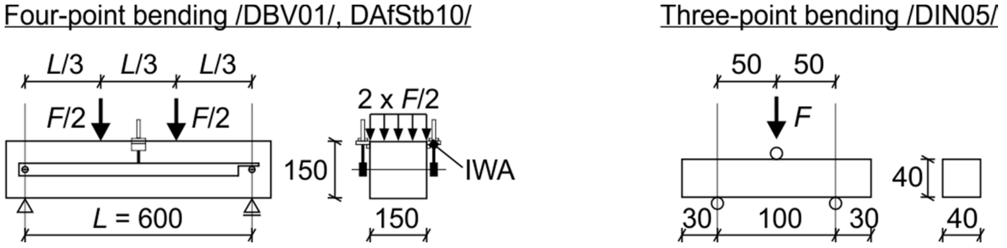

Fig. 4.2 Test setups of four-point bending test on beams /DAfStb10, DBV01/, /DAfStb10, DBV01/ and three point bending tests on small prisms /DIN05/

Depending on the test specimen, equation (4.11) delivers a tensile strength of about 10.3 MPa (small prisms) or 6.5 MPa (beams).

Equation (4.11) is based on findings summarised in /CEB93/. The original relationship was presented in the following form:

$$\frac{f_{ct,fl}}{f_{ctm}} = \frac{1+\alpha_{fl}\cdot\left(\frac{h}{h_0}\right)^{0.7}}{\alpha_{fl}\cdot\left(\frac{h}{h_0}\right)^{0.7}} \tag{4.12}$$

Again, h_0 is the control height and set to 100 mm. α_{fl} is a non-dimensional coefficient, which was determined empirically by finite element simulations /CEB93/ as follows:

$$\alpha_{fl} = 0.8 + \frac{5}{\left(l_{ch}/l_{cho}\right)^{1.5}} \tag{4.13}$$

l_{cho} is a control length of 100 mm. The characteristic length l_{ch} (equation (4.14)) is an indicator of the brittleness of a particular concrete. With increasing characteristic length a particular concrete becomes more brittle.

$$l_{ch} = \frac{E_{cm}\cdot G_f}{f_{ctm}^2} \tag{4.14}$$

In Model Code 1990 /CEB90/ α_{fl} was determined to 1.5, hence assuming $l_{ch} = 375$ mm for normal strength concrete with maximum grain size of 32 mm. Even though, for $\alpha_{fl} = 1.15$ with corresponding $l_{ch} = 600$ mm, a better agreement with test results was obtained (cp. Fig. 4.3) /CEB93/.

Obviously, the ratio of flexural strength $f_{ct,fl}$ and tensile strength f_{ctm} is not constant. Neither for constant height of the test specimen, as assumed in equation (4.11), nor for different types of concrete, since it strongly depends on the characteristic length l_{ch}. In Fig. 4.3, results of flexural and tensile testing on NSC specimen with a maximum aggregate size of 32 mm and varying depths of the specimens are shown.

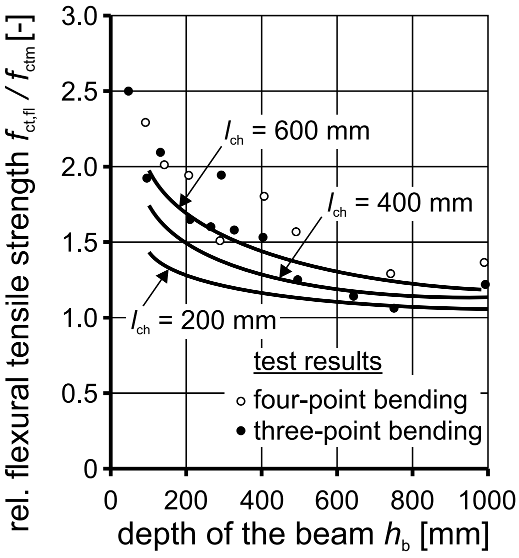

Fig. 4.3 **Experimental results /DAfStb76/ and effect of beam depth on relative flexural strength according to equations (4.12)-(4.14) (reproduced from /CEB93/)**

The effects of varying depths of the test specimens and the influence of characteristic lengths make a general conversion from flexural to tensile strength for UHPFRC difficult, especially without tensile testing. Then, values of the fracture energy G_f and the tensile strength f_{ctm} can only be assumed to determine the characteristic length l_{ch} or profound investigations have to be carried out.

Another approach can be found in Eurocode 2 including German annex /DIN04/. A relationship for HSC (up to class C100/115) is provided to determine the uniaxial tensile strength from the uniaxial compression strength only (equation (4.15)). Even though UHPFRC is not regulated in Eurocode 2 /DIN04/, BERTRAM /Ber12/ applied equation (4.15) to determine tensile strength of UHPFRC. Since, increasing fibre content leads to increasing tensile strength, but not necessarily to increasing compressive strength, the same average values for tensile strength are determined applying equation (4.15). Nevertheless, these values were in better agreement with results of direct tension tests by BERTRAM /Ber12/ as determined values from equation (4.11) using tests results from prisms (40x40x160 mm³) under three-point bending.

$$f_{ctm} = 2.12 \cdot \ln\left(1 + f_{cm}/10\right) \tag{4.15}$$

From material testing on the applied UHPFRC mixture M3Q with 0.9 Vol.-% steel fibres (cp. Table 3.1), a uniaxial compression strength $f_{cm,28d}$ of about 150 MPa was determined, which yields a tensile strength of about 5.9 MPa.

Both approaches result in unsatisfying values of the tensile strength since they are either strongly dependent on the specimen size and special material characteristics have to be known in advance or they do not account for different fibre contents.

Consequently, a simplified approach was derived to determine the uniaxial tensile strength from beam tests according to /DBV01/, /DAfStb10/ under flexural loading. Therefore, the theoretical relationships of stress-displacement relationships summarised in chapter 4.2 were considered. With equation (4.7) the theoretical tensile strength can be determined from mainly geometric properties only. However, for the applied UHPFRC mixture, this equation can only lead to appropriate values by assuming high values of fibre efficiencies g. The same issues were observed by Leutbecher (cp. Table 4.2). In contrast, for equation (4.1) the uniaxial tensile strength f_{ctm} has to be determined from experimental testing or assumed. Additionally, the fracture energy G_f controls the decreasing tensile stresses for increasing crack widths. Behloul and Leutbecher used equation (4.9) to describe the off-peak behaviour of tensile stresses for increasing crack width. Since equation (4.9) is a quadratic function, a priori, a very ductile behaviour is assumed, which fits well for high fibre ratios, e.g. 2.5 Vol.-%. Mathematically, equation (4.9) shows a minimum at maximum crack widths. Hence, for an integration case, distinctions have to be made for parts in cross-sections, where the maximum crack width is reached and no stresses can be carried. The same issue results for linear or bi-linear approaches for stress-crack widths relationships. A linear softening approach could be used for the applied UHPFRC, by decreasing maximum crack width and hence fracture energy. To find a closed solution, the exponential approach (equation (4.1)) was applied for the following examinations on rectangular cross-sections.

Fig. 4.4 shows a free body cut of a beam under flexural loading. The corresponding strain distribution (Bernoulli hypothesis) may lead to the depicted stress distribution after first cracking. The compressive zone (x_0) is assumed to result in a linear stress distribution. The same applies to the tensile zone, which remains un-cracked (x_1). For the cracked zone (x_2) the tensile stresses are assumed to decrease exponentially according to equation (4.1).

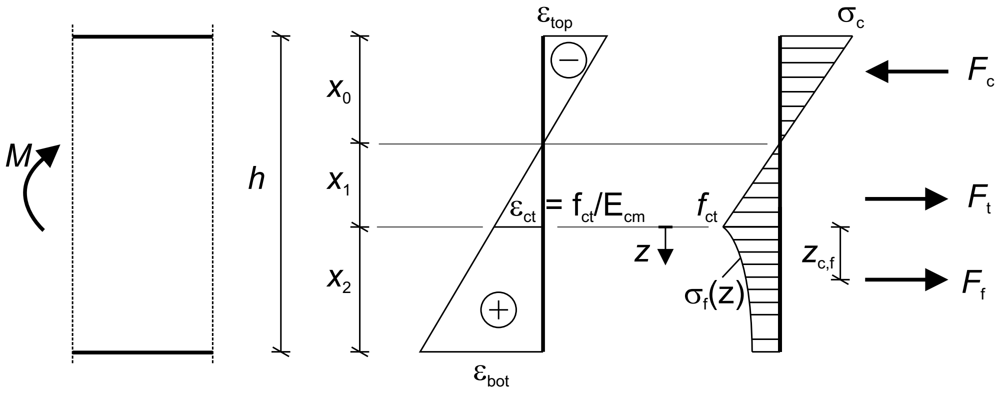

Fig. 4.4 Stress and strain distribution for a cracked UHPFRC beam element

By applying the strain ε rather than crack width w to equation (4.1) according to /AFGC13/, one obtains the stress-strain relationship for concrete under tensile loading as follows:

$$\begin{aligned} &\varepsilon = \frac{f_{ct}}{E_{cm}} + \frac{w}{l_c} = \varepsilon_{ct} + \frac{w}{l_c} \\ &\quad \Rightarrow \sigma(\varepsilon) = f_{ct} \cdot \exp\left(-\frac{1}{w_1} \left(\varepsilon \cdot l_c - \varepsilon_{ct} \cdot l_c \right) \right) \end{aligned} \tag{4.16}$$

Besides the strain ε, the stress is dependent on w_1 (ratio of fracture energy G_f and tensile strength f_{ct}), Young's modulus E_{cm} and a length l_c. The length l_c is often called characteristic length /AFGC13/ but must not be confused with the characteristic length l_{ch} according to equation (4.14). l_c is the length of an influence zone in the vicinity of cracks. In /AFGC13/, it is proposed that the characteristic length l_c can be approximated by 2/3 h (h: height of cross-section) for rectangular cross-sections to convert stress-displacement relationships. Nevertheless, l_c is dependent on the cracking behaviour of a concrete member which is influenced by different parameters such as height of the specimen, fibre content or reinforcement ratio. Hence, the parameter l_c has to be chosen carefully for larger heights. For the investigations in this section, l_c was approximated by 2/3 h since the heights of the specimens were rather small. Since the stress varies over the height, the strain is introduced as a function of the control variable z (cp. Fig. 4.4) (theorem of intersecting lines).

$$\begin{aligned} &\varepsilon(z) = \varepsilon_{bot} \cdot \frac{z}{x_2} + \varepsilon_{ct} \\ &\quad \Rightarrow \sigma(z) = f_{ct} \cdot \exp\left(-\frac{1}{w_1} \cdot \frac{\varepsilon_{bot} \cdot l_c}{x_2} \cdot z \right) \end{aligned} \tag{4.17}$$

The depicted forces F_c, F_t and F_f can be determined as follows:

$$\begin{aligned} F_c &= \frac{1}{2} \varepsilon_{top} \cdot E_{cm} \cdot b \cdot x_0 \\ F_t &= \frac{1}{2} \varepsilon_{ct} \cdot E_{cm} \cdot b \cdot x_1 \\ F_f &= \int_0^{x_2} b \cdot \sigma(z) dz \\ &= b \cdot f_{ct} \cdot \int_0^{x_2} \exp\left(-\frac{1}{w_1} \cdot \frac{\varepsilon_{bot} \cdot l_c}{x_2} \cdot z \right) dz \\ &= b \cdot f_{ct} \cdot \frac{w_1}{\varepsilon_{bot} \cdot l_c} \cdot x_2 \cdot \left(1 - \exp\left(-\frac{\varepsilon_{bot} \cdot l_c}{w_1} \right) \right) \end{aligned} \tag{4.18}$$

It needs to be checked that the concrete compression strain remains smaller than 4.0 ‰. The corresponding heights of resulting forces are directly related to the strains:

$$\begin{aligned}
\frac{x_0}{h} &= \frac{\varepsilon_{top}}{\varepsilon_{top} + \varepsilon_{bot}} \\
\frac{x_1}{h} &= \frac{\varepsilon_{ct}}{\varepsilon_{top} + \varepsilon_{bot}} \\
\frac{x_2}{h} &= 1 - \frac{x_0}{h} - \frac{x_1}{h} = \frac{\varepsilon_{bot} - \varepsilon_{ct}}{\varepsilon_{top} + \varepsilon_{bot}}
\end{aligned} \tag{4.19}$$

From horizontal equilibrium (equation (4.20)), one can determine the upper strain ε_{top} as a function of ε_{bot}.

$$\begin{aligned}
&\sum H = 0: \\
&\Leftrightarrow F_c - F_t - F_f = 0 \\
&\Rightarrow \varepsilon_{top} = \varepsilon_{ct} \cdot \sqrt{1 + 2 \cdot \varepsilon_{ct} \cdot \frac{w_1}{\varepsilon_{bot} \cdot l_c} \cdot \left(\frac{\varepsilon_{bot}}{\varepsilon_{ct}} - 1 \right) \cdot \left(1 - \exp\left(-\frac{l_c \cdot \varepsilon_{bot}}{w_1} \right) \right)}
\end{aligned} \tag{4.20}$$

For the exponential stress distribution of cracked concrete, the lever arm is determined as follows:

$$\begin{aligned}
z_{c,f} &= \frac{1}{F_f} \int_0^{x_2} b \cdot z \cdot \sigma(z) dz \\
&= \frac{b \cdot f_{ct}}{F_f} \cdot \int_0^{x_2} z \cdot \exp\left(-\frac{1}{w_1} \cdot \frac{\varepsilon_{bot} \cdot l_c}{x_2} \cdot z \right) dz \\
&= \frac{b \cdot f_{ct}}{F_f} \cdot \left(\frac{w_1 \cdot x_2}{\varepsilon_{bot} \cdot l_c} \right)^2 \cdot \left[1 - \exp\left(-\frac{\varepsilon_{bot} \cdot l_c}{w_1} \right) \cdot \left(1 + \frac{\varepsilon_{bot} \cdot l_c}{w_1} \right) \right] \\
&= \frac{w_1 \cdot x_2}{\varepsilon_{bot} \cdot l_c} \cdot \frac{1 - \exp\left(-\frac{\varepsilon_{bot} \cdot l_c}{w_1} \right) \cdot \left(1 + \frac{\varepsilon_{bot} \cdot l_c}{w_1} \right)}{1 - \exp\left(-\frac{\varepsilon_{bot} \cdot l_c}{w_1} \right)}
\end{aligned} \tag{4.21}$$

Hence, the equilibrium of moments leads to an acting moment M:

$$M = F_c \cdot \left(\frac{2}{3} x_0 + x_1 \right) - F_t \cdot \frac{x_1}{3} + F_f \cdot z_{c,f} \tag{4.22}$$

The curvature κ is calculated from resulting strain distribution (BERNOULLI hypothesis).

$$\kappa = \frac{\varepsilon_{top} + \varepsilon_{bot}}{h} = -\frac{d^2w/ds^2}{\sqrt{1-(dw/ds)^2}} \approx -\frac{d^2w}{dx^2} = -\frac{M}{EI} \qquad (4.23)$$

Since, the curvature κ can be approximated by the second derivative of the deflection w (equation (4.23)), the deflection is estimated by integration (equation (4.24)). For small deflections, the chord s is assumed to be of same length as control variable x. Hence, the parts due to kinematic considerations of forming cracks were neglected. The constants can be determined by boundary conditions, in the case of a simply supported beam by zero deflection at the supports.

$$\begin{aligned} & w(x) = -\frac{\kappa}{2} \cdot x^2 + C_1 \cdot x + C_2 \\ & \text{Simply supported beam}: w(0) = 0,\ w(L) = 0 \\ & \Rightarrow w(x) = -\frac{\kappa}{2} \cdot x^2 + \frac{\kappa}{2} \cdot L \cdot x \\ & \Rightarrow w(L/2) = \kappa \cdot \frac{L^2}{8} \end{aligned} \qquad (4.24)$$

In Fig. 4.5, moment-curvature and load-deflection relationships are exemplarily shown for a beam under four-point loading according to /DBV01/, /DAfStb10/ (cp. Fig. 4.2).

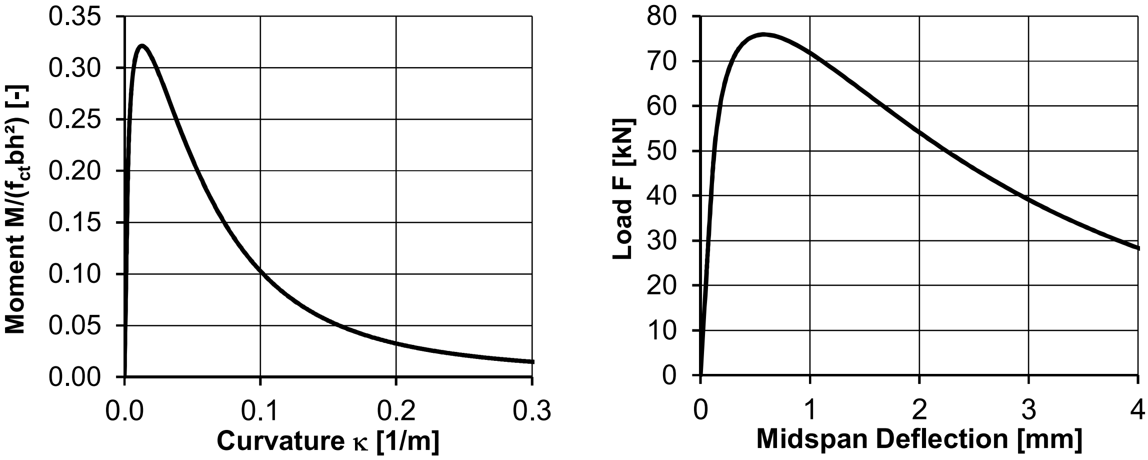

Fig. 4.5 Example of theoretical moment-curvature (left) and load-deflection (right) relationships for f_{ct} = 7.0 MPa and w_1 = 0.5

For experimentally determined load-deflection responses, the tensile strength f_{ctm} and parameter w_1 (ratio of fracture energy G_f and uniaxial tensile strengths f_{ctm}) can be iteratively altered until maximum load and residual loads at 4 mm deflection coincide.

For validation, an issue observed by BERTRAM /Ber12/ was investigated closely. Amongst others, BERTRAM /Ber12/ tested coarse-grained UHPFRC with small fibre content of 0.9 Vol.-% in four-point bending tests according to /DBV01/, /DAfStb10/ and under direct tensile load according to /RILEM01/. The mixture was based on B4Q

/Feh05/, /Spe07/. The direct tension tests were performed on saw-cuts (prisms, 50 x web thickness x 150 mm³) from beams under shear loading. Afterwards, the prisms were notched to provide a residual cross-section of about 20 cm². Due to this procedure, the tensile tests were conducted approximately 60 days after casting, whereas flexural beam tests were performed after 28 days. Comparing the results of tension tests and calculated values of tensile strength from flexural testing, BERTRAM /Ber12/ observed differences. The material properties determined by BERTRAM are shown in Table 4.3. In Fig. 4.6 representative experimental results of flexural tests under four-point loading are shown.

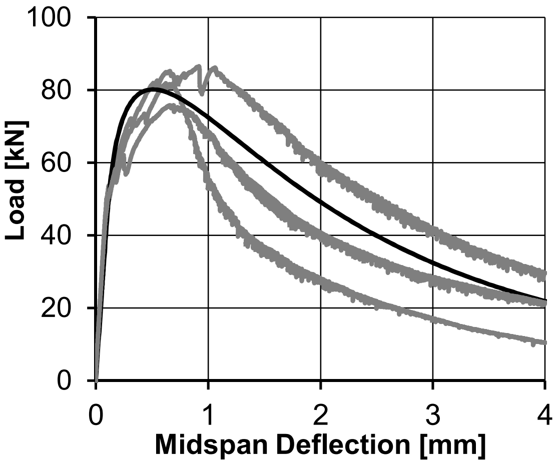

Fig. 4.6 **Comparison of representative results from flexural beam tests (grey) and calculated load-deflection relationship (black) for coarse-grained UHPFRC with 0.9 Vol.-% (17.5 mm, Ø0.15 mm)**

To determine tensile strength f_{ctm} and fracture energy G_{f} of the applied UHPFRC mixture, the maximum load and corresponding load at 4 mm deflection from experimental testing according to /DAfStb10/ were iteratively compared to theoretically determined values using equations (4.22) to (4.24). The parameter l_{c} was assumed to be $2/3 \cdot h = 100$ mm. In Table 4.3, the values of tensile strength $f_{\mathrm{ct,det}}$ and $G_{\mathrm{f,det}}$ are shown. The tensile strength $f_{\mathrm{ct,det}}$ corresponds well to the experimentally determined tensile strength $f_{\mathrm{ct,exp}}$ for UHPFRC (0.9 Vol.-%). For comparison, the calculated load-deflection response is shown in Fig. 4.6.

Table 4.3: **Material properties from experimental testing /Ber12/ and derived tensile strength and fracture energy using the simplified approach**

ρ_{f} [Vol.-%]	$f_{\mathrm{cm,cube},100}$ [MPa]	E_{cm} [GPa]	$f_{\mathrm{ct,exp}}$ [MPa]	$f_{\mathrm{ct,flex}}$ [MPa]	$f_{\mathrm{ct,\,eq.\,(4.11)}}$ [MPa]	$f_{\mathrm{ct,\,eq.\,(4.15)}}$ [MPa]	$f_{\mathrm{ct,det}}$ [MPa]	$G_{\mathrm{f,det}}$ [N/mm]
0.9	~180	~50	~6.5	~25	~12.7	~6.3	7.7	2.9

For the UHPFRC (M3Q, $\rho_{\mathrm{f}} = 0.9$ Vol.-%) used for the development of sandwich panels (cp. following chapters), the approach was applied in the same manner since direct tension tests were not conducted. In Fig. 4.7, representative test results (grey) of flexural testing on small beams /DAfStb10/ are shown. The theoretically determined load-deflection relationship (black) is shown for comparison. Again, l_c was assumed to 100 mm which corresponds to $2/3 \cdot h$.

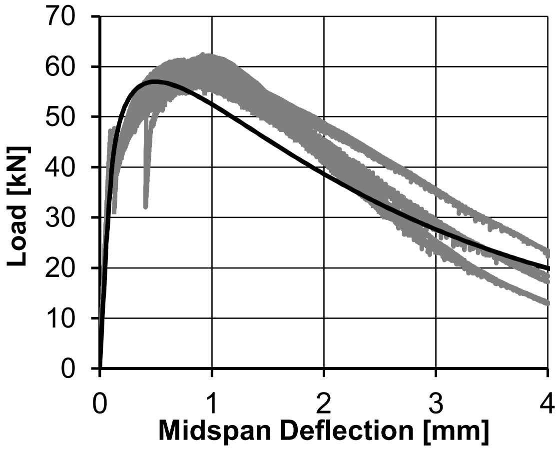

Fig. 4.7 Comparison of representative results from flexural beam tests (grey) and calculated load-deflection relationship (black)

A tensile strength f_{ctm} of 5.0 MPa and corresponding fracture energy G_f of 2.5 Nmm/mm² were determined. Tests on small prisms in three-point bending according to /DIN05/ (Fig. 4.2) showed a mean flexural strength of 20 MPa with corresponding maximum load of about 9.5 kN. Since only maximum load is measured in these tests, fracture energy cannot be derived. Nevertheless, assuming the same value of $w_1 = 0.5$, results in a tensile strength of 4.8 MPa which is in accordance with results from four-point bending tests on beams. The mean values after one day, where determined to $f_{ctm} = 2.5$ MPa and $G_f = 1.25$ Nmm/mm². Since beam tests were not conducted parallel to each experimental investigation, the mean values were taken into account. Based on these values ($f_{ctm} = 5.0$ MPa, $G_f = 2.5$ Nmm/mm²), all further investigations were conducted, unless stated otherwise. The values of tensile strength and fracture energy were used to establish the exponential stress-displacement relationship according to equation (4.1) as basis for further considerations in terms of numerical and theoretical investigations.

4.4 Flexural Behaviour of UHPFRC with CFRP Reinforcement

For theoretical investigations on sandwich panels with UHPFRC facings subjected to flexural loading (cp. chapter 7), the residual strength of cracked UHPFRC layers has to be determined in dependence on applied loading. The cross-sections of investigated sandwich sections were either reinforced or prestressed with CFRP rebars or seven-wire strands, respectively. Hence, the bearing ratios of fibres and reinforcement have to be determined. In Fig. 4.8, a rectangular cross-section of a fibre reinforced concrete member prestressed with CFRP reinforcement as well as corresponding strain (BERNOULLI hypothesis) and stress distributions is shown. This strain and stress distributions are only valid for predominant flexural loading. For predominant axial force *N* (tension or compression), the strain and stress distributions have to be altered in the well-known manner as for standard design of RC.

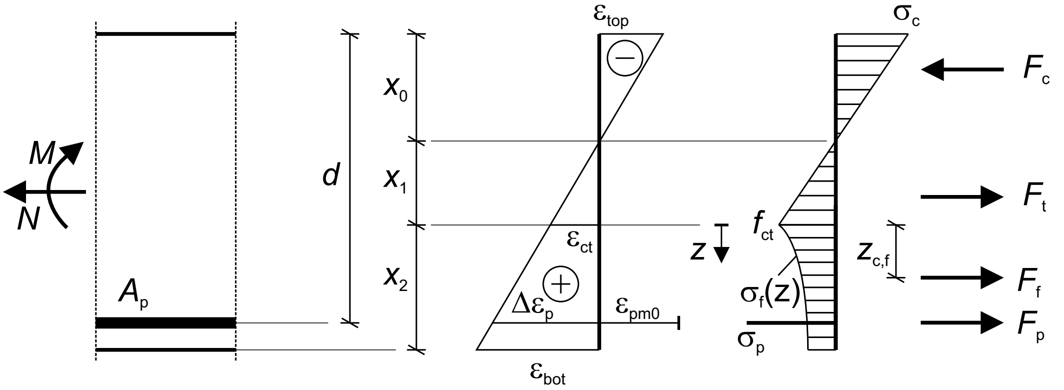

Fig. 4.8 **Strain and stress distribution of a cross-section made of fibre reinforced concrete subjected to flexural loading**

The same assumptions as in the previous section were made for UHPFRC under compression and tension (cp. equation (4.18)). In this procedure, the assumption of critical length $l_c = 2/3 \cdot h$ has to be verified, since this approximation is established for conversion of stress-displacement and stress-strain relationships. The crack distances are strongly dependent on the reinforcement ratio. According to /CEB12/, the characteristic length l_c can be determined as minimum value of the distance between cracks s_{rm} and the distance from the neutral axis to the extreme tensile fibre z_{ext}.

$$l_c = \min\{s_{rm}, z_{ext}\} \tag{4.25}$$

The mean distance between cracks can be approximated by the following empirical equation according to /CNR07/:

$$s_{rm} = \xi \cdot \left[50 + 0.25 \cdot k_1 \cdot k_2 \cdot \frac{\phi}{\rho} \right] \tag{4.26}$$

s_{rm}	average distance of cracks [mm]
y	distance of neutral axis to exterme tensile fibre [mm]
ξ	non - dimensional parameter : $\xi = 1$ for $l_f/d_f < 50$ $\xi = 50 \cdot d_f/l_f$ for $50 \le l_f/d_f \le 100$ $\xi = 0.5$ for $l_f/d_f > 100$
d_f	diamater of fibres [mm]
l_f	length of fibres [mm]
k_1	0.8 for high bond bars, 1.6 for smooth bars
k_2	0.5 for pure bending, 1.0 for pure tension
ϕ	diamater of reinforcing bars [mm]
ρ	geomtric reinforcement ratio

In case of the applied UHPFRC mixture using short steel fibres (d_f = 0.15-0.17 mm, l_f = 9 mm), ξ equals 1.0. For a plane layer (height: 60 mm, width: 300 mm) and four CFRP single wires (4x15.2 mm²), as applied for flat sandwich sections in chapter 7, a mean distance of cracks of approximately s_{rm} = 42 mm is obtained. In this case, high bonded bars and pure-bending were assumed. Since the distance of the neutral axis to the extreme tensile fibre y is 30 mm, l_c equals 30 mm.

For CFRP reinforcement, a linear elastic material behaviour without yielding was assumed. Hence, it is constrained by the linear strain distribution. The resulting force in the pre-tensioned CFRP reinforcement F_p and the corresponding strain from the strain distribution are calculated as follows. In case of non-prestressed members, ε_{p0} vanishes.

$$F_p = \left(\Delta\varepsilon_p + \varepsilon_{p0}\right) \cdot E_p \cdot A_p; \;\; \Delta\varepsilon_p = \frac{d - x_0}{x_0} \cdot \varepsilon_{top} \tag{4.27}$$

From horizontal equilibrium, one can determine the upper strain ε_{top} as a function of ε_{bot} for a rectangular cross-section (equation (4.29)) applying equations (4.16) to (4.19).

$$\begin{aligned}
&\sum H = 0: \\
&\Rightarrow F_c - F_t - F_f - F_p + N = 0 \\
&\Rightarrow \frac{1}{2}\varepsilon_{top} \cdot E_{cm} \cdot b \cdot x_0 - \frac{1}{2}\varepsilon_{ct} \cdot E_{cm} \cdot b \cdot x_1 - \ldots \\
&\ldots - b \cdot f_{ct} \cdot \frac{w_1}{\varepsilon_{bot} \cdot l_c} \cdot x_2 \cdot \left(1 - \exp\left(-\frac{\varepsilon_{bot} \cdot l_c}{w_1}\right)\right) - \ldots \\
&\ldots - \left(\frac{d - x_0}{x_0} \cdot \varepsilon_{top} + \varepsilon_{p0}\right) \cdot E_p \cdot A_p + N = 0 \\
&\Leftrightarrow \varepsilon_{top}^2 \cdot \left(\frac{1}{2} + \frac{E_p \cdot A_p}{E_{cm} \cdot b \cdot h} \cdot \left(1 - \frac{d}{h}\right)\right) - \ldots \\
&\ldots - \varepsilon_{top} \cdot \left(\frac{E_p \cdot A_p}{E_{cm} \cdot b \cdot h} \cdot \left(2 \cdot \frac{d}{h} \cdot \varepsilon_{bot} + \varepsilon_{p0} - \varepsilon_{bot} - \frac{N}{E_p \cdot A_p}\right)\right) - \ldots \\
&\ldots - \frac{1}{2} \cdot \varepsilon_{ct}^2 - \varepsilon_{ct} \cdot \frac{w_1}{l_c \cdot \varepsilon_{bot}} \cdot \left(\varepsilon_{bot} - \varepsilon_{ct}\right) \cdot \left(1 - \exp\left(-\frac{l_c \cdot \varepsilon_{bot}}{w_1}\right)\right) - \ldots \\
&\ldots - \frac{E_p \cdot A_p}{E_{cm} \cdot b \cdot h} \cdot \left(\frac{d}{h} \cdot \varepsilon_{bot}^2 + \varepsilon_{p0} \cdot \varepsilon_{bot} - \frac{N}{E_p \cdot A_p} \cdot \varepsilon_{bot}\right) = 0
\end{aligned} \tag{4.28}$$

For clarity, the solution of the quadratic function (equation (4.28)) is presented as follows. By inserting A, B and C, ε_{top} is calculated as a function of ε_{bot} similar to equation (4.20).

$$\begin{aligned}
&A := \frac{1}{2} + \frac{E_p \cdot A_p}{E_{cm} \cdot b \cdot h} \cdot \left(1 - \frac{d}{h}\right) \\
&B := \frac{E_p \cdot A_p}{E_{cm} \cdot b \cdot h} \cdot \left(2 \cdot \frac{d}{h} \cdot \varepsilon_{bot} + \varepsilon_p - \varepsilon_{bot} - \frac{N}{E_p \cdot A_p}\right) \\
&C := \frac{1}{2} \cdot \varepsilon_{ct} + \varepsilon_{ct} \cdot \frac{w_1}{l_c \cdot \varepsilon_{bot}} \cdot \left(\varepsilon_{bot} - \varepsilon_{ct}\right) \cdot \left(1 - \exp\left(-\frac{l_c \cdot \varepsilon_{bot}}{w_1}\right)\right) + \ldots \\
&\ldots + \frac{E_p \cdot A_p}{E_{cm} \cdot b \cdot h} \cdot \left(\frac{d}{h} \cdot \varepsilon_{bot}^2 + \varepsilon_p \cdot \varepsilon_{bot} - \frac{N}{E_p \cdot A_p} \cdot \varepsilon_{bot}\right) \\
&\Rightarrow \varepsilon_{top}^2 \cdot A - \varepsilon_{top} \cdot B - C = 0 \\
&\varepsilon_{top} = \frac{B}{2 \cdot A} \pm \sqrt{\left(\frac{B}{2 \cdot A}\right)^2 + \frac{C}{A}}
\end{aligned} \tag{4.29}$$

As mentioned before, ε_{top} is supposed to be smaller than the maximum concrete compressive strain at peak. The moment equilibrium is established as follows:

$$M = -F_c \cdot \frac{x_0}{3} + F_t \cdot \left(\frac{2}{3} x_1 + x_0\right) + F_f \cdot \left(z_{c,f} + x_0 + x_1\right) + F_p \cdot d - N \cdot \frac{h}{2} \tag{4.30}$$

Equations (4.22) and (4.23) were applied in the same manner as before to determine curvatures and deflections.

For cross-sections with varying width, e.g. I- or T-beams, equation (4.29) needs to be modified by case-by-case analysis accounting for different widths over x_0, x_1 and x_2. Depending on the complexity of the cross-section, a varying width results in cumbersome equations, which can only be solved numerically since linear, quadratic and exponential terms of ε_{top} arise in one equation. Hence, the approach was modified. This can either be done by simplifying the stress-displacement relationship or by accounting for different widths in other ways. Since for linear or quadratic stress-displacement approaches also case-by-case analysis would have to be conducted, and due to the aforementioned disadvantages for UHPFRC with low fibre content, these approaches were not applied. To account for varying widths in the tensile zone, a resulting, constant tensile force based on equation (4.16) was assumed. This approach is discussed below for an upside down T-beam.

In Fig. 4.9, an upside down T-beam with pre-tensioned CFRP reinforcement subjected to axial and flexural loading is shown. The CFRP reinforcement is assumed to be placed at the centre line of the bottom flange. The bottom flange is idealised as two parts of width $b_{\text{fl}}/2$, left and right of the web, under pure tension. The web height is reduced by half the thickness of the bottom flange. Hence, the strain ε_{bot} at bottom side of the cross-section coincides with the average strain in the bottom flange and CFRP reinforcement.

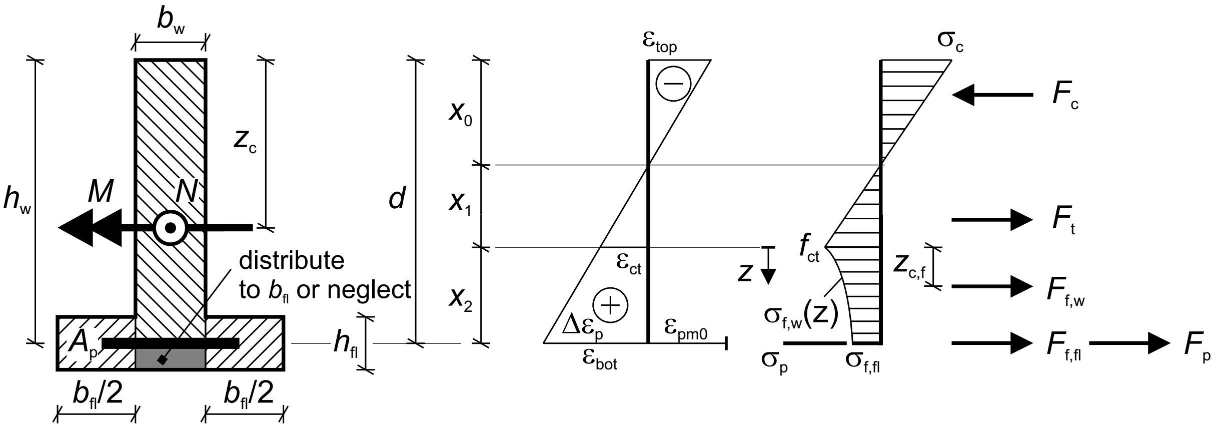

Fig. 4.9 **Applied approach for UHPFRC T-beams: Strain and stress distribution as well as resulting section forces**

The resulting forces F_c, F_t, $F_{f,w}$ and F_p were determined in the same manner as shown above. For clarity, the equations are recapitulated with changed nomenclature. Additionally, the resulting tensile force in the bottom flange $F_{f,fl}$ is specified.

$$\begin{aligned}
F_c &= \frac{1}{2}\varepsilon_{top} \cdot E_{cm} \cdot b_w \cdot x_0 \\
F_t &= \frac{1}{2}\varepsilon_{ct} \cdot E_{cm} \cdot b_w \cdot x_1 \\
F_{f,w} &= b_w \cdot f_{ct} \cdot \frac{w_1}{\varepsilon_{bot} \cdot l_c} \cdot x_2 \cdot \left(1 - \exp\left(-\frac{\varepsilon_{bot} \cdot l_c}{w_1}\right)\right) \\
F_{f,fl} &= b_{fl} \cdot h_{fl} \cdot f_{ct} \cdot \exp\left(-\frac{1}{w_1}\left(\varepsilon_{bot} \cdot l_c - \varepsilon_{ct} \cdot l_c\right)\right) \\
F_p &= \left(\Delta\varepsilon_p + \varepsilon_p\right) \cdot E_p \cdot A_p = \left(\varepsilon_{bot} + \varepsilon_p\right) \cdot E_p \cdot A_p
\end{aligned} \tag{4.31}$$

The heights of the compressive zone, linear elastic tensile zone and cracked tensile zone remain the same:

$$\begin{aligned}
\frac{x_0}{h} &= \frac{\varepsilon_{top}}{\varepsilon_{top} + \varepsilon_{bot}} \\
\frac{x_1}{h} &= \frac{\varepsilon_{ct}}{\varepsilon_{top} + \varepsilon_{bot}} \\
\frac{x_2}{h} &= 1 - \frac{x_0}{h} - \frac{x_1}{h} = \frac{\varepsilon_{bot} - \varepsilon_{ct}}{\varepsilon_{top} + \varepsilon_{bot}}
\end{aligned} \tag{4.32}$$

Equilibrium of axial forces results in the relationship below:

$$
\begin{aligned}
&\sum H = 0: \\
&\Rightarrow F_c - F_t - F_{f,w} - F_{f,fl} - F_p + N = 0 \\
&\Rightarrow \frac{1}{2}\varepsilon_{top} \cdot E_{cm} \cdot b_w \cdot x_0 - \frac{1}{2}\varepsilon_{ct} \cdot E_{cm} \cdot b_w \cdot x_1 - \ldots \\
&\ldots - b_w \cdot f_{ct} \cdot \frac{w_1}{\varepsilon_{bot} \cdot l_c} \cdot x_2 \cdot \left(1 - \exp\left(-\frac{\varepsilon_{bot} \cdot l_c}{w_1}\right)\right) - \ldots \\
&\ldots - b_{fl} \cdot h_{fl} \cdot f_{ct} \cdot \exp\left(-\frac{(\varepsilon_{bot} - \varepsilon_{ct}) \cdot l_c}{w_1}\right) - \ldots \\
&\ldots - (\varepsilon_{bot} + \varepsilon_p) \cdot E_p \cdot A_p + N = 0 \\
&\Leftrightarrow \varepsilon_{top}^2 \cdot \frac{1}{2} - \varepsilon_{top} \cdot \frac{E_p \cdot A_p \cdot (\varepsilon_{bot} + \varepsilon_{pm0})}{E_{cm} \cdot b_w \cdot h_w} - \ldots \qquad (4.33) \\
&\ldots - \frac{\varepsilon_{top}}{E_{cm} \cdot b_w \cdot h_w} \cdot \left(b_{fl} \cdot h_{fl} \cdot f_{ct} \cdot \exp\left(-\frac{(\varepsilon_{bot} - \varepsilon_{ct}) \cdot l_c}{w_1}\right) - N\right) - \ldots \\
&\ldots - \frac{1}{2} \cdot \varepsilon_{ct}^2 - \varepsilon_{ct} \cdot \frac{w_1}{l_c \cdot \varepsilon_{bot}} \cdot (\varepsilon_{bot} - \varepsilon_{ct}) \cdot \left(1 - \exp\left(-\frac{l_c \cdot \varepsilon_{bot}}{w_1}\right)\right) - \ldots \\
&- \varepsilon_{bot} \cdot \varepsilon_{ct} \cdot \frac{b_{fl} \cdot h_{fl}}{b_w \cdot h_w} \cdot \left(\exp\left(-\frac{(\varepsilon_{bot} - \varepsilon_{ct}) \cdot l_c}{w_1}\right)\right) - \ldots \\
&\ldots - \frac{E_p \cdot A_p}{E_{cm} \cdot b_w \cdot h_w} \cdot \left(\varepsilon_{bot}^2 + \varepsilon_p \cdot \varepsilon_{bot} - \frac{N}{E_p \cdot A_p} \cdot \varepsilon_{bot}\right) = 0
\end{aligned}
$$

Again, for clarity, the solution of the quadratic function is presented as follows. By inserting A, B and C, ε_{top} is calculated as a function of ε_{bot}.

$$
\begin{aligned}
&A := \frac{1}{2} \\
&B := \frac{1}{E_{cm} \cdot b_w \cdot h_w} \cdot E_p \cdot A_p \cdot (\varepsilon_{bot} + \varepsilon_p) + \ldots \\
&\ldots + \frac{1}{E_{cm} \cdot b_w \cdot h_w} \cdot \left(b_{fl} \cdot h_{fl} \cdot f_{ct} \cdot \exp\left(-\frac{(\varepsilon_{bot} - \varepsilon_{ct}) \cdot l_c}{w_1}\right) - N\right) \\
&C := \frac{1}{2} \cdot \varepsilon_{ct}^2 + \varepsilon_{ct} \cdot \frac{w_1}{l_c \cdot \varepsilon_u} \cdot (\varepsilon_{bot} - \varepsilon_{ct}) \cdot \left(1 - \exp\left(-\frac{l_c \cdot \varepsilon_{bot}}{w_1}\right)\right) + \ldots \\
&\ldots + \varepsilon_{bot} \cdot \varepsilon_{ct} \cdot \frac{b_{fl} \cdot h_{fl}}{b_w \cdot h_w} \cdot \left(\exp\left(-\frac{(\varepsilon_{bot} - \varepsilon_{ct}) \cdot l_c}{w_1}\right)\right) \qquad (4.34) \\
&+ \ldots \frac{E_p \cdot A_p}{E_{cm} \cdot b_w \cdot h_w} \cdot \left(\varepsilon_{bot}^2 + \varepsilon_p \cdot \varepsilon_{bot} - \frac{N}{E_p \cdot A_p} \cdot \varepsilon_{bot}\right) \\
&\Rightarrow \varepsilon_{top}^2 \cdot A - \varepsilon_{top} \cdot B - C = 0 \\
&\varepsilon_{top} = \frac{B}{2 \cdot A} \pm \sqrt{\left(\frac{B}{2 \cdot A}\right)^2 + \frac{C}{A}}
\end{aligned}
$$

As mentioned before, $\varepsilon_{\mathrm{bot}}$ is supposed to be smaller than maximum concrete compressive strain at peak. The moment equilibrium is established as follows:

$$\begin{aligned} M &= -F_c \cdot \frac{x_0}{3} + F_t \cdot \left(x_0 + \frac{2}{3} x_1 \right) + F_{f,w} \cdot \left(z_{c,f} + x_0 + x_1 \right) + \ldots \\ &\ldots + \left(F_{f,fl} + F_p \right) \cdot h_w - N \cdot z_c \end{aligned} \qquad (4.35)$$

Validations of the proposed model are presented in chapter 7. Additionally, with the aid of these findings, in chapter 7, it was accounted for cracking of outer sandwich layers made of CFRP reinforced UHPFRC under flexural loading.

4.5 Conclusions

In this chapter, a simplified approach was shown to determine tensile strength f_{ctm} and fracture energy G_{f} of UHPFRC from test results under flexural loading. Therefore, based on tensile stress-displacement relationships, theoretical moment-curvature and load-displacement relationships were derived by equilibrium of forces and moments. By comparison with results from flexural testing, f_{ctm} and G_{f} were determined. Additionally, an approach was derived to determine moment-curvature and load-displacement relationships for CFRP reinforced or prestressed UHPFRC members under combined axial and flexural loading. Based on these findings, further theoretical and numerical investigations were conducted in the following chapters.

5 Bond Behaviour of CFRP Reinforcement in UHPFRC

5.1 Preface

For a safe design of reinforced concrete members, the bond behaviour of reinforcement needs to be investigated. For prestressing tendons, an a priori determination of the transfer length is essential. The minimum thickness for a crack-free transmission zone has to be determined for thin concrete elements. Since a new material combination of CFRP reinforcement and UHPFRC was applied to sandwich panels, the bond behaviour was investigated experimentally and theoretically. By means of pull-out tests, local bond strengths were determined for different release states of pre-tensioning forces (lateral extension of the reinforcement). Tests on small-scale beams were conducted to determine the transfer length and minimum dimensions of thin UHPFRC elements for different types of CFRP prestressing tendons. By means of numerical and theoretical models, the bond behaviour was further investigated. Major results of experimental testing in this chapter are based on published work (e.g. /Sta13/ and /Sta16c/).

5.2 Pull-Out Testing

5.2.1 Test Set-up and Procedure

Pull-out tests were conducted to determine the local bond strength of CFRP reinforcement in UHPFRC for different release steps of the prestressing force. In these tests, the influence of the wedge effect (Hoyer effect) on the bond stress-slip relationships was identified.

Test specimens were chosen in dependence on /RILEM73/ (Fig. 5.1). According to /RILEM73/, the bond length should be $5 \cdot d_p$. Since a high bond strength was expected, the bond length was decreased to $2 \cdot d_p$ to avoid significant differences in reinforcement stress over the bond length and to allow for pull-out failure. The constant edge length of 150 mm lead to concrete cover ratios from $c/d_p = 7.6$ up to $c/d_p = 14.5$ depending on the type of prestressing member. Small ratios of $c/d_p = 2.5$ were investigated to identify the influence of a small concrete cover, as they were expected in UHPFRC facings in sandwich panels.

One batch of tests comprised nine single tests (3x3), as depicted in Fig. 5.1. After three bars or strands were pre-tensioned in a stiff rig, nine samples were concreted, three on each bar or strand. After a specified time interval, in general one day, the pull-out tests were performed. On each tendon, three tests were carried out with the same release of prestressing force, i.e. lateral extension.

The first three tests on one bar or strand were done without any change in prestressing force (0 %). After releasing roughly 50 % of the prestressing, the next three tests were conducted on the second bar or strand. The last three tests were carried out with nearly 100 % release. While releasing the prestressing force, half of the estimated pull-out force should remain in the strand or bar to ensure that the lateral extension of bar or strand remains roughly constant. With this method, the bond conditions along the transfer length can be represented (e.g. /Nit01/, /Ber12/). A release of 100 % equals the end of a concrete member, 50 % release corresponds to roughly the mid of the transfer length and 0 % release corresponds to the end of the transfer length (compare Fig. 5.12).

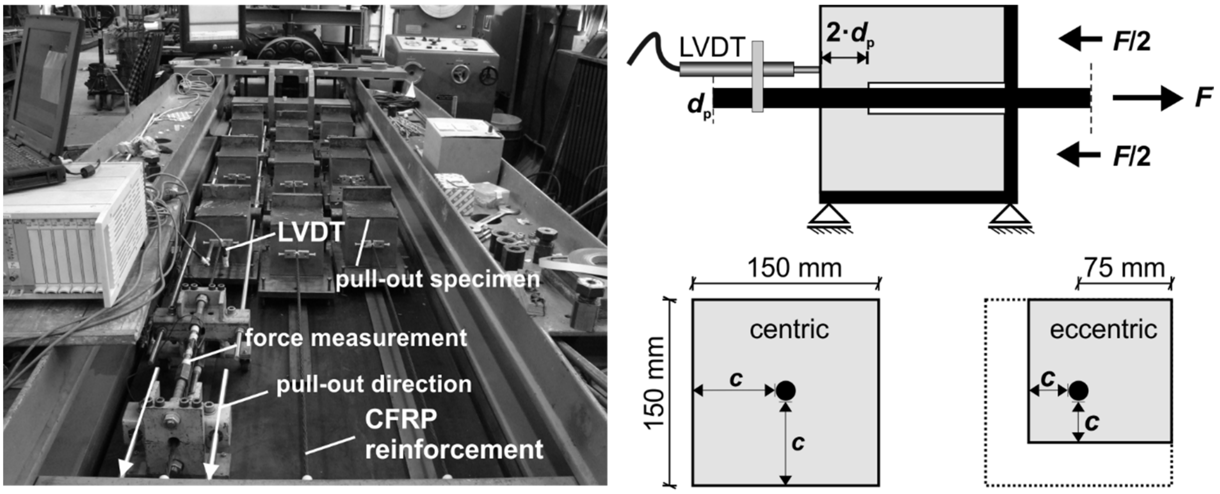

Fig. 5.1 Test setup of pull-out tests

All tests were carried out with 80 N/s. Prestressing force, pull-out force and relative slip were measured continuously. The bond stress was calculated using the nominal diameter of the tendons, as suggested in /DIN04/. Detailed parameter variations are shown in appendix A.

5.2.2 Experimental Results

In this section, only key results are discussed. Further results can be found in appendix A and /Sta13/. The derived tensile strength f_{ctm} (cp. chapter 4) was about 2.5 MPa for all specimens. The influence of the cross-sectional shape on the bond stress distributions of centrically placed tendons is depicted in Fig. 5.2. For comparison, tests results on 3/8” steel strands are shown. For clarity, only one out of three results is depicted.

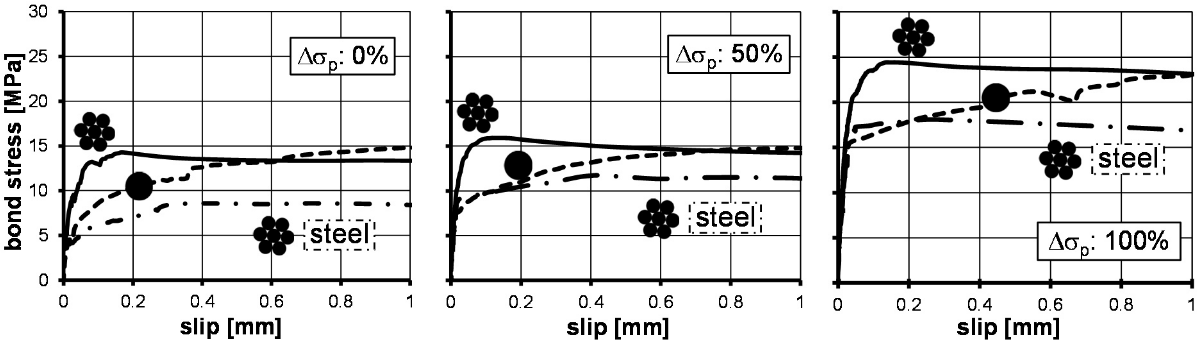

Fig. 5.2 Influence of material, cross-sectional shape and lateral extension due to release in pre-tensioning force (σ_{pm0} = 1,350 MPa)

The different concrete cover ratios c/d_p are comparable, since the concrete cubes remained uncracked. Without release of prestressing force, a maximum bond strength of about 15 MPa (basic and slip-dependent parts, cp. Fig. 5.12) was observed for both types of CFRP tendons. Only half the bond strength was identified for the investigated steel strand since the surface of CFRP reinforcement shows a rather rough surface. Generally, the CFRP strand showed a less pronounced slip-dependent part, i.e. reaching the maximum bond strength at less than 0.2 mm slip. Due to the release of prestressing force, the reinforcement extends laterally and the HOYER (wedge) effect is activated. Steel strands showed a pronounced HOYER effect, which increased linearly for both releases of prestressing force, reaching 17 MPa for 100 % release. For either CFRP reinforcement, only little increase in bond strength could be observed for 50 % release. Only for a full release, a pronounced increase in bond strength was identified. 23 MPa were reached for both types of CFRP tendons.

Tests with little concrete cover ratios of 2.5 c/d_p showed no decrease in bond strength for all stress states. Tests on strands with doubled concrete compression strength (curing of three days) indicated only little increase in bond strength since the bond strength increases disproportionately compared to the compressive strength. The same effect was observed by /Nit01/, /Heg10/, /Ber12/.

5.3 Tests on the Transfer Length

5.3.1 Test Set-up and Procedure

Tests on the transfer length were carried out to determine minimum concrete cover and spacing between bars and strands for a crack-free transmission zone as well as the transfer lengths. The test setup comprises small beams with two centrically placed CFRP prestressing tendons. Since the test results were used to determine minimum dimensions of thin UHPFRC elements, only two bars or strands were applied. Similar to pull-out testing, the reinforcement was pre-tensioned in a stiff rig. The prestressing force was released after one day of concrete hardening in steps of 20 %. At each step, the concrete compression strains were determined from extensometer measurement at mid height. The end slip of prestressing tendons was continuously identified by displacement transducers. Additionally, the pre-tensioning force was measured with load cells.

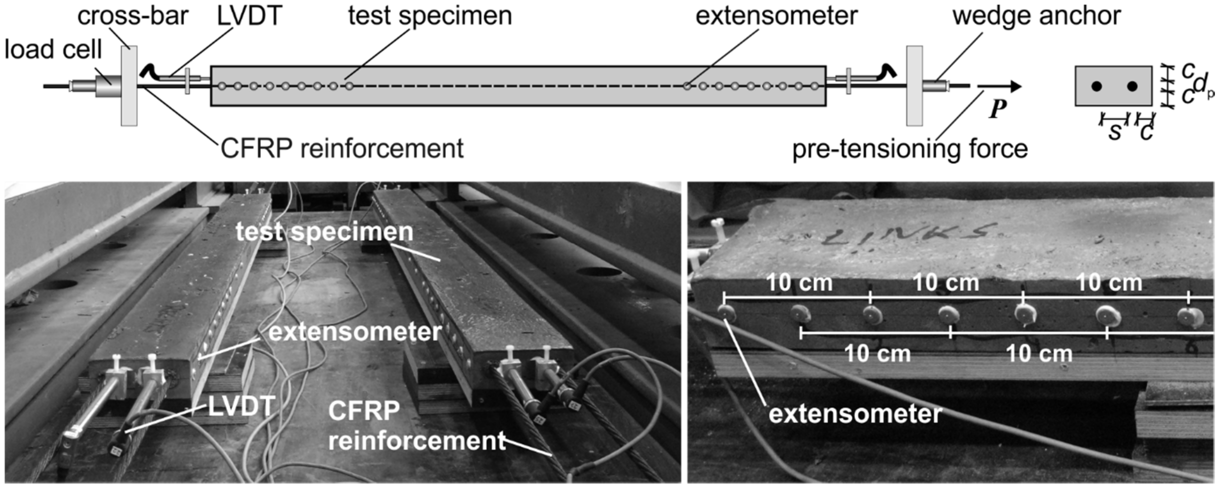

Fig. 5.3 **Test setup of tests on the transfer length (reproduced from /Sta13/)**

The detailed parameter variations are shown in appendix A.

5.3.2 Experimental Results

In this section, only key results are discussed. Further results can be found in appendix A and /Sta13/. The derived tensile strength f_{ctm} (cp. chapter 4) was about 2.5 MPa for all specimens.

During the tests, attention was mainly turned on crack-free minimum dimensions to provide preferably thin UHPFRC elements. Besides visual examination, cracking can be identified by disproportionate increase in end slip since the crack width of fibre reinforced concrete is often limited to some hundredth of a millimetre. Fig. 5.4 exemplarily shows the influence of cracking on the end slip for beams prestressed with CFRP strands (σ_{p} = 1,350 MPa).

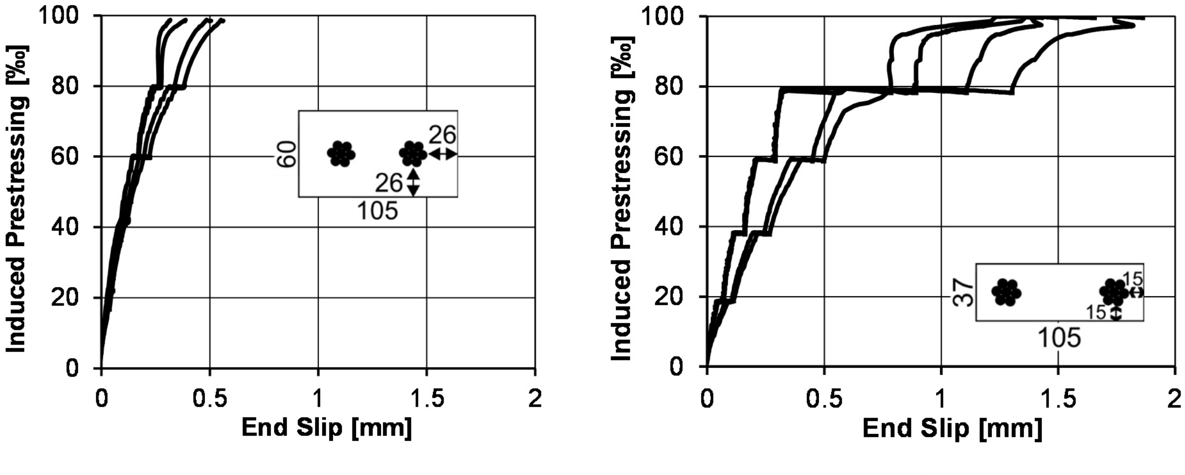

Fig. 5.4 **End slip of intact and cracked transmission zones (seven-wire strand, σ_{pm0} = 1350 MPa)**

For intact cross-sections, the end slip increases almost proportionate to the induced prestressing force. The prestressing force was released in five steps and at each step, a small increase in end slip was observed. This may have been caused by bond creep. When concrete cover was not sufficient to remain un-cracked, a disproportional increase in end slip was observed at a particular release step. Beams prestressed with CFRP bars showed a similar behaviour, even though the small increases in end slip at release step were not observed.

The concrete compression strains were derived from extensometer measurements. According to /DIBt80/ the transfer length is determined by multiplying the length, needed for 80 % maximum strain by 1.35. Even though the guideline was established for steel strands, it seems reasonable for CFRP reinforcement due to the similar behaviour. For each release of 20 % prestressing force, the compression strains increased by an approximately constant value.

Tests with intact transmission zone showed a transfer length of less than 150 mm for CFRP bars and strands (σ_{mp0} = 1350 MPa). Reducing the prestressing force by 50 %, the transfer lengths decreased about 10-15 % (cp appendix A). In tests on steel strands in UHPFRC conducted by BERTRAM /Ber12/, a transfer length of 200 mm was measured for a prestressing of 1350 MPa, even though the uniaxial compression strength was about 120 MPa (three days of concrete curing before release).

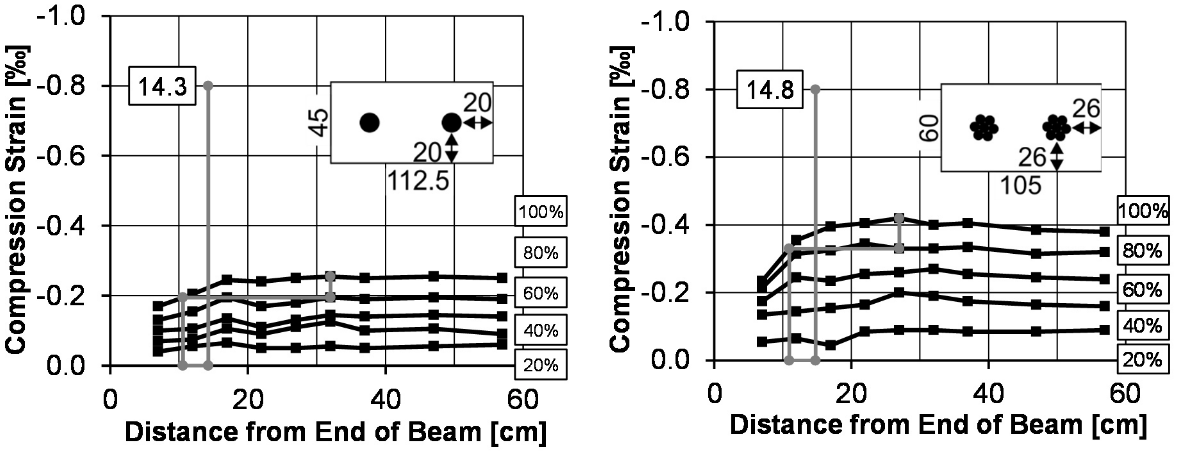

Fig. 5.5 **Concrete compression strains and transfer lengths for pre-tensioned (1,350 MPa) CFRP bars and CFRP strands**

Variation of spacing s/d_{p} had no important influence on the transfer length.

5.4 Numerical Investigations

In this section, the release of prestressing force is investigated numerically. For this purpose, the reinforcement was discretely modelled using continuum elements (cp. section 3.6). A friction law was applied for contact between CFRP reinforcement and surrounding UHPFRC. CFRP bars and CFRP strands were idealised as circular cross-sections. The diameter of CFRP strands was derived from the cross-sectional area of 31.1 mm^2. For UHPFRC and CFRP tendons, the material properties and approaches summarised in chapters 3 and 4 were used. For UHPFRC, after one day of hardening, a tensile strength f_{ct} of 2.5 MPa and fracture energy G_f of 1.25 N/mm were obtained by the derived conversion approach (cp. chapter 4.3). Compression strength and Young's modulus were used from results of material testing (cp. section 3.2.1). The modelling techniques are described in chapter 3.

The model is exemplarily depicted in Fig. 5.6. The mesh sensitivity was tested. It was found that for a mesh size of less than 10 mm no variations could be observed. Using doubly-symmetry, one quarter was modelled to reduce the computational effort.

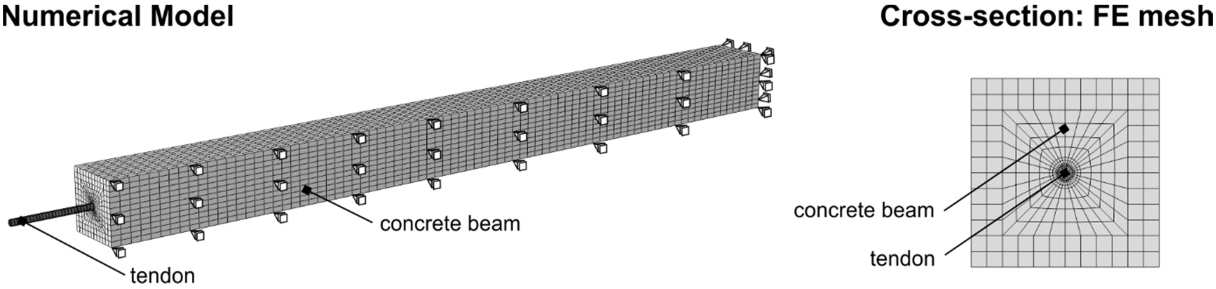

Fig. 5.6 Numerical model of tests on the transfer length

In the first step, tests TL-6 with CFRP bars and TL-16 using CFRP strands were modelled. For both test specimens, the CFRP reinforcement was pre-tensioned to 1,350 MPa and the specimens remained un-cracked at the outer surface. By applying an initial longitudinal stress to the tendons, the pre-tensioning stress was applied. A parameter study was carried out to determine the transfer lengths for different friction coefficients μ. In Fig. 5.7, the influence of the friction coefficient on the transfer length for a CFRP bar and strand are shown.

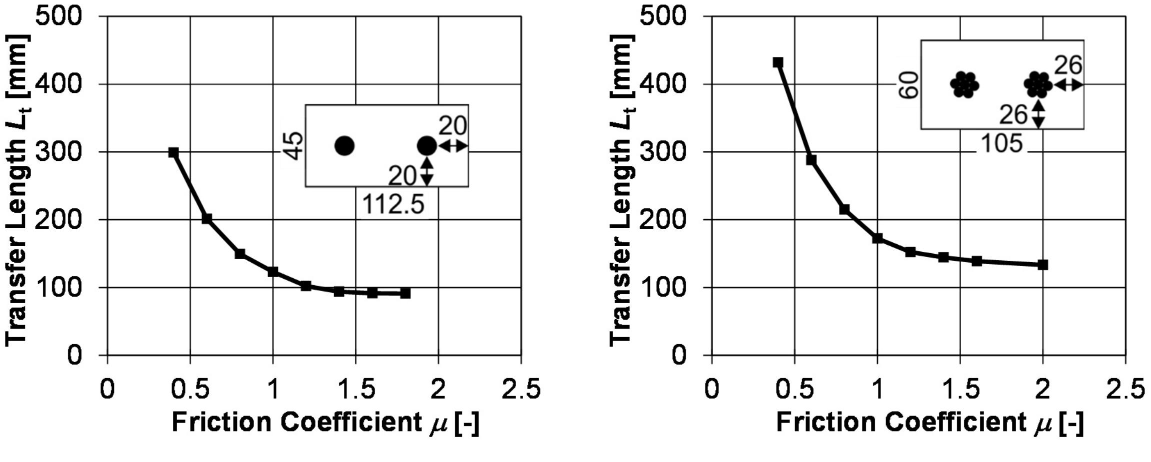

Fig. 5.7 Influence of different friction coefficients μ on the transfer length L_t for pre-tensioned (1,350 MPa) CFRP bars (left) and CFRP strands (right)

The comparison with test results shows a good agreement for $\mu = 0.8$ for CFRP bars and $\mu = 1.4$ for CFRP strands. In Fig. 5.8, the numerically determined concrete compression strains are shown in comparison to experimental results. The numerical results were found to be almost congruent with the test results.

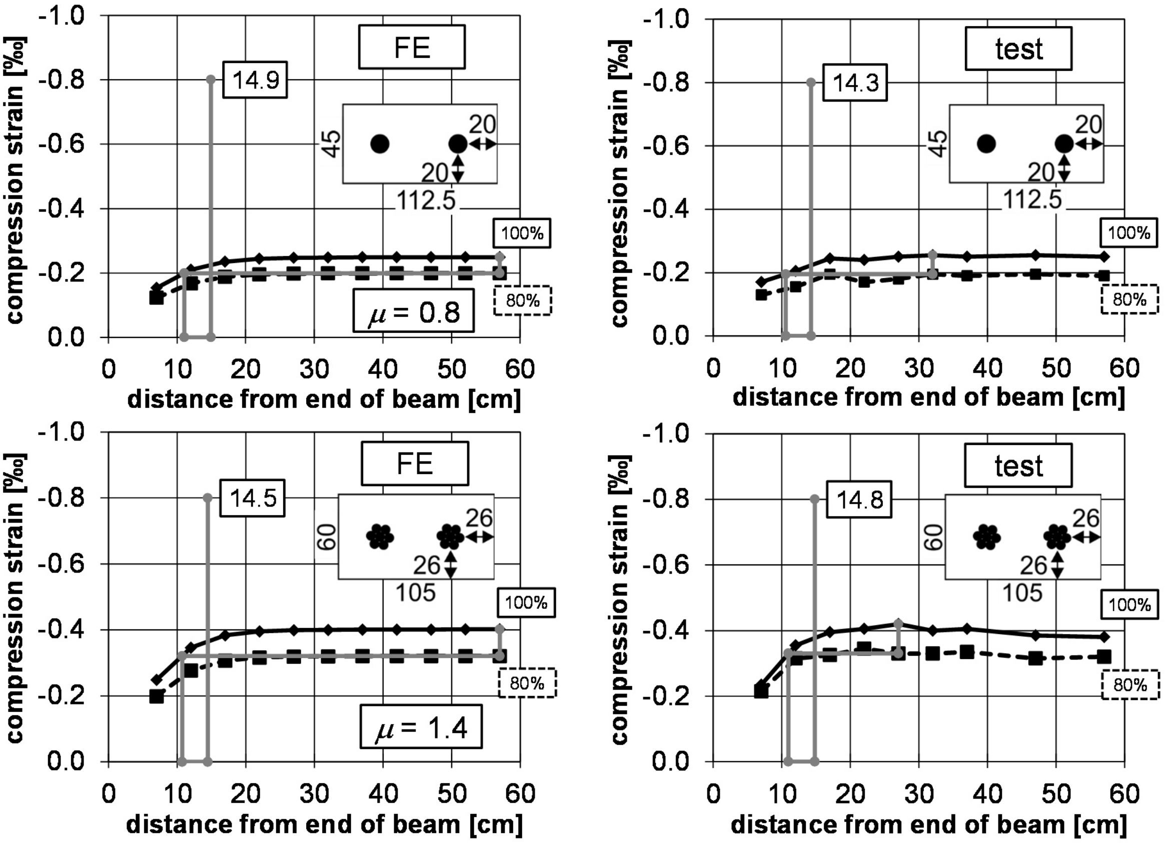

Fig. 5.8 **Concrete compression strains at the free end of beams with pre-tensioned (1,350 MPa) CFRP bars (top) and CFRP strands (bottom): Numerical (left) and experimental (right) results**

Since the compression strains were predicted in accordance with test results, the obtained maximum values of end slip were compared in the next step. The numerical results for beams prestressed with CFRP bars (1,350 MPa) seem to overestimate the end slip (Fig. 5.9). Even though, the experimentally determined end slip does not increase for induced prestressing forces over 80 %. This may be caused by deflection of the CFRP bar at full release. However, the gradient of slip was predicted in good agreement for two of four measuring points. For beams, prestressed with CFRP strands (1,350 MPa), the end slip was predicted almost congruent to the test results. Since the friction coefficient μ was determined about 75 % higher for strands, it seems plausible that a higher end slip was determined for CFRP bars, even though this was not observed during testing.

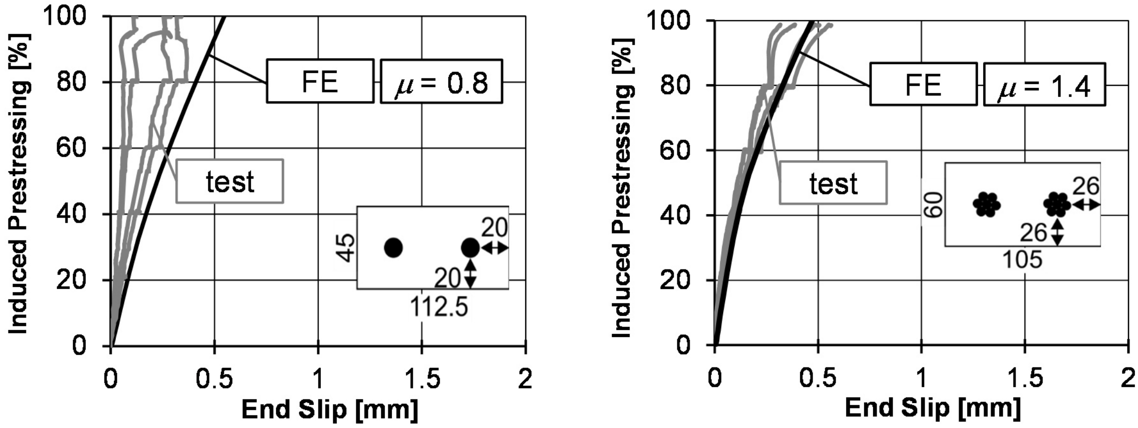

Fig. 5.9 Comparison of experimental and numerical determined end slip distribution: CFRP bars (left) and CFRP strand (right)

In Fig. 5.10, the longitudinal stress distributions of tendons are depicted. The stresses increase approximately linear to 1,000 MPa. For both tendon types, a stress of roughly 1,300 MPa was sustained.

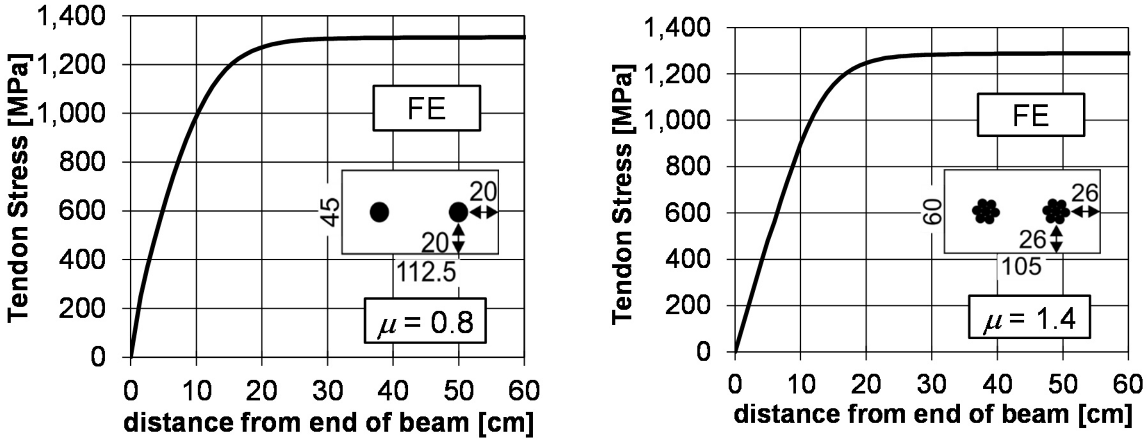

Fig. 5.10 Tendon stress for pre-tensioned (1,350 MPa) CFRP bars (left) and CFRP strands (right)

Even though no splitting cracks were observed during testing of these specimens, with the aid of the numerical models, cracking in the vicinity of the tendons was determined. In Fig. 5.11, the distribution of plastic strains at the free end of a beam prestressed with CFRP bars (1,350 MPa) is exemplarily shown. The distribution of plastic strains shows a maximum close to the free end and decreases over the transfer length.

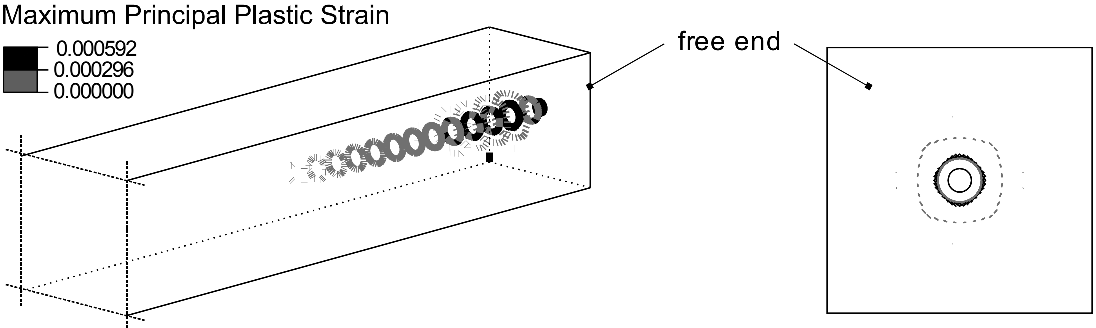

Fig. 5.11 **Example of the distribution of plastic concrete strains over the transfer length for CFRP bars (σ_p = 1,350 MPa)**

Cracking in the vicinity of tendons was further investigated in section 5.5.3.

5.5 Theoretical Approaches

5.5.1 Preface

The accurate determination of transfer lengths for prestressed concrete members can be of major interest, especially for load transfer in the vicinity of supports. For each material combination of tendon and concrete, different interface conditions result in different transfer lengths. Since excessive experimental testing is costly in terms of time and labour, theoretical models need to be derived. Especially for further investigations on stress and strain distributions in the transmission zone, standard models (e.g. /ACI04/ or /DIN04/) to determine the transfer length are not suitable.

In the next sections, two different approaches are applied to determine the transfer length of CFRP bars and strands in UHPFRC. On the one hand, an empirical approach was derived from experimental results and on the other hand, a thick-walled cylinder model (TWCM) was applied to derive bond properties.

5.5.2 Empirical Approach

In /Ber12/, /Bül08/, /Emp95/, /Nit01/ an empirical approach was used to determine the bond-stress slip relationship for steel strands in NSC, HPC and UHPC. The bond stress-slip relationships were experimentally identified from pull-out tests. In Fig. 5.12 a free end of a prestressed concrete member is depicted. Due to the release of prestressing force, the tendon expands laterally and induces a pressure at the interface to the surrounding concrete. This hoop stresses result from bond stresses. The distance from the free end of the beam to the cross-section, where the prestressing force is fully transmitted to the concrete, i.e. no lateral expansion of the tendon takes place, is equal to the transfer length L_t.

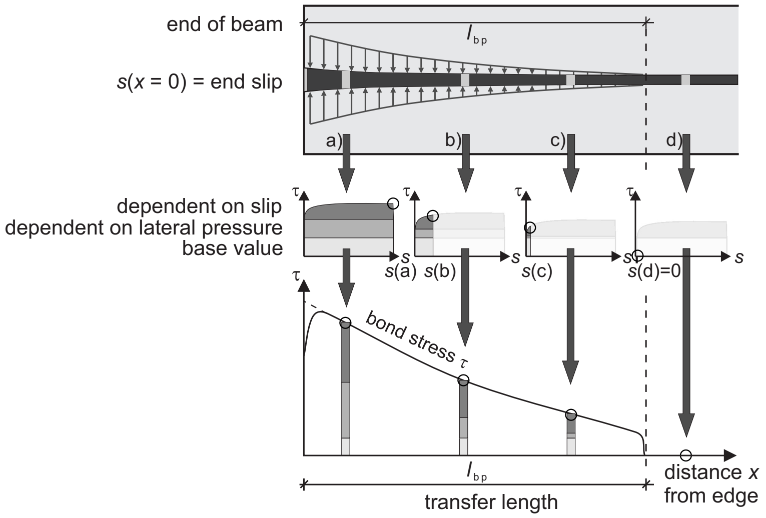

Fig. 5.12 **Schematic bond-stress distribution along the transfer length (reproduced from /Ber12/)**

In /Ber12/, /Bül08/, /Emp95/, /Nit01/, bond-stress slip relationships at different positions ((a), (b) and (c)) were derived from experimental pull-out testing. The end of the beam represents the situation of a 100 % release of pre-tensioning force. The end of the transfer length, i.e. where only minimal slip occurs, can be represented by a 0 % release state and a position in between corresponds to a 50 % release state. According to /Ber12/, /Bül08/, /Emp95/, /Nit01/, the bond stress can be subdivided in three different parts. On the one hand, a base value and on the other hand, a part dependent on lateral pressure, i.e. release of pre-tensioning force, the so-called HOYER-effect and a slip dependent part, due to the lack of fit.

τ = basic part + stress-dependent part + slip dependent part

$$\tau = \left(A + \left(B \cdot \Delta\sigma_p\right)^b + C \cdot s(x)^c \right) \cdot f_{ct,flex} \tag{5.1}$$

A, B, C, b, c	material-related coefficients
$\Delta\sigma_p$	change in pre-tensioning (positive for releasing)
$s(x)$	slip at position x

The circumference of the reinforcement was assumed to $U_p = \pi \cdot d_p$ /Ber12/, /DIN04/. Subsequently, the empirical approach is exemplarily explained and applied for the CFRP seven-wire strand.

Without any release in prestressing force, the basic part can be determined to $A = 4.5 / f_{ct,flex} = 0.45$. With the same bond stress-slip relationship, the coefficient of the slip-dependent part was identified. The maximum bond stress of 9 MPa was reached at approximately 0.16 mm slip. The non-linear part can be expressed by $c = 0.35$, leading to $C = 9.0 / (f_{ct,flex} \cdot 0.16^{0.35}) = 1.7$. Since the stress-dependent part was found to increase non-linearly for the different release steps, the exponent b is unequal to 1.0. For 50 %

release of the prestressing force, $f_{ct,flex} \cdot B \cdot 600^{b} = 2.0$ was obtained and for full release $f_{ct,flex} \cdot B \cdot 1200^{b} = 10.0$. Hence, $b = 2.3$ and $B = 7.0 \cdot 10^{-08}$ were determined. Since no decrease in bond strength was determined with the lowest tested concrete cover, no reduction ratio was introduced. Even though, for an estimate of transfer length for concrete covers smaller than the tested ratios, one has to bear in mind that splitting cracks may occur and transfer lengths may be underestimated.

To determine the transfer length L_t, the bond differential equation was applied. This differential equation (ODE) is derived by equilibrium at a differential element with the length dx. This element is composed of two parts, such as a tendon in surrounding concrete (Fig. 5.13).

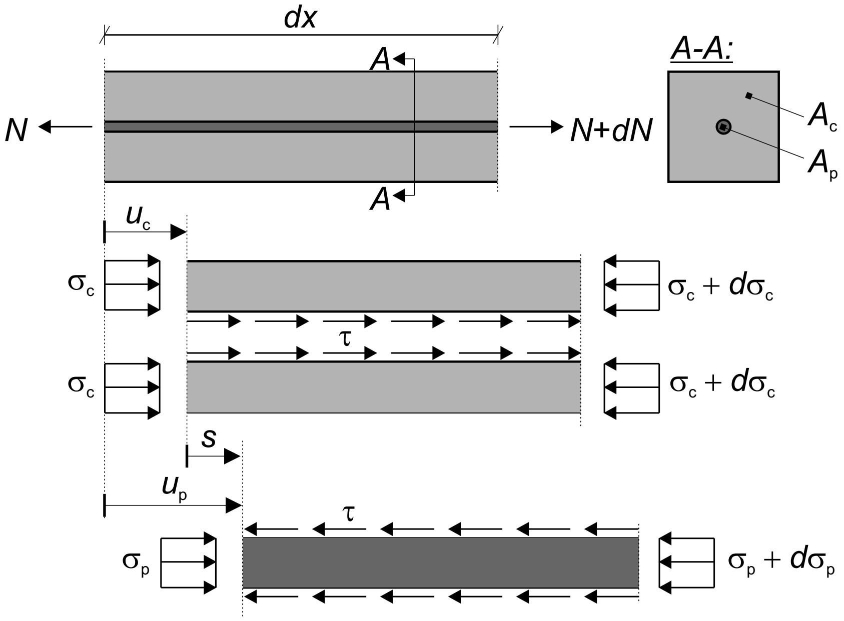

Fig. 5.13 Equilibrium of rebar surrounded by concrete under tensile loading

Considering equilibrium yields the relationship between bond stress and tendon stress.

$$\frac{d\sigma_p}{dx} = \tau \cdot \frac{U_p}{A_p} \tag{5.2}$$

In the same manner, the relationship between bond stress and concrete stress can be established.

$$\frac{d\sigma_c}{dx} = -\tau \cdot \frac{U_p}{A_c} \tag{5.3}$$

The slip s is the relative displacement between the rebar and the concrete element.

$$s_p(x) = u_p - u_c \tag{5.4}$$

Differentiating equation (5.4) and applying HOOKE'S LAW leads to the relationship between the change in slip and strains in concrete and rebar.

$$\frac{ds_p(x)}{dx} = \frac{\sigma_p}{E_p} - \frac{\sigma_c}{E_c} \tag{5.5}$$

Differentiating and rearranging equation (5.5) yields the well-known differential equation.

$$\frac{d^2 s_\mathrm{p}(x)}{dx^2} = \frac{1}{E_\mathrm{p}} \cdot \left(\tau(s_\mathrm{p}; \sigma_\mathrm{p}) \cdot \frac{U_\mathrm{p}}{A_\mathrm{p}} \right) \cdot \left(1 + \alpha_\mathrm{p} \cdot \rho_\mathrm{p}\right) \tag{5.6}$$

$s_\mathrm{p}(x)$	slip at position x
x	distance from end of beam
$\sigma_\mathrm{p}(x)$	stress of reinforcement at position x
E_p	Young' s Moduls of pre - tensioned reinforcement
E_c	Young' s Moduls of concrete
τ	bond stress relationship
U_p	circumference of reinforcement
A_p	cross - sectionional area of reinforcement
$\alpha_\mathrm{p} = E_p / E_\mathrm{c}$	ratio of Young' s Moduli
$\rho_\mathrm{p} = A_\mathrm{p} / A_\mathrm{c}$	reinforcement ratio

The right-hand side of equation (5.6) comprises the bond stress τ. The relationships of τ found empirically from pull-out testing by applying equation (5.1) were used to determine the transfer lengths for un-cracked specimens prestressed with CFRP bars and strands by stepwise integration. For this purpose, the transmission zone is divided in a finite number of elements (Fig. 5.14). The end slip is iteratively increased until the full prestressing force is transmitted. At each element *i*, equilibrium has to be satisfied.

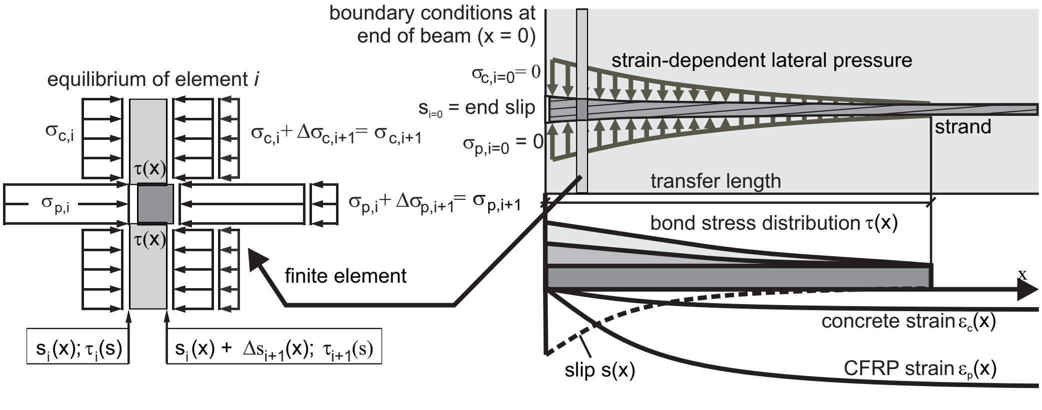

Fig. 5.14 **Finite element method and equilibrium conditions (reproduced from /Ber12/)**

In Fig. 5.15, the procedure to calculate the transfer length is exemplarily shown for test TL-16. First, stress and slip over the length of the beam were determined (Fig. 5.15, bottom). The corresponding experimental results of pull-out tests are depicted on the top left of Fig. 5.15. The calculated bond stress is shown in Fig. 5.15 on the top right side. Based on the calculated stresses and slip, one can identify the local bond strength for each release step (designated by points). These local bond strengths are not necessarily the maximum values of the experimental results, they have to be determined in dependence on slip /Ber12/.

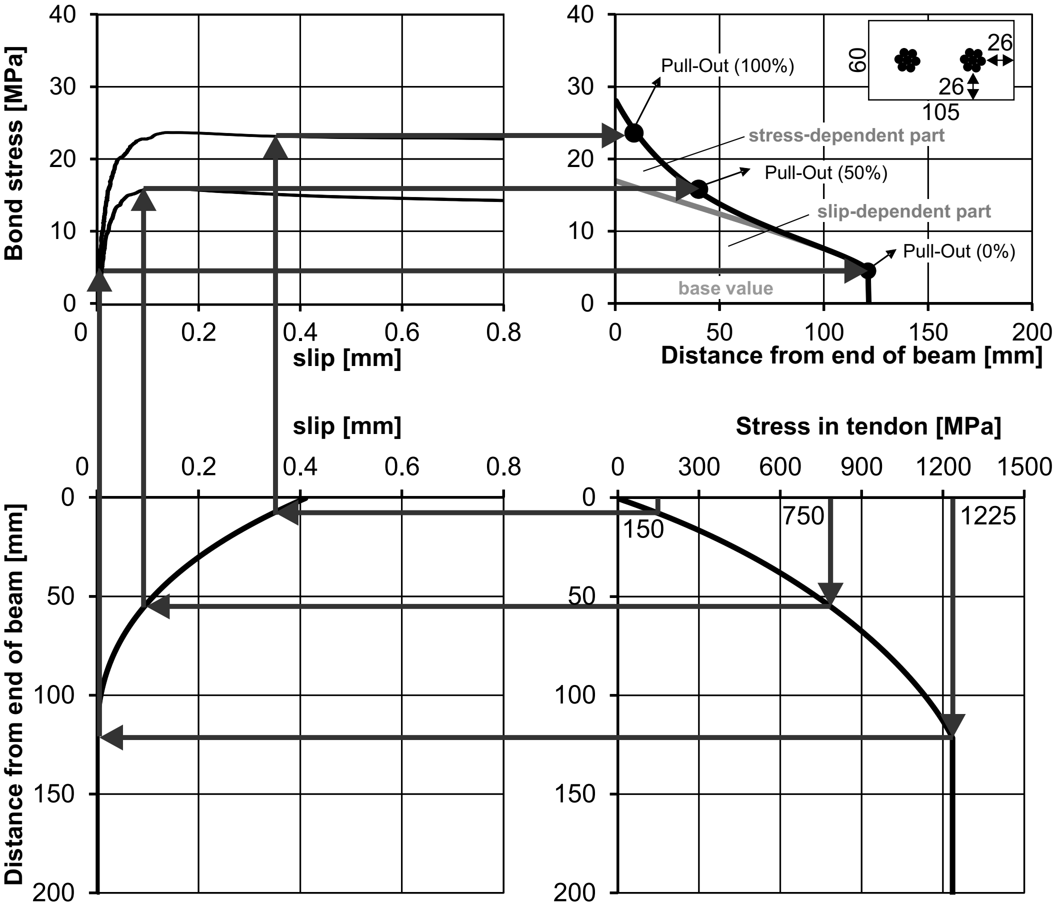

Fig. 5.15 **Empirically determined transfer length of test TL-16**

The comparison of the experimental and calculated values of the transfer length shows a good agreement. The transfer length of test TL-16 was determined experimentally to $L_{pt,exp} = 14.5$ cm (end slip $s_{exp} = 0.5$) and calculated to $L_{pt,calc} = 12.5$ cm (end slip $s_{exp} = 0.41$).

Nevertheless, this approach can only be used for exactly the same material combinations tested experimentally in pull-out tests. Additionally, transfer lengths for specimen with relatively small concrete covers cannot be predicted since it is not possible to safely predict the performance of cracked specimens. During pull-out testing, no reduction in bond stress was observed, even for c/d_p ratios of 2.5, but cracks were observed in the transmission zone in tests on the transfer length for the same ratio which indicates issues with this procedure. Additionally, exponents *b* and *c* in equation (5.1) result in inconsistent units. For further investigations, a mechanically based approach was applied in the next section.

5.5.3 Application of a Thick-walled Cylinder Model

Mechanical or analytical approaches to determine the transfer length are often based on THICK-WALLED CYLINDER MODELS. Besides the transfer length, tendon stress, bond stress and resulting pressure perpendicular to the axial direction of the tendon can be analysed. The THICK-WALLED CYLINDER MODEL has been widely applied, modified and further developed for steel rebars or steel prestressing tendons (e.g. /Tep79/, /Oh06/, /Han16/). The model can be used for bond investigations in RC or PC since rebars or prestressing tendons confined by surrounding concrete represent the situation of a hollow concrete cylinder subjected to internal pressure. The equilibrium equations are usually derived for a ring element of size *dz* at a distance *z*. The corresponding stresses are shown in Fig. 5.16.

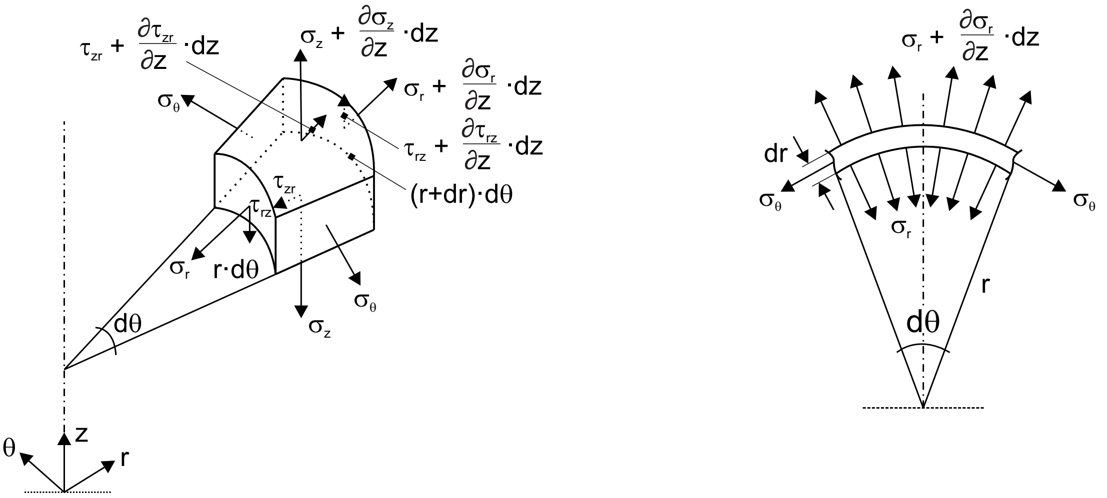

Fig. 5.16 Free-body cut of thick-walled cylinder with corresponding stresses (left) (reproduced from /Oh06/) and simplified detail (right)

The derivation of the equations was shown by different researchers (e.g. /Tep79/, /Oh06/, /Han16/) or can be found in lecture notes. For the sake of clarity, the derivation of the equations is shown again. Equilibrium of forces in radial direction leads to the following equation by assuming all variables to be independent of *z*-direction and neglecting body forces:

$$\begin{aligned} &\sum F_r = 0: \\ &\Rightarrow (\sigma_r + d\sigma_r)(r + dr)d\theta dL - \sigma_r r d\theta dL - 2\sigma_\theta dr dL \sin(d\theta/2) = 0 \\ &\qquad \sigma_r: \quad \text{normal stress in radial direction} \\ &\qquad \sigma_\theta: \quad \text{hoop stress in circumferential direction} \end{aligned} \tag{5.7}$$

Assuming small angles and neglecting higher order terms, equation (5.7) reduces:

$$\sigma_r + \frac{d\sigma_r}{dr} \cdot r - \sigma_\theta = 0 \tag{5.8}$$

In Fig. 5.17, a schematic cross-section of a solid cylinder is depicted, representing a rebar or prestressing tendon in a hollow cylinder, representing the surrounding concrete.

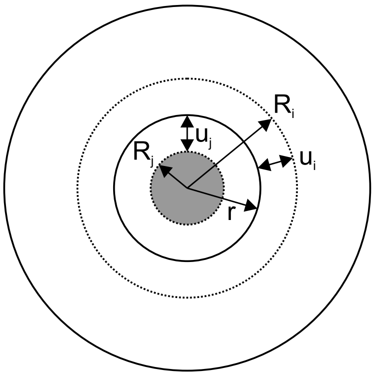

r: interface radius
R_i: initial radius of tendon
R_j: decreased radius of tendon after pre-tensioning
u_i: displacement of tendon due to release of pre-tensioning force
u_j: displacement of conrete due to internal pressure

Fig. 5.17 Stressed cylinder in thick-walled concrete hollow cylinder: Relative radial displacements (reproduced from /Oh06/, /Han16/)

The prestressing tendon with initial radius R_i is pre-tensioned, resulting in radius R_j due to the lateral deformation. After casting concrete and releasing the prestressing force, the tendon expands laterally, leading to a final displacement u_i. The surrounded concrete deforms by u_j. Since compatibility of displacements must be fulfilled, the following relationship arises:

$$R_i + u_i = R_j + u_j \tag{5.9}$$

From the THEORY OF ELASTICITY, the stress-strain relationships can be expressed in a cylindrical coordinate system as follows:

$$\begin{aligned} \sigma_r &= \frac{E}{1-\nu^2}\left(\varepsilon_r + \nu \cdot \varepsilon_\theta\right) + \frac{\nu(1+\nu)\sigma_z}{1-\nu^2} \\ \sigma_\theta &= \frac{E}{1-\nu^2}\left(\varepsilon_\theta + \nu \cdot \varepsilon_r\right) + \frac{\nu(1+\nu)\sigma_z}{1-\nu^2} \end{aligned} \tag{5.10}$$

The strains in radial and circumferential directions are expressed in dependence on the radial direction only:

$$\varepsilon_r = \frac{du}{dr}, \qquad \varepsilon_\theta = \frac{2\pi(r+u) - 2\pi r}{2\pi r} = \frac{u}{r} \tag{5.11}$$

Applying σ_r and σ_θ from equations (5.10) in equation (5.8) and considering relationships of strains (equation (5.11)) results in an ordinary differential equation (ODE) of radial displacement (equation (5.12)). For this second order ODE, a typical solution is given by equation (5.13) with two integration constants c_1 and c_2.

$$r\frac{d^2u}{dr^2}+\frac{du}{dr}-\frac{u}{r}=0 \tag{5.12}$$

$$u=c_1 r+\frac{c_2}{r} \tag{5.13}$$

Hence, the stresses σ_r and σ_θ can be expressed as follows:

$$\sigma_r = E\left[\frac{c_1}{1-\nu}-\frac{c_2}{(1+\nu)r^2}\right]+\frac{\nu\cdot\sigma_z}{1-\nu} \tag{5.14}$$

$$\sigma_\theta = E\left[\frac{c_1}{1-\nu}+\frac{c_2}{(1+\nu)r^2}\right]+\frac{\nu\cdot\sigma_z}{1-\nu} \tag{5.15}$$

In the next step, the constants c_1 and c_2 can be determined separately for the boundary conditions of a solid cylinder (prestressing tendon) and hollow cylinder (surrounding concrete).

For the solid cylinder, the displacement is zero ($u = 0$) at $r = 0$. Hence, the constant c_2 must be zero. Thus, the radial and circumferential stresses are equal, and independent of r. At $r = R_i$ (radius of the cylinder), the radial and circumferential stresses are set to a radial stress p. The longitudinal stress σ_z is treated as the stress in the tendon f_{pz} at a distance z from the free beam end. Elastic modulus and Poisson's ratio of the prestressing tendon are expressed by E_p and ν_p, respectively. Hence, the displacement u_i of the tendon is given as:

$$u_i=\frac{-p(1-\nu_p)-\nu_p\cdot f_{pz}}{E_p}\cdot R_i \tag{5.16}$$

For the hollow cylinder, the radial stress equals p at $r = R_j$ and zero at $r = C$. Thus the expressions for σ_r and σ_θ are obtained as follows:

$$\begin{aligned}\sigma_r &= -p\cdot\frac{1/C^2-1/r^2}{1/C^2-1/R_j^2}\\ \sigma_\theta &= -p\cdot\frac{1/C^2+1/r^2}{1/C^2-1/R_j^2}\end{aligned} \tag{5.17}$$

The resulting displacement u_j at the inner surface of the concrete cylinder is summarised in equation (5.18). f_{pz} is the axial stress in the concrete member at a distance z from the free end. Elastic modulus and Poisson's ratio of concrete are expressed by E_c and ν_c, respectively.

$$u_j = \frac{-p \cdot R_j}{E_c\left(1/C^2 - 1/R_j^2\right)} \left[\frac{1-\nu_c}{C^2} + \frac{1+\nu_c}{R_j^2}\right] - \frac{\nu_c \cdot f_{cz} \cdot R_j}{E_c} \tag{5.18}$$

Applying equation (5.9) gives the solution of the interface pressure p (equation (5.19)).

$$p = \frac{R_i\left(1-\nu_p \cdot f_{pz}/E_p\right) - R_j\left(1-\nu_c \cdot f_{cz}/E_c\right)}{\left(1-\nu_p\right)R_i/E_p + \left[\nu_c - \left(R_j^2 + C^2\right)\Big/\left(\left(R_j^2 - C^2\right)\right)\right]R_j/E_c} \tag{5.19}$$

The reduced radius R_j due to jacking stress f_{pj} is usually simply calculated using Poisson's ratio ν_p as follows:

$$R_j = \left(1 - \frac{f_{pj}}{E_p}\nu_p\right) \cdot R_i \tag{5.20}$$

For the above mentioned equations, a linear elastic material behaviour is assumed. Considering an example similar to the tested specimen without cracking of the outer surface (cp. section 5.3.2), the stress distributions in radial and circumferential direction can be determined with equations (5.17). The material and geometric properties are shown in Fig. 5.18. The same approach was applied for steel tendons in NSC by /Oh06/.

In Fig. 5.18, a CFRP strand (Ø7.5 mm) with corresponding stress distributions of σ_r and σ_θ in a hollow concrete section at the free end of the beam element are depicted.

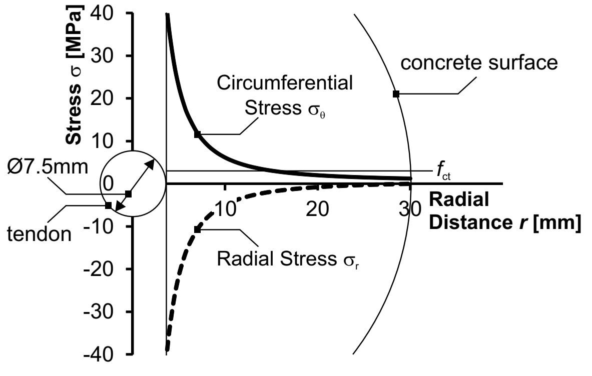

Reinforcement:
CFRP seven-wire strand Ø7.5
E_p = 150,000 MPa, ν_p = 0.2
f_{pj} = 1350 MPa

Concrete:
UHPFRC
C = 30 mm
$E_{cm,1d}$ = 32,000 MPa
f_{ct} = 2.5 MPa

Fig. 5.18 **Isotropic, elastic analysis of radial and circumferential stresses of a pre-tensioned CFRP strand in UHPFRC (illustration in dependence on /Oh06/)**

The calculated stresses in the vicinity of the tendon are about 15 times greater than the tensile strength f_{ct} of the concrete. The stresses decrease over the radial distance r and are smaller than f_{ct} at roughly 15 mm. Hence, radial cracks around the tendon are predicted, whereas the outer surface of the concrete element remains un-cracked. The same phenomena was observed by OH /Oh06/ for steel tendons in NSC. The cracking tendency of concrete in the vicinity of the tendon can be checked by calculating the circumferential strain $\varepsilon_\theta(\mathrm{R_j})$ from the radial displacement u_j with equation (5.18). In case $\varepsilon_\theta(R_j)$ exceeds the cracking strain of concrete $\varepsilon_{cr} = f_{ct} / E_{cm}$, cracking occurs. For the example shown in Fig. 5.18, ε_{cr} is about 0.08 ‰. The circumferential strain $\varepsilon_\theta(R_j)$ was determined to 1.6 ‰, which clearly exceeds ε_{cr}.

In case of cracked sections, different approaches have to be applied. Amongst others, in /Oh06/ and /Han16/, the thick-walled cylinder model was modified to account for cracking of concrete. Generally, three different states of concrete behaviour are assumed. This can be a linear elastic behaviour, as described above, and a partly cracked or a fully cracked concrete element.

Subsequent, the approach suggested in /Han16/ to account for cracking of NSC sections with pre-tensioned steel strands by application of a modified THICK-WALLED CYLINDER MODEL is shown and applied for CFRP tendons in UHPFRC. The state of a partly cracked specimen, observed in Fig. 5.18, is depicted in Fig. 5.19. The variables R_i, R_j, u_i and u_j remain the same as before. To evaluate the length of the cracks, the variable R_c is introduced.

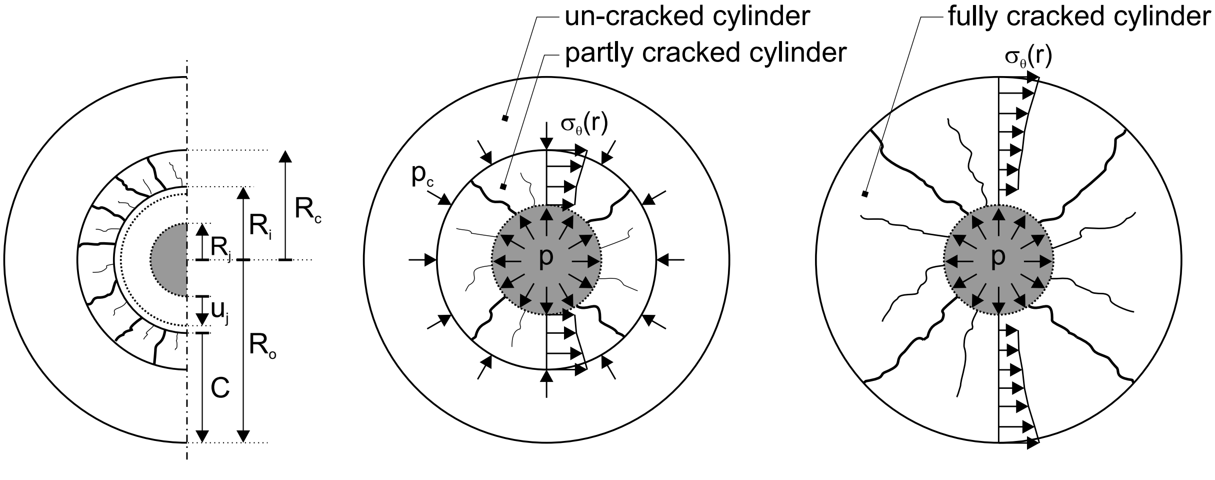

Fig. 5.19 **Cracking in a thick-walled cylinder (left), equilibrium of forces in a partly (mid) and fully (right) cracked cross-section in (reproduced from /Han16/)**

HAN ET AL /Han14/, /Han16/ proposed to assume a linear elastic displacement field of the hollow concrete cylinder. From equations (5.14) and (5.15), the radial and circumferential stresses σ_r and σ_θ, respectively, are determined by applying $\sigma_\theta = f_{ct}$ at $r = R_c$ and $\sigma_r = 0$ at $r = C$:

$$\sigma_r(r) = f_{ct} \cdot \frac{1/C^2 - 1/r^2}{1/C^2 + 1/R_c^2} \tag{5.21}$$

$$\sigma_\theta(r) = f_{ct} \cdot \frac{1/C^2 + 1/r^2}{1/C^2 + 1/R_c^2} \tag{5.22}$$

The radial displacement $u(r)$ and tangential strain $\varepsilon_\theta(r)$ are derived from equations (5.21) and (5.22) as follows:

$$u(r) = \frac{f_{ct}}{E_{cm}} \cdot r \cdot \frac{1/C^2 + 1/r^2}{1/C^2 + 1/R_c^2} \tag{5.23}$$

$$\varepsilon_\theta(r) = \frac{f_{ct}}{E_{cm}} \cdot \frac{1/C^2 + 1/r^2}{1/C^2 + 1/R_c^2} \tag{5.24}$$

If the circumferential strain $\varepsilon_\theta(R_j)$ at the interface between tendon and concrete derived from equation (5.18) exceeds the cracking strain ε_{cr}, the cross-section is partly cracked. In this case, HAN ET AL /Han16/ suggested to derive the cracking length R_c by comparing equation (5.18) with equation (5.23) at $r = R_j$.

$$\frac{-p \cdot R_j}{E_c\left(1/C^2 - 1/R_j^2\right)}\left[\frac{1-\nu_c}{C^2} + \frac{1+\nu_c}{R_j^2}\right] - \frac{\nu_c \cdot f_{cz} \cdot R_j}{E_c} = \frac{f_{ct}}{E_{cm}} \cdot R_j \cdot \frac{1/C^2 + 1/R_j^2}{1/C^2 + 1/R_c^2} \tag{5.25}$$

After the cracking length R_c is determined, the circumferential strain distribution $\varepsilon_\theta(r)$ can be calculated with equation (5.22) in dependence on the distance r. To account for cracking of concrete, a tension softening curve has to be applied. HAN ET AL /Han16/ used the bilinear softening curve according to /CEB12/. Since mainly the ability to reach a cracked state should be accounted for and to avoid case-by-case analysis, a linear softening was assumed in this study (Fig. 5.20). Hence, the following three cases have to be analysed.

$$\begin{aligned}
&\sigma_\theta(r) = E_{cm} \cdot \varepsilon_\theta(r), && \varepsilon_\theta(r) \le \varepsilon_{cr} \\
&\sigma_\theta(r) = f_{ct} \cdot \frac{\varepsilon_u - \varepsilon_\theta(r)}{\varepsilon_u - \varepsilon_{cr}}, && \varepsilon_{cr} < \varepsilon_\theta(r) \le \varepsilon_u \\
&\sigma_\theta(r) = 0, && \varepsilon_\theta(r) > \varepsilon_u
\end{aligned} \tag{5.26}$$

The cracking strain was calculated by tensile strength f_{ct} (~2.5 MPa) and Young's modulus E_{cm} (~32,000 MPa) after one day of concrete hardening. The ultimate strain ε_u was derived from the findings in chapter 4. For the own investigations a linear softening approach was applied. To avoid an overestimation of ductility, the gradient of the linear softening relationship was derived in the manner that fracture energy was equal to that of the exponential softening relationship used in chapter 4 (Fig. 5.20).

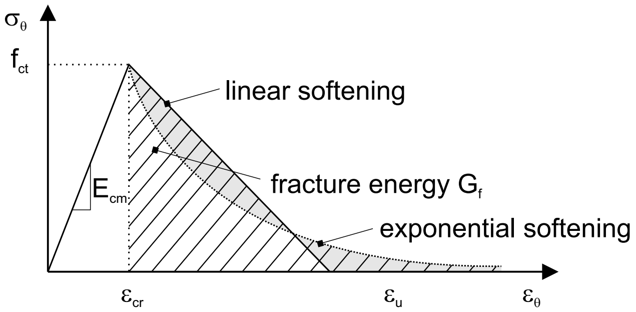

Fig. 5.20 Stress-strain relationship to account for tension softening of concrete

In case of a partly cracked concrete cylinder (cp. Fig. 5.19), equilibrium of pressure p from expansion of the tendon, stresses p_c at the crack tip and residual stresses $\sigma_\theta(r)$ provide the following relationship:

$$p \cdot R_j = p_c \cdot R_c + \int_{R_j}^{R_c} \sigma_\theta(r) dr \tag{5.27}$$

The stresses p_c at the crack tip, i.e. $\sigma_\theta(R_c)$, can be assumed to be identical with the tensile concrete strength f_{ct}. Hence, equation (5.21) delivers p_c as follows:

$$\sigma_r(R_c) = -p_c = f_{ct} \cdot \frac{1/C^2 - 1/R_c^2}{1/C^2 + 1/R_c^2} \tag{5.28}$$

In case of a fully cracked concrete cylinder, the pressure p_c vanishes and R_c becomes C (cp. Fig. 5.19). Hence, HAN ET AL calculated the displacement and corresponding circumferential strain from equations (5.23) and (5.24) as follows:

$$u(r) = \varepsilon_{\theta c} \cdot r \cdot \frac{1/C^2 + 1/r^2}{2} \tag{5.29}$$

$$\varepsilon_\theta(r) = \varepsilon_{\theta c} \cdot \frac{1/C^2 + 1/r^2}{2} \tag{5.30}$$

The variable $\varepsilon_{\theta c}$ is the circumferential strain at the outer concrete surface, which is determined by combining equations (5.23) and (5.29):

$$\frac{-p \cdot R_j}{E_c \left(1/C^2 - 1/R_j^2\right)} \left[\frac{1-\nu_c}{C^2} + \frac{1+\nu_c}{R_j^2} \right] - \frac{\nu_c \cdot f_{cz} \cdot R_j}{E_c} = \varepsilon_{\theta c} \cdot R_j \cdot \frac{1/C^2 + 1/R_j^2}{2} \tag{5.31}$$

Hence, $\sigma_\theta(r)$ according to equation (5.26) can be calculated by applying equation (5.30). Again the pressure p due to expansion of the tendon is determined by equation (5.27), whereas p_c equals zero.

The bond stress τ in the interface zone between tendon and concrete is calculated using COULOMB FRICTION (equation (5.32)).

$$\tau = p \cdot \cot\alpha \tag{5.32}$$

$\cot\alpha$ represents a coefficient of friction. For applications of steel tendons in NSC, values of 0.4 to 1.4 are reported (e.g. /Tep79/, /Lal88/, /Wan04/). In /Nan92/, a numerically determined value of 2.1 for FRP tendons in NSC was proposed. HAN ET AL /Han16/ used a friction coefficient of 0.5 for steel tendons in NSC. The value of $\cot\alpha$ was investigated closer by the aid of finite element modelling (cp. section 5.4) and determination of transfer lengths for the applied material combination of CFRP and UHPFRC.

For the determination of the transfer length a beam member is subdivided in n elements of a small length Δz each (cp. section 5.5.2). The stress in the prestressing tendon is calculated from bond stress τ in each element Δz (cp. equation (5.2)) as follows:

$$\Delta f_{pz} = \frac{U_p}{A_p} \cdot \tau \cdot \Delta z \tag{5.33}$$

Since the stress in the tendon at the beam end is zero, the stress in the tendon at the n^{th} element $f_{\text{pz,n}}$ is the sum of increments Δf_{pz} (equation (5.34)).

$$f_{pz,n} = \sum_{k=0}^{n} \Delta f_{pz} \tag{5.34}$$

Additionally, the corresponding strain change $\Delta\varepsilon_{\text{pz,n}}$ at the n^{th} element is determined as follows:

$$\Delta\varepsilon_{pz,n} = \varepsilon_{pi} - \frac{f_{pz,n}}{E_p} \tag{5.35}$$

The concrete strain at the n^{th} element is calculated from tendon stress $f_{\text{pz,n}}$.

$$\varepsilon_{cz,n} = \frac{f_{pz,n} \cdot A_p}{E_c}\left(\frac{1}{A_c} + \frac{e}{I} y\right) \tag{5.36}$$

For centrically placed tendons, the eccentricity e vanishes.

The transfer length L_t is determined at the element where the strain change in the prestressing tendon $\Delta\varepsilon_{pz,n}$ is equal to the concrete strain $\varepsilon_{cz,n}$ /Han16/. The analysis is conducted with an initial value of $f_{pz,n} = 0$ (free beam end).

Usually multiple tendons are applied in a specimen for tests of the transfer length. HAN ET AL /Han16/ applied the approach of DEN UIJL /Den98/ to determine a effective concrete cover thickness by accounting for the influence of strand spacing as follows:

$$C_{eff} = \frac{2 \cdot C_c + 1.5 \cdot (n_p - 1) \cdot s_p}{2 \cdot n_p} \tag{5.37}$$

C_{eff} is the clear concrete cover thickness, n_p the number and s_p the spacing of tendons.

HAN ET AL /Han16/ determined the transfer lengths of about 56 test specimen using centrically and eccentrically placed steel strands with different diameters in NSC beams of different dimensions. For a friction coefficient of 0.5, the mean value of the ratio of $L_{t,cal}$ and $L_{t,exp}$ was about 1.03 with a corresponding COV of 0.225.

The proposed model by /Han16/ was applied and validated with test results (section 5.3.2) of specimens made of UHPFRC and pre-tensioned CFRP. Therefore, the beams of 1640 mm length were subdivided in elements of 0.5 mm length. According to /Han16/ the calculation procedure can be summarised as follows:

Table 5.1: Procedure to determine the transfer length L_t according to /Han16/

1.	Determination of reduced radius R_j due to jacking stress f_{pi} (equation (5.20))
2.	Start with $f_{pz,n} = 0$ (free beam end)
3.	Calculation of f_{cz} based on prestressing force and eccentricity of tendons
4.	Calculation of interface pressure p (equation (5.19))
5.	Calculation of concrete displacement u_j (equation (5.18)); check, if $\varepsilon_\theta(R_j) \geq \varepsilon_{cr}$
6.	If step 5 is fulfilled, determine R_c (equation (5.25) and go to step 7; otherwise, go to step 11
7.	Calculation of p_c (equation (5.28)) and of p (equation (5.27));
8.	Check, if $R_c \geq C$
9.	If step 8 is fulfilled, go to step 10 and set $R_c = C$; otherwise, go to step 11
10.	Calculation of ε_{qc} (equation (5.31)) and p (equation (5.27), $p_c = 0$)
11.	Calculation of τ (equation (5.32))
12.	Calculation of Δf_{pz} (equation (5.33)) and $f_{pz,n}$ (equation (5.34))
13.	Calculation of $\Delta\varepsilon_{pz}$ (equation (5.35)) and $\varepsilon_{cz,n}$ (equation (5.36)
14.	Check, if $\Delta\varepsilon_{pz} = \varepsilon_{cz,n}$
15.	If step 14 is fulfilled, determine L_t; otherwise, go to step 3

The material properties of CFRP and UHPFRC were used in accordance with chapters 3 and 4, besides parameter variations.

One key factor of this approach is the determination of the friction coefficient μ to calculate the bond stress τ from pressure p. In Fig. 5.21, the influence of varying friction coefficients μ are exemplarily shown for a CFRP bar Ø5 mm and CFRP strand Ø7.5 mm. The tensile strength f_{ct} is set to 2.5 MPa and one centrically placed tendon with a pre-tensioning stress of 1,350 MPa is assumed. The cross-sections were adopted from test specimens which did not crack at the surface during the prestressing process.

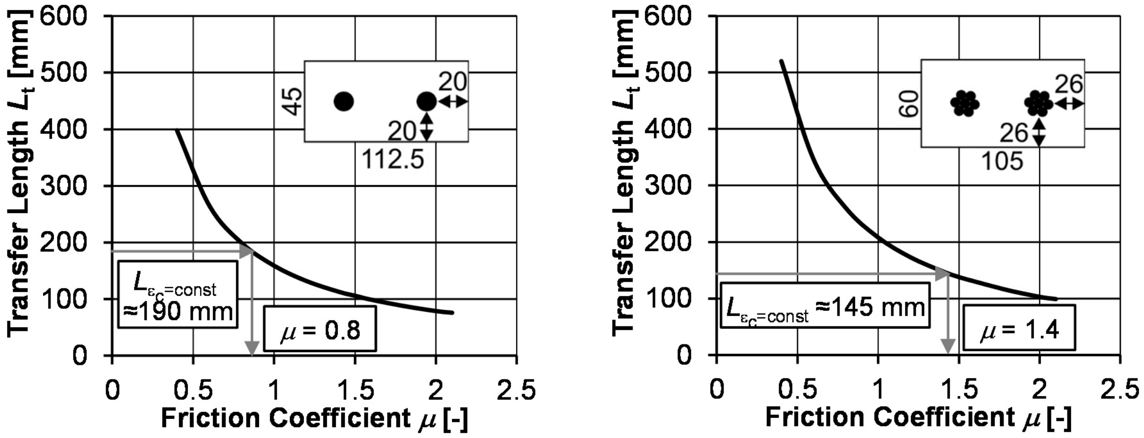

Fig. 5.21 **Influence of different friction coefficients μ on the transfer length L_t**

For the evaluation of experimental results (cp. section 5.3.2), the transfer length was determined according to /DIBt80/. With this method, the maximum strains determined from testing do not necessarily occur at the end of the transfer length. This is due to small imperfections and measurement inaccuracy. Hence, for the determination of the friction coefficient, the positions of maximum strain $L_{\varepsilon c=\mathrm{const}}$ were used. For the CFRP strand, the value of $L_{\varepsilon c=\mathrm{const}}$ coincides with the transfer length L_t ,whereas for the CFRP bar, the $L_{\varepsilon c=\mathrm{const}}$ is about 25 % higher than the determined L_t. With this approach, a friction coefficient of 0.8 was determined for CFRP bars and 1.4 for CFRP strands by comparing the transfer length with test results (TL-6, TL-16; without splitting cracks at the concrete surface). For both cases, cracking occurred only in the vicinity of the tendon and did not proceed to the outer concrete surface. These results are in accordance with numerical simulations.

In Fig. 5.22, results of tests on the transfer length are compared with calculated concrete compression strains for a CFRP bar Ø5 mm and a strand CFRP strand Ø7.5 mm pre-tensioned with 1,350 MPa. In the tests as well as in the calculations, no cracks proceeded to the outer concrete surface. Even though, the model predicted cracking in the vicinity of the tendons. For both tendons, the model according to /Han16/ predicted the transfer length in very good agreement with test results.

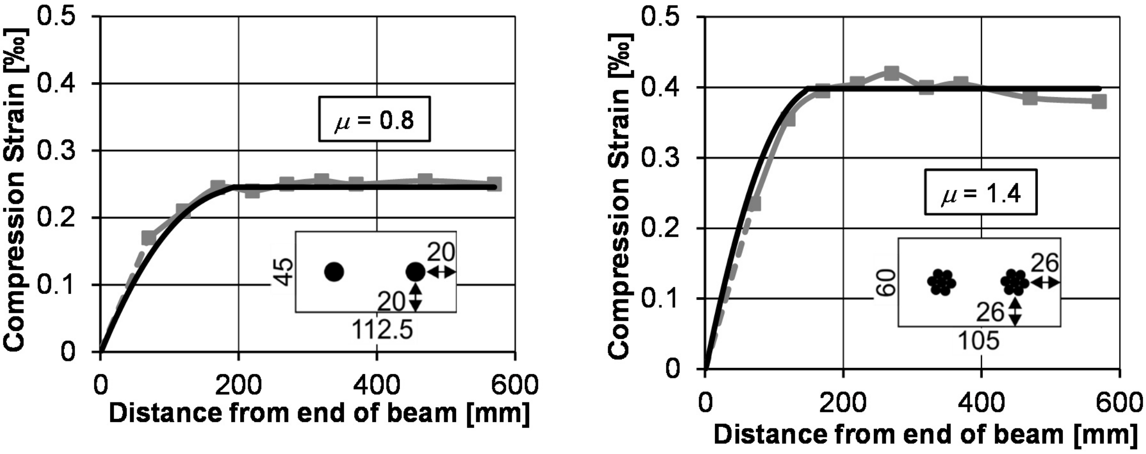

Fig. 5.22 **Transfer length L_t over the distance from the free beam end for tests TL-6 (left) and TL-16 (right): Experimental results (grey) and calculated relationships (black)**

In Fig. 5.23 (left), the distribution of tendon stress over the transfer length is exemplarily shown for a partly cracked specimen. The tendon stress increases over the transfer length and reaches the maximum of about 1,290 MPa at the end of the transfer length. The maximum stress and the distribution over the transfer length coincides with the numerical results.

The bond stress (Fig. 5.23 (right)) results from the lateral extension of the tendon (HOYER-effect) and the slip between tendon and concrete. Since the slip decreases over the transfer length, the bond stress decreases until the prestressing force is transferred to the concrete member. The corresponding distribution of radial stresses can be obtained by dividing the bond stress by the friction coefficient. The maximum radial pressure at the free end was about 17 MPa, leading to a maximum bond stress of 25 MPa. This magnitude was also determined in pull-out tests (cp. section 5.2.2).

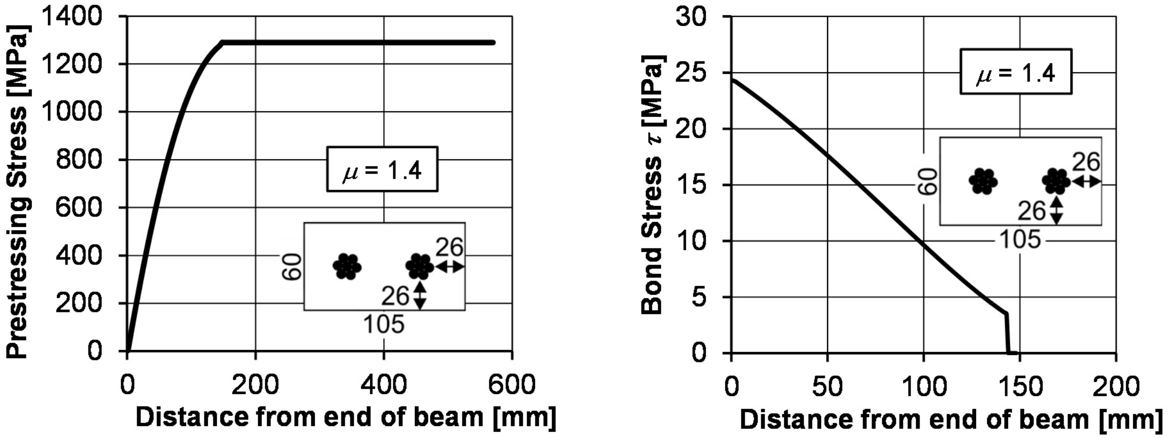

Fig. 5.23 **Prestressing stress f_{pz} (left) and corresponding bond stress τ (right) over the distance from the end of the beam for a partly cracked specimen**

Hereafter, the influence of parameter variations on the transfer lengths is exemplarily analysed. For these investigations, the friction coefficient μ was consistently set to 0.8 for CFRP bars and 1.4 for CFRP strands. First, the influence of varying concrete covers C are investigated for a CFRP bar Ø5 mm and CFRP strand Ø7.5 mm (Fig. 5.24). The pre-tensioning stress f_{pj} was set to 1,350 MPa. The concrete tensile strength $f_{\mathrm{ct}} = 2.5$ MPa was adopted from testing after one day. For the analysis, a quadratic cross-section of 200x200 mm² was used. The varying concrete cover C results in different eccentricities e.

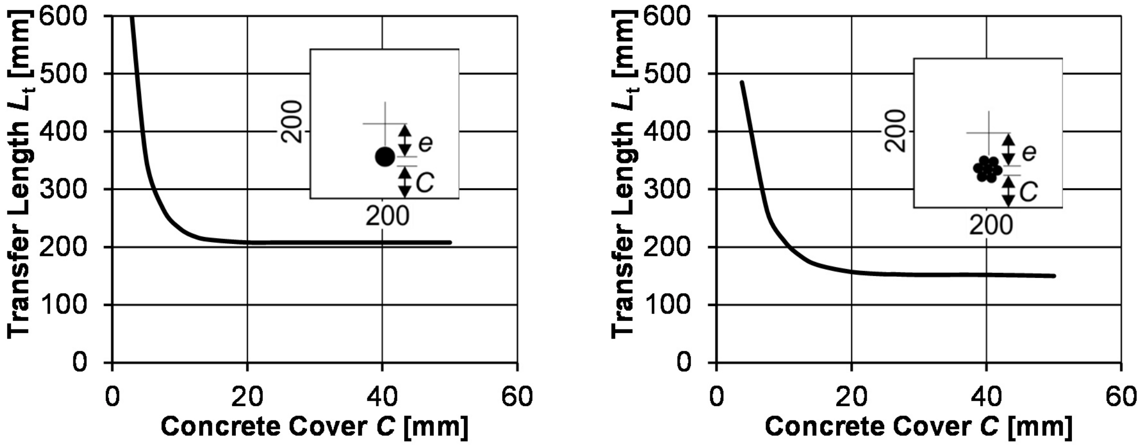

Fig. 5.24 **Transfer length L_t over the distance from the free beam end dependent on the concrete cover C for CFRP bars Ø5mm (left) and CFRP strands Ø7.5 mm (right)**

In both cases, a concrete cover of twice the tendon diameter led to excessive cracking. As expected, the transfer lengths decreased for increasing concrete covers. For concrete cover ratios of $c/d_{\mathrm{p}} > 3.5$ for CFRP bars and $c/d_{\mathrm{p}} > 3.0$ for CFRP strands, the transfer lengths remained constant. These results are in accordance with test results. During testing, cracking only proceeded to the concrete surface for smaller ratios.

In Fig. 5.25, the influences of tensile strength f_{ct} and pre-tensioning stress f_{pj} on the transfer length are depicted. The cross-section in either cases was set to 105x60 mm². Hence, a clear concrete cover of 26.25 mm is confining the concrete. For the analysis of the tensile strength f_{ct}, a CFRP strand Ø7.5 mm with jacking stress of 1,350 MPa was assumed. Since the Young's modulus varies with concrete strength, it was adjusted for different tensile strengths. Since hardly any information can be found in literature about values of Young's moduli dependent on the tensile strength of green UHPFRC, for this analysis, Young's moduli were interpolated from test values of one and three days as well as 28 days of concrete hardening. For the investigations on the influence of jacking stresses f_{pj}, the tensile strength f_{ct} was set to 2.5 MPa. As shown in Fig. 5.25 (left), the determined transfer length L_t decreases from roughly 300 mm for $f_{\mathrm{ct}} = 1$ MPa to 100 mm for $f_{\mathrm{ct}} = 5$ MPa, which corresponds to the tensile strength after 28 days. During experimental testing, the prestressing forces were released after one day of concrete hardening which complies with the tensile strength of 2.5 MPa. For a tensile strength of less than 1.5 MPa, excessive cracking was predicted from the model.

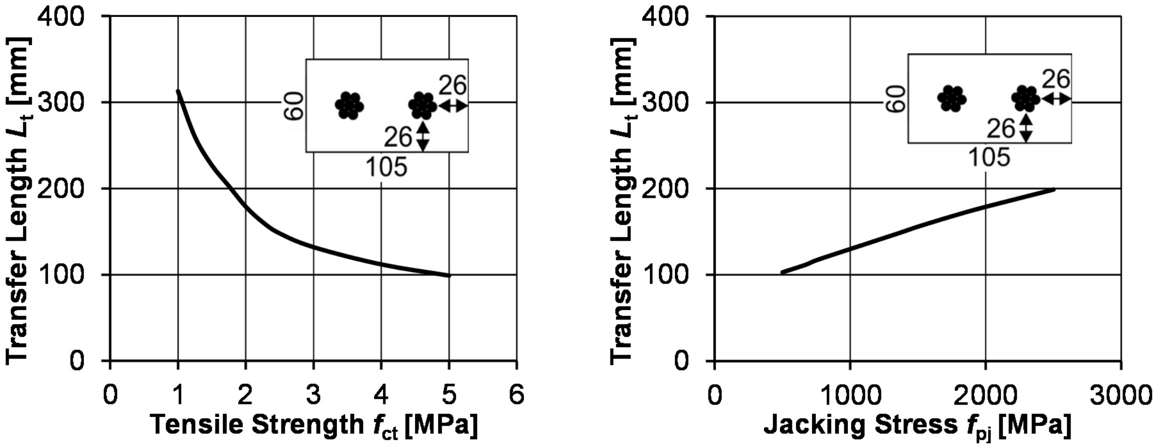

Fig. 5.25 **Transfer length L_t over the distance from the free beam end dependent on concrete tensile strength f_{ct} (left) and pre-tensioning stress f_{pj} (right) for CFRP strands Ø7.5 mm**

Fig. 5.25 (right) shows that the transfer length increases linearly with increasing pre-tensioning stress. For this cross-section, cracks did not proceed to the outer concrete surface. Nevertheless, to provide sufficient capacity in tensile strength of CFRP, prestressing of over 1,500 MPa is not favourable.

5.6 Conclusions

In this chapter, the bond behaviour of CFRP prestressing tendons in UHPFRC was investigated. Based on experimental testing, maximum bond stresses, minimum concrete covers and transfer lengths were determined. Bond strength of up to 25 MPa (σ_p = 1,350 MPa) were reached for CFRP bars and seven-wire strands. The high bond stresses resulted in a transfer length of less than 150 mm for the same pre-tensioning stress. In numerical investigations using non-linear material behaviour, friction coefficients for CFRP bars and strands were derived to 0.8 and 1.4, respectively. For these friction coefficients, compression strains and slip of tendons were found in good agreement with the test results. Two different models were applied to determine the transfer length theoretically. Based on results from pull-out testing, bond stress distributions were empirically derived. With the aid of the bond differential equation, the transfer length was determined in good accordance with the test results. Since this empirical model uses test results, it is only suitable for parameter variations by further testing. Additionally, a THICK-WALLED CYLINDER MODEL proposed by HAN ET AL /Han16/ was applied and further investigations on CFRP tendons in UHPFRC were conducted. Besides the determination of friction coefficients, which were in agreement with numerical results, transfer lengths have been determined. The model was found in very good agreement with test results.

6 Sandwich Sections under Tensile and Shear Loading

6.1 Preface

The load-bearing capacity of sandwich panels is strongly controlled by the interface zone between core material and outer layers. To investigate the quality of the production method of foaming in pack of polyurethane (cp. section 3.5) tensile and shear tests were conducted on small-scale specimens. The test results of tensile and shear strength as well as stiffness, served as basis for numerical models and theoretical approaches. Major experimental results presented in this chapter have also been published in /Sha13/ and /Sha15a/ together with investigations on sandwich sections with TRC facings conducted by SHAMS.

6.2 Tensile Tests

6.2.1 Test Set-up and Procedure

Tensile testing was carried out on small-scale quadratic specimen (Fig. 6.1) based on the setup applied by HORSTMANN /Hor10/ and SHAMS /Sha15b/.The load was induced by cast-in channels since high bond strength was expected. Hence, the thickness of UHPFRC layers was chosen to 80 mm in order to anchor the cast-in channels.

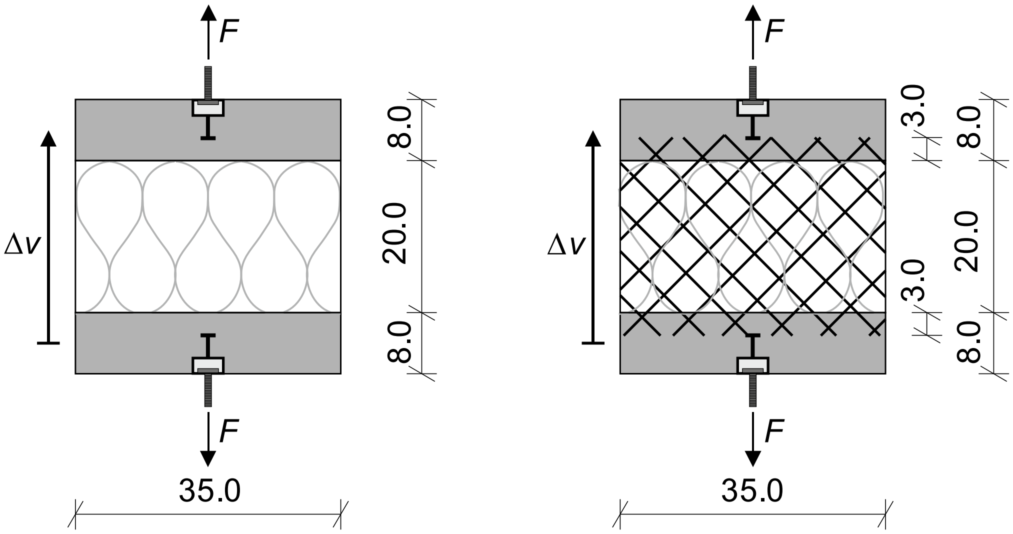

Fig. 6.1 Experimental set-ups of tensile tests

In all tests, the thickness of the core foam was chosen to 200 mm. Tests without connector elements between the outer layers served for the verification of bond strength compared to the tensile strength of the core material only. The application of a CFRP shear grid was exemplarily investigated with an embedment length of 30 mm. The load was induced displacement controlled with 1.0 mm/min. Besides the load, LVDT's were used to measure the relative displacement *Δv* of the UHPFRC layers.

6.2.2 Experimental Results: Tensile Loading

The adhesive strength between UHFRPC and PU foam was determined in tests without connecting devices. The load-displacement response was mainly linear elastic until failure. The production method of foaming in pack resulted in a high and reproducible bond strength. Due to the high bond strength of foamed PU, the application of a CFRP shear grid did not lead to an increase in maximum tensile load, but to a pronounced post-peak behaviour. After reaching the bond strength of the PU foam, the CFRP shear grid failed by rupture of one roving after the other. In Fig. 6.2, representative test results are shown. The embedment length of 30 mm was sufficient to prevent the shear grid from pulling out. Smaller embedment lengths were not investigated, since thicknesses of UHPFRC facings of beam elements (cp. chapter 7) were determined to 60 mm. The maximum tensile stresses were about 0.22 MPa.

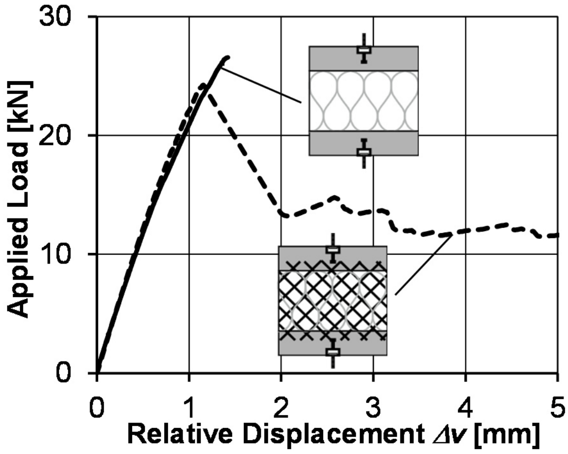

Fig. 6.2 Representative test results of tensile tests on sandwich sections

The bond strength between UHPFRC and PU is about 40 % of the uniaxial tensile strength of PU (cp. section 3.2.3). The results show similar maximum loads and load-displacement relationships as observed by SHAMS in tests with TRC layers and PU foam of roughly the same density, even though in /Sha15b/ the surfaces of the TRC layers were pre-treated to enhance the bond quality. Tests conducted by HORSTMANN /Hor10/, /Sha14/ using slabstock foams and TRC facings, showed only about 50 % of the bond strength for PU with similar density compared to the presented tests.

6.3 Shear Tests

6.3.1 Test Set-up and Procedure

Generally, different set-ups of shear or push-out tests on sandwich elements are available to determine shear strength and shear modulus. For this purpose usually small-scale specimen are used (e.g. /Foe89/, /Riz09/, /Hor10/, /Pah11/, /Zan13/, /Sha15b/), since for large, full-scale specimen additional influences may be observed. Different set-ups do not lead to the same results and vary in complexity and costs. Below, two different types of test specimen are briefly discussed.

A doubly symmetric set-up (Fig. 6.3, left)) was chosen by Horstmann /Hor10/. A stiff frame reduced the influence of load eccentricities. Nevertheless, bending effects due to misalignments could not be avoided /Hor10/. The production of doubly symmetric sandwich elements and the test procedure were cost-intensive and complex. Shams /Sha13/, /Sha15b/ used a set-up with only two concrete layers and a stiff frame (Fig. 6.3, right)) to provide an easy way to test sandwich panels under shear loading. The lever arm (core height and thickness of the concrete layer) induces a bending moment, which results in tensile stresses at the top of the specimen and compressive stresses at the bottom.

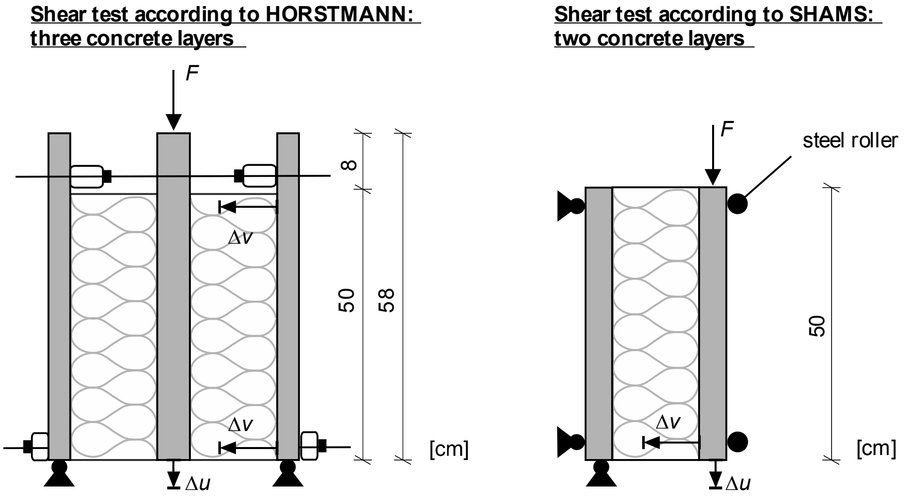

Fig. 6.3 Set-ups of shear tests by Horstmann /Hor10/ (left) and Shams /Sha13/, /Sha15b/ (right)

For the conducted study, the test set-up used by Shams /Sha15b/ (Fig. 6.3, right)) for flat test specimens was adopted to investigate the influences of core heights and shear connectors in flat specimens. Negative effects due to bending were accepted at first. Subsequently, the test set-up was modified to be applicable to folded plate cross-sections. The analysed cross-sections are shown in Fig. 6.4. The test load *F* as well as vertical and horizontal relative displacements Δu and Δv, respectively, were continuously measured. Test specimens were loaded displacement controlled with 1.0 mm/min.

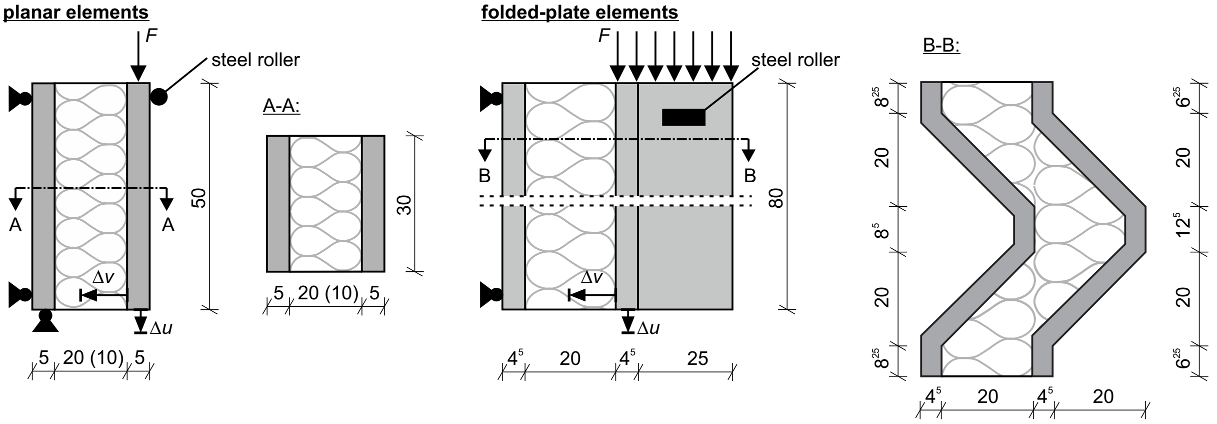

Fig. 6.4 **Set-up for shear tests on flat and folded plate elements in dependence on /Sha15b/**

Besides the identification of influences on the load-deformation response due to parameter variation, shear tests were performed to obtain the shear strength of the interface between UHPFRC and PU. Due to bending effects using standard test setups, the direct determination of bond strength and shear modulus from these tests seemed problematic. To reduce influences from bending effects, a cylindrical test specimen was introduced. With this test set-up only circumferential bending moments occur, which do not lead to direct tension and compression at top and bottom, respectively, as for standard test set-ups. The cylindrical test specimen consists of a standard concrete cylinder for material testing (Ø: 150 mm, height: 300 mm) in combination with a concrete cuboid with a block out (Fig. 6.5). The volume between cylinder and surrounding concrete was foamed in pack. Within these tests, the core height was altered but no shear connectors were applied. The test load *F* and vertical relative displacement *Δu* were continuously measured. The test specimens were loaded displacement controlled with 1.0 mm/min.

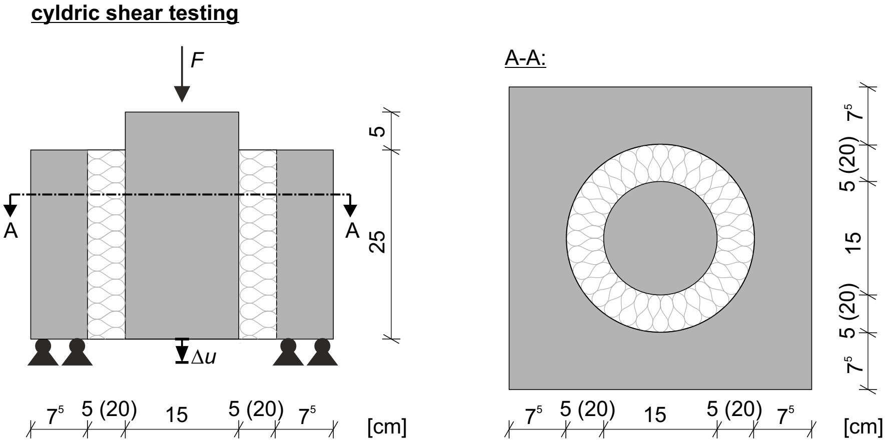

Fig. 6.5 **Cylindrical set-up for shear tests**

6.3.2 Experimental Results: Shear Loading

The influences of core height and application of shear connectors were determined with the test set-up using flat elements. As expected, the core height has a major influence on shear stiffness of sandwich sections (Fig. 6.6 a)). Tests on sections without shear connectors with a core height of 200 mm resisted roughly 25 % less test load at the same relative displacement Δu compared to sections with a core height of 100 mm. The application of a CFRP shear grid (cp. Fig. 3.1) generally resulted in a stiffer behaviour and a pronounced post-failure state (Fig. 6.6 b)). For the applied CFRP shear grid a sufficient amount of remaining load-bearing capacity ($\approx$80 % of maximum test load) was observed, leading to an increase of over 100 % in relative displacement Δu. This behaviour was observed for 100 mm and 200 mm core heights as well as for one or two applied shear grids (cp. Appendix B). CFRP shear grids with embedment length of 30 mm in the UHPFRC facings, failed within the free length between the facings. Hence, the short embedment length was sufficient. GFRP pin connectors (cp. Fig. 3.1) with embedment length of 30 mm failed at maximum load and did not lead to remaining load-bearing capacity. For core heights of 100 mm and 200 mm, the maximum shear stresses were derived to 0.38 MPa and 0.27 MPa, respectively. The load-displacement behaviour until maximum load showed no significant difference compared to tests on specimens without connectors (cp. Appendix B). The elements failed due to diagonal cracks in the core material or by debonding. As mentioned before, the induced bending moment resulted in tensile forces at top and compression forces at bottom of the specimen. The acting bending moment, led to slight tilting of the specimens. Hence, a proper support of the specimen in horizontal direction could not be achieved.

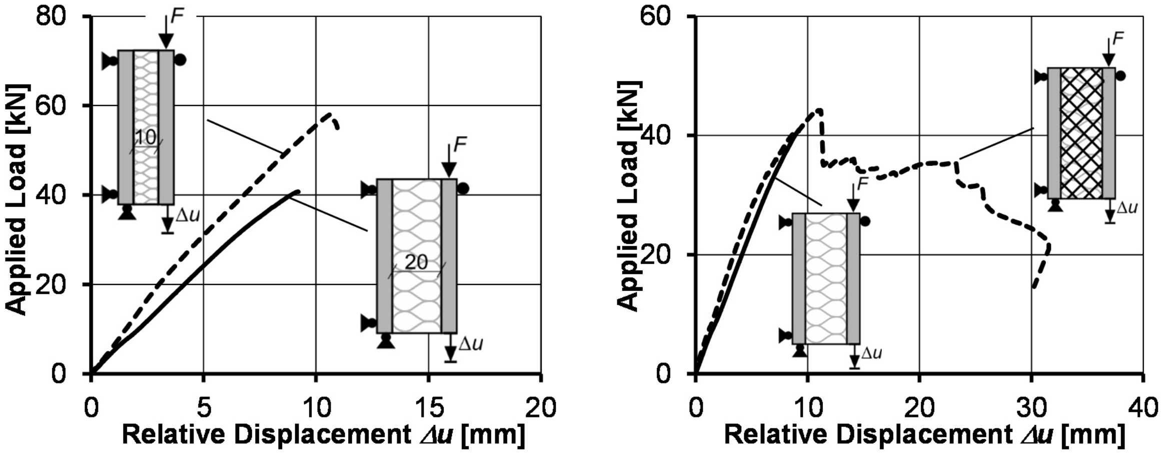

Fig. 6.6 **Representative results of shear tests on planar sandwich sections: Influence of core height h_c, (left) and CFRP shear grid (right)**

The investigated folded plate cross-section with a core height of 200 mm showed an about 50 % higher stiffness compared to flat sections with the same core height (Fig. 6.7). For this comparison, the applied load was normalised by the bond area. Again, slight tilting of the specimen could not be avoided. The elements failed due to shear cracks in the core material and partially from debonding at the top part of the specimens. In chapter 7, the influence of non-flat cross-sections was further investigated.

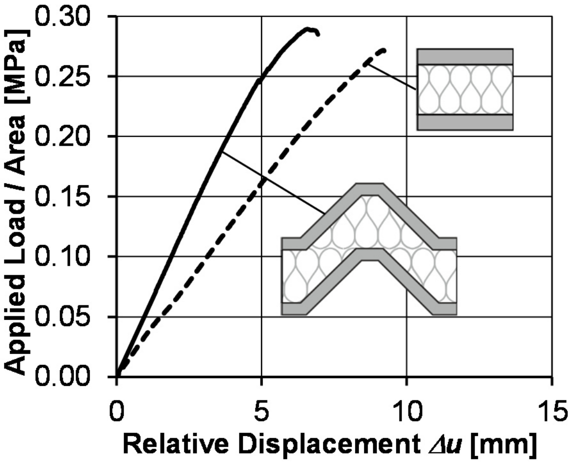

Fig. 6.7 **Representative results of shear tests on sandwich sections with core height of h_c = 200 mm: Influence of the cross-section**

As mentioned before, specimens tested with the set-ups in dependence on /Sha15b/ or /Hor10/ experience relatively high bending moments, i.e. tensile and compressive forces at top and bottom, respectively, and not mainly shear forces. Even though, these test set-ups seemed adequate to evaluate different configurations and material combinations. The derivation of input parameters for theoretical approaches and especially numerical models directly from these test results seemed problematic. The proposed set-up of a doubly symmetric cylindrically shaped push-out specimen (Fig. 6.5) showed only little influence on the load-deflection behaviour because of circular bending moments.

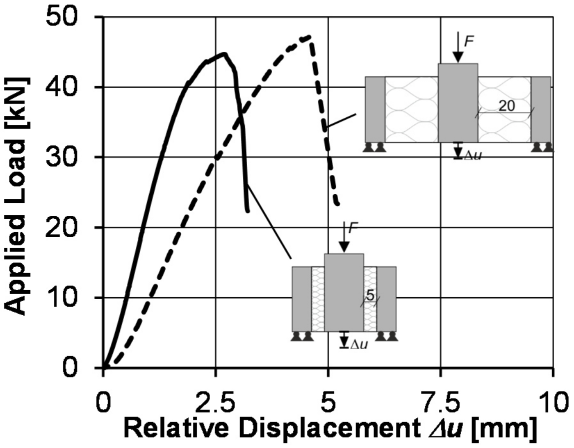

Fig. 6.8 **Representative results of shear tests on circular sandwich sections: Influence of the core-height**

For either core-thicknesses, the maximum stress in the bond zone was about 0.4 MPa. In contrast to the flat test set-up, the maximum stress was about 35 % higher and corresponding relative displacement about 70 % smaller. The evaluation of shear modulus G_c shows a significant influence of the test set-up. The shear modulus was determined according to /DIN13b/ (equation (6.1)). Load F_{el} and relative displacement Δu_{el} were to be determined from linear-elastic behaviour.

$$G_c = \frac{h_c \cdot F_{el}}{A \cdot \Delta u_{el}} \tag{6.1}$$

From material testing (cp. section 3.2.3), G_{c} was about 11.5 MPa. Results from flat shear tests showed a resulting shear modulus of about 6.5 MPa, whereas for the folded plate specimen, G_{c} was determined to 10 MPa. In these tests, tilting of the specimens due to acting bending moment may have resulted in this reduction. By developing the circumference of the cylindrical specimen into a planar width, the shear modulus from cylindrical shear tests was determined in the range of 10.5 MPa for a thickness of 50 mm and about 12 MPa for a thickness of 200 mm. For investigations on large-scale elements, a value of 11.5 MPa was taken into account, since the results of material testing are standardised. In chapter 7 the influence of the shear modulus on the structural performance of sandwich panels under flexural loading was further investigated.

6.4 Calibration and Validation of Numerical Models

The load transfer of sandwich sections under tensile and shear loading is greatly influenced by the strength of the bond zone and the material performance of the core. In the first step, the applicability of the crushable foam material law (cp. chapter 3) for the applied polyurethane core was verified. Material samples under compressive, tensile and shear loading according to /DIN13b, DIN13c, DIN13d/ (cp. Fig. 3.2) were modelled using the techniques described in chapter 3.6. The parameters of the core material (PU) were determined from material testing. The foam hardening part was derived from tests under compression. Hence, plastic deformations were assumed to start at a stress of 0.53 MPa (about 21 KN in the compression test). Further input parameters are summarised in section 3.6.5. The mesh size was set to 10 mm for the investigations of PU material properties. In Fig. 6.9, numerical and experimental results for compressive, tensile and shear loading are shown. For shear loading, the resultant forces of one half of the specimen (cp. section 3.2.3) are shown.

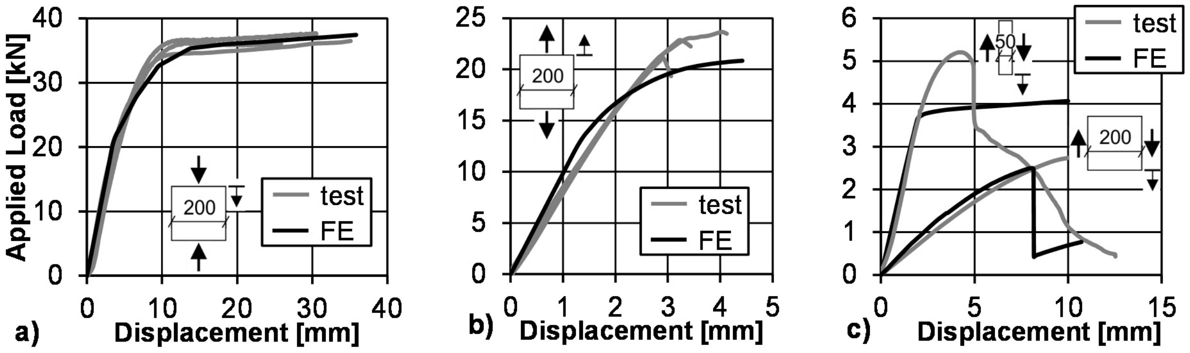

Fig. 6.9 **Comparison of numerical (black) and test (grey) results of PU-foam under a) compressive, b) tensile and c) shear loading**

For all loading cases, the predicted load-deformation response was in good agreement with the test results. Only for shear loading on specimens with a thickness of 50 mm, failure was predicted inaccurately after 80 % of maximum load was reached. Since the thickness of 50 mm was not further applied during testing on sandwich panels, the phenomenon was not investigated closely.

In the next step, sandwich sections under tensile and shear loading were modelled. The interface between UHPFRC and core material was modelled with a layer (thickness: 1.0 mm) of cohesive elements (compare chapter 3.6.6). Since no cracking of UHPFRC was expected, a linear elastic behaviour was assumed for the simulations of tensile and shear tests. The same results are achieved using the damage plasticity model for UHPFRC, but with more computational effort.

For the normal direction, a strength $t_{n,0}$ of 0.22 MPa was derived from tensile tests (cp. section 6.2.2). In shear tests a strength of 0.4 MPa was observed. Since values for both shear directions need to be provided, for $t_{s,0}$ and $t_{t,0}$ the same strengths were assumed. The numerical models were set up to provide the same conditions as in experimental testing. For tensile loading, the load was applied only at the positions of cast-in channels (cp. Fig. 6.1). During shear testing, small tilting effects were observed for flat and folded plate specimens (cp. section 6.3). For the finite element simulations, horizontal springs as boundary conditions were not modelled, because the amount of horizontal displacement from tilting and bond zone could not be distinguished properly. Hence, the ideal situation of a fixed support facing and horizontal boundary condition at the load facings (cp. Fig. 6.4) were assumed in the model.

In Fig. 6.10 (left) the comparison of experimental results and numerical simulations for tests under tensile loading are shown. Since the tensile behaviour was derived directly from test results, the predictions of stiffness and maximum load were found in very good agreement. For shear tests, the input parameters were derived from results on cylindrical specimens. In Fig. 6.10 (right) the numerically determined load-displacement response is shown in comparison to test results. As mentioned before, the horizontal boundary condition of the simulation represents an infinite stiff support, which does not represent the conditions during testing. As expected, a slightly stiffer behaviour was determined in the simulation compared to the test result. Even though, the maximum load was in good agreement. A mixed mode failure of plastic deformations and debonding was predicted. During the experimental investigations, the sandwich sections failed either in the interface between UHPFRC facings and core material at the top of the specimens or by diagonal cracks in the core material.

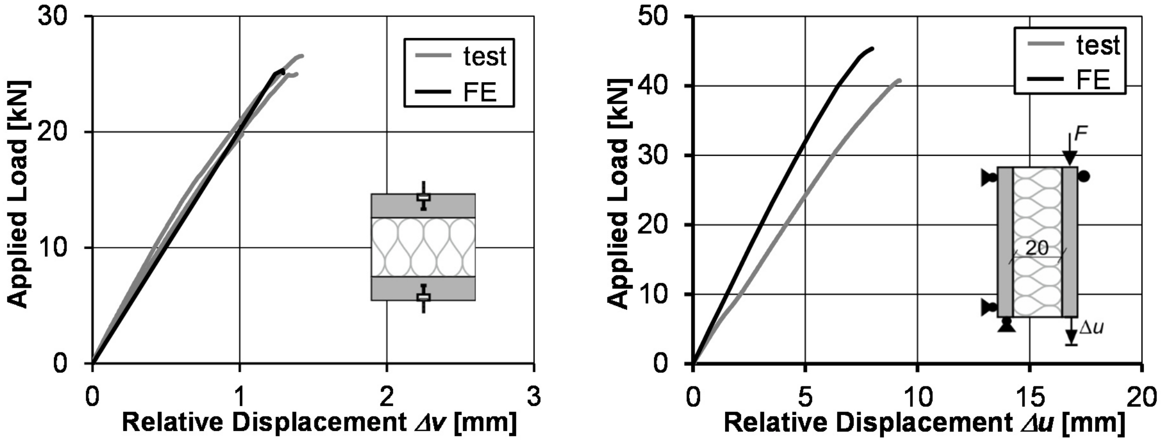

Fig. 6.10 Comparison of representative experimental test results and numerical simulations on sandwich sections under tensile (left) and shear (right) loading

Besides influences of the test setup, the model was capable to predict the load-deformation response of flat sandwich sections under shear loading. In the next step, the approaches were applied on a spatially shaped cross-section. The shear test on a folded plate cross-section was modelled according to the set-up shown in Fig. 6.4. Again, the rollers were assumed as horizontal boundary conditions. In Fig. 6.11, the load-displacement relationships of tests on folded plate elements are compared to the numerically determined response. Since tilting could not be fully avoided, like described before, the numerical results showed a slightly stiffer response. As for the flat section, the maximum loads were found in good agreement with the test results. In the numerical simulation, the elements failed due to plastic deformations of the core and a partially bond failure at the top of the specimens. In the tests, shear cracks and debonding at the top of the specimens were observed, similarly to flat panels.

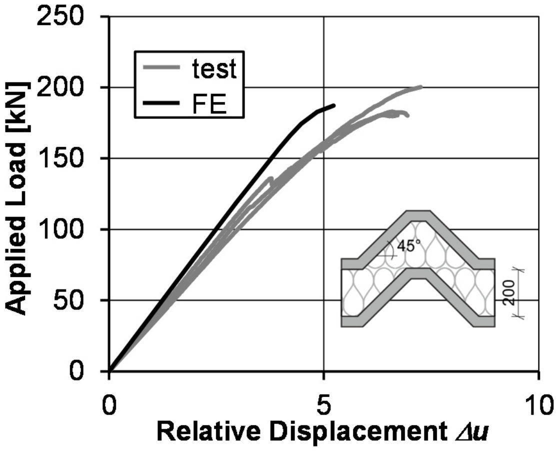

Fig. 6.11 Folded plate sandwich section under shear loading: Comparison of experimental results and numerical simulation

The numerical results show a good agreement with the test results of small-scale sandwich sections under tensile and shear loading. Therefore, the models seemed adequate to be applied for further investigations on large-scale sandwich panels under flexural loading (cp. chapter 7).

6.5 Spring model for shear stiffness of core and shear connectors

The bearing behaviour of sandwich panels under shear load can be estimated with spring models /Hor10/. For this purpose, HORSTMANN /Hor10/ used parallel connected elastic springs to idealise the bearing mechanisms of core material and shear connectors. In Fig. 6.12 the spring model is depicted.

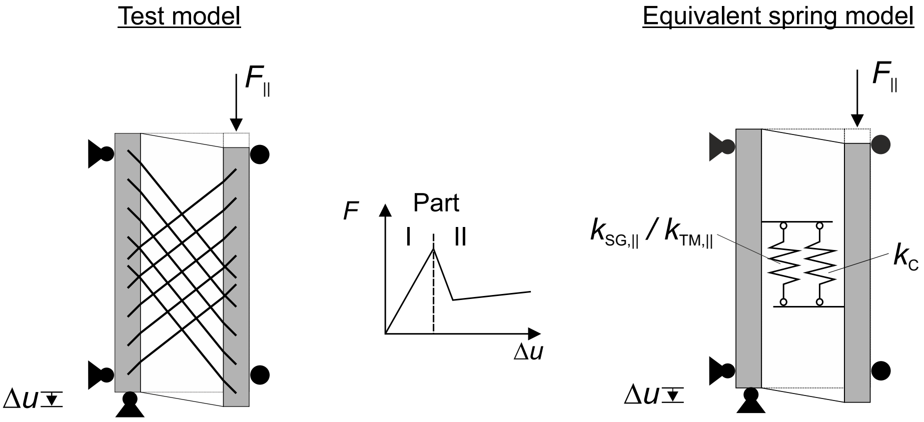

Fig. 6.12 **Spring models for shear loading of sandwich sections (reproduced from /Hor10/ and /Sha15b/)**

The shear stiffness is composed of single stiffnesses of core material (C) and shear connectors (SG: shear grid, P: Pin connector), which act as parallel springs. The resulting forces are obtained by multiplication of the corresponding deformation (equation (6.2)).

$$F_{||} = F_{C,||} + F_{SG,||} + F_{pin,||} = (k_{C,||} + k_{SG,||} + k_{pin,||}) \cdot \Delta u \qquad (6.2)$$

The shear stiffness of the core material $k_{C,||}$ is determined from shear Modulus G_C and the geometric parameters of bond zone $\Delta L \cdot b$ and core height h_C (Fig. 6.13).

$$k_{C,||} = G_C \cdot \frac{b \cdot \Delta l}{h_C} \qquad (6.3)$$

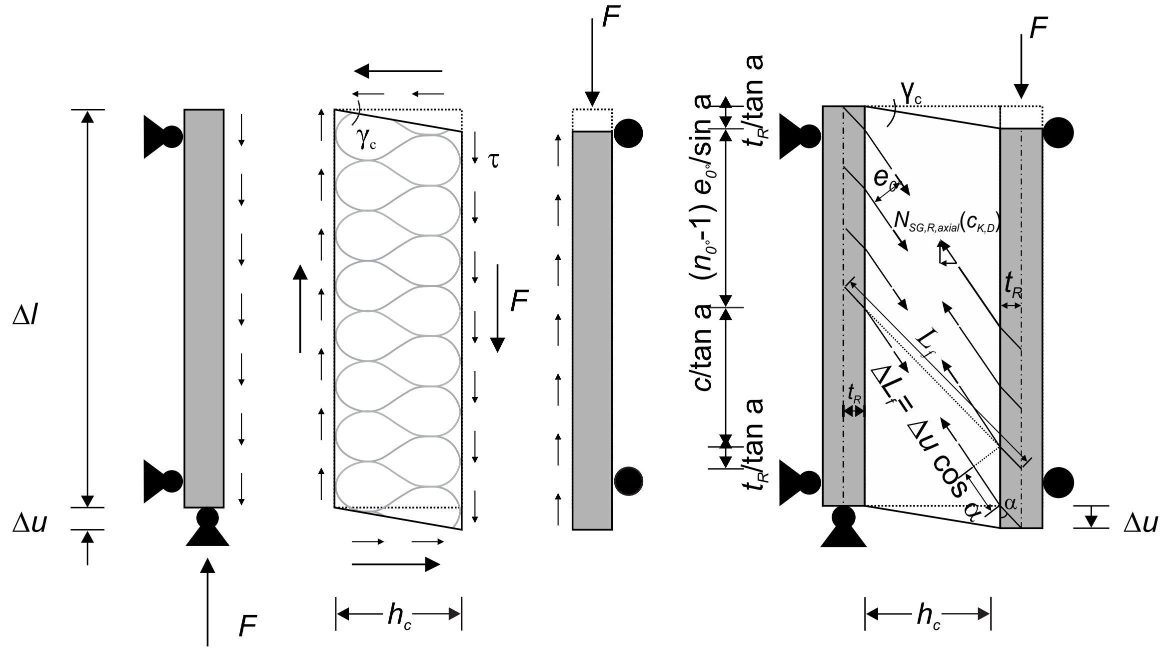

Fig. 6.13 **Derivation of shear load capacity of core and shear grid (reproduced from /Hor10/ and /Sha15b/)**

The final equations, which were derived by HORSTMANN /Hor10/, are summarised in /Sha15b/. For a better understanding of the procedure, the equations are shortly summarised again.

The shear stiffness $k_{SG,||}$ of the shear grid is composed of the axial stiffness of one roving $k_{SG,R}$ ($k_{C,c}$), the number of rovings in 0°-direction $n_{0°}$ and α is the angle of the rovings.

$$k_{SG,||} = k_{SG,R}(k_{C,c}) \cdot n_{0°} \cdot \cos^2 \alpha \tag{6.4}$$

The axial stiffness of one roving $k_{SG,R}$ ($k_{C,c}$) is determined from strain stiffness $k_{SG,R}$ of the roving and compressive rigidity of the core material $k_{C,c}$. The equations can be summarised as follows:

$$\begin{aligned}
k_{SG,R}(k_{C,c}) &= k_{SG,R} \cdot \left(1 - \frac{\tan\alpha}{\left(\dfrac{k_{C,c}}{n_{0°} \cdot k_{SG,R}} \cdot \dfrac{1}{\sin\alpha \cdot \cos\alpha} + \tan\alpha \right)} \right) \\
k_{SG,R} &= \frac{1}{\dfrac{L_f}{E_{R,0°} \cdot A_{R,0°}} + \dfrac{2}{k_{\sup,a}}} \\
k_{C,c} &= \frac{E_{C,c} \cdot b \cdot \Delta L}{h_c}
\end{aligned} \tag{6.5}$$

$$L_f = \frac{h_c + 2 \cdot t_R}{\cos \alpha}$$

$$\Delta L = \frac{h_c + 2 \cdot t_R}{\tan \alpha} + \frac{(n_{0^\circ} - 1) e_{0^\circ}}{\cos \alpha} \tag{6.6}$$

n_{0°	Number of rovings in 0° direction
$k_{\sup,a}$	Average stiffness of support in concrete (12.5kN/mm for $t_R = 40$ mm)
$E_{R,0^\circ}$	Young's Modulus of shear grid in 0° direction
$A_{R,0^\circ}$	Cross - section of rovings in 0° direction
t_R / α	Embedment length /embedment angle
L_f	Span of rovings (clamping at $t_R / 2$)
ΔL	Effective length

For the shear stiffness of pin connectors (cp. Fig. 3.1) a beam, which is clamped at both supports, was assumed in /Hor10/. The resulting stiffness $k_{\text{pin},||}$ was derived as follows:

$$k_{pin,||} = \frac{12 \cdot E_{pin} \cdot I_{pin}}{d_p^3} \tag{6.7}$$

E_{pin} and I_{pin} are the pin's elastic modulus and moment of inertia, respectively. The bending length d_{p} is composed of the core height h_{c} and the embedment length x_{e} in both facings (equation (6.8)).

$$d_p = h_c + 2 \cdot x_e, \qquad x_e = \left(1 - \frac{1}{1 + t_p / h_c}\right) \cdot \frac{t_p}{3} \tag{6.8}$$

For validation of the approaches to determine the resulting spring stiffness, the linear elastic stiffness of experimental results was derived based on load F and corresponding relative displacement Δu. Due to the acting bending moment, the shear tests on flat panels showed a less stiff behaviour. As mentioned before, shear modulus derived from material testing was determined to 11.5 MPa, whereas the values of shear modulus directly derived from shear tests on sandwich sections, gives about 6.5 MPa, due to the induced bending moment (cp. section 6.3.2). To show the effect of parallel acting springs, i.e. the interaction of core material and shear grid or pin-connector, the shear modulus, which was derived from testing on flat sandwich panels was adopted. For further investigations on sandwich panels under flexural loading, the value of 11.5 MPa was applied, since these negative bending effects do not occur. In Fig. 6.14 ratios of the experimental and theoretical shear stiffness for load levels of 50 % and 75 % are depicted.

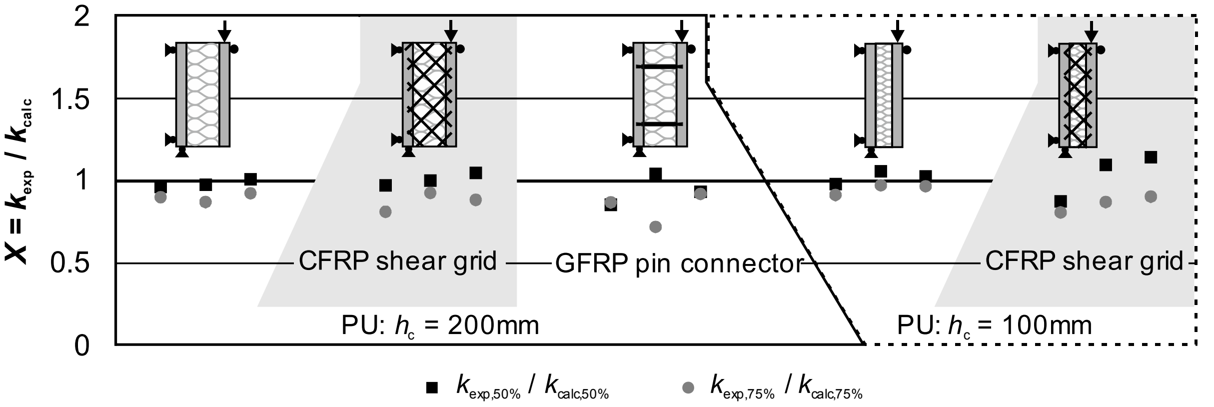

Fig. 6.14 **Ratios of experimental and theoretical shear stiffness (based on spring model)**

Since the mean shear modulus was derived from these tests at this stage, the predicted stiffnesses for sandwich sections without shear connectors show a good agreement for investigated core thicknesses of 200 mm and 100 mm. In shear tests with shear connectors, a high increase in stiffness compared to section without shear connectors was not observed. For these test configurations, the calculated stiffness was slightly overestimated. This may be caused, by the high bond strength between core and facings, which resulted in high test loads at failure of the bond zone. This load was close to the maximum load of the shear grid. Further investigations on the application of shear grids were conducted in chapter 7.

6.6 Conclusions

In this chapter, the chosen production technique of sandwich panels by foaming in pack was validated. The test results showed high bond strengths under tensile and shear loading. Based on the test results, numerical models were validated. These models serve as basis for further investigations on sandwich panels under flexural loading (chapter 7). The determination of the shear stiffness of sandwich cross-sections is a key factor for the prediction of maximum loads. To establish the background for an analytical approach (chapter 7), the theoretical stiffnesses of shear connectors were determined.

7 Investigations on Sandwich Panels under Flexural Loading

7.1 Preface

In this chapter, the results of investigations on small-scale specimens were used to set up sandwich panels with spatially shaped facings. In total, three different cross-sections were investigated. For the validation of the production method on large-scale specimen, elements with flat facings were produced and tested according to findings from HORSTMANN /Hor10/ and SHAMS /Sha15b/. For elements with non-flat facings, a folded plate cross-section and doubly curved configuration were analysed. The cross-sectional shapes of these sandwich sections were inspired by RC and PC elements as they were built in the 1960's and 1970's (cp. section 2.3). The cross-sections were modified in order to account for increased material properties and to achieve a good producibility as well as dimensions, which can easily be tested in the laboratory. At first, single folded plate and doubly curved UHPFRC elements were investigated. With the aid of these findings, the sandwich elements were produced and analysed.

Experimental testing with realistic loading cases, such as wind and snow induced surface loads or temperature loads requires high effort. Instead, flexural tests under three-point or four-point bending are usually conducted. Realistic loading cases are often covered by theoretical approaches /DIN13a/, /Hor10/, /Sta74/. Large-scale tests under flexural loading are necessary to verify whether homogenous bond between UHPFRC layers and core material is achievable. The transferability of PU material properties from small-scale tests to large-scale elements needs to be investigated. Test results presented in this chapter have partly been published in /Sta16a/, /Sta16b/ and together with results of tests on sandwich panels with TRC facings conducted by SHAMS in /Sha15a/.

7.2 Experimental Investigations

7.2.1 Test Set-up and Procedure

The flexural behaviour of prestressed sandwich panels was investigated on simply supported beam elements. Flat and folded plate elements were tested with 2.4 m span under three-point loading. The span was increased to 4.0 m and four-point loading for doubly curved elements. All test specimens were loaded displacement controlled with 1.0 mm/min. Besides the test load, deflections and deformations were measured continuously with LVDTs. The test setups of sandwich beams are depicted in Fig. 7.1. For evaluation of the sandwich effect, single folded plate and doubly curved elements were investigated. The test setups are shown in appendix C. Folded plate and doubly curved elements were supported and loaded continuously over their width to provide support conditions with practical relevance. Due to the complexity in production, at this stage shear connectors were only assembled for the flat elements.

Besides the cross-sectional shape, the influence of prestressing (pre-tensioned CFRP reinforcement) was investigated. For flat elements, four bars or four seven-wire strands were applied in mid-height. The CFRP reinforcement in folded plate elements was placed in the bottom flanges of the UHPFRC layers. In doubly curved elements, the reinforcement was placed diagonal as straight, but skew lines (cp. sections 2.3, 2.4, 3.4). Prestressing forces were released in the same manner as shown in chapter 5.3 for small beams. Concrete compression strains and end slip of the CFRP reinforcement were measured. All results are summarised in appendices C and D.

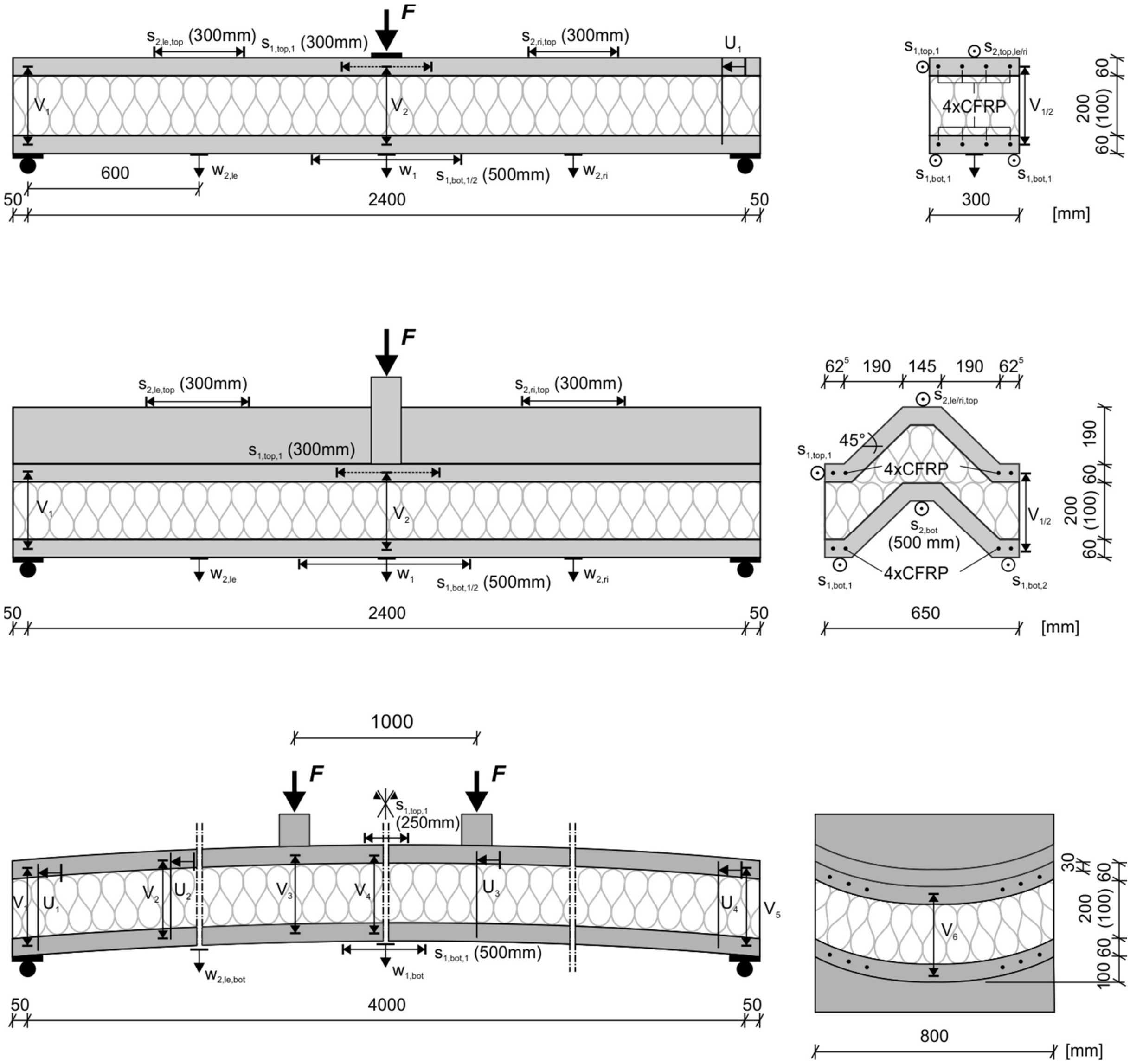

Fig. 7.1 **Test setups of bending tests on sandwich panels**

A detailed overview of all test parameters is given in appendices C and D.

7.2.2 Experimental Results

In this section, representative test results are exemplarily shown. For further information, detailed results can be found in appendices C and D. Additionally, for comparison with numerical and theoretical results, further experimental results are presented in sections 7.3 and 7.5.

Flexural tests on flat sandwich sections showed a satisfying reproducibility of bond zone quality and material properties of the PU core. Nevertheless, depending on the production procedure, the valley side of facings was in the later bond zone in some cases. The rough surface seemed to harm the bond quality. Since this was only the case for flat elements (folded plate and doubly curved elements were cast with closed formwork), this issue was not further investigated. In case of application of four CFRP bars or pre-tensioned strands, the UHPFRC facings showed maximum crack widths of about 2 mm at maximum load, i.e. the steel fibres still bridged the crack and the layers carried load. The application of a CFRP shear grid (cp. Fig. 3.1) enhanced the load capacity, since the relative slip of UHPFRC layers was decreased. Prestressing of the facings resulted in less deflection and cracking of the panels. Depending on the parameter variation, deflections of L/60 were reached at maximum load. The most common failure mode was multiple shear cracks in the core material. Only for test specimen without CFRP reinforcement (bars or strands), without CFRP shear grid or with reduced core height failed in the bond zone (cp. appendix D).

Subsequently, two tests are discussed closely. In Fig. 7.2, the load-deflection response of tests SB 3 (CFRP shear grid, bars without pre-tensioning) and SB 6 (CFRP shear grid, strands with pre-tensioning) are depicted. Both tests showed roughly the same maximum load, but about 25 % less deflection in test SB 6.

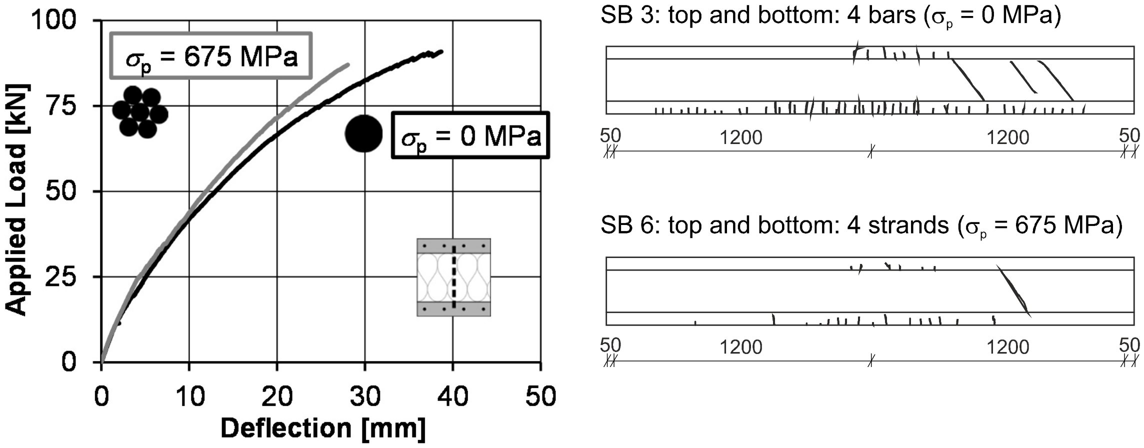

Fig. 7.2 **Comparison of planar sandwich beams SB 3 (shear grid, bars without pre-tensioning) and SB 6 (shear grid, strand with pre-tensioning σ_{pm0} = 675 MPa): Load-deflection behaviour (left) and corresponding crack patterns after testing (right)**

Failure of the test without prestressing (SB 3) was indicated by multiple cracking with small crack width and spacing (Fig. 7.2, right)). At maximum load, test SB 6 (with prestressing) showed considerably less cracks. Both tests failed due to shear cracking of the PU core in combination with cracking of the UHPFRC facings.

The structural performance of flat sandwich beams showed a positive effect of the chosen production method of foaming in pack. Even though, the elements should be cast in a way that the valley side of facings is not placed in the later bond zone for future studies. In sandwich beams with shear connectors (CFRP shear grid), delamination was not observed. One tested beam without CFRP bars or strands in the top facing failed in flexure of the top layer and crack widths exceeded 4 mm (cp. appendix D). UHPFRC facings in combination with CFRP reinforcement showed a relatively ductile material behaviour. Prestressing of the flat UHPFRC facings led to considerably less cracks and deflections, but to no increase in test load.

In the following section, the structural performance of folded plate cross-sections is discussed. At first, single folded plate elements were tested to investigate the influence of different prestressing forces and reinforcement arrangements. Afterwards, different arrangements of reinforcement and prestressing force were applied to folded plate sandwich beams. The test results of single folded plate elements were additionally used as reference to evaluate the sandwich action. In Fig. 7.3 (left) the load-deflection responses of prestressed and non-prestressed single folded plate elements and folded plate sandwich elements are exemplarily compared. For sandwich elements with equal prestressing and arrangement of reinforcement, the maximum load was 2.5 to 3 times higher compared to single folded plate elements. The corresponding maximum deflection of sandwich elements was about the same as for single folded plate elements.

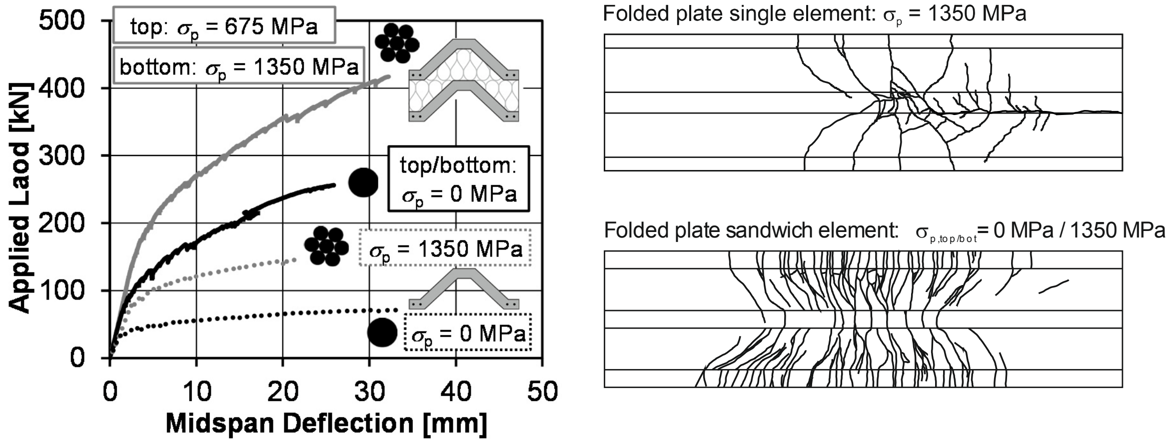

Fig. 7.3 **Single folded plate elements and folded plate sandwich elements with different prestressing forces (FP-1, FP-6 (Appendix C) and SFP-4, SFP-6 (Appendix D)): Load-deflection behaviour (left), crack patterns after testing (bottom view) of prestressed elements (right)**

Crack widths remained less than 2.5 mm until 80 % of maximum load for single folded plate beams and sandwich elements. In Fig. 7.3 (right), the crack patterns of prestressed elements are shown. For clarification, only the bottom views of the crack patterns are depicted. For single elements and sandwich panels, flexural cracks first developed at mid span in the bottom flanges at roughly 30-40 % of the maximum load. Increasing test loads resulted in further cracks in the bottom flanges. After the bottom flanges were cracked at several positions, the flexural cracks proceeded into the webs at an angle up to 45°. This could either be caused due to shear stresses or due to the inclination of the webs. However, no relative displacement of the crack edges was observed during testing. The single folded plate elements with high prestressing finally failed due to a longitudinal cracks, which started growing at one support. Defects from manufacturing were not detected. The diagonal cracks and cracking at the support were further investigated by numerical investigations in section 7.3.1. All other tested elements did not show this failure type. The sandwich panels were subjected to an additional axial loading from sandwich action, which resulted in more uniformly spaced cracks. For the investigated single folded plate elements, no deformations in transverse direction were observed, i.e. the stiffness of the folded plate elements was sufficient. Tests on single folded plate elements without any CFRP reinforcement indicated a relatively brittle flexural failure by one major crack (Appendix C). Prestressing of the elements led to increased loads with less deflections. Nevertheless, folded plate elements, which were reinforced with CFRP bars without pre-tensioning, showed a ductile load-deflection response. The folded plate sandwich elements failed either due to cracking in the core material or from a combined failure of the UHPFRC facings and core material. Again, the shear failure of the core material demonstrates a high bond strength, even without connecting devices. Further results of tests on folded plate elements are shown in sections 7.3 and 7.5.

In Fig. 7.4 (left) the load-deflection behaviour of doubly curved single and sandwich elements with different prestressing forces (six bars or strands) under four-point flexural loading is depicted. As observed for folded plate elements, the crack widths for single and sandwich elements remained less than 2.5 mm. However, for single doubly curved elements a compression failure was observed (Fig. 7.4 (right)). The failure was induced in the vicinity of the load application at deflection ratios of $L/60$ to $L/40$, depending on the prestressing. This failure mode was further analysed by numerical models (cp. section 7.3.1). The results of flexural tests on sandwich sections showed no increase in test load due to prestressing, but less deflection. In contrast to folded plate elements, doubly curved sandwich sections failed at considerably less deflection, but at four to five times the maximum load compared to single doubly curved elements. The failure of sandwich elements was induced by shear cracks in the core material due to relative slip of the outer UHPFRC layers. Compression failure, as observed for single doubly curved elements, did not occur in tests on sandwich elements. Deformations in transverse direction of the elements due to loading were not observed.

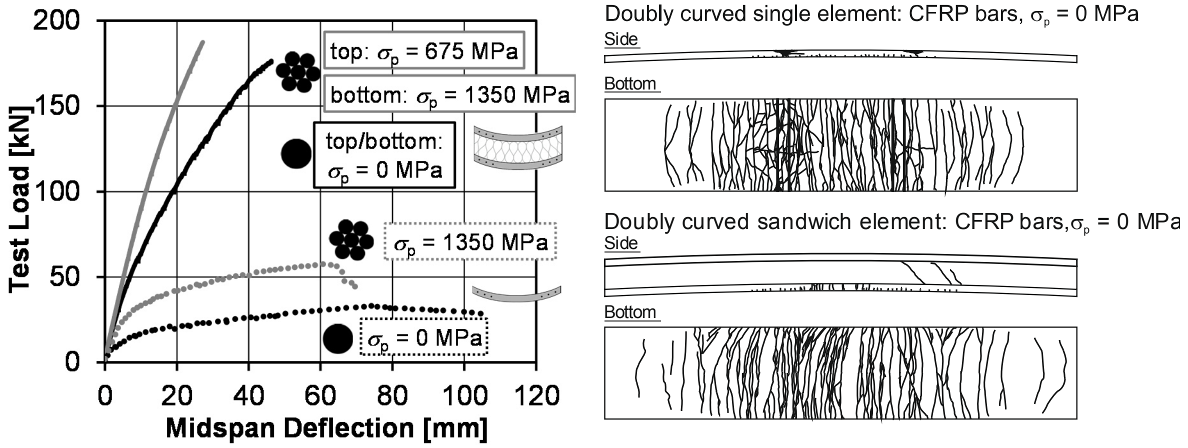

Fig. 7.4 **Single doubly curved elements and doubly curved sandwich elements with different prestressing forces (HP-1, HP-5 (Appendix C) and SHP-1, SFP-5 (Appendix D)): Load-deflection behaviour (left), crack patterns after testing for elements without prestressing of facings (right)**

Since prestressing of the UHPFRC facings of doubly curved sandwich elements did no lead to an increase in maximum load but to considerably less deflection, the influence of prestressing on internal displacements was further investigated. In Fig. 7.5 the deflection, the relative displacement of UHPFRC facings as well as the core compressions at the centre line and outer edge of the cross-section are depicted over the length of the sandwich panels. The results are shown in 20 % load steps. In Fig. 7.5 the results for a non-prestressed (left) and for a prestressed (top and bottom facing) sandwich panel are shown. The positions of LVDTs are indicated in each diagram. The sandwich panels without prestressing showed considerable greater deflections for all load steps compared to the element with prestressed facings. In case of non-prestressed facings, maximum deflections of $L/80$ were reached, whereas the prestressing of the facings led to maximum deflections of $L/100$. The relative displacements of the UHPFRC facings showed roughly the same values independently of prestressing. This was either caused by variations in the material properties or by a different load transfer due to prestressing of the facings. The core compressions at the outer edges of the cross-sections were about the same over the length of the panels. Only at midspan, the panel with prestressed facings showed considerable less compression strains of the core material. At the centre line, in the core material, tensile strains were determined at midspan. Hence, over the length and the width at midspan the load transfer changed from compression to tension. Further test results with variations of prestressing strands, length or core heights are summarised in appendix D. For comparison of numerical and theoretical models, further results are additionally shown in sections 7.3 and 7.5.

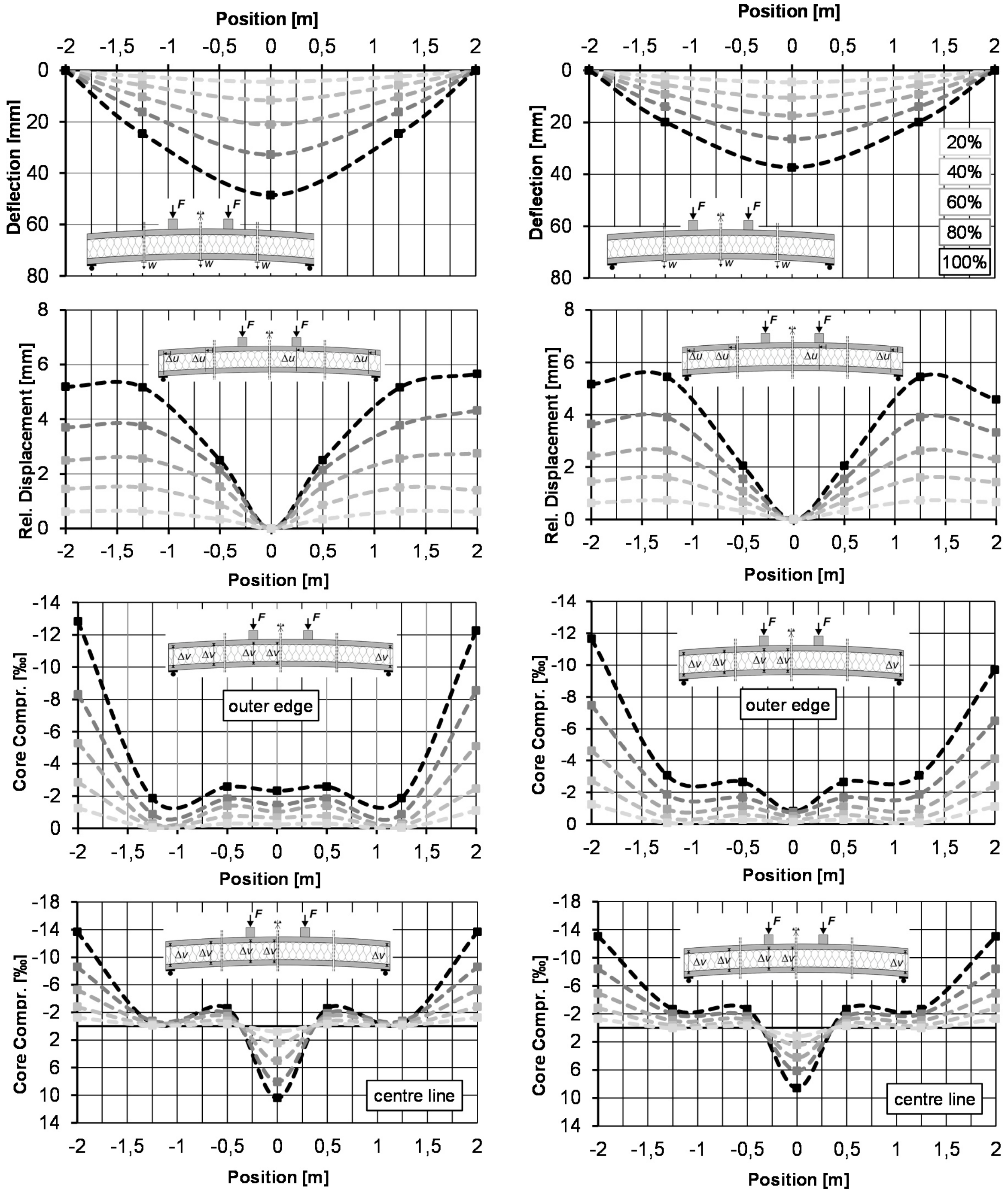

Fig. 7.5 **Deflection, relative displacement of top and bottom facings and core compression strains at outer edge and centre line over the length of doubly curved sandwich panels: non-prestressed (top and bottom: Ø5 mm, σ_{pm0} = 0 MPa; test SHP-1) (left) and prestressed (top and bottom: Ø7.5 mm, σ_{pm0} = 675 MPa; test SHP-3) (right)**

A reasonable comparison of the load behaviour of flat, folded plate and doubly curved sandwich elements from test results is not possible, since cross-sections (moment of inertia and area of bond zone) and effective depth had to be altered within the tests. Setting the cross-sections to the same moment of inertia, the area of bond zone and effective depth would differ and vice versa. Hence, standard methods to compare beams with different length, width or effective depths were not applied.

7.3 Validation of Numerical Models

7.3.1 UHPFRC Facings

In this section, numerical models using the DAMAGE PLASTICITY MODEL for UHPFRC in combination with previously derived parameters (cp. chapters 3 and 4) were validated by test data. For this purpose, the flexural performance of CFRP prestressed and non-prestressed folded plate and doubly curved elements was investigated. The numerical models were assembled, loaded and supported in the same way as the experimental investigations. All parts were modelled as continuum elements, besides reinforcement, which was assumed as fully embedded truss elements. The mesh of folded plate elements was generated within the finite elements programme, whereas the elements of doubly curved elements were created with aid of a source code, since extrusion or revolution techniques could not be applied for the doubly curved shape. Within this programme code, the number of elements and direction of reinforcement were determined on the basis of length, width, height and thickness of the doubly curved cross-section. The determined mesh of each part was imported into the finite element software.

In Fig. 7.6, the numerical models of folded plate and doubly curved elements are shown. Since both models are doubly-symmetric, modelling of a quarter with appropriate boundary conditions can reduce computing time. Nevertheless, for doubly curved elements, this procedure was not applied since restrictions in the number of elements and element size of reinforcement and concrete would have been arisen, while meshing the parts with the aid of a programme code. A mesh size of 25 mm in longitudinal direction was applied for folded plate sections and for doubly curved sections.

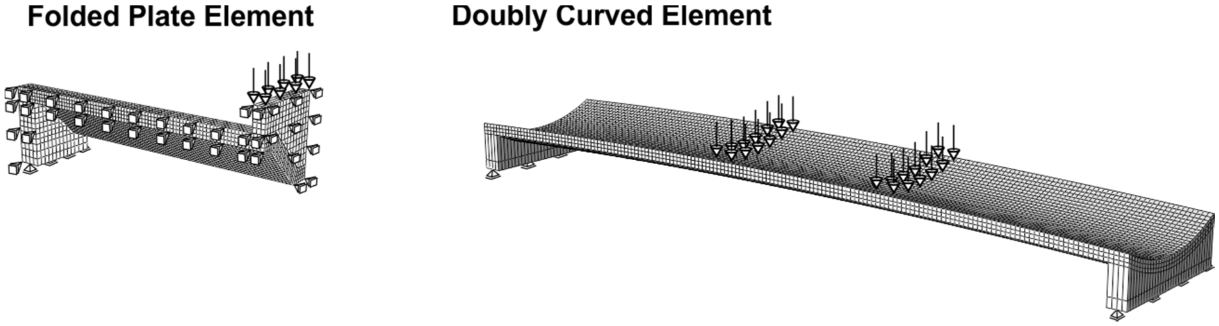

Fig. 7.6 **Numerical models of folded plate (left) and doubly curved (right) elements (illustration not to scale)**

In Fig. 7.7 (left) representative results of the load-deflection responses of folded plate elements with and without prestressing are depicted. The stiffnesses in the un-cracked and cracked state as well as cracking loads were determined in very good agreement with the test results. The failure loads and corresponding deflections were also described satisfactorily. For the folded plate elements without (test FP-6, Appendix C) and with medium prestressing (test FP-5, Appendix C), excessive cracking of UHPFRC was determined by the numerical model, as it was observed in the test. The CFRP bar without prestressing and the CFRP strand with medium prestressing were found close to maximum tensile strength at failure of the elements. The folded plate element, which was prestressed with CFRP strands and a jacking stress of 1,350 MPa (test FP-1, Appendix C), failed due to cracking of the top flange close to the support in the test (cp. Appendix C). Manufacturing defects of the test specimen were not observed. Nevertheless, the numerical model predicted a failure from excessive cracking of UHPFRC at midspan and rupture of the prestressing tendons.

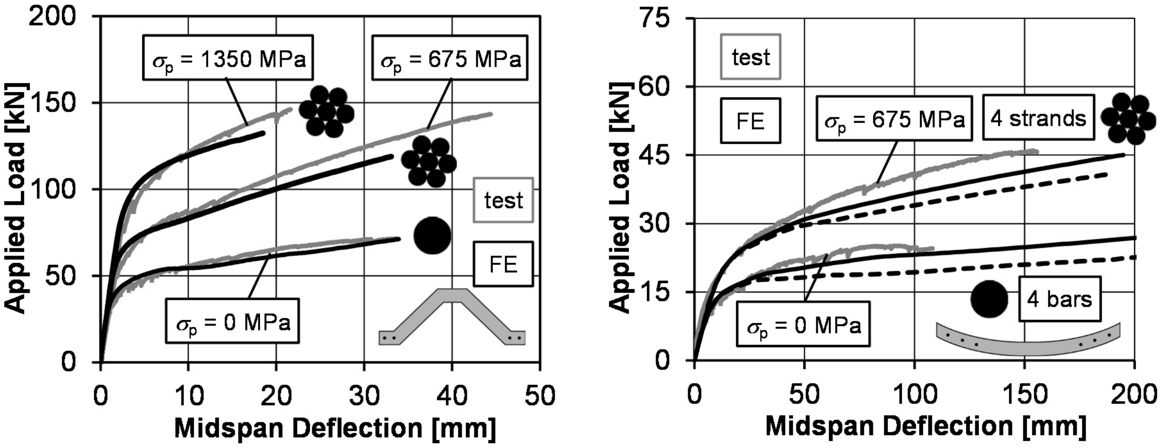

Fig. 7.7 **Numerical and experimental results of flexural tests on folded plate (left) and doubly curved (right) elements: load-deflection behaviour**

The overall response of doubly curved elements was also in satisfying agreement (Fig. 7.7, right). Applying the tensile strength and fracture energy according to results obtained in chapter 4, led to a good prediction of cracking loads, but to less increase of load in the cracked state (dashed lines). Material samples did not show a significant variation of tensile strength compared to other tests. This may be explained by the production process of doubly curved elements (cp. chapter 3), which has a significant difference in casting the UHPFRC. For folded plate elements, it was cast longitudinally over the length from the top opening of the formwork. Hence, the flow direction of UHPFRC was from top to bottom and the fibres distributed mainly uniformly, only influenced by the formwork. Hence, basically the same condition were reached as for the material samples, from which the tensile strength and fracture energy were derived. In contrast, for doubly curved elements, it was necessary to choose a different process, which made smooth surfaces without significant air inclusions possible. At each end of the closed formwork of doubly curved elements, an opening was arranged (cp. chapter 3). It was cast from one side, until the UHPFRC reached the other opening. Hence, ventilation was possible and only small air inclusion occurred. The longitudinal flow direction influenced the fibre orientation. Hence, more fibres were aligned in longitudinal direction compared to casting of folded plate elements. Longitudinally aligned fibres act perpendicular to flexural cracks. Since small fibres usually do not contribute to a pronounced increase in tensile strength after cracking of the matrix, but to a ductile post-peak behaviour, only the fracture energy increases. Therefore, the fracture energy was estimated to have increased to 5.0 Nmm/mm² in the numerical model (continuous line). This value would be obtained in a beam test according to /DAfStb10/, /DBV01/ (cp. chapter 4) for a residual load of 35 kN at 4 mm deflection. The application of an increased fracture energy led to a good agreement of the load deflection responses for element with and without prestressing. Only for doubly curved elements without prestressing (test HP-2, Appendix C), the maximum deflection was considerably overestimated. The doubly curved elements were predicted to fail from cracking of UHPFRC. The corresponding tensile stresses in the tendons and bars at failure were found less than 1,500 MPa.

Additionally, the crack patterns of the tested elements were compared to plastic strains obtained by the smeared cracking approach of the numerical model (Fig. 7.8). The maximum plastic strains are depicted in black and graded continuously to white. It can be seen that the distributions of plastic strains resemble the crack patterns. Even though, the compression failure of doubly curved elements (cp. section 7.2.2) was not observed in the simulations, compression strains were determined to be about 4.0 ‰, which indicates a multiaxial stress state at the loading position.

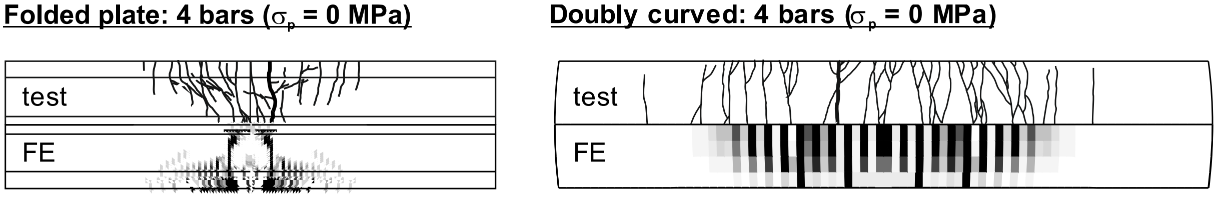
Folded plate: 4 bars (σ_p = 0 MPa)

Doubly curved: 4 bars (σ_p = 0 MPa)

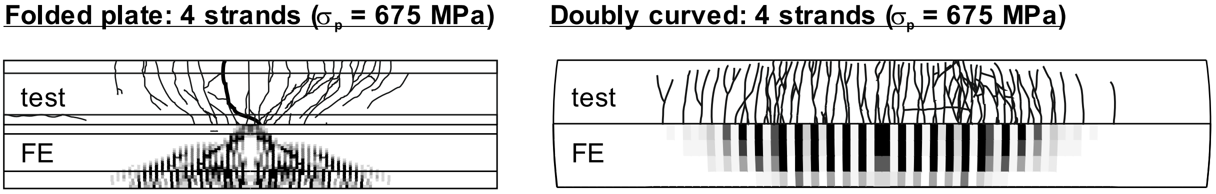
Folded plate: 4 strands (σ_p = 675 MPa)

Doubly curved: 4 strands (σ_p = 675 MPa)

Fig. 7.8 Comparison of numerical and test results of flexural tests on folded plate (left) and doubly curved (right) elements (not to scale): crack patterns and plastic strains

Besides the load-deflection response and smeared crack patterns, the damage plasticity model was validated regarding strains in the tensile zone. For this purpose the strains (engineering strains, averaged over length of 500 mm) were investigated. Bottom strains determined numerically and experimentally are exemplarily shown in Fig. 7.9 for a non-prestressed folded plate element and for a prestressed doubly curved element. The comparison of test results and simulation showed a satisfying agreement.

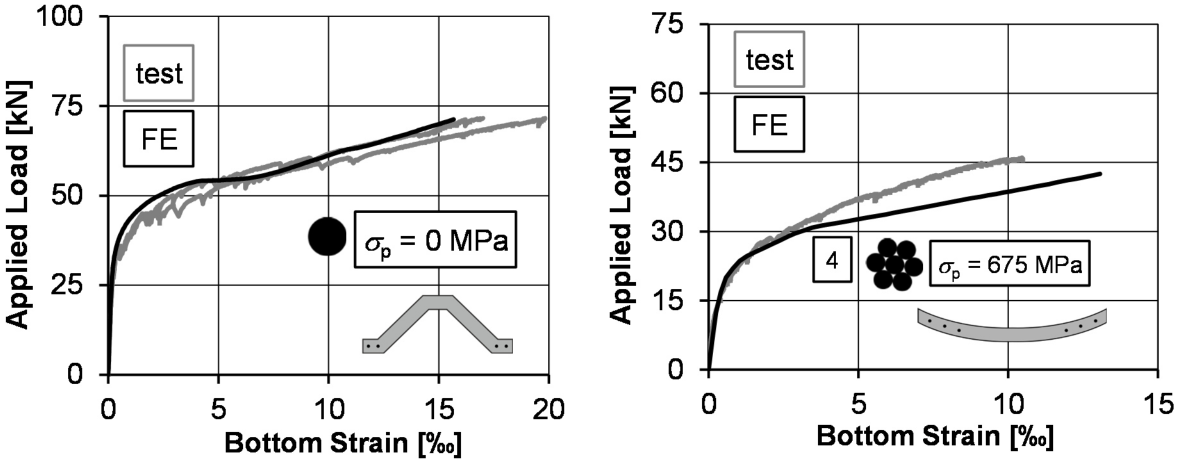

Fig. 7.9 **Comparison of representative strains from numerical and experimental results of tests FP-6 and HP-4 (Appendix C)**

In section 7.2 the inclination of cracks in folded plate elements as well as the compression failure of doubly curved elements was mentioned. These phenomena were investigated closer by inspection of principal stresses. In Fig. 7.10, the principal stresses in folded plate elements for different load steps are shown.

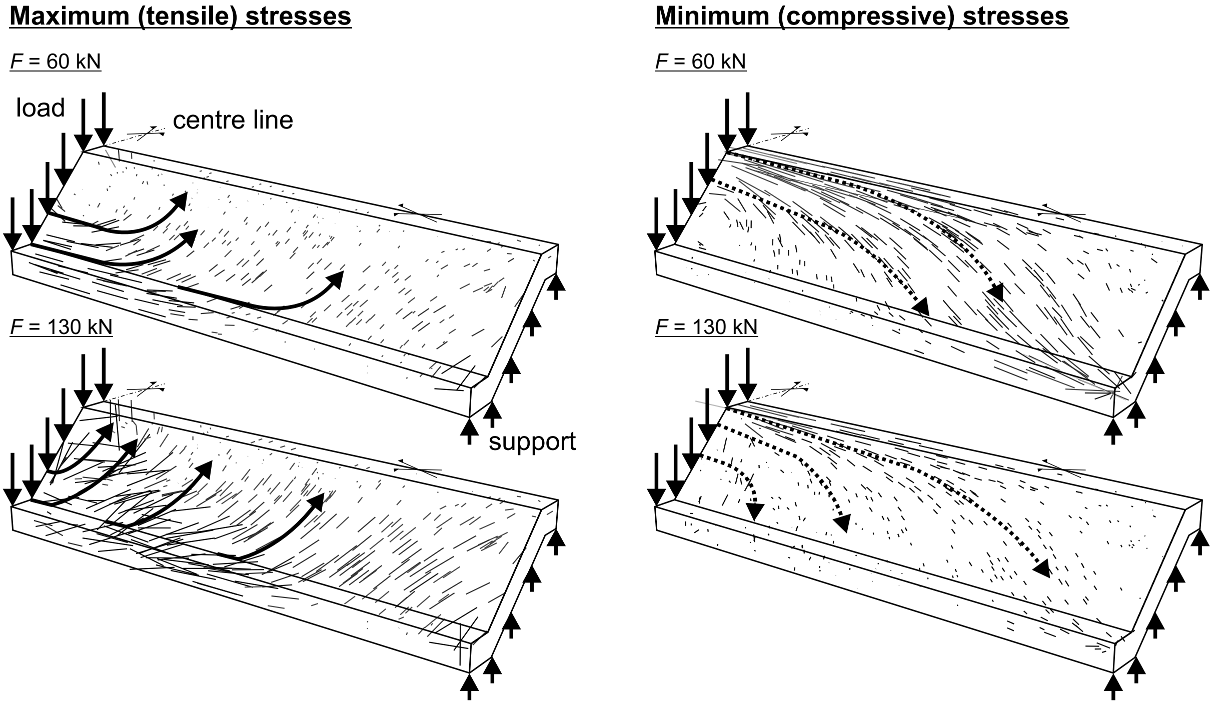

Fig. 7.10 **Direction of maximum (left) and minimum (right) principal stresses in prestressed (4 strands, σ_p = 1350 MPa) folded plate element (test FP-1) for different load steps**

For a load of 60 kN (~40 % F_{max}) maximum and minimum principal stresses are distributed in axial direction at midspan, i.e. loading point. For increased loading (130 kN, ~90 % F_{max}) compressive and tensile stresses are inclined. The directions of tensile stresses are corresponding to the crack angles in the webs. Additionally, tensile stresses at the top of the elements in the support region were determined. The direction of tensile stresses was found perpendicular to the major crack observed for the folded plate element with four strand pre-tensioned to 1,350 MPa. Nevertheless, at this position a failure was not observed in the numerical model.

The experimentally tested doubly curved elements failed due to concrete crushing in the compression zone, whereas distributed cracking was observed in the tensile zone. In Fig. 7.11, the maximum and minimum principal stresses of a doubly curved element with six CFRP bars are shown for different loading steps. For a deflection of 1 mm, the stresses are distributed in axial direction between loading points and arching between supports and loading point. For increased load, maximum and minimum stresses start arching between the loading points. At a deflection of 100 mm arching increases and starts building a strut at the outer edges between the loading points. This phenomena was also observed over the width at each support. Even though, the numerical model did not fail at this point, high compression strains of 4.0 ‰ were observed at maximum load. Hence, this strains were close to exceed the maximum strains before failure.

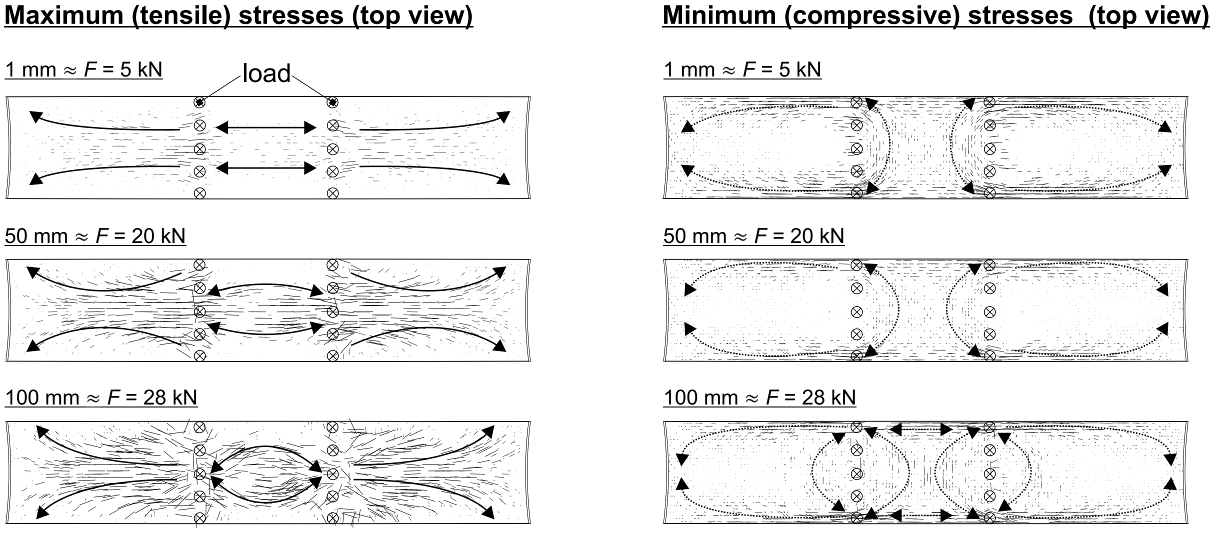
Maximum (tensile) stresses (top view)

Minimum (compressive) stresses (top view)

Fig. 7.11 **Direction of maximum (left) and minimum (right) principal stresses in doubly curved element with-out prestressing (6 bars, σ_p = 0 MPa) for different load steps (test HP-6)**

It was shown that the load-deflection response of single facings can be numerically determined in good agreement with test results, especially until 80 % of maximum load. In the next section, the models were applied for folded plate and doubly curved sandwich panels.

7.3.2 Sandwich Sections

In this section, the load behaviour of prestressed sandwich beams was investigated by means of numerical modelling. The material models were based on characterisations for PU, bond zone, CFRP and UHPFRC from chapters 3.6 and 6.4. At first, the flat sandwich beams were investigated to evaluate the material models, which were tested on small-scale tests. The mesh size was set to 15 mm. Generally, the mesh size needed to be small enough to predict the load behaviour accurately, but with adequate time effort for calculation. Even though, during testing of sandwich beam under flexural loading, only in certain cases a major failure of bond zone was observed, for further studies, it was necessary to allow for a possible failure. In section 6.4, it was shown that bond failure can be described by a layer of cohesive elements. This procedure was applied for the numerically investigated sandwich panels in this section. The Young's modulus of the core material was set to 32 MPa, which was determined from material testing (compressive behaviour). Poisson's ratio was applied as 0.41 (cp. chapter 3), which is in accordance with a shear modulus of 11.5 MPa, which was derived from material testing. In case of an applied shear grid, only the tensile trusses were modelled to avoid numerical instabilities from buckling of the compressive trusses. This procedure was also successfully applied in investigations conducted in /Hor10/.

In Fig. 7.12 the numerically determined load-deflection responses at midspan (w_1) and quarter points (w_2) for sandwich beams without and with CFRP shear grid is shown. As mentioned before, the production procedure of elements without shear grid led to a rough concrete surface (valley side). This obviously resulted in a reduction of the bond strength. Hence, the maximum load was overestimated by the numerical model. For elements with CFRP shear grids a continuous bond zone was achieved. For this configuration, the load-deflection response was determined in very good agreement with test results. The model predicted a mixed mode failure of concrete cracking and plastic deformations of the core material. Even though, shear cracks as obtained in the tests were not developed. As in the tests, the CFRP tendons did not fail in the simulation, but were stressed up to 2,500 MPa at maximum, depending on the initial prestressing.

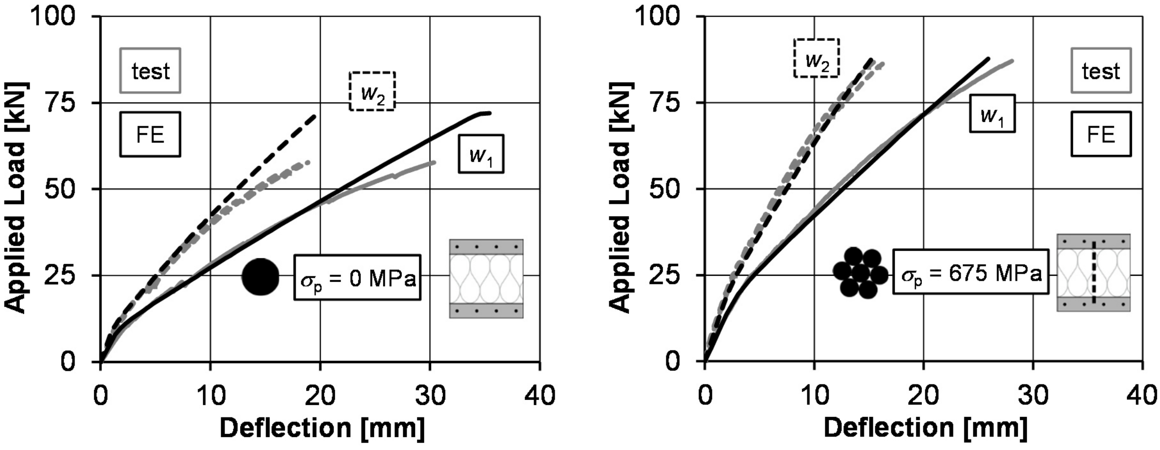

Fig. 7.12 **Numerical and experimental results of flexural tests on planar sandwich beams: Without pre-tensioning and without CFRP shear grid (left, test SB-2) and with pre-tensioned strands and CFRP shear grid (right, test SB-6)**

For further conclusions the results for different measuring points were compared. In Fig. 7.13 representative results of concrete tensile strains at bottom ($s_{1,\mathrm{bot}}$) and relative displacement between top and bottom facing at support (U_1) are shown. Concrete strains were found in very good agreement with test results. However, the relative displacement was underestimated. Since the bond zone parameters were validated by results of small-scale testing, there can be issues in the transferability. But, the correct prediction of that parameter is very challenging, since small variations in bond quality can result in relatively pronounced deviations in relative displacement.

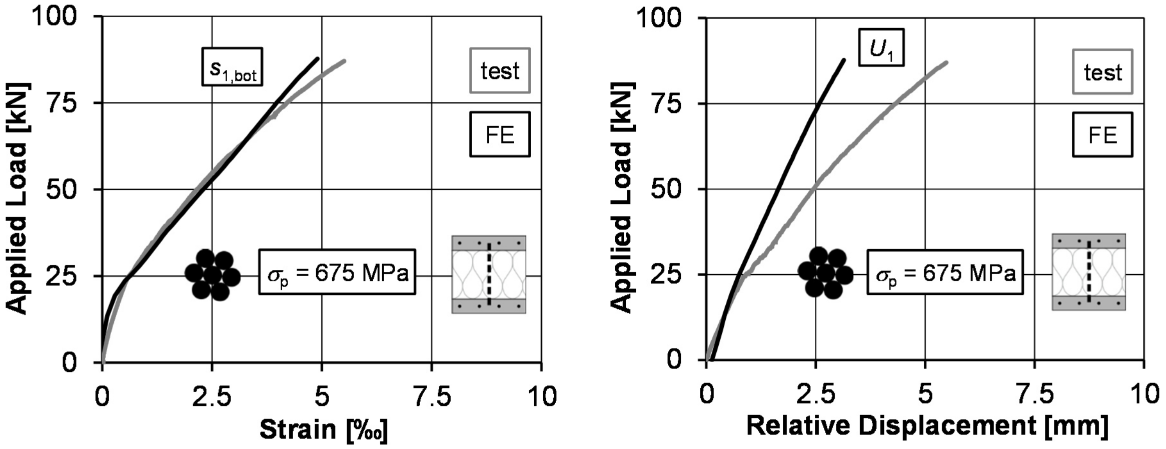

Fig. 7.13 Numerical and experimental results of flexural test on planar sandwich beam with pre-tensioned strands and CFRP shear grid (test SB-6): Strain at midspan (left) and relative displacement at support (right)

All in all, the material models and material parameters, which were validated with results of small-scale tests (cp. chapters 3 and 4), seem appropriate for the prediction of the load behaviour of flat sandwich beams.

In the next step, the applicability of the non-linear material models was investigated for sandwich panels with folded plate and doubly curved cross-sections. In the previous section it was shown, that the damage plasticity model was capable to determine the overall load-deflection response of folded plate and doubly curved UHPFRC elements. Even though the final failure mode of the sections was not always predicted correctly, crack initiation and stiffness in cracked stage were simulated in satisfying agreement. In Fig. 7.14 the applied numerical models are shown. As for single layers (cp. section 7.3.1), the folded plate elements were investigated on one quarter with adequate boundary conditions to account for symmetry. Again, for doubly curved elements symmetry conditions were not applied to avoid restrictions in mesh size of skew reinforcement. The overall mesh size was determined to 25 mm in longitudinal direction for folded plate and for doubly curved elements.

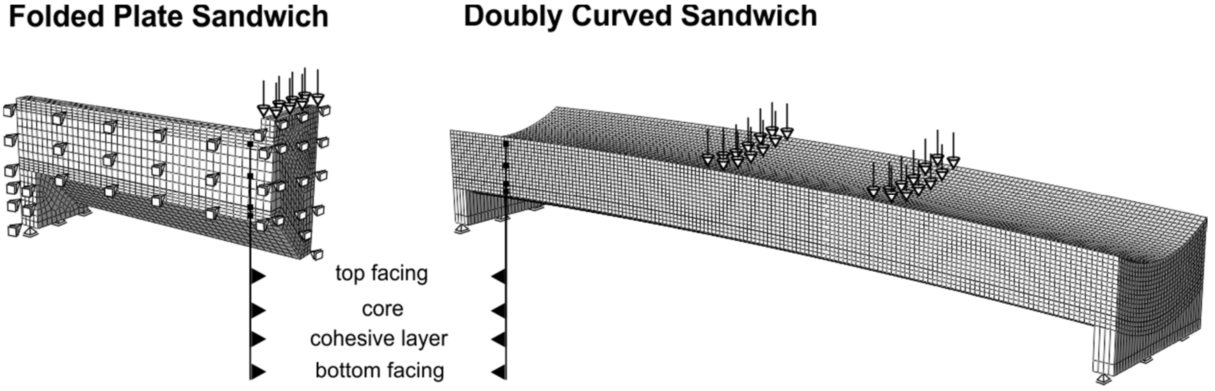

Fig. 7.14 **Numerical models of folded plate (left) and doubly curved (right) sandwich elements (not to scale)**

In contrast to flat sandwich beams, the experimental investigations on folded plate sandwich elements showed a significant influence of prestressing of UHPFRC layers, even for the relatively short span of 2.4 m. Applying the non-linear material laws (chapter 3) for each material, the load-deflection responses were determined in good agreement with the test results. The failure mode of the sandwich panels always was a mixed mode from excessive cracking of the facings and plastic deformation of the core material. The prestressing tendons were stressed up to 2,600 MPa for prestressing of 1,350 MPa, which is close the maximum tensile strength of 2,650 MPa. Prestressing of 675 MPa resulted in maximum stresses of about 2,000 MPa at failure of the elements. As in the tests, the interface between core and facings did not fail. For all combinations of reinforcement and prestressing forces, the load-deflection response was almost congruent. Hence, validated material laws for PU and interface from small-scale testing led to an appropriate prediction of the load behaviour of sandwich panels under flexural loading.

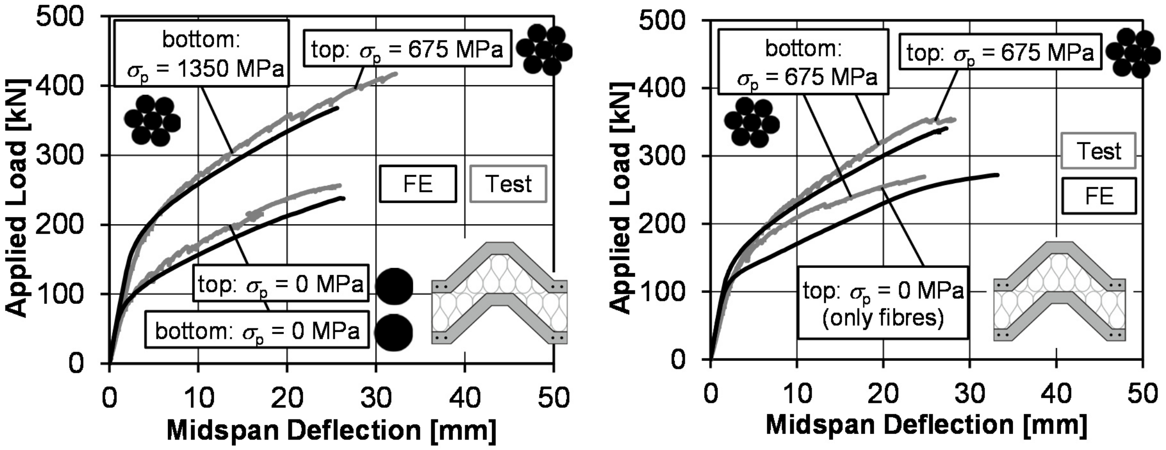

Fig. 7.15 **Numerical and experimental results of flexural test on folded plate sandwich beams (left: tests SFP-4 and SFP-6; right: SFP-1 and SFP-5): load-deflection response**

Subsequently, further results are compared to test results. The comparison of crack patterns and distributions of plastic strains in the UHPFRC facings shows a good agreement, even though inclined plastic regions were not developed (Fig. 7.16). This was already the case for UHPFRC single layers (cp. section 7.3.1).

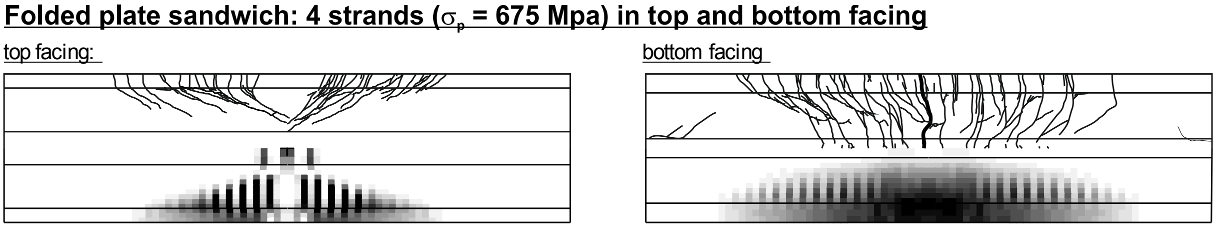

Fig. 7.16 Comparison of numerical and test results of flexural tests on folded plate sandwich panel of top facing and bottom facing: crack patterns and plastic strains

Even though shear cracks over the height of the core material were not predicted by the numerical model, regions of plastic strains developed at the top and bottom of the core layer. Maximum values of tensile stresses were obtained in the middle between support and loading. The directions of maximum principal stresses in the core layer show predominant axial tensile stresses at midspan (Fig. 7.17, left). Due to the shape of folded plates, the stresses were found inclined in the middle between loading and support. The experimental results showed a failure in the core material either close to midspan or in between midspan and support for a core thickness of 200 mm, which was mainly induced due to cracking of the UHPFRC layers (Fig. 7.17, right). The direction of maximum tensile stresses were in agreement with both, typical crack directions (Fig. 7.17). In all tests, plastic deformations of the core material were observed at the supports.

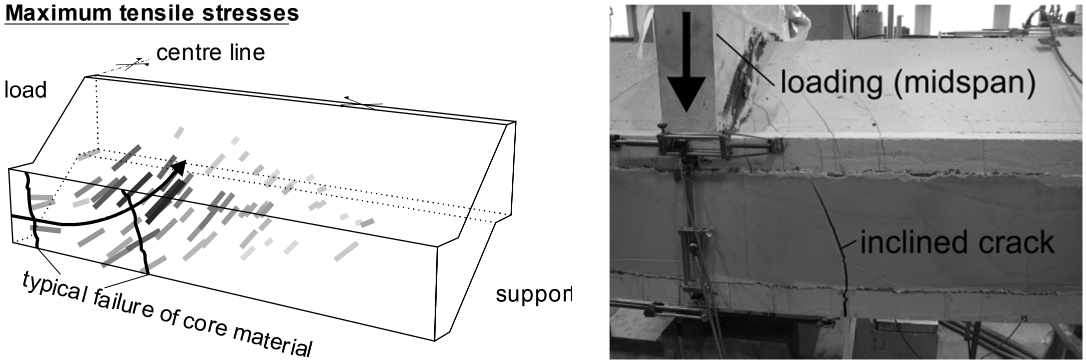

Fig. 7.17 Numerically determined direction of maximum principal stresses in core material of prestressed (4 strands, σ_p = 675 MPa in top and bottom facing) folded plate sandwich element at maximum load (left) and inclined crack in core material at failure in the test (right)

Since the global load behaviour was determined in good agreement with test results, further gauges were investigated to verify the contribution of the materials.

In Fig. 7.18, determined deflections at midspan (w_1) and quarter point (w_2), tensile strains at bottom of bottom facing $s_{1,\mathrm{bot}}$ as well as core compression at support (V_1) and midspan (V_2) of folded plate sandwich elements without (left) and with (right) prestressing are compared to test results.

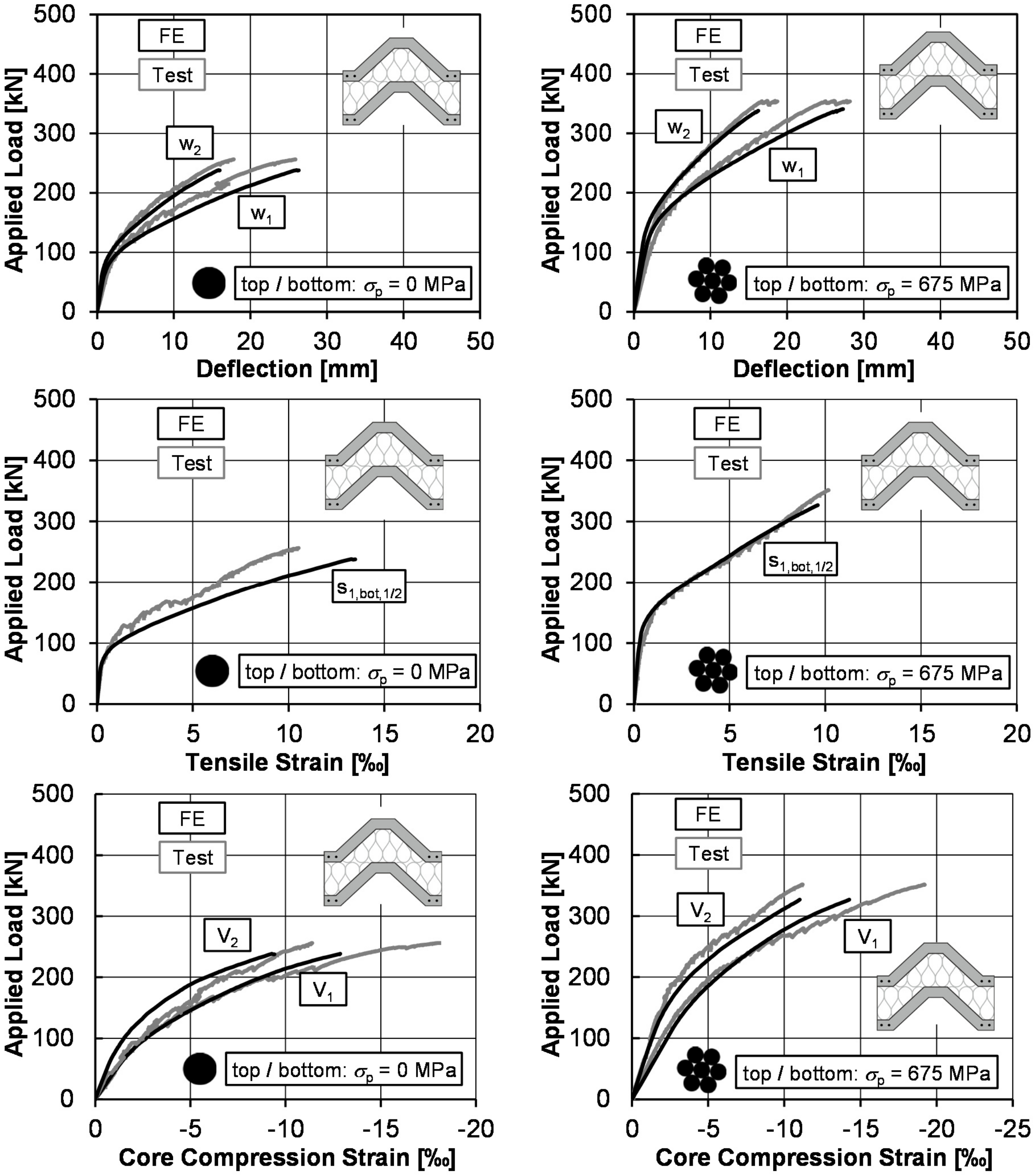

Fig. 7.18 Numerical and experimental results of flexural test on folded plate sandwich panels (left: SFP-4; right: SFP-5): Deflections, tensile strain (concrete) and core compression strains

The deflections at midspan and quarter points are in accordance with the test results, i.e. the deflection curves were predicted accurately by the model. The concrete tensile strains as well as compression strains at midspan and support were found in very good agreement with the test results. Hence, it can be stated that the numerical model allocated the contributions of different materials correctly. As for the flat elements, the derived material parameters from small-scale testing were found to be appropriate for the determination of the structural performance of folded plate sandwich panels.

In the next step, the applicability of the material laws was tested for doubly curved sandwich panels. In the first step, all material parameters were applied in the same manner as for flat and folded plate sandwich panels. Hence, the compressive value of Young’s modulus of 32 MPa was used. This led to an underestimation of stiffness for the global load-carrying response (cp. Fig. 7.19, continuous lines). An increased fracture energy as assumed for single elements (cp. section 7.3.1), did not change the stiffness and maximum load significantly, since the model predicted cracking of the facings, but not a failure of the facings. This is in accordance with the test results. Overall cracking occurred, but with small crack widths. The numerical results predicted a final failure in the bond zone at the supports, which was not observed in the tests.

The global stiffness of the panels is controlled by the shear modulus of the core material. Since the stiffness of the doubly curved sandwich panels was underestimated and tensile stresses occurred in the core material in the midspan area (cp. section 7.2.2), the tensile Young’s modulus was applied for test purposes. This led to a concurrent increase of the shear modulus. The results of the global load-deflection responses showed a very good agreement with the experimental data (cp. Fig. 7.19, dashed lines). For all prestressed panels, the maximum loads and corresponding deflections were determined in satisfying agreement. Reaching these loads, cracking of UHPFRC facings and again a bond failure were predicted. The bond zone was damaged at the outer edges in the vicinity of the supports in the numerical models. In contrast, during experimental testing, the specimens finally failed due to shear cracks in the core material rather than bond failure. The reinforcement was stressed up to 1,700 MPa at failure for the highest prestressing. The load and deflection of the doubly curved sandwich panel without prestressing (cp. Fig. 7.19, bottom right), were largely underestimated by the numerical model. Again, a combined failure of UHPFRC facings and finally of the bond zone was predicted. In contrast, in the tests, multiple diagonal cracks in the core material were observed at failure. Even tough, the failure modes of the numerical model did not resemble the failure mode observed during experimental testing, the overall load-deflection responses were in good agreement for prestressed sandwich panels. Only for non prestressed panels, both failure mode as well as maximum load and deflection were predicted inaccurately.

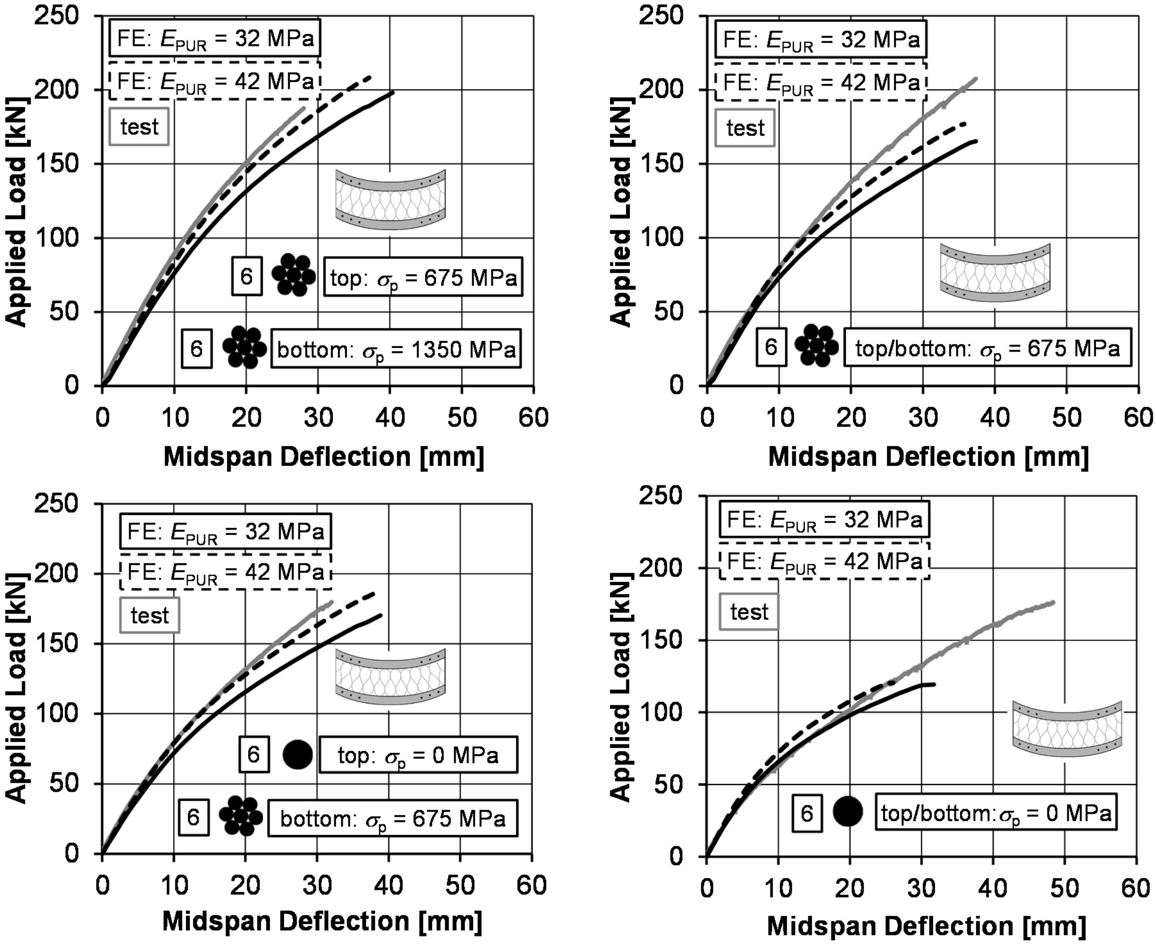

Fig. 7.19 **Comparison of numerical and experimental results of flexural test on doubly curved sandwich beams (tests SHP-5, SHP-3, SHP-4 and SHP-1): Load-deflection responses**

As shown in Fig. 7.19, the artificially increased shear modulus resulted in a globally enhanced load-deflection behaviour for prestressed elements. Nevertheless the prediction of failure modes was not improved. To apply the consistent material models, the established Young's modulus and shear modulus of 32 MPa and 11.5 MPa, respectively, were subsequently used for further investigations.

In Fig. 7.20, different strains at midspan are compared to verify the concrete contribution for two different prestressing states. The strain at midspan at the bottom facings $s_{1,\mathrm{bot},1}$, at top facing $s_{1,\mathrm{top},1}$ as well as at the outer edge at the top facing $s_{1,\mathrm{top},2}$ are shown. Top and bottom strains at the different positions were in relatively good agreement with the test results, although higher deflections were predicted in the numerical model compared to the test results. Concrete strains are not only dependent on the deflection, but also on the acting axial forces due to sandwich moment.

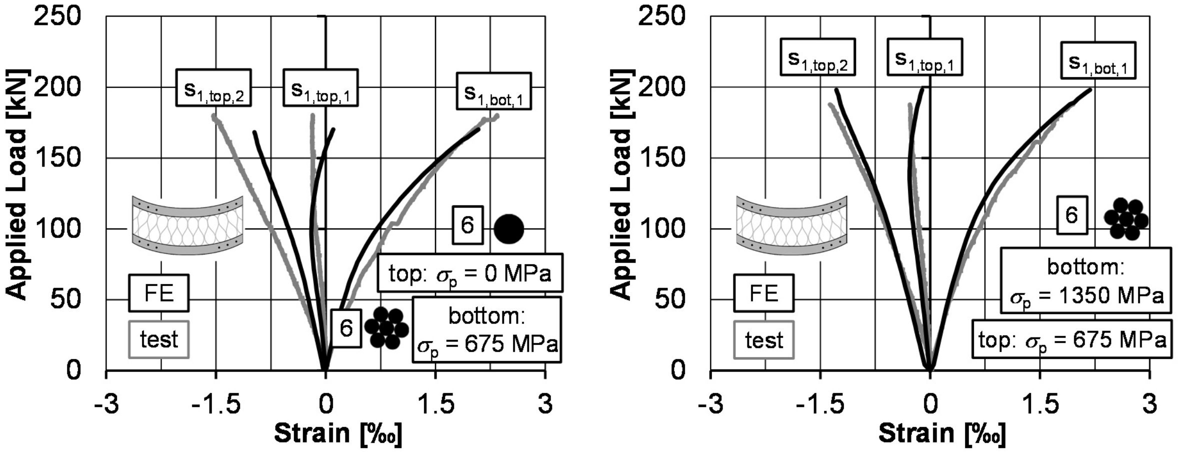

Fig. 7.20 Numerical and experimental results of flexural test on doubly curved sandwich beams (left: SHP-4; right: SHP-5): Concrete strains

A further look at compression strains of core material showed a relatively good agreement at the support (V_1, support-side; V_6, mid support), whereas the strains between both loading positions (V_3) were found to differ greatly from test results. This is the position, where tensile stresses were determined at centreline of the cross-section (cp. Fig. 7.5). At side position, compressive stresses were determined (cp. Fig. 7.5). Directly under the loading points, the compression stresses (V_4) were also overestimated. As for flat and folded plate panels, the relative displacements (U) between top and bottom facings were underestimated.

It was shown that local deformations of the tests on doubly curved sandwich panels could partially not be described accurately. This may be caused by the prediction of different failure modes compared to test results. It was concluded that positive effects due to the geometry of the curved shape, which could develop in reality, were not represented by the numerical model, yet. However, the global load-deflection responses of prestressed members were found in relatively good agreement.

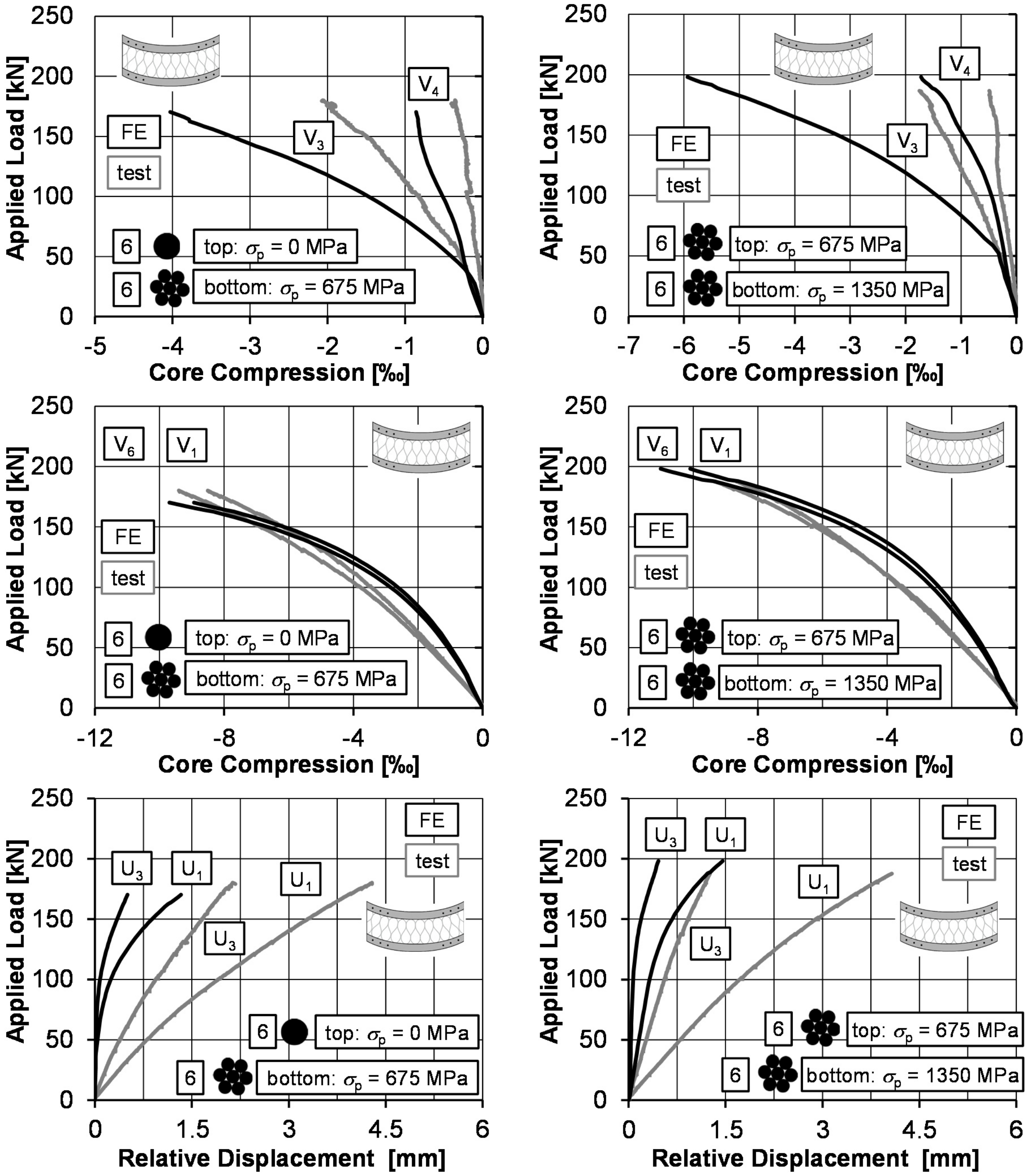

Fig. 7.21 **Numerical and experimental results of flexural test on doubly curved sandwich panels (left: SHP-4; right: SHP-5): Core compression strains and relative slip**

The comparison of crack patterns and plastic strains shows a good prediction of cracked regions. In Fig. 7.22 the comparison is exemplarily shown for a specimen with prestressed bottom facing and reinforced top facing. This behaviour coincides with the comparisons of measured and predicted strains (cp. Fig. 7.20).

Bottom: 6 strands (σ_p = 675 MPa), top: 6 bars (σ_p = 0 MPa)

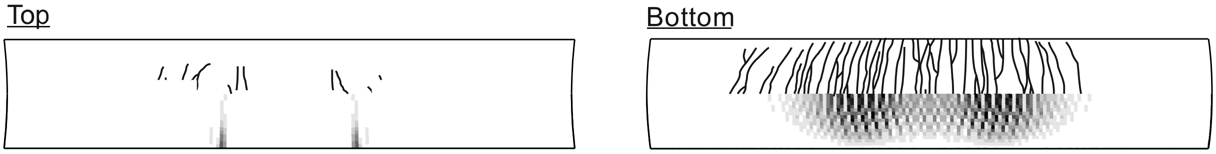
Top

Bottom

Fig. 7.22 Comparison of numerical and test results of flexural tests on doubly curved sandwich panel of top facing and bottom facing: crack patterns and plastic strains

The numerical approaches showed an overall good prediction of the load-deflection response and contributions of the materials for flat, folded plate and doubly curved sandwich panels. For flat and folded plate panels, only the relative displacement of the UHPFRC facings was underestimated. For doubly curved panels the global behaviour was predicted in good agreement, but local contributions of the core material and bond zone could not be covered by the numerical model. In the next sections, a theoretical approach, based on the SANDWICH THEORY, was applied to provide a framework for the determination of cracking and maximum loads of prestressed sandwich panels with UHPFRC facings.

7.4 Analytical Model for Sandwich Panels under Flexural Loading

7.4.1 General

Sandwich panels applied as façade or roof structures have to fulfil several requirements to resist wind, snow or temperature loadings. One key factor is the utilisation of the sandwich effect. Hence, a durable and load-bearing interface between outer layers and core material has to be provided.

The design of such sandwich elements is rather complex compared to typical concrete structures. Due to the complexity, standard sandwich elements with thick RC facings and prefabricated slabstock foam as core material are usually designed neglecting the sandwich action induced by the core material. Hence, the load transfer of the outer layers is assumed to be depending on the shear connectors only. Since the bond quality between RC layers and slabstock foam is usually scattering, this approach seems reasonable. The production method of foaming in pack between hardened concrete layers leads to predictable and repeatable bond strength. Hence, neglecting the bond action would result in an uneconomic approach. Additionally, the load-deflection responses of investigated panels without shear connectors, would not be determinable.

For a conservative prediction of the load-carrying capacity, the sandwich panels can be designed to withstand external forces without cracking of the concrete facings. Hence, only the linear elastic part of the load-deflection curve needs to be predicted. This must be accompanied by sufficient ductility in the cracked state. To predict the linear-elastic behaviour of sandwich panels, internal forces and deflections need to be determined accurately. This can either be done by finite element modelling or by applying sandwich theory. Cracking of the concrete facings can be predicted by comparison of predicted stresses in the facings and uniaxial tensile strength of the concrete.

For the prediction of the maximum load and deflections, either non-linear finite element modelling needs to conducted or approaches to account for degradation of concrete stiffness have to be derived. HORSTMANN /Hor10/ und SHAMS /Sha15b/ proposed approaches to consider cracking of TRC facings of flat elements. These approaches did not comprise prestressing, crack-bridging effects of steel fibres and non-flat cross-sections. In the following sections, approaches were derived to predict the load-deflection response of sandwich elements with UHPFRC facings, pre-tensioned CFRP reinforcement and non-flat cross-sections. Subsequently, the proposed models were validated by results from flexural tests. Furthermore, variation of material properties, spans and different load cases, such as distributed loads, were exemplarily investigated.

7.4.2 Mechanical Background

For the following derivation, a plane sandwich element is considered. A low density core material of thickness h_c separates two stiff facings with arbitrary thicknesses t_{bot} and t_{top}. In this section either materials are assumed isotropic. Based on the assumptions of /Sta74/ (chapter 2.2.3), a distorted configuration of an infinitesimal sandwich element of length *dx* is considered (Fig. 7.23).

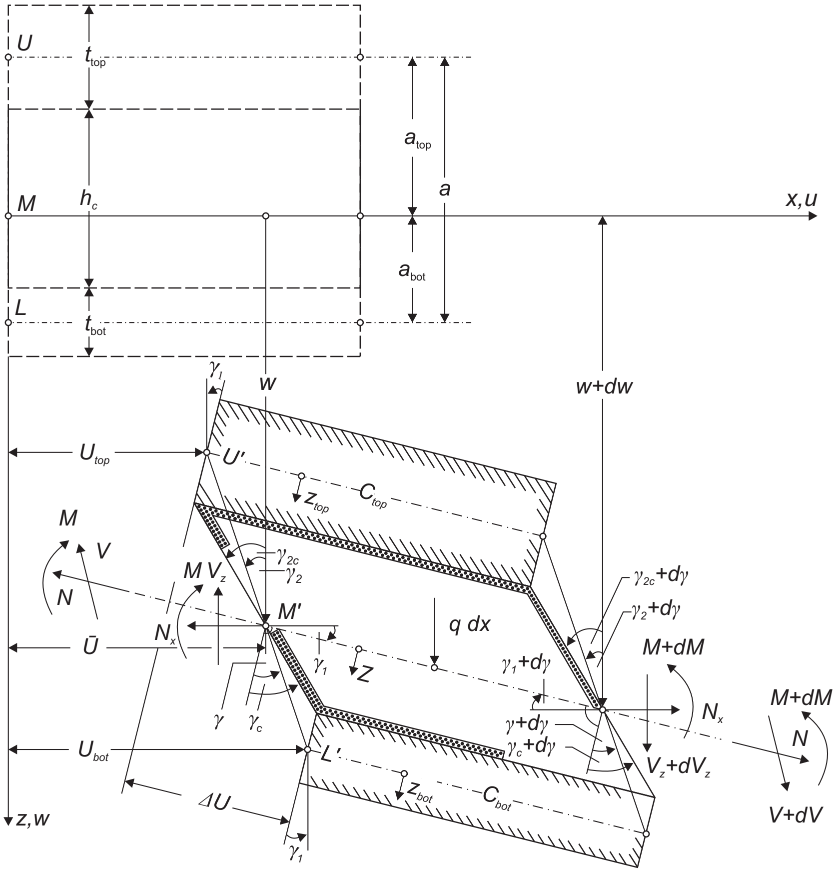

Fig. 7.23 Distorted sandwich element of length *dx* with corresponding internal forces (reproduced from /Sta74/)

From relationships between angles and displacements, strains are derived and stresses calculated (HOOKE's law). By integrating these stress components, internal forces can be derived (equation (7.1)).

$$\begin{aligned} N &= D\bar{u}' \\ M &= B_s\gamma' - Bw'' \\ V &= A\gamma - (B_{bot} + B_{top})w''' \end{aligned} \tag{7.1}$$

N, M, V	Internal forces
w	Deflection
γ	Transverse shear strain
A	Shear stiffness of core - material
B_{top}	Flexural rigidity of top facing
B_{bot}	Flexural rigidity of bottom facing
B_s	Flexural rigidity due to sandwich effect
B	Flexural rigidity $(B_{top} + B_{bot} + B_s)$
D	Extensional stiffness of the sandwich element

The entire derivation of these equations can be found in appendix E or in /Sta74/.

The shear stiffness A is determined from the shear modulus G, core height h_c, width b and distance between centre lines of outer facings a.

$$A = G \cdot \frac{b \cdot a^2}{h_c} \tag{7.2}$$

Since no external axial forces act on the investigated sandwich panels, this component was not considered further. For solutions of sandwich elements with axial loadings, it is referred to /Sha15b/. Total bending moments and shear forces are composed of parts from two facings and sandwich actions.

Applying well known relationships of bending moment M, shear force V and distributed load q to equation (7.1) leads to the following equations:

$$Bs\left(\gamma'' - w'''\right) - A\gamma = 0, \quad A\gamma' - \left(B_{bot} + B_{top}\right)w^{IV} = -q \tag{7.3}$$

Eliminating γ and w results in decoupled ODE's for arbitrary transverse loading and support conditions (cp. Appendix E). For simply supported beams, relationships for deflection w, moment M and shear force V can be applied directly. By combining equations (7.1) and (7.3), the differential equations are arranged in dependence on w (equation (7.4)) and γ (equation (7.5)) only.

$$-\frac{B_{bot}+B_{top}}{A}w^{\mathrm{IV}}+\frac{B}{B_s}w''=-\frac{M}{B_s}-\frac{q}{A} \tag{7.4}$$

$$-\frac{B_{bot}+B_{top}}{A}\gamma''+\frac{B}{B_s}\gamma=\frac{V}{A} \tag{7.5}$$

Furthermore, γ can be expressed as function of w only (equation (7.6)). Solutions for arbitrary loading and boundary conditions can be found.

$$\gamma=\frac{B_s}{A^2}\left[\left(B_{bot}+B_{top}\right)w^{\mathrm{V}}-A\,w'''-q'\right] \tag{7.6}$$

STAMM and WITTE /Sta74/ used mathematical substitutions of flexural rigidities according to equation (7.7). The resulting ODE's for deflection w and shear angle γ provide a clearly arranged form to determine the solution for different loading cases.

$$\alpha=\frac{B_{bot}+B_{top}}{B_s},\quad \beta=\frac{B_s}{A\cdot L^2},\quad \lambda^2=\frac{1+\alpha}{\alpha\cdot\beta} \tag{7.7}$$

$$w^{\mathrm{IV}}-\left(\frac{\lambda}{L}\right)^2 w''=\frac{1}{B}\left(\frac{\lambda}{L}\right)^2\left(M+\beta L^2 q\right) \tag{7.8}$$

$$\gamma=L^2\beta\left[\left(\frac{L}{\lambda}\right)^2(1+\alpha)w^{V}-w'''-\frac{q'}{A}\right] \tag{7.9}$$

A general solution of equation (7.8) can be obtained as follows:

$$w=C_i\cosh\left(\frac{\lambda x}{L}\right)-C_{i+1}\sinh\left(\frac{\lambda x}{L}\right)+C_{i+2}+C_{i+3}x+w_p \tag{7.10}$$

The constants C_i to C_{i+3} and minority parts w_p of the solution can be determined in dependence of the loading case and boundary conditions.

Amongst others, STAMM and WITTE /Sta74/ provide solutions for one single point load or uniformly distributed loads (cp. Appendix E). The arsing equations for deformations as well as sectional forces and moments have a rather cumbersome profile, but can easily be implemented in spreadsheet software. A straight solution for two point loads is not incorporated. Therefore, the usual procedure is to add up the solutions for two positions of single point loads $F/2$ with corresponding distances from the supports. Since it is often more straightforward to work with the final results, the arising equations due to four-point bending are summarised in appendix E.

In contrast to uniformly distributed loading, the bending moment distribution shows discontinuities for concentrated loads. Hence, the beam is subdivided in different parts (Fig. 7.24). As another approach, the DIRAC delta function could be applied.

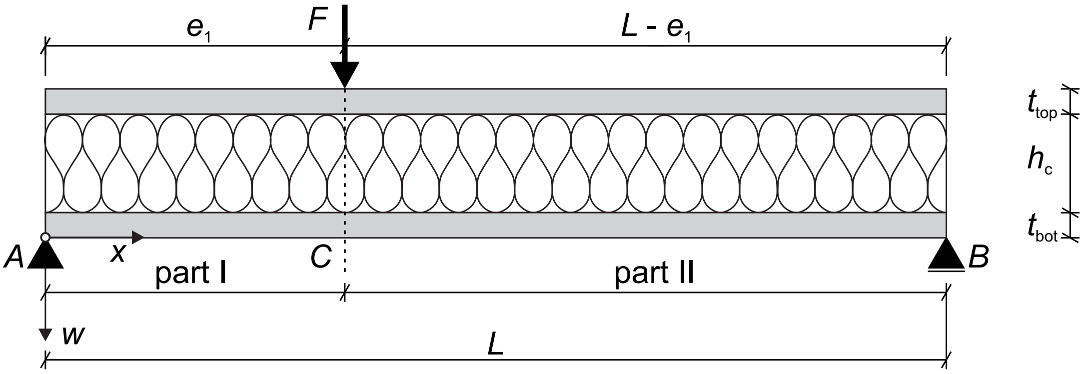

Fig. 7.24 **Subdivision of simply supported sandwich element subjected to three-point bending into two parts due to discontinuity in the bending moment distribution**

For each part, the following bending moment distribution results:

$$\begin{aligned}
&\text{Part I } (\xi \le \varepsilon):\ M_I = F \cdot L \cdot (1-\varepsilon) \cdot \xi \\
&\text{Part II } (\xi \ge \varepsilon):\ M_{II} = F \cdot L \cdot \varepsilon \cdot (1-\xi)
\end{aligned} \tag{7.11}$$

The parameters ε and ξ equation (7.12) are normalised distances between support and first point load e_1 and between either point loads e_2 as well as control variable x.

$$\begin{aligned}
\varepsilon &= \frac{e_1}{L} \\
\xi &= \frac{x}{L}
\end{aligned} \tag{7.12}$$

Solving equation (7.8) and applying equations (7.11), the solutions for deflection w for a simply supported beam are obtained. For each of the parts four constants arise, which can be solved by applying boundary and compatibility conditions. At the supports, deflection w and bending moment M are zero. At positions of concentrated loads, deflections w and their derivatives w' (inclination of deflected element) as well as transverse shear strains γ and their derivatives γ' must fulfil compatibility conditions. The following equations for deflection w are obtained for the case of three-point bending /Sta74/.

$$\begin{aligned}
w_I &= \frac{FL^3}{B}\left[\frac{1}{6}(1-\varepsilon)\xi\left(2\varepsilon - \varepsilon^2 - \xi^2\right) + \frac{1}{\alpha\lambda^2}(1-\varepsilon)\xi - \frac{1}{\alpha\lambda^3}\frac{\sinh\lambda(1-\varepsilon)}{\sinh\lambda}\sinh\lambda\xi\right] \\
w_{II} &= \frac{FL^3}{B}\left[\frac{1}{6}\varepsilon(1-\xi)\left(-\varepsilon^2 + 2\xi - \xi^2\right) + \frac{1}{\alpha\lambda^2}\varepsilon(1-\xi) - \frac{1}{\alpha\lambda^3}\frac{\sinh\lambda\varepsilon}{\sinh\lambda}\sinh\lambda(1-\xi)\right]
\end{aligned} \tag{7.13}$$

The corresponding shear angle γ can be calculated by applying equations (7.13) to equation (7.9) (cp. Appendix E).

For each loading condition the internal forces can be calculated at any position x of the simply supported beam. Bending moment M and shear forces V are composed of parts from bottom and top layer as well as sandwich action. The summation of the three parts results in moments and shear forces from linear elastic EULER-BERNOULLI theory. In Fig. 7.25 the composition of bending moments and shear forces is exemplarily depicted for four-point loading.

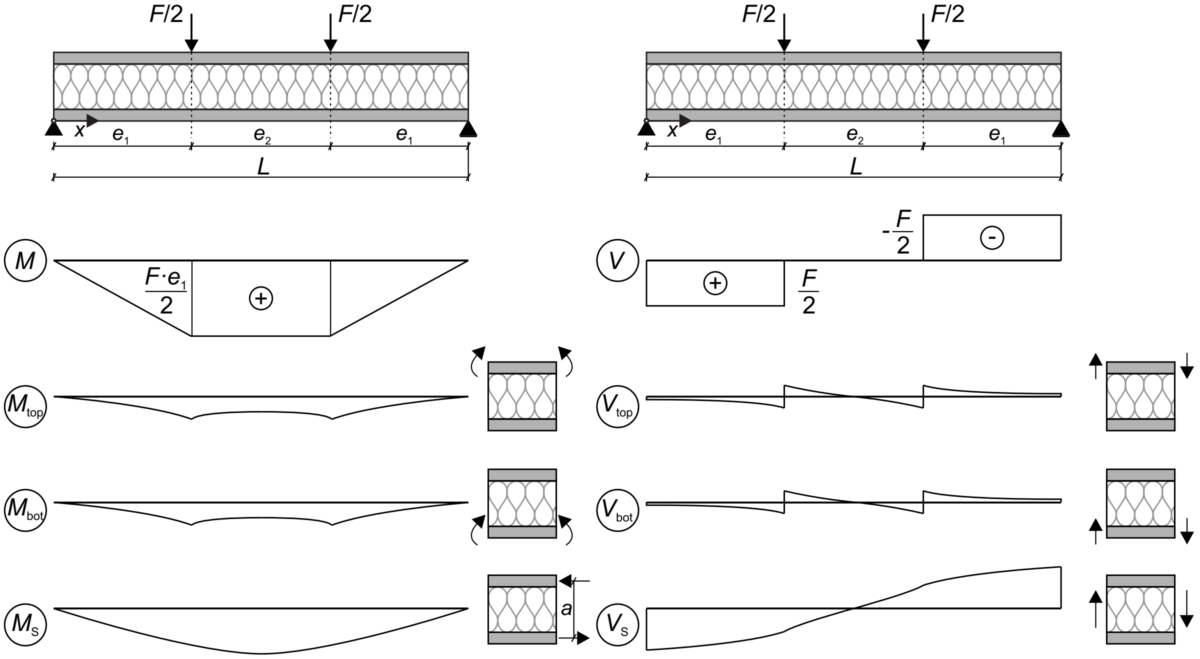

Fig. 7.25 **Bending moments and shear forces of simply supported sandwich beam**

Subsequently, only bending moments of the top facing M_{top} and bottom facing M_{bot} as well as arising sandwich action M_{s} with three-point loading are presented.

Bending moments for the three different parts I and II of the top and bottom facings as well as sandwich action are calculated as follows /Sta74/:

$$
\begin{aligned}
M_{bot/top,I} &= FL\frac{\alpha_{bot/top}}{1+\alpha}\left[(1-\varepsilon)\xi+\frac{\sinh\lambda(1-\varepsilon)}{\alpha\lambda\sinh\lambda}\sinh\lambda\xi\right]\\
M_{bot/top,II} &= FL\frac{\alpha_{bot/top}}{1+\alpha}\left[\varepsilon(1-\xi)+\frac{\sinh\lambda\varepsilon}{\alpha\lambda\sinh\lambda}\sinh\lambda(1-\xi)\right]
\end{aligned}
\qquad (7.14)
$$

$$
\begin{aligned}
M_{s,I} &= FL\frac{1}{1+\alpha}\left[(1-\varepsilon)\xi-\frac{\sinh\lambda(1-\varepsilon)}{\lambda\sinh\lambda}\sinh\lambda\xi\right]\\
M_{s,II} &= FL\frac{1}{1+\alpha}\left[\varepsilon(1-\xi)-\frac{\sinh\lambda\varepsilon}{\lambda\sinh\lambda}\sinh\lambda(1-\xi)\right]
\end{aligned}
\qquad (7.15)
$$

Results for shear forces *V* and other loading cases can be found in Appendix E.

7.4.3 Cracking of Prestressed UHPFRC Facings with CFRP Reinforcement under Flexural Loading

The failure of sandwich panels with concrete facings is usually induced by cracking of concrete layers, core layer or by delamination. In the presented experimental results, mainly a combined failure of core and facings was observed. Hence, for increased loading, the stiffness of the UHPFRC facings reduces after first cracking. For the equations based on work of STAMM and WITTE /Sta74/ with solutions for further loadings cases, a constant stiffness of each layer is assumed. Hence, solutions of the ODE's (e.g. equations (7.13)-(7.15)) lead to a linear-elastic load-deflection response.

In this section, the basic ideas are shown to apply solutions of ODE's and to account for cracking of the facings at the same time. First, the procedure was derived for sandwich panels with flat facings. In section 7.4.4, the derivations were extended for spatially shaped cross-sections. To account for the reduced stiffness of the concrete facings, a reduced mean value of stiffness is used over the full length of the sandwich beams, rather than a stiffness function to provide a simple approach /Hor10/, /Sha15b/. Therefore, the sandwich beam is subdivided into a finite number of elements with equal length ΔL (Fig. 7.26). The extensional stiffness *D* and flexural stiffness *B* are determined for each part depending on the stress state, i.e. cracked or un-cracked conditions. The mean stiffness of the concrete facings are a composition of the partial stiffnesses.

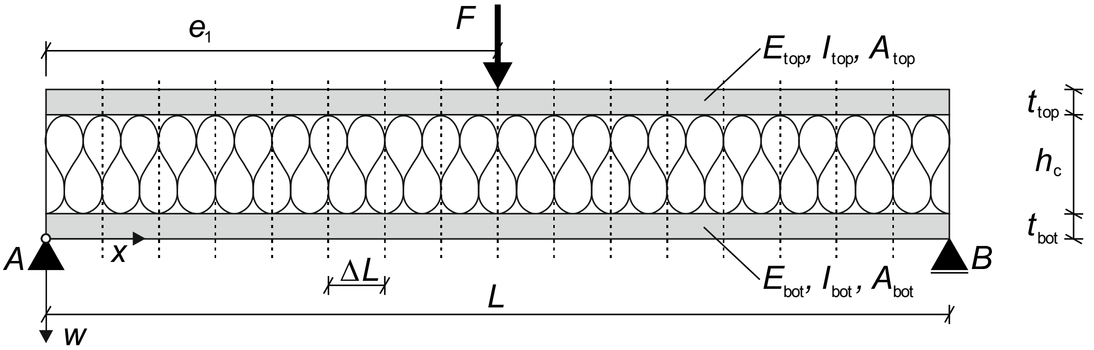

Fig. 7.26 Sandwich element subdivided into finite number of elements with equal length (in dependence on /Hor10, Sha15b/)

The load is applied incrementally as depicted in Fig. 7.27. For each load step the extensional and bending stiffnesses *EA* and *EI* of each part ΔL are determined depending whether the facings are cracked or intact. With this information a smeared rigidity is defined for the whole length of the beam. Hence, the incremental deflection Δw_i is calculated and added up to the overall deflection *w* for each load step.

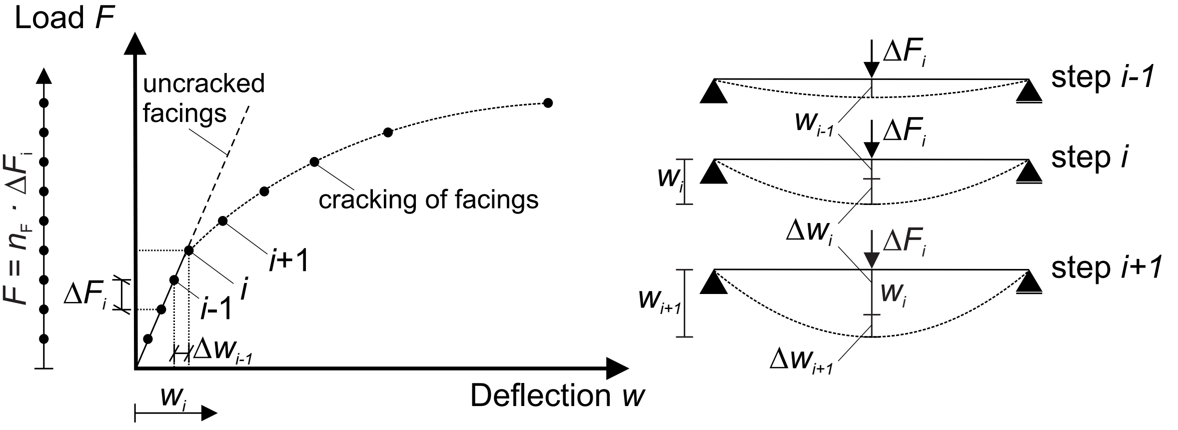

Fig. 7.27 Load-deflection curve due to transverse loading with incremental method (in dependence on /Hor10/, /Sha15b/)

In general, stresses in the concrete facings may be calculated with bending moments and axial forces using equation (7.16). The stresses at bottom and top of each facing can be compared with the uniaxial tensile strength of the concrete.

$$\sigma_{bot/top,bot/top} = \pm \frac{M_{bot/top}}{I_{bot/top} / z_{bot/top}} + \frac{N_{bot/top}}{A_{bot/top}} \tag{7.16}$$

HORSTMANN /Hor10/ and SHAMS /Sha15b/ considered three different stress states for the top and bottom facings during their investigations on sandwich panels with TRC facings. These three stress states were treated as equivalent to cracking states of the facings.

$$\begin{array}{ll} \sigma_{bot/top,bot} < f_{ct}, & \text{top/bottom facings: uncracked} \\ \sigma_{bot/top,top} < 0 \wedge \sigma_{bot/top,bot} \geq f_{ct}, & \text{top/bottom facings: bending cracks} \\ \sigma_{bot/top,top} \geq 0 \wedge \sigma_{bot/top,bot} \geq f_{ct}, & \text{top/bottom facings: cracks over full height} \end{array}$$

In the investigations on sandwich panels with TRC facings, HORSTMANN and SHAMS only analysed concrete layers without fibres or by neglecting fibre contribution. In /Hor10/ and /Sha15b/ the depth of the compression zone x was iteratively determined using a constant stress block for concrete under compression. In chapter 4, general solutions for the moment-curvature relationships of UHPFRC elements with (pre-tensioned) CFRP reinforcement under flexural and axial loading were derived. Hence, in case of cracking the residual bending stiffness $B_{\text{bot/top,i}}$ of each element of length ΔL can be calculated as ratio of moment and curvature.

$$B_{bot/top,i} = EI^{II}_{bot/top,i} = \frac{M_{bot/top,i}}{\kappa_{bot/top,i}} \tag{7.17}$$

At the beginning, the sections remain un-cracked, and $B_{\text{bot/top,i}}$ is equal to the linear elastic bending stiffness. After stresses are exceeding the concrete tensile strength, the bending stiffness is reduced.

For this purpose, for each load-step F_i the resulting moments in UHPFRC layers M_{bot} and M_{top} as well the sandwich moment M_s are determined. From sandwich moment M_s, axial forces in the UHPFRC layers were obtained by dividing the distance between facings centroids a. The axial forces were applied to determine the moment-curvature relationships (cp. chapter 4, equations (4.23), (4.29) and (4.30)) for prestressed or non-prestressed facings. According to chapter 5, the prestressing forces were reduced by about 5 % to account for residual tendon stresses in the UHPFRC members.

The extensional stiffness $D_{\text{bot/top,i}}$ of UHPFRC facings with bending cracks was simplified as sum of concrete contribution and stiffness of the reinforcement for each element of length ΔL. HORSTMANN and SHAMS only considered the concrete contribution over the height of the compression zone. Hence, the tensile strength of the concrete was neglected. In the following, the concrete contribution is assumed to consist of heights of the compression and tension zones, x_0 and x_1 (cp. chapter 4, equation (4.19)). The contribution of the cracked zone x_2 was neglected.

$$D_{bot/top} = EA^{II}_{bot/top} = E_c \cdot b \cdot \left(x_0 + x_1\right)_{, bot/top} + E_p \cdot \sum_i A_{p,bot/top} \tag{7.18}$$

For cracks over the full height of the facings, the stress state is governed by a predominant tensile loading. In this case, exceeding the maximum possible crack width to be bridged by fibres, the concrete contribution vanishes. Hence, the extensional stiffness is only dependent on the reinforcement as long as the maximum tensile strength is not exceeded. Experimental results and theoretical considerations showed that exceeding the maximum crack width of applied UHPFRC is accompanied by rupture of the CFRP prestressing tendons.

Since the equations presented in chapter 7.4.2 assume constant bending and extensional stiffnesses, a smeared approach for cracked cross-sections needs to be applied. Generally, different approaches to determine smeared rigidities of cracked facings can be used. Arithmetic average or weighting by deflection or bending moment distribution are examples. In /Hor10/, the deflection-based approach was found to deliver a good agreement with test results. SHAMS /Sha15b/ achieved conformity with test results by applying the arithmetic average since combined flexural and axial loading cases were investigated. Hence, a deflection-based approach would yield too small bearing capacities. Weighting by bending moment distribution leads to an overestimation of stiffness degradation in the vicinity of the loading points /Hor10/.

As stated before, the flexural rigidities and extensional stiffnesses can be calculated for each element ΔL for top and bottom facing separately. The deflection-based approach weights the rigidities by the deflections at each element ΔL (equation (7.19)).

$$B_{bot\,/\,top} = \frac{\sum_{i=1}^{n} EI_{i,bot\,/\,top} \cdot w_i}{\sum_{i=1}^{n} w_i}, \quad D_{bot\,/\,top} = \frac{\sum_{i=1}^{n} EA_{i,bot\,/\,top} \cdot w_i}{\sum_{i=1}^{n} w_i} \tag{7.19}$$

In contrast, the arithmetic average (equation (7.20)) simply determines the rigidities without weighting, i.e. accounting for disproportional crack growth. Since external axial loading of the elements was not investigated, this approach was not further considered in the following investigations.

$$B_{bot\,/\,top} = \frac{1}{n} \cdot \sum_{i=1}^{n} EI_{i,bot\,/\,top}, \quad D_{bot\,/\,top} = \frac{1}{n} \cdot \sum_{i=1}^{n} EA_{i,bot\,/\,top} \tag{7.20}$$

Fig. 7.28 shows the resulting stiffness using the weighted, deflection-based average.

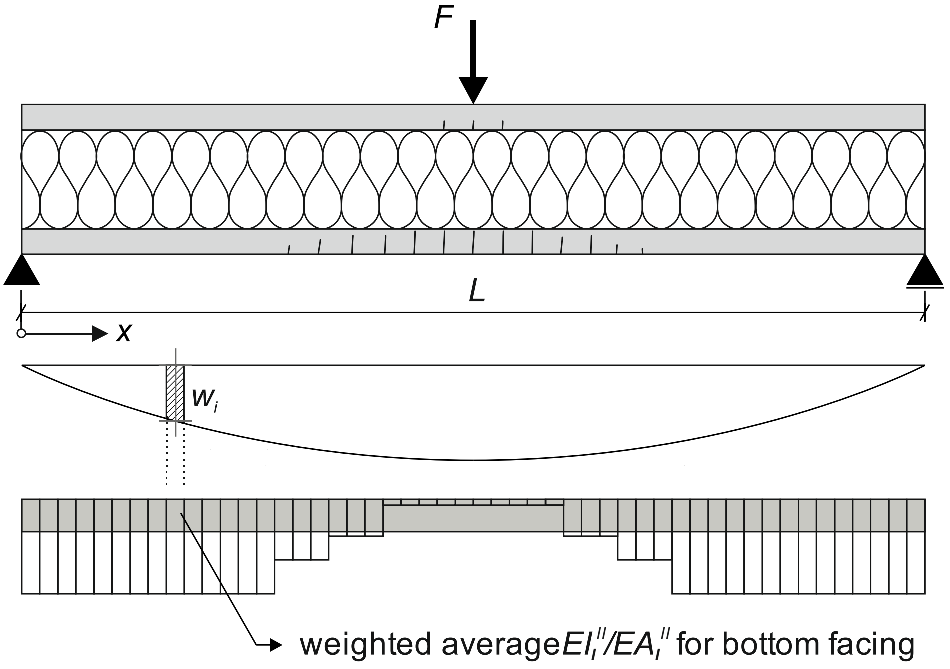

Fig. 7.28 Equivalent stiffness of the sandwich element using a deflection-based weighted average (in dependence on /Sha15b/)

The previous findings can be applied automatically to determine the theoretical load-deformation relationships. Since moment-curvature relationship of the UHPFRC facings were determined separately (cp. chapter 4), a convenient and time-saving calculation is possible.

In Fig. 7.29, the procedure of the calculation method is schematically depicted. First, geometric properties (length, width, thickness of facings and core), the reinforcement ratio and pre-tensioning forces as well as material properties are entered. For sandwich panels without shear connectors, the shear stiffness can be determined by equation (7.2). In case of applied shear connectors, the increased stiffness can be accounted for by applying the findings made in section 6.5. The stiffness of core and shear connectors were derived from small-scale testing. By applying the adequate length and number of shear connectors, the resulting stiffness k_{res} can be determined. The resulting shear stiffness A_{res} is to be obtained as follows:

$$A_{res} = k_{res} \cdot \frac{a^2}{\Delta l} \tag{7.21}$$

Depending on the problem to solve, the solutions of the ODE’s are provided for different support conditions and loading cases. Additionally, one has to choose the number of parts ΔL to subdivide the beam in n_{L} elements and the incremental, constant loading step ΔF. The number of parts n_{L} needs to be chosen in dependence of a assumed crack distance. For all elements this distance was set to $t/2$ (cp. chapter 4). The calculation starts for $F = 0$ by determination of flexural rigidities and axial stiffness in the elastic range. Afterwards, the loading is increased incrementally by ΔF and deflection w as well as moments and axial forces are determined in each part ΔL. After the stresses in the facings are exceeding the tensile strength of UHPFRC, the parameter combination of M_{bot} and N_{bot} as well as M_{top} and N_{top} are applied to determine the curvature κ, heights of compressive x_0 and elastic tensile zone x_1 by using the theoretical findings from chapter 4. The length L_{c} to convert the stress-displacement relationship of UHPFRC into a stress-strain relationships was consistently set to half the thickness of the facings. Applying equations (7.17) and (7.18), the flexural rigidities and axial stiffness for each part ΔL are calculated. The average rigidities are determined using the deflection-based approach (cp. equation (7.19)). In case neither of these is zero, the next load step ΔF is applied. This is carried out until failure of the element is reached. During the analysis shear stresses in the bond zone and maximum stresses in the shear connectors were checked. The shear stresses are determined from shear angle and shear modulus. In case of an applied shear grid, the maximum stresses in the shear grid were determined based on equation (6.2). The resulting tensile load in the rovings (cp. chapter 6) is divided by the cross-sectional area and needs to be smaller than its tensile strength.

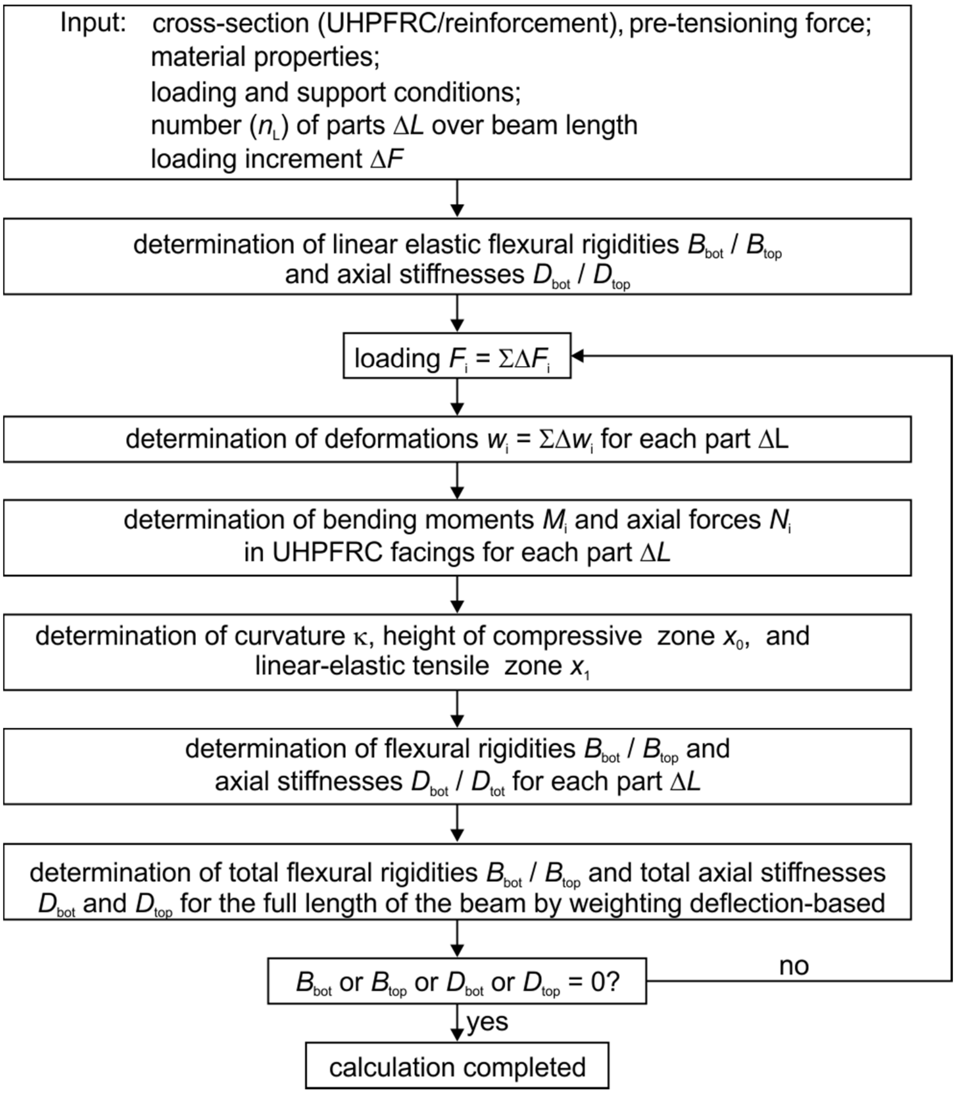

Fig. 7.29 **Calculation method to determine the theoretical load-deformation response of sandwich panels with prestressed UHPFRC facings subjected to flexural loading**

For two calculation steps the procedure to determine $B_{bot} = EI^{II}$ is exemplarily shown for a cracked bottom layer for one Element ΔL at load step F_i and F_{i+1}.

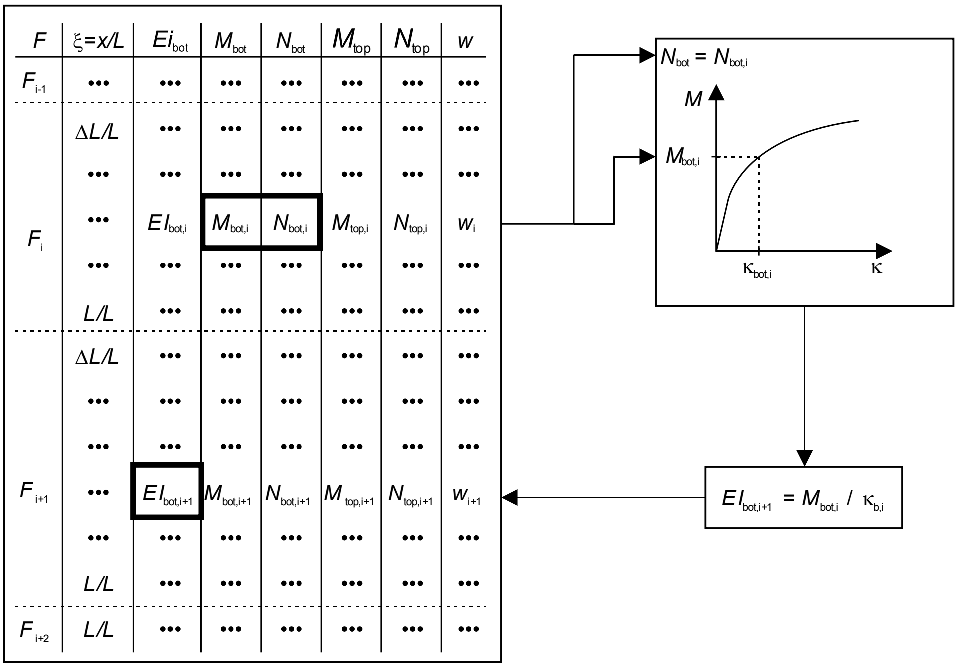

Fig. 7.30 Example of determination of EI^{II} for bottom layer at load steps *i* and *i*+1

Hence, the flexural and axial stiffnesses of cracked concrete sections can be determined for known moment-curvature relationships. In the next section, the procedure is discussed for panels with non-flat facings.

7.4.4 Folded Plate and Doubly Curved Facings

All previous derivations and explanations were based on the assumption of flat sandwich panels. These derivations are still valid for non-flat elements with constant cross-sectional properties over the length of the sandwich panel, if flexural rigidities $B = EI$ and axial stiffnesses $D = EA$ are determined based on the respective cross-section. Additionally, the varying shear stiffness A of the core-material needs to be determined. In /Sta74/ the procedure was shown for profiled sandwich panels with thin metal facings.

Depending on the complexity of the cross-section, the second moment of area and the cross-sectional area can be identified by hand calculation or computer-assisted. In the following, the equations are shown for a folded plate and a cylindrical shape. Since sandwich elements with concrete facings usually have thick layers compared to sandwich elements with steel facings, the second moment of area of partial areas has to be taken into account, rather than only using the parallel axis theorem. In Fig. 7.31 examples of a folded plate and a cylindrical cross-section are shown.

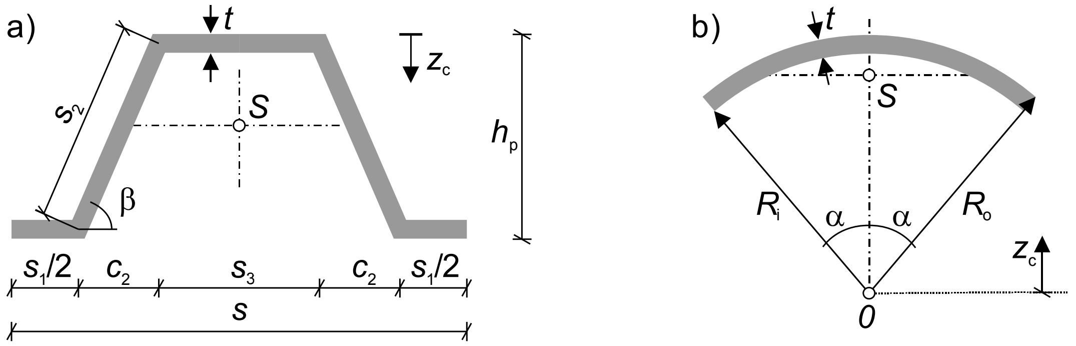

Fig. 7.31 Examples of folded plate and cylindrical-shaped facings

The folded plate element can be divided into two bottom flanges, one top flange and two inclined webs. The length of each part was determined by the intersections of the centrelines. The following equations can be used to estimate the centroid z_c, second moment of area I_{yy} and area A_c to calculate the flexural rigidity B and axial stiffness D.

$$z_c = \frac{\left(h_p - \frac{t}{2}\right)s_1 + h_p s_2 + \frac{t}{2} s_3}{s_1 + 2s_2 + s_3} \tag{7.22}$$

$$\begin{aligned} I_{yy} &= s_1 \frac{t^3}{12} + s_1 t \left(h_p - \frac{t}{2} - z_c \right)^2 + 2\left(t \frac{(s_2 \sin\alpha)^3}{12} + s_2 \cos\alpha \frac{t^3}{12} \right) \\ &\quad + s_2 t \left(\frac{h_p}{2} - z_c \right)^2 + s_3 \frac{t^3}{12} + s_3 t \left(z_c - \frac{t}{2} \right)^2 \\ A_c &= t \cdot (s_1 + 2s_2 + s_3) \end{aligned} \tag{7.23}$$

$$\begin{aligned} B &= EI_{yy} \\ D &= EA_c \end{aligned} \tag{7.24}$$

For cylindrical shaped elements, the cross-sectional properties are determined using polar coordinates. The area, centroid and second moment of area are computed as follows:

$$A_c = \left(R_o^2 - R_i^2\right) \cdot \alpha, \quad \alpha \text{ in [rad]} \tag{7.25}$$

$$
\begin{aligned}
z_c &= \frac{1}{A_c}\cdot\int_A \bar{z}\, dA_c = \frac{1}{A_c}\cdot\int_{R_i}^{R_o}\int_{\frac{\pi}{2}-\alpha}^{\frac{\pi}{2}+\alpha} r\cdot\sin\varphi\cdot r\, dr d\varphi \\
&= \frac{1}{A_c}\cdot\int_{R_i}^{R_o} r^2 \int_{\frac{\pi}{2}-\alpha}^{\frac{\pi}{2}+\alpha}\sin\varphi\, d\varphi dr = \frac{1}{A_c}\cdot\left[\frac{1}{3}r^3\right]_{R_i}^{R_o}\cdot\left[\cos\varphi\right]_{\frac{\pi}{2}-\alpha}^{\frac{\pi}{2}+\alpha} \\
&= \frac{1}{A_c}\cdot\frac{1}{3}\left(R_o^3 - R_i^3\right)\cdot\left[\cos\left(\frac{\pi}{2}+\alpha\right) - \cos\left(\frac{\pi}{2}-\alpha\right)\right] \\
&= \frac{1}{A_c}\cdot\frac{1}{3}\left(R_o^3 - R_i^3\right)\cdot\left[2\sin\alpha\right] = \frac{2}{3}\frac{R_o^3 - R_i^3}{R_o^2 - R_i^2}\cdot\frac{\sin\alpha}{\alpha}
\end{aligned}
\tag{7.26}
$$

The equation of the second moment of area based on the origin *O* (cp. Fig. 7.31) is set up as follows:

$$
\begin{aligned}
I_{\bar{y}\bar{y}} &= \int_A \bar{z}^2\, dA_c = \int_{R_i}^{R_o}\int_{\frac{\pi}{2}-\alpha}^{\frac{\pi}{2}+\alpha} \left(r\cdot\sin\varphi\right)^2\cdot r\, dr d\varphi \\
&= \int_{R_i}^{R_o} r^3 \int_{\frac{\pi}{2}-\alpha}^{\frac{\pi}{2}+\alpha} \sin^2\varphi\, d\varphi dr = \left[\frac{1}{4}r^4\right]_{R_i}^{R_o}\cdot\frac{1}{2}\left[\varphi - \sin\varphi\cos\varphi\right]_{\frac{\pi}{2}-\alpha}^{\frac{\pi}{2}+\alpha} \\
&= \frac{1}{4}\left(R_o^4 - R_i^4\right)\cdot\left[\alpha + \sin\alpha\cos\alpha\right]
\end{aligned}
\tag{7.27}
$$

Since the second moment of area needs to be determined at centroid, the parallel axis theorem is to be applied:

$$
\begin{aligned}
I_{yy} &= I_{\bar{y}\bar{y}} - z_c^2\cdot A_c \\
&= \frac{1}{4}\left(R_o^4 - R_i^4\right)\cdot\left[\alpha + \sin\alpha\cos\alpha\right] - \left(\frac{2}{3}\frac{R_o^3 - R_i^3}{R_o^2 - R_i^2}\cdot\frac{\sin\alpha}{\alpha}\right)^2\cdot\left(R_o^2 - R_i^2\right)\cdot\alpha \\
&= \frac{1}{4}\left(R_o^4 - R_i^4\right)\cdot\left[\alpha + \sin\alpha\cos\alpha\right] - \frac{2}{3}\cdot\frac{\sin^2\alpha}{\alpha}\cdot\frac{\left(R_o^3 - R_i^3\right)^2}{R_o^2 - R_i^2}
\end{aligned}
\tag{7.28}
$$

The specified equations can be applied to establish $B = EI$ and $D = EA$ for top and bottom facings as long as these cross-sections remain constant over the length of the sandwich panels.

For varying cross-sectional properties $B_s(x)$, $B_{top}(x)$, $B_{bot}(x)$ and $A(x)$, the relationships for moments (cp. equation (7.1)) remains the same, whereas the shear force has to be calculated in the following way:

$$V = A\gamma - \left[(B_{bot} + B_{top})w''\right]' \tag{7.29}$$

Decoupling equations for moment (equation (7.1)) and shear force (equation (7.29) result in ODE's of fourth order for w and γ with varying coefficients. Since these equations usually cannot be solved exactly, approximation methods, such as numerical methods, have to be applied. Since the camber in longitudinal direction of doubly curved sandwich panels represents no variation of the cross-section, but different stiffness, the procedure becomes complex. Additionally, the inner lever arm of the resulting reinforcement forces varies over the length of the elements. Therefore, the camber in longitudinal direction was neglected for further considerations using sandwich theory.

The shear stiffness A of sandwich elements with non-flat facings can be determined by considering a small element of length ΔL /Sta74/ (Fig. 7.32). This element is to be loaded by axial shear forces T (resulting from facings) and vertical shear forces V.

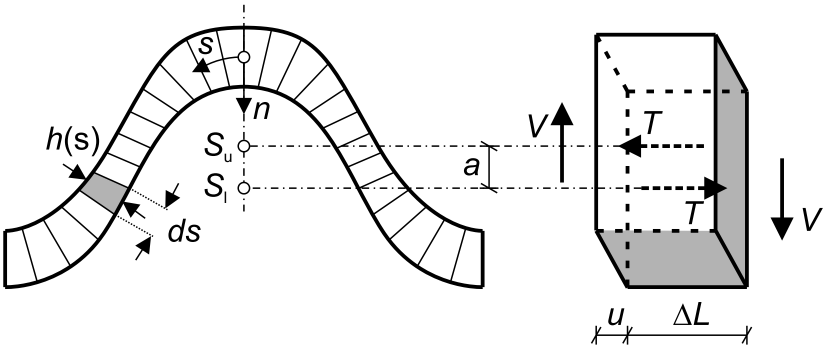

Fig. 7.32 Cross-section of non-planar sandwich element (reproduced from /Sta74/)

This results in a relative displacement u between the facings. In doing so, the cross-section is subdivided in lamellas (perpendicular to coordinate s) of width ds and height $h(s)$. With this assumption, the shear stresses τ_{xn} in each lamella (equation (7.30)), are independent on shear stresses and shear angles of neighbouring lamellas. Hence, shear stresses τ_{xs} are neglected.

$$\tau_{xn} = G \cdot \gamma_{xn} = G \cdot \frac{u}{h(s)} \tag{7.30}$$

By applying the shear angle $\gamma = u / a$, it follows:

$$\tau_{xn} = G \cdot \frac{a}{h(s)} \cdot \gamma, \qquad T = \int_s \tau_{xn} \Delta L ds \tag{7.31}$$

Using the relationship of axial and vertical shear forces in equation (7.32), one obtains the shear stiffness A according to equation (7.33).

$$T = Q \cdot \frac{\Delta L}{a} \tag{7.32}$$

$$V = A \cdot \gamma, \qquad A = G \cdot a^2 \cdot \int_s \frac{1}{h(s)} ds \tag{7.33}$$

For flat elements with constant height h and width b, equation (7.33) simplifies to equation (7.2).

Generally, cross-sections are subdivided in elements with approximate the same height, as shown Fig. 7.32. The investigated cross-sections (cp. section 7.2.1) can be subdivided as shown in Fig. 7.33. Depending on the size of cross-sections, a more detailed subdivision can be necessary.

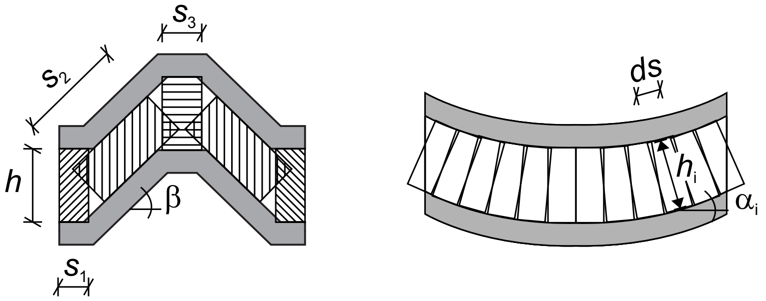

Fig. 7.33 Subdivision of tested folded plate and curved cross-sections

Hence, for the folded plate cross-section the shear stiffness A can be estimated by applying equation (7.33) as follows:

$$A = G \cdot \frac{a^2}{h} \cdot \left[s_1 + 2 \cdot \frac{s_2}{\cos\beta} + s_3 \right] \tag{7.34}$$

The cylindrical cross-section of HP elements is represented by a parabola. The angle α at each element is to be determined by the first derivative of the parabola equation. With the aid of the angle, the orthogonal height can be determined. Hence, the shear stiffness A is calculated as follows:

$$\begin{aligned} y(x) &= ax^2 \\ y'(x) &= 2ax \\ A &= G \cdot \frac{a^2}{h} \cdot \sum_i \frac{ds}{\cos\ (\arctan\ (y'(x_i)))} \end{aligned} \tag{7.35}$$

In the next sections, the derived approaches to account for cracking of UHPFRC facings and modifications to account for non-flat beams are validated by results of experimental testing.

7.5 Validation of Derived Approaches

7.5.1 Sandwich Panels with Flat Facings

In the first step, the derived approach was applied to predict the load-deflection response of flat sandwich panels under flexural loading. The geometric parameters were used according to section 7.2 and material parameters were applied in accordance with chapters 3 and 4. The spring stiffness of the connecting device (CFRP grid) was determined based on derivations made in chapter 6. After determination of axial and flexural stiffnesses of each layer, the load F was stepwise applied in steps of 5 kN. The axial forces and bending moments as well deflections were calculated for each element (top and bottom facing) with aid of the constitutive equations of section 7.4.2. For each element ΔL, the axial force N and bending moment M were applied to determine the corresponding curvature κ and residual heights of the cross-section to transfer internal forces (x_0, x_1) according to equations (4.19), (4.29) and (4.30) (chapter 4). Hence, the axial and flexural stiffnesses were calculated and weighted deflection based (Fig. 7.28) to determine mean values for the next load step. With this iterative process, the load was increased until failure of UHPFRC facings, bond zone or connecting devices was determined.

In Fig. 7.34 the calculated load-deflection responses at midspan and quarter points of flat sandwich panels with and without pre-tensioning of the CFRP reinforcement is compared to the test results. For these elements, one CFRP shear grid was applied. The predicted load deflection response is in good agreement with test results for prestressed and non-prestressed facings.

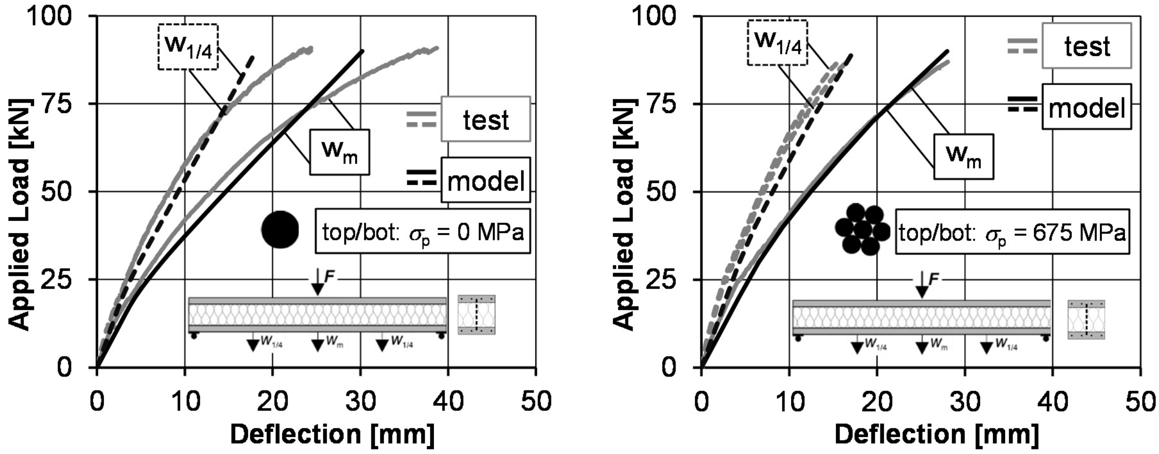

Fig. 7.34 **Load-deflection response of flat sandwich panels with CFRP shear grid: without (left: SB-3) and with (right: SB-6) prestressed facings**

The predicted failure modes were a combined failure of the facings and the bond zone. In case of applied shear grids, test specimens failed due to shear cracks in the core material, which was induced by high relative displacement of the facings, but relatively good bond conditions. The model predicted about the same relative displacement at failure and cracking of the facings. In the vicinity of the supports, debonding was determined over a length of about 250 mm at maximum load by the model.

As mentioned before, the production procedure of flat sandwich panels without CFRP shear grid resulted in rough concrete surfaces in the bond zone. This may have affected the bond quality negatively (cp. section 7.2). In Fig. 7.35, the predicted load-deflection response of sandwich panels without CFRP shear grid is depicted. Independent of prestressing of facings, the test results showed considerably more deflection and less maximum load capacity compared to results of the analytical approach. Even though, the load-deflection response of the prestressed panel was determined congruently until bond failure in the test. Hence, only the maximum bond strength seemed to be reduced in this test specimen, rather than the overall stiffness.

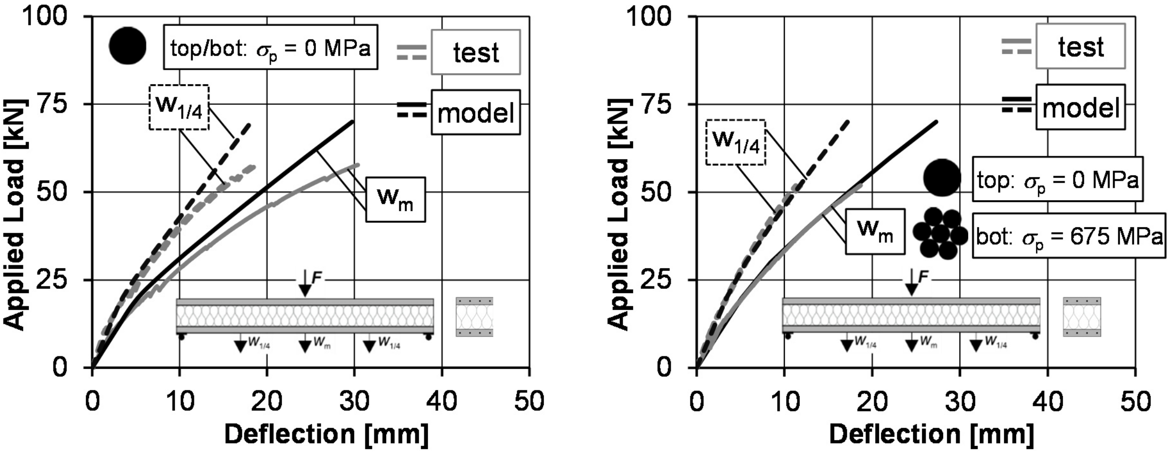

Fig. 7.35 **Load-deflection response of flat sandwich panels without connecting devices and without (left: SB-2) and with (right: SB-5) prestressed facings**

With the aid of the constitutive equations (cp. section 7.4.2) the relative displacement of the UHPFRC facings was estimated. In Fig. 7.36, the calculated relative displacement at the beam end is shown in comparison to test results.

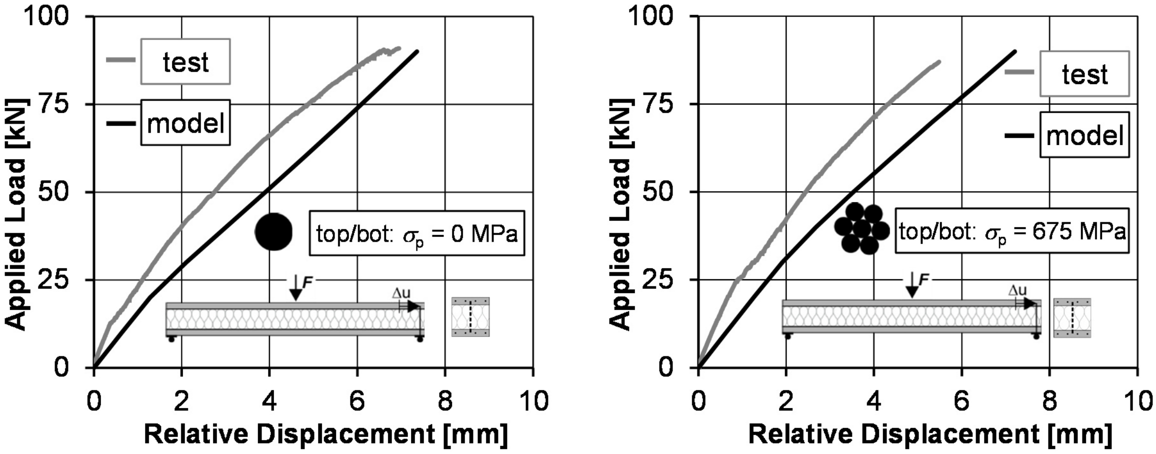

Fig. 7.36 Relative displacement of UHPFRC facings without (left: SB-3) and with (right: SB-6) prestressing

Even though, the relative displacement was predicted slightly too soft in the linear elastic stage, the overall response was predicted in good agreement with test results. Since relative displacement was only measured at the supports, the response over the full length of the beams was predicted by the analytical model to show the influence of a CFRP shear grid. The calculated relative displacement of top and bottom facings are exemplarily depicted in Fig. 7.37. For an applied load of 10 kN, the distribution of relative displacements was about the same, independent on an applied shear grid. At predicted maximum load (70 kN) of the panel without shear grid, the relative displacement increased up to 7.5 mm. For comparison, the smaller relative displacements of the panel with shear grid is shown for the same load level, which equals about 80 % of maximum load (90 kN) in the analysis. Even though the results are not directly comparable, since the top facing of the panel with shear connector was additionally prestressed, the positive influence of shear grid can be concluded.

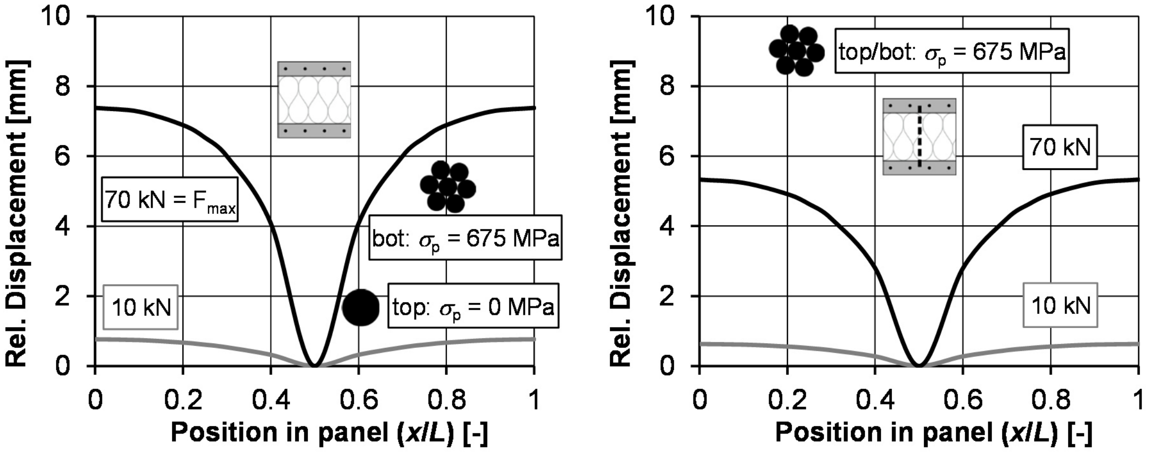

Fig. 7.37 Relative displacement of UHPFRC facings over the beam length for sandwich panels without (left: SB-5) and with (right: SB-6) CFRP shear grid

In the following sections, the approaches were further validated.

7.5.2 Sandwich Panels with Folded Plate Facings

In this section, the proposed model to determine the load behaviour of folded plate sandwich panels under flexural loading is validated. The derivations made in sections 7.4.2 and 7.4.3 were applied in combination with derivations and assumptions proposed in section 7.4.4 to account for non-flat cross-sections. The geometric parameters were used according to section 7.2 and material parameters were applied in accordance with chapters 3 and 4.

For the determination of theoretical moment-curvature relationships (cp. chapter 4), the folded plate cross-section was converted in a cross-section with area by area constant width, such as an inverted T-beam. For this purpose, mean values of widths were applied. As stated in chapter 4, a web with constant resulting width and two flanges were assumed. The bottom strain was then supposed to act at the bottom side of the web. Hence, the strains of reinforcement and flanges were to be the same. For simplicity, the difference in width of the top flange was neglected. For other folded plate cross-sections, with differing width of top flange and web, a case-by-case analysis for the resulting compression force has to be applied. In Fig. 7.38, the derived cross-section is shown. The overall area and second moment of area were about the same as for the folded plate element.

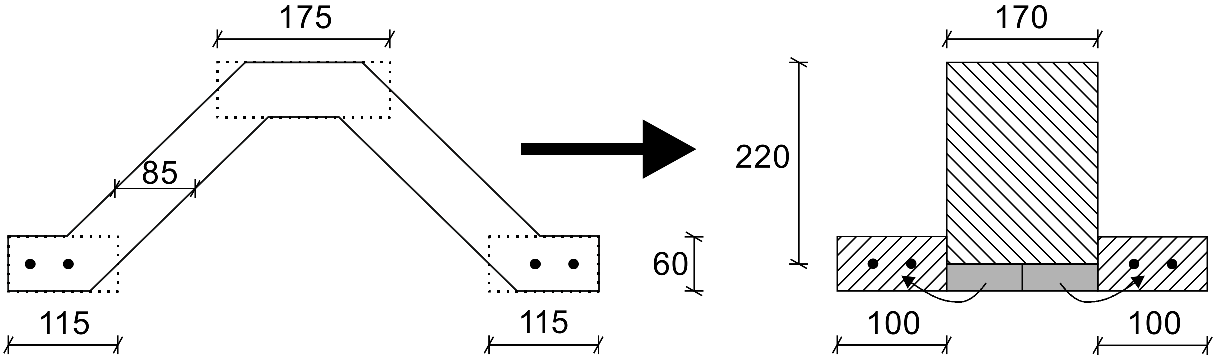

Fig. 7.38 **Transformation of folded plate element into beam with area by area constant widths**

With aid of this cross-section, moment-curvature relationships were determined for the cracked state of prestressed folded-plate sandwich panels. By determination of the strain distribution, section forces as well as corresponding lever arms, resulting bending moments and curvature can be calculated. To validate the approach, first, the load-deflection response of single folded plate elements was determined and compared to test results. As described in chapter 4, applied loading was derived from the resulting bending moments and deflection was calculated by integrating curvature. Subsequently, different types of reinforcement (bar Ø5 mm / strand Ø7.5 mm) and different pre-tensioning stresses (0 MPa, 675 MPa and 1350 MPa) were investigated to compare the results with test data. In Fig. 7.39, the proposed model is validated with the load-deflection response of single folded plate elements. The length l_c was consistently set to half the thickness of the facings, i.e. to 30 mm (cp. chapter 4). For different pretensioning stresses, the load-deflection responses were found in very good agreement. Only for a prestressing of 1,350 MPa a deviation in the cracked state was observed, which was caused by a different failure mode of test FP-1 (cp. Appendix C). The element failed due to a longitudinal crack growing from the support. The cracking loads were determined to the same values as measured in the tests. For all cases, the maximum deflection was overestimated, especially for elements with CFRP bars and no prestressing. Since the facings of sandwich panels are not subjected to the same cracking state as the single elements, the model seemed applicable to account for cracked folded plate facings.

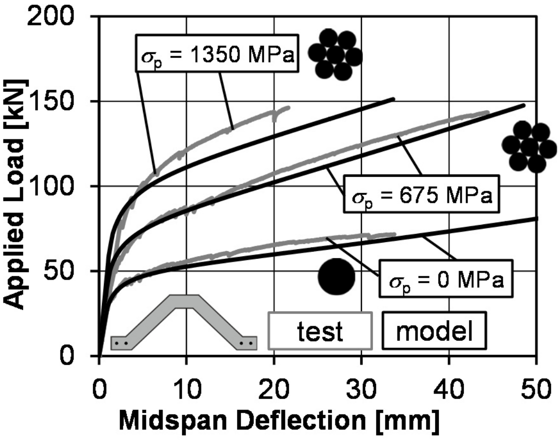

Fig. 7.39 **Comparison of load-deflection curves from derived model and test data for folded plate elements (FP-1, FP-5, FP-6))**

In the next step, the shear stiffness A of the core material was calculated based on the findings from Fig. 7.33 for the cross-sections investigated experimentally in section 7.2. The shear stiffness was determined numerically based on a finite number of elements. For a shear modulus G of 11.5 MPa, a core height h of 200 mm and a distance between the centre-lines of the facings a of 260 mm, the shear stiffness A of the trapezoidal cross-section was determined to $3.8 \cdot 10^6$ N. A flat element with same widths and core height would possess a shear stiffness A of $2.2 \cdot 10^6$ N. Hence, the trapezoidal shape, which was applied during testing, increases the shear stiffness by about 70 %.

The derived model was applied to determine the load-deflection response of sandwich panels with folded plate cross-sections. The calculation procedure remains the same as for flat elements (cp. Fig. 7.29). The moment curvature relationships in dependence on the axial force were calculated based on the findings for inversed T-beams (cp. chapter 4).

In Fig. 7.40 the determined load-deflection response is shown for folded plate sandwich panels without prestressing and with prestressing of the facings. The cracking loads as well as maximum loads were determined in good agreement with the test results at midspan (w_1) and at quarter points (w_2) for the panel without prestressing. For the prestressed sandwich panel, the cracking load was slightly overestimated. The failure of the panels was predicted by cracking of the facings and small parts of debonding at the supports. The stresses in CFRP reinforcement were determined up to 2,600 MPa, which is close to the maximum capacity of CFRP strands. For short spans, the approach of transforming the folded plate cross-section into an inversed T-beam showed satisfying results.

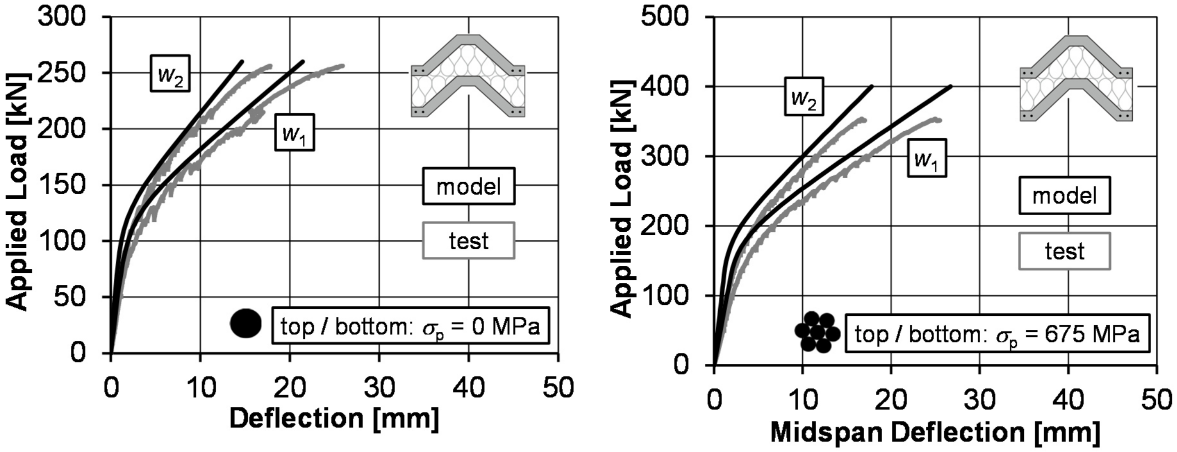

Fig. 7.40 Comparison of the load-deflection response at midspan (w_1) and at quarter points (w_2) of derived model and test data for folded plate sandwich panels with CFRP bars (left: SFP-4) and with CFRP strands (right: SFP-5)

Since relative slip between the top and bottom layer was not measured during the experimental testing on folded plate elements, the calculated response over the beam length was determined exemplarily for two cases. In Fig. 7.41 the influence of prestressed bottom and top facings on the relative displacement Δu is depicted. For an applied load of 100 kN, the panel without prestressing started cracking. The corresponding relative displacement of the facings is slightly higher than for the prestressed element.

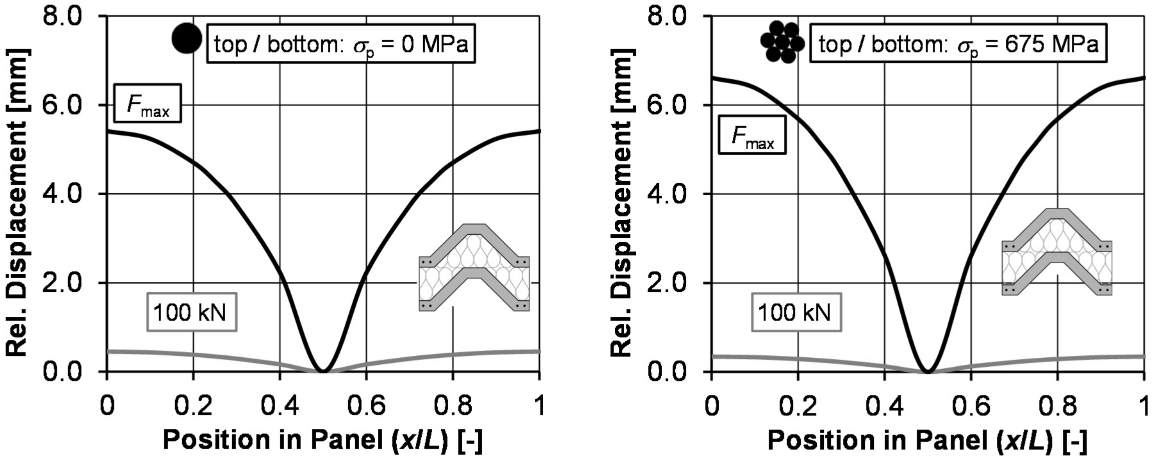

Fig. 7.41 Relative displacement Δu over the beam length for folded plate sandwich panels with CFRP bars (left: SFP-4) and CFRP strands (right: SFP-5)

At maximum load (cp. Fig. 7.40), the relative displacement was about seven to thirteen times higher than at cracking load depending on the prestressing force. The prestressed sandwich panel reached a maximum load about 60 % higher, while relative displacement of the facings increased only by about 15 %. This value is in accordance with the corresponding deflections.

7.5.3 Sandwich Panels with Curved Facings

In this section, the proposed approaches to determine the load behaviour of curved sandwich panels under flexural loading were verified. As stated before, the camber in longitudinal direction of the doubly curved element leads to equations, which can only be solved numerically. Additionally the varying position of reinforcement, i.e. inner lever arm of resulting reinforcement force, represents different cross-sections at each element ΔL in case that the concrete tensile strength is taken into account.

In Fig. 7.42 the positions of reinforcement over the longitudinal axis and corresponding cross-sections of the investigated doubly curved element are shown.

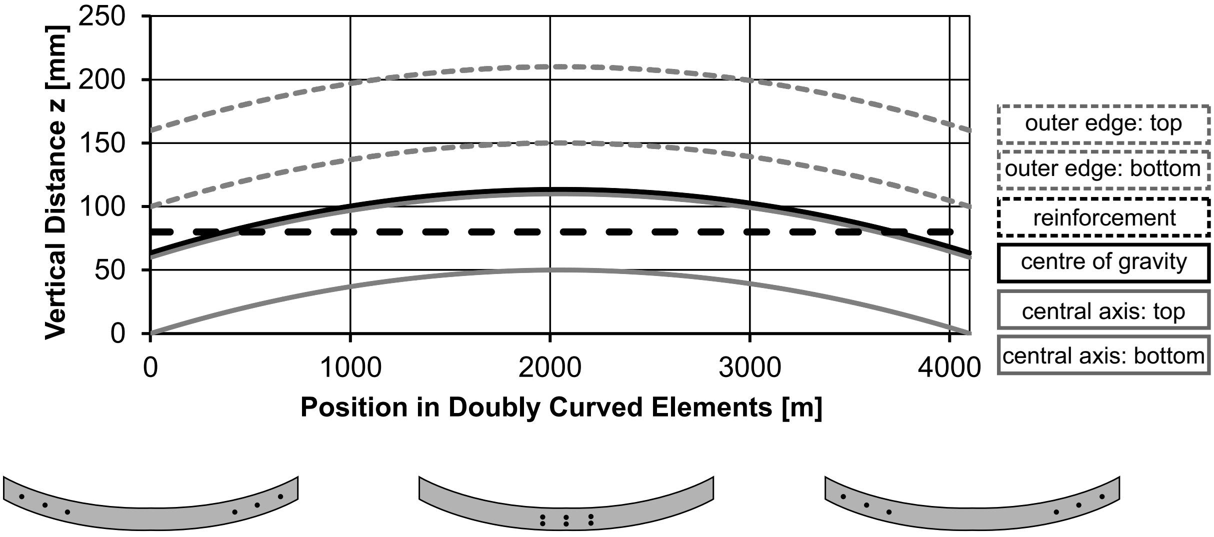

Fig. 7.42 **Average position of prestressing tendons in investigated doubly curved elements**

Since the lever arm varies over the full length of the element, no adequate replacement of a mean lever arm for an element without camber can be found. For example, the lever arm to achieve the same mean deflection from prestressing, which is close to zero, results in an underestimation of the lever arm in the area of the maximum bending moment. Vice versa, using the lever arm in the middle of the element at position of the maximum bending moment results in an overestimation. Hence, no replacement of the cross-section was used. For the following applications of analytical models, the camber in longitudinal direction was neglected.

First, the derivation of stiffness of the core material was verified. The shear stiffness A was determined to $2.88 \cdot 10^6$ N (cp. equation (7.35)). The axial stiffness D and flexural stiffness *B* were determined by applying equations (7.25) and (7.28) as well as the Young's modulus *E* of UHPFRC. Applying sandwich theory, yields the linear elastic behaviour of the section. In Fig. 7.43, the comparison of test results and calculated linear elastic behaviour is shown for sandwich beams without and with prestressing of the UHPFRC facings. The prestressing force was applied at centroid of the facings, which is roughly the resultant position over the full length.

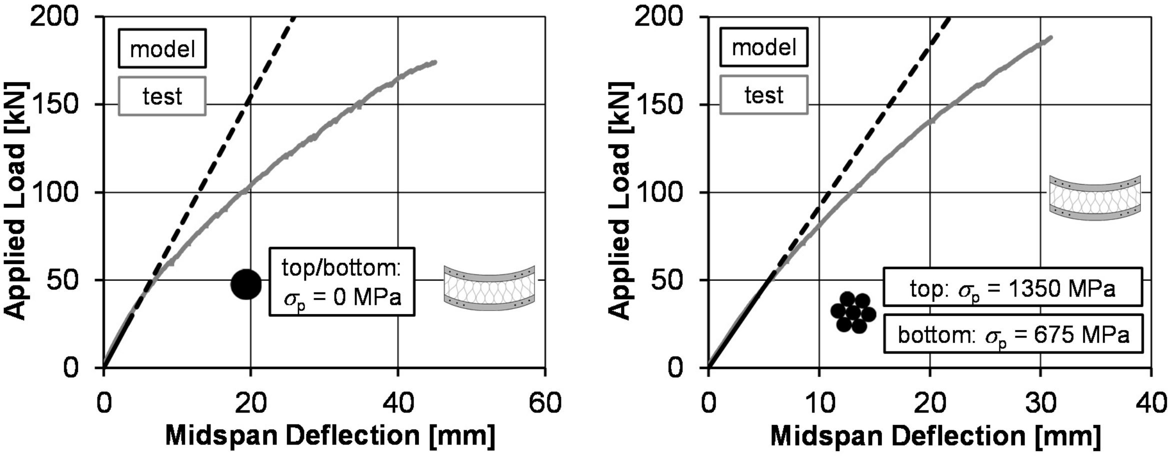

Fig. 7.43 **Comparison of determined linear-elastic load-deflection response of curved sandwich panels and test results of doubly-curved sandwich panels without prestressing (left: SHP-1) and with prestressing (right: SHP-5)**

The results show that the determined shear stiffness *A* leads to a satisfying response of the linear elastic part (continuous black line), even though the camber (50 mm) was neglected. In case of the prestressed panel, the stiffness was determined slightly less stiff compared to test results. Cracking of the facings leads to a non-linear behaviour after reaching the maximum tensile strength, which is obviously not predicted by the elastic sandwich theory (dashed black line). For the linear-elastic investigation, the stresses at the bottom of each facings were determined from the moment and axial force in the facings. For the element without prestressing, the bottom stresses at the bottom facing reached about 5.5 MPa for an applied load of 25 kN at midspan. For the prestressed curved sandwich panel, about the same stresses were reached at an applied load of 50 kN. These loads are in accordance with cracking loads during testing.

Approaches to account for cracking of UHPFRC facings during the analysis were not further considered, since neglecting of camber and idealisation of curved shape to a cross-section with area by area constant width would result in high error. The effort to combine sandwich theory with cracking of curved cross-sections is higher than using non-linear finite element modelling. Hence, it is proposed to use the derived finite element solutions to predict the overall structural performance of doubly curved sandwich panels.

7.6 Aspects of Long-term Effects

In the present study, it was not particularly focused on long-term tests. However, one tentative test was carried out on a doubly curved sandwich panel to verify the long-term behaviour. The sandwich panel (cp. section 7.2 and Appendix D, test HP-S-4) was reinforced with six CFRP rebars (Ø5 mm) without pre-tensioning in the top facing and with six CFRP strands (Ø7.5 mm) pre-tensioned to 675 MPa in the bottom facing. The specimen was simply supported and loaded in four-point bending (cp. Fig. 7.1). The dead load of 22 kN, represents 50 % of the cracking load of test HP-S-4. The same measurement technique was applied as for the static tests. In Fig. 7.44, the progress of deflection over loading duration at midspan (w_1) and between support and loading (w_2) is shown. The deflections after loading (0 h) are the same as for test HP-S-4 at 50 % of linear elastic load. The deflections w_1 and w_2 increase over the first 400 h loading about 0.75 mm and 0.50 mm, respectively. In the next 400 h another 0.2 mm and 0.1 mm increase took place. Afterwards, only small increments of deflection were observed. The test was ended after 1000 h of loading. No cracking of the UHPFRC facings or core material was visible. After unloading deflections of w_1 = 1.38 mm and w_2 = 0.54 mm remained as inelastic deformations. The measurements of core compressions and relative slip showed only a slight, insignificant increase over the loading time.

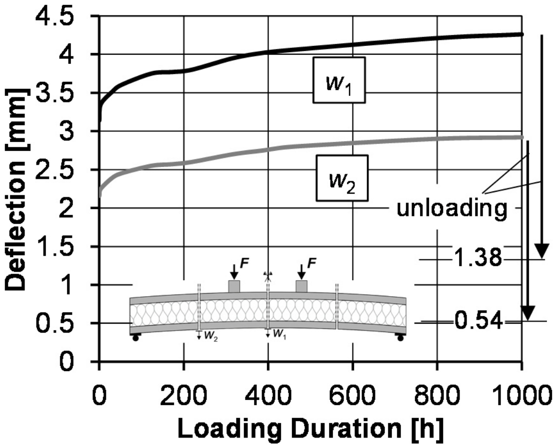

Fig. 7.44 Relationship between deflection and loading duration

After unloading, the specimen was tested displacement controlled in the same manner as described in section 7.2.1. Compared to the specimen with the same configuration of reinforcement and prestressing (HP-S-4, cp Appendix D), without long-term loading, the maximum load decreased by approximately 25%. This may be caused by long-term loading. However, only one tentative test was conducted and it cannot be ruled out that variations in material properties may have led to the reduction.

7.7 Case Studies

In the previous sections and chapters, it was shown that the structural performance of sandwich panels with UHPFRC facings can be described and predicted in good agreement by the derived analytical and numerical models. Therefore, the influence of different parameter variations is exemplarily shown in case studies. On the one hand, the effect of distributed loading rather than three-point bending or four-point bending is shown. On the other hand, the influences of length and decreased core stiffness are discussed. The cross-sections remain the same as for the investigated panels in section 7.2.1, besides the folded plate and doubly curved panels with length of 24 m. The solution of the analytical model for a simply supported beam with distributed loading can be found in appendix E. To show the influence of parameter variations, no application of a shear grid was assumed. In Fig. 7.45 the variation of parameters is summarised.

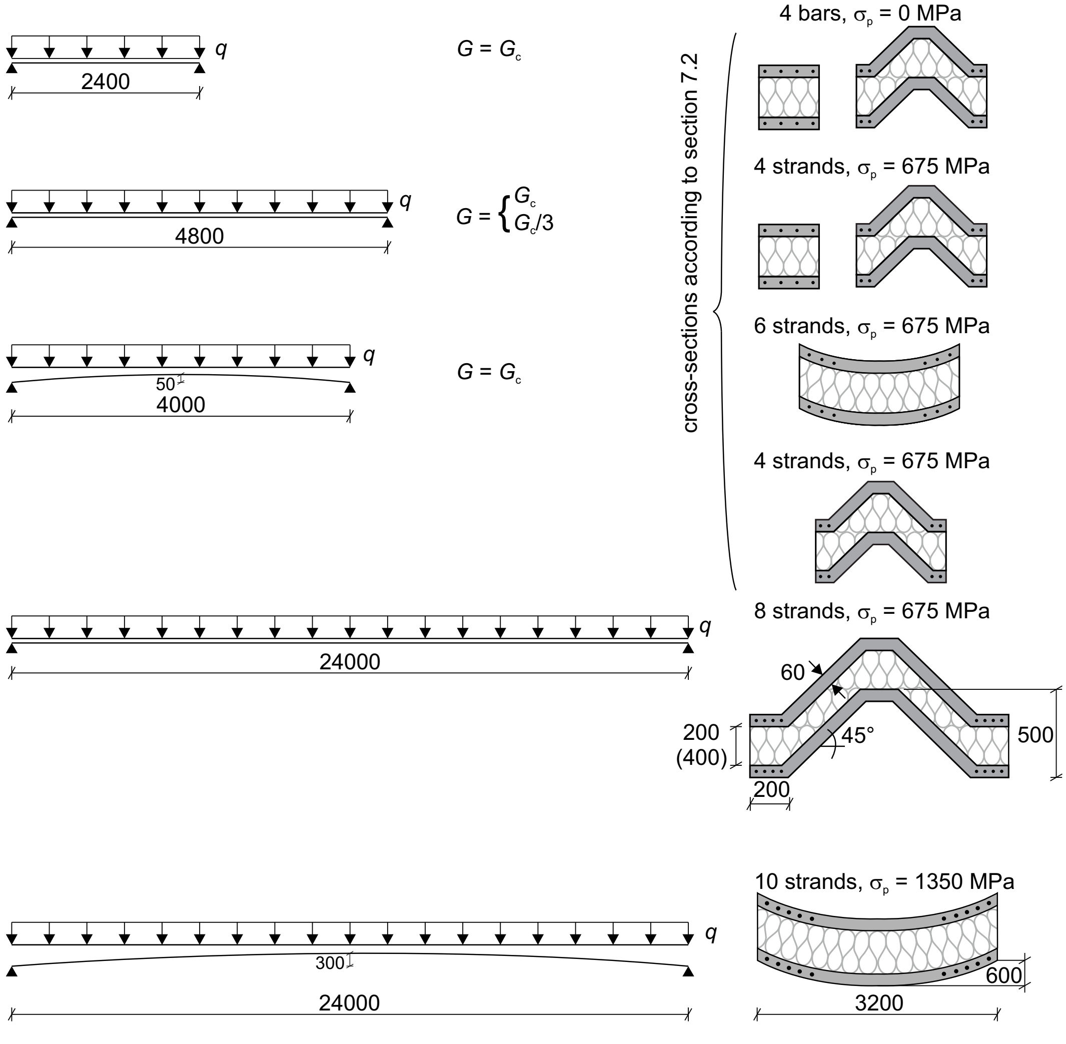

Fig. 7.45 Case studies of flat, folded plate and doubly curved sandwich panels

Roof elements are usually subjected to self-weight, snow, wind and temperature loading. Additionally, long-term effects can play a key role, depending on the applied materials. At this stage, only the effect of distributed loading was investigated. Effects from long-term loading were exemplarily discussed in section 7.8. For effects from temperature loading, it is referred to solutions of the analytical model provided in /Sta74/.

In Fig. 7.46, the effect of distributed loading compared to three-point bending is shown for flat and folded plate sandwich panels. For a length of 2.4 m, the flat panel and folded plate panel were investigated without prestressing and four CFRP bars (Ø5 mm) each in bottom and top facings. Experimental results from tests under three-point bending are depicted for comparison. For both loading cases the resultant load is depicted. Hence in case of three-point bending, *F* and in case of distributed loading, $q{\cdot}L$ are denoted. The results show, that the behaviour under distributed loading is stiffer and reaches a higher maximum load with less corresponding deflection. One has to keep in mind that this comparison does not result in the same bending moment. Since the total bending moment of sandwich elements is composed of parts from facings and sandwich action, a comparison of resulting bending moments is not suitable. From the arising axial forces in the facings, the sandwich moment is calculated. Hence, the cracking behaviour for both loading cases is predicted differently. Additionally, different failure modes may be obtained for different loading cases. For flat panels subjected to three-point bending, a mixed-mode failure of cracking of UHPFRC section and debonding were determined. Additionally, the relative slip of the facings was in the range of a shear failure of the core material. In contrast, for distributed loading debonding was not predicted and the panels failed from cracking of UHPFRC facings and rupture of CFRP reinforcement. For the folded plate sandwich panels without prestressing of the facings, debonding was not observed in either cases. For three-point bending loads, relative slip was in the range of a shear failure of the core material. Under distributed loading, the panel showed excessive cracking of UHPFRC and failed from rupture of the reinforcement.

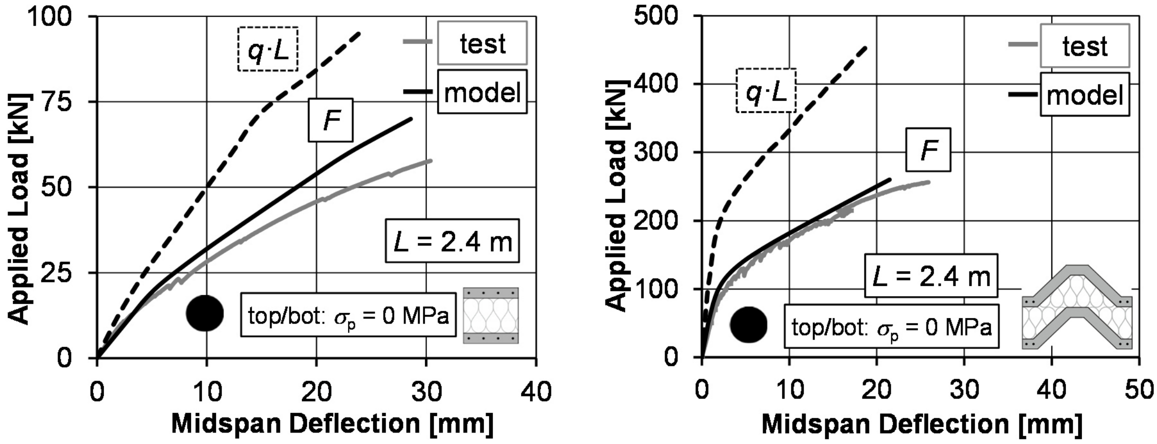

Fig. 7.46 Comparison of load-deflection response from three-point bending and distributed loading for flat (left) and folded plate (right) sandwich panels

In the next step, the length of the panels was doubled to 4.8 m and a distributed load was applied. In Fig. 7.47 the predicted load-deflection responses of flat and folded plate panels is shown. In both cases, the facings were prestressed with four CFRP strands (Ø7.5 mm, σ_p = 675 MPa). To demonstrate the effect of a reduced shear modulus of $G_c/3$, again no application of shear grids was assumed. In this case, the maximum deflection was doubled for both elements. For flat elements, the load-deflection response was determined to be less stiff in the linear-elastic stage, since the flexural rigidity of the facings is relatively low. In contrast, the linear elastic stage was about the same for both shear moduli for folded plate elements, since the facings show a high flexural rigidity. The sandwich panels were predicted to fail from excessive cracking of the UHPFRC facings and rupture of reinforcement independent on the cross-sectional shape and the stiffness of the core material. It has to be mentioned that the bond strength τ_c was not reduced in this study. In section 7.8, further studies have been conducted on this topic.

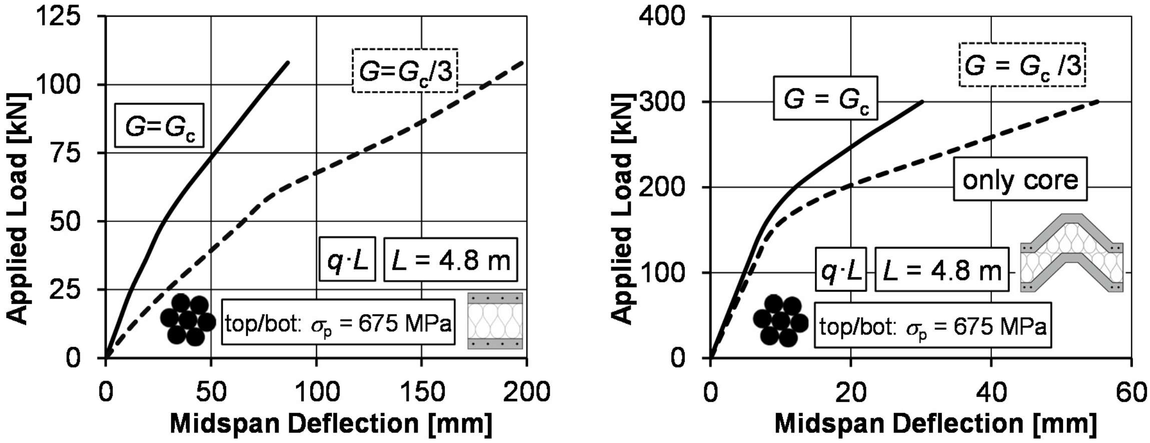

Fig. 7.47 Comparison of load-deflection response from distributed loading for a shear modulus G_c and a decreased shear modulus of $G_c/3$ for flat (left) and folded plate (right) sandwich panels

For long-span roof structures, as they were built in the 1960's and 1970's of the last century, typically, elements with a length of 24 m were applied. For the prediction of the structural performance of the developed folded-plate elements, in Fig. 7.48 (left) the load deflection response for a length of 24 m is depicted. Four strands (Ø7.5 mm) with pre-tensioning of 675 MPa in both facings were assumed. For comparison, the performance of a single facing is shown. The maximum load represents an applied surface load of 2.4 kN/m². As for the short length, the comparison of the maximum loads shows an increase of about 400 % compared to a single facing.

To establish a higher load-bearing capacity, additionally a larger cross-section (cp. Fig. 7.45) was investigated. Again, the strands (Ø7.5 mm) were pre-tensioned to 675 MPa. The number of strands was increased to eight strands for each facing. For a core height h_c of 200 mm, the maximum load was four times higher compared to a single facing. Increasing the core height to 400 mm led to a further increase in maximum load of about 25 %. In both cases, the failure of elements was predicted by excessive cracking of the bottom facings and rupture of the CFRP strands.

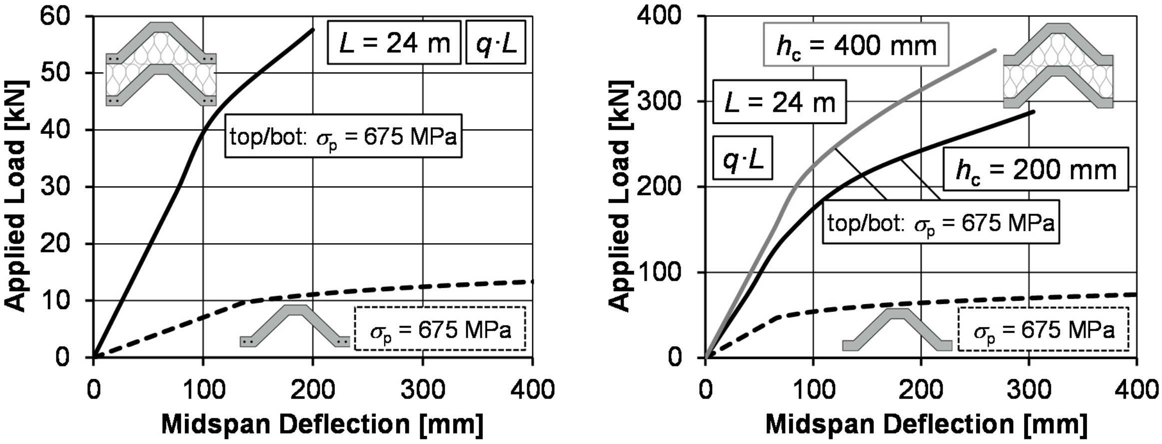

Fig. 7.48 **Load-deflection response from distributed loading of elements with span of 24 m: Cross-section according to section 7.2 (left) and modified cross-section according to Fig. 7.45 (right)**

For the doubly curved elements, the influence of parameter variation was investigated with the numerical model, shown in section 7.3.2. Even though the local material contribution were partly found differing from test results, the overall load-deflection responses were determined in satisfying agreement. In Fig. 7.49 (left), the numerically determined load-deflection responses from four-point loading and distributed loading are compared. The tests results from four-point bending are additionally depicted. As for the flat and folded plate elements, the behaviour was observed to be stiffer and maximum load increased for distributed loading. Again, elements with spans of 24 m were investigated. In Fig. 7.49 (right), the load-deflection response for these elements with a length of 24 m is shown. For this purpose the width and height of the facings of the 24 m elements was determined in dependence on typical elements, which were built in the 1960's and 1970's. The camber in longitudinal direction was set to 300 mm. The thickness of facings was kept constant at 60 mm. The width of the elements was determined to 3,200 mm. Ten rather than six pre-tensioned CFRP strands (σ_P = 1,350 MPa) were applied. For comparison, the performance of a single facing is shown. The maximum load of the sandwich panel was determined to 340 kN, which represents a surface load of about 4.4 kN/m². Compared to the single facing, the load was increased about 230 %. The elements were predicted to fail from excessive cracking of the bottom facing and from rupture of the CFRP strands.

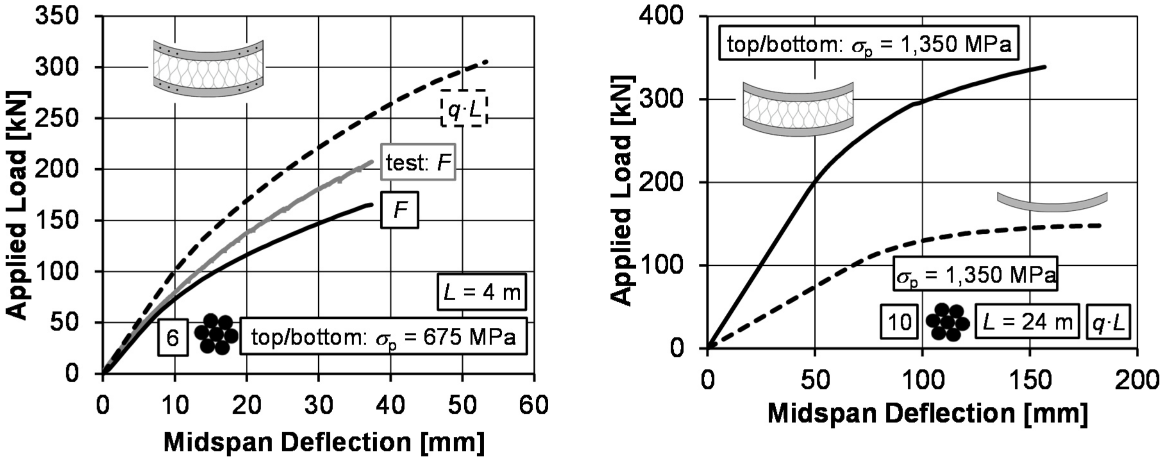

Fig. 7.49 **Comparison of load-deflection response of doubly curved sandwich panels from four-point bending and distributed loading (left) and load-deflection response of elements with 24 m length (right)**

With the case studies it was exemplarily shown that the variation of key parameters has a major influence on the load-carrying capacity of sandwich panels. The variation of shear modulus already confirms the importance of the selection of materials as well as considerations of long-term effects. In the next section, further investigations on this topic were conducted.

7.8 Aspects of Design Approaches

The derived analytical approach and numerical models were shown to be suitable to predict the load-deflection responses of the investigated sandwich panels. Nevertheless, for the approaches, the model uncertainty cannot be predicted at this stage. Additionally, for the design in the ultimate limit state, partial safety factors are used in most common codes (e.g. /DIN04/ or /ACI05/). The material properties and bond strength of the interface layer vary for different production techniques and foam cores. These material characteristics have to be determined by experimental testing for each case. Since the number of tests results, presented in chapter 7.2 and appendices B-D, is limited, no partial safety factors were derived. The long-term behaviour is another key factor for the design. The material strengths, especially of CFRP tendons and core, may reduce significantly over time. For different types of UHPFRC, CFRP and PU different partial safety factors and reduction factors to account for environmental actions or sustained stress can be found in codes and literature. Material testing under environmental actions or sustained load was not conducted in the present study.

Nevertheless, to establish a rough estimation of the reduction in design strength, partial safety factors and reduction factors were summarised from literature. The design values of material properties, which were determined during testing, were derived according to Eurocode 0 /DIN10a/.

For UHPFRC, the design methods according to /AFGC13/ and /DIN04/ were applied. The compressive strength was calculated from mean values f_{cm} and transformed to characteristic strength f_{ck} (COV = 0.1, log-normal distribution). The reduction factor for compression α_{cc} was set to 0.85 and the partial safety factor γ_c to 1.5 /AFGC13/, as for NSC and HPC according to /DIN04/. The characteristic tensile strength f_{ctk} was deduced from mean tensile strength f_{ctm} by assuming a COV of 0.1 and a log-normal distribution /DIN10a/. A K-factor of 1.25, which accounts for global fibre orientation, was applied according to /AFGC13/. The design tensile strength f_{ctd} was calculated by dividing by the K-factor and the partial safety factor γ_c.

For CFRP, the mean tensile strength $f_{u,m}$ was transformed into the characteristic tensile strength $f_{u,k}$ (COV of 0.1, log-normal distribution). The partial safety factor γ_{CFRP} was applied in dependence on /Jus15/ to 1.2. The range for reduction factors α_{CFRP} given in /CEB07/ varies between 0.6 and 1.0 for life-expectancy of a construction. For the following investigations, α_{CFRP} was set to 0.8. One has to bear in mind that α_{CFRP} is a very decisive factor; e.g., the reduction factors and partial safety factors may lead to small allowable design values, may be smaller than jacking stress. Even though, CFRP shows an abrupt rupture at maximum stress rather than pronounced yielding, decreasing the allowable design stress to half or even a third of the mean strength seems not adequate. Hence, further testing has to be conducted for specific materials to ensure an economic and safe design.

For PU, the creep coefficient ϕ_c is given in the range of 2.1 to 7.0 (/Ber78/, /Jus83/), which reduces the shear modulus. As an assumption, the bond strength between core material and UHPFRC facings was reduced in the same way. Since no detailed experimental results of the applied PU exist for long-term loading, the creep coefficient is exemplarily assumed to be 3.0. As partial safety factor γ_{PU} of 1.5 was assumed.

In Table 7.1, the deduced material properties are shown. From mean values, characteristic values were calculated. By applying reduction and partial safety factors, design values were obtained.

Table 7.1: Derived Design Values of Material Parameters

UHPFRC					
f_{ctm}	f_{ctk}	f_{ctd}	f_{cm}	f_{ck}	f_{cd}
5.0	4.0	2.2	150	120	68
CFRP					
$f_{um,strand}$ ($f_{um,bar}$)	$f_{uk,strand}$ ($f_{um,bar}$)	$f_{ud,strand}$ ($f_{um,bar}$)	$f_{um,grid}$	$f_{uk,grid}$	$f_{ud,grid}$
2,650 (3,200)	2,170 (2,625)	1,450 (1,750)	2,400	2,000	1,330
PU					
G_{cm}	G_{ck}	G_{cd}	τ_{cm}	τ_{ck}	τ_{cd}
11.5	9.4	1.6	0.4	0.33	0.1

For a rough estimation, these design values were exemplarily applied to the analytical and numerical models, even though not only maximum allowable loads in the ultimate limit state were determined. Hence, the reduced material properties were applied for the estimation of structural performance, even for the linear-elastic range.

The results for flat sandwich panels (cp. section 7.2.1) with a length of 4.8 m are shown in Fig. 7.50 (left). For comparison, the calculated load-deflection behaviour of sandwich panels with mean values is presented. The elements were subjected to a distributed loading and the resulting bending moments are shown. The investigated CFRP shear grid (cp. Fig. 3.1) was applied four times. This can be done for example, by applying two shear grids with doubled cross-sectional area. The top and bottom layer were prestressed with four CFRP strands each (σ_p = 675 MPa).

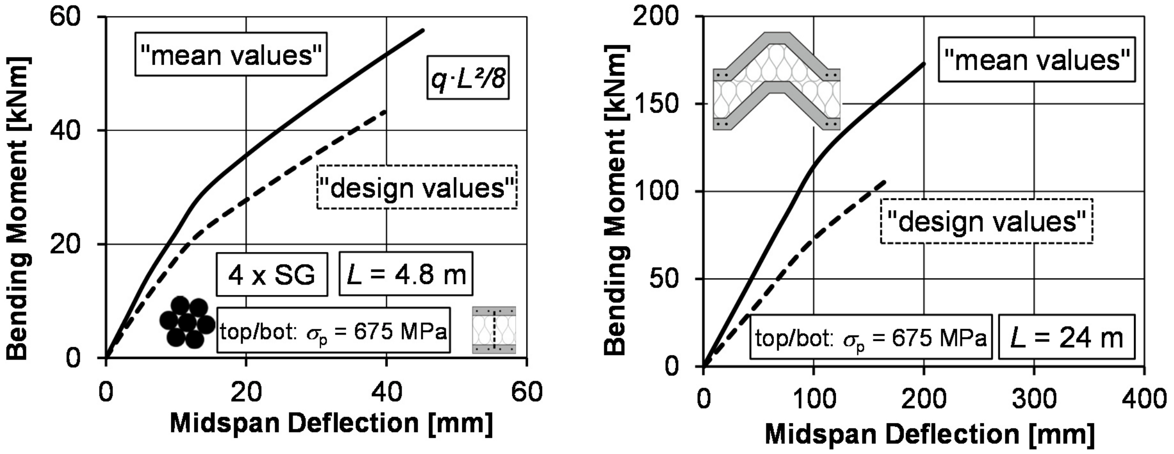

Fig. 7.50 **Comparison of bending moment-deflection response of flat and folded plate sandwich elements for mean and estimated design-values (cross-sections according to section 7.2)**

In the same manner, the results for the investigated folded plate cross-section (cp. section 7.2) are shown in Fig. 7.50 (right) for a length of 24 m. In this case, no shear grid was applied.

The maximum load reduces to about 70 % for flat elements for a length of 4.8 m using estimated design values for the materials compared to mean values. For the long-span folded plate sandwich panel, the load is even reduced to 60 % compared to the maximum load predicted for mean values of material strengths. A load case of self-weight, snow and wind may lead to the following distributed design loads. The self-weight was determined with material densities to about 1.0 kN/m for the flat element and 2.4 kN/m for the folded plate element. The snow load is assumed to 0.5 kN/m² and a constant wind pressure (flat roof) to 0.5 kN/m². The combination of load cases according to /DIN10a/ results in q_{Ed} = 1.7 kN/m for flat elements and q_{Ed} = 4.0 kN/m for folded plate elements. Hence, the resultant bending moment of 4.9 kNm for the short flat element is much below the cracking load. For the folded plate element, the arising bending moment of about 290 kNm exceeds the maximum load, even for the applied mean values of material strengths. For the modified cross-section (cp. Fig. 7.45), a design load of about 9 kN/m was determined, which induces a resulting bending moment of about 650 kNm. To sustain these loads, the cross-section according to Fig. 7.45 was assumed to be prestressed with eight CFRP strands (σ_{p} = 675 MPa). For this purpose, the cross-section of the strands was increased ($A_{\mathrm{p,strand}}$ = 57.8 mm²). In this case, no application of shear grids was assumed. The calculated flexural design capacity is about 850 kNm (Fig. 7.51, left). The application of mean values of material strengths resulted in a maximum bending moment of about 1,100 kNm. The elements were predicted to fail from excessive cracking of the bottom facing and from rupture of the CFRP reinforcement for both cases of assumed material properties. Hence, with this cross-section large spans of 24 m can be achieved. It should be mentioned that the analytical model needs to be validated by experimental testing for increased spans.

For a doubly curved sandwich panel with length of 24 m (cp. Fig. 7.45) the same procedure was conducted, but with aid of numerical modelling. In this case, again no application of shear grids was assumed. The modelling techniques and material input parameters were derived according to chapter 3. In Fig. 7.51 (right), the structural response of an element prestressed with 20 CFRP strands ($A_{\mathrm{p,strand}}$ = 57.8 mm², σ_{p} = 675 MPa) is shown. For comparison, the results are depicted using mean values of material parameters. The maximum bending moment decreases by about 20 %. The linear-elastic stage is only slightly less stiff. Considering the above mentioned loading case of self-weight, wind and snow leads to a distributed design load of q_{Ed} = 17 kN/m. This results in an acting bending moment of M_{Ed} = 1225 kNm. Thus, M_{Ed} is roughly 10 % smaller than the bending moment resistance, even though no shear grid was applied. After reaching the cracking load of the facings in the numerical model, the load could be increased by another 60 % before failure of the panel would occur. As for the folded plate panels, the elements were predicted to fail from excessive cracking of the bottom facing and from rupture of the CFRP reinforcement for both cases of assumed material properties.

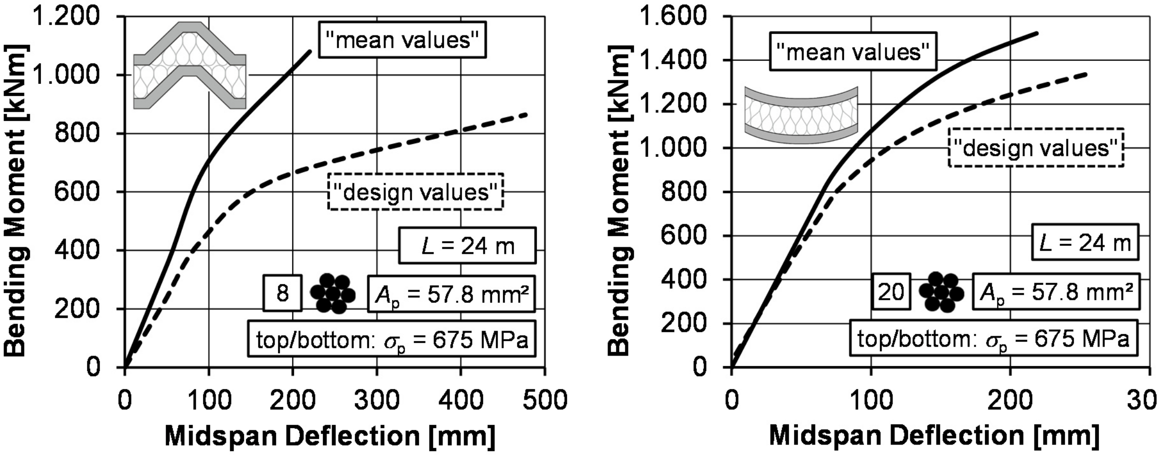

Fig. 7.51 Comparison of bending moment-deflection response of folded plate elements (left) and doubly-curved sandwich element (right) for mean and estimated design-values (modified cross-sections according to Fig. 7.45)

As mentioned before, the examples are aimed as a rough estimation to check the applicability of the material combination for sandwich panels under practical conditions. Since the estimated design values of material strengths were derived from codes and literature, further extensive investigations have to be conducted, to establish a safe design, especially to evaluate the model uncertainty. Nevertheless, the simplified calculations already show the effectiveness of the conceptual designs. Depending on the prestressing and thickness of the UHPFRC layers, even longer spans seem possible.

At the serviceability limit state, mainly a deflection limitation needs to be checked, which involves limitation in stresses and cracks in concrete layers. Usually, sandwich panels with concrete facings should remain un-cracked, since functionality needs to be ensured. In case of façade elements, even small cracks lead to impairment of appearance.

The deflection of sandwich panels with flat, folded plate or curved facings made of UHPFRC can be determined by the proposed analytical model or numerical investigations by application of characteristic material properties. To calculate the cracking load of facings, the relationships of bending moments and axial forces from sandwich theory can be used. For the facings, the cross-sectional area and second moment of area need to be applied. The resulting stresses at top and bottom of each facing can easily be determined from corresponding bending moments and axial forces. The comparison with uniaxial tensile strength delivers the cracking load. The same procedure is applicable for numerical modelling.

7.9 Conclusions

In this chapter, the developed methods, i.e. production techniques, determination of geometric properties and material laws, were combined to establish sandwich panels with UHPFRC facings and pre-tensioned CFRP tendons. Flexural tests on flat, folded plate and doubly curved panels showed a high load-carrying capacity with pronounced indication of failure from cracking of UHPFRC facings until maximum load. Applied numerical models showed a satisfying agreement with the test results of panels under flexural loading. Based on sandwich theory, an analytical approach was derived to determine the load behaviour of sandwich panels under flexural loading, which accounts for bridge-cracking effects from fibre concrete and pre-tensioned CFRP reinforcement. The validation of this model showed a good agreement with the test results. In a case study, influences of geometric and material parameters were shown exemplarily. Additionally, some thoughts about design in ultimate and serviceability limit states have been summarised.

8 Summary and Conclusions

8.1 Summary

High performance materials for application in the building industry have been widely investigated over the last decades. The corrosion resistance and high tensile strength of CFRP reinforcement make applications to thin-walled concrete structures desirable. UHPFRC with high strength and stiffness, already after one day, is especially suitable for pre-tensioned concrete. Sandwich structures are widely applied to modern building envelopes since they feature several characteristics at the same time, such as high load-bearing capacity, light weight or heat and sound insulation.

This thesis describes the development of folded plate and doubly curved sandwich panels made of high performance materials. Step-by-step, different materials and the interaction of materials and components were investigated and production methods were proposed.

For the spatially shaped sandwich panels, the production method was adopted from sandwich panels with metal facings. By foaming in pack of polyurethane, a high bond strength was established and limits in design flexibility were overcome. For the jacking process of CFRP reinforcement, which is sensitive to lateral pressure, an anchorage was proposed with long and reusable aluminium wedges as well as resin to establish a circular cross-section on CFRP strands. With this method, tensile stresses of up to 2,650 MPa - 3,200 MPa could be applied, depending on the type of CFRP. For doubly curved facings, the formwork and prestressing frame were developed, which allow for prestressing and casting of thin UHPFRC elements with CFRP tendons.

For numerical and theoretical models, knowledge of material parameters is essential. One key factor is the determination of the concrete tensile strength. Since the results of direct tensile tests tends to scatter, an approach was proposed to determine the tensile strength and the fracture energy from flexural testing by applying cross-sectional equilibrium of forces. For crack-bridging effects of fibres, an exponential softening approach was assumed. The results were used to perform numerical and theoretical investigations. In the same manner, theoretical moment-curvature relationships of UHPFRC elements with pre-tensioned CFRP tendons were derived. These results were applied to investigations on sandwich panels under flexural loading to account for cracking of the facings.

The bond behaviour of pre-tensioned CFRP reinforcement in UHPFRC is crucial for the load-transfer in structural members. By means of bond tests, bond strength, minimum dimensions of crack-free element and transfer lengths were determined for CFRP bars and strands. For pre-tensioned CFRP bars and strands ($\sigma_p = 1350$ MPa), the bond strength was determined to 25 MPa after one day of concrete hardening. The minimum thickness to avoid cracking was determined to 60 mm (for prestressing after one day of concrete hardening). The transfer lengths were determined to less than 150 mm for both types of CFRP tendons. With the aid of numerical and theoretical models, further investigations on the bond strength and transfer length were conducted. The results of bond tests were applied to determine the minimum dimensions of prestressed UHPFRC facings.

Small-scale tests on sandwich sections were conducted to validate the production method and to derive material properties. Bond strengths between UHPFRC and PU under tensile and shear loading were determined to 0.22 MPa and 0.4 MPa, respectively. Numerical models of small-scale test specimens were validated under tensile and shear loading. Additionally, the resulting stiffness of PU and shear connectors were deduced as a basis for theoretical models for sandwich sections under flexural loading.

The combination of all results was applied to establish prestressed sandwich panels with UHPFRC facings and CFRP reinforcement. First, flat panels were produced to validate the production method. A position of the valley side of UHPFRC led to a reduction in bond strength compared to tests with either board sides in the bond zones. The application of shear grids resulted in an increase of the test load. Folded plate and doubly curved UHPFRC single elements were tested to investigate the structural behaviour depending on different prestressing forces and CFRP types. Based on these results, different reinforcement arrangements were applied to folded plate and doubly curved sandwich panels. The hardened UHPFRC facings were foamed in pack with the same method used for small-scale test specimens. In this case, only smooth surfaces of board sides due to closed formwork were placed in the bond zones, which led to high bond strengths. The results of flexural tests showed a high and repeatable bond strength, even though no shear connectors were applied. The sandwich action without shear connectors resulted in 2.5 to 4 times the maximum load of tested single facings, depending on the prestressing force. Numerical models using non-linear material laws were validated by test results. It was shown that the derivation of materials laws from small-scale tests leads to a satisfying agreement of the load-deflection responses under flexural loading.

Finally, an analytical model based on sandwich theory according to STAMM and WITTE /Sta74/ was proposed to analyse sandwich panels with UHPFRC facings and pre-tensioned CFRP tendons. This model comprises the cracking behaviour of UHPFRC and the residual stresses due to the crack bridging effect of fibres. For this purpose, derived moment-curvature relationships of UHPFRC elements with pre-tensioned CFRP reinforcement and axial force were applied. For flat and folded plate elements, the model showed a very good agreement of the structural behaviour compared to test results. For doubly curved sandwich panels, the analytical model can be applied with simplifications to determine cracking loads. To predict the overall structural performance, non-linear finite element analysis was proposed. With the aid of the analytical and numerical models, the effects of varying parameters on the structural behaviour were exemplarily shown.

It can be concluded, that an efficient method to establish and analyse load-bearing sandwich panels was proposed. The high bond quality achieved by the production process in combination with increased load capacities of spatially shaped UHPFRC layers can lead to long-span roof structures that feature multi-functional properties.

8.2 Future Studies

The derived numerical models and theoretical approaches to determine the structural performance of flat, folded plate and doubly curved sandwich panels provide an appropriate background for further investigations. In consecutive studies, the models and approaches should be validated for different cross-sections of folded plate and doubly curved sandwich panels, different types of reinforcement and prestressing as well as varying concrete strength and types of core material. Additionally, models derived by SHAMS /Sha15b/ in combination with presented findings for UHPFRC should be validated for wall elements.

For the practical use of the developed sandwich panels, questions regarding shear connectors between the concrete facings, time-dependent behaviour of high performance materials as well as heat and fire resistance need to be investigated closely. Based on this, profound investigations need to be conducted, to increase the database for a safe design. For practical design reasons, it seems favourable to provided tables with information about cracking loads, deflections and maximum loads for different standardised cross-sections and spans of elements. To establish these tables, the database needs to be covered by comprehensive experimental studies.

9 Bilbliography

/Aba14/ Abaqus 6.14: documentation. Dassault Systemes Simulia Corporation, 2014.

/ACI04/ ACI 440.4R-04: Prestressing concrete Structures with FRP Tendons. American Concrete Institute (ACI), 2004 (2011).

/ACI05/ ACI 318: Building Code Requirements for Structural Concrete (ACI 318-05) and Commentary (ACI 318R-05). American Concrete Institute (ACI), 2005.

/AFGC13/ Association Française de Génie Civil (AFGC): Ultra High Performance Fibre-Reinforced Concretes - Recommendations, 2013.

/Aic87/ AICHER, S.; ROTH, W.: Ein modifiziertes γ-Verfahren für das mechanische Analogon: dreischichtiger Sandwichverbund - zweiteiliger verschieblicher Verbund. In: Bautechnik, 64 (1), 1987, pp. 21–29.

/Al01/ AL-MAYAH, A.; SOUDKI, K.; PLUMTREE, A.: Experimental and analytical investigation of a stainless steel anchorage for CFRP prestressing tendons. In: PCI Journal, 46 (2), 2001, pp. 88–99.

/All69/ ALLEN, H.G.: Analysis and Design of Structural Sandwich Panels. Oxford Pergamon Press, 1969.

/Bal97/ BALAN, T.; FILIPPOU, F.; POPOV, E.: Constitutive model for 3D cyclic analysis of concrete structures. In: Journal of engineering mechanics, 123 (2), 1997, pp. 143–153.

/Beh96a/ BEHLOUL, M.: Les micro-bétons renforcés de fibres. In: De l'éprouvette aux structures. XIVèmes Journées de l'AUGC, Clermont-Ferrand. Prix Jeunes Chercheurs "René Houpert", 1996.

/Beh96b/ BEHLOUL, M.: Analyse et modélisation du comportement d'un matériau à matrice cimentaire fibrée à ultra hautes perfomances. PhD Thesis, E.N.S. Cachan, France, 1996.

/Ber12/ BERTRAM, G.: Zum Verbund- und Querkrafttragverhalten von Spannbetonträgern aus ultra-hochfestem Beton. Dissertation, RWTH Aachen University, 2012.

/Ber78/ BERNER, K.: Stahl/Polyrethan-Sandwichtragwerke unter Temperatur- und Brandbeanspruchung. Dissertation, Technische Hochschule Darmstadt, 1978.

/Ber98/ BERNER, K.: Praxisgerechte Nachweise zur Trag ‐ und Gebrauchsfähigkeit von Sandwichbauteilen. In: Stahlbau, 67 (12), 1998, pp. 910‐925.

/Bil82/ BILLINGTON, D.P.: Thin shell concrete structures. McGraw-Hill College, 1982.

/Bor04/ BORNEMANN, R.; FABER, S.: UHPC with steel and non-corroding high-strength polymer fibres under static and cyclic loading. In: Ultra High Performance Concrete (UHPC), Proceedings of the International Symposium on Ultra-High Performance Concrete, 2004, pp. 673–681.

/Bül08/ BÜLTE, S.: Zum Verbundverhalten von Spannstahl mit sofortigem Verbund unter Betriebsbeanspruchung. Dissertation, RWTH Aachen University, 2008.

/Bus94/ BUSH, T.; STINE, G..: Flexural behavior of composite precast concrete sandwich panels with continuous truss connectors. In: PCI Journal, 39 (2), 1994, pp. 112–121.

/CAN12/ Design and construction of building components with fibre-reinforced polymers. CAN/CSA S806, 2012.

/CEB07/ CEB-FIP fib Bulletin 40: FRP Reinforcement for RC Structures. Technical Report on the Design and Use of Fibre Reinforced Polymer Reinforcement (FRP) for Reinforced Concrete Structures, 2007.

/CEB12/ CEB-FIP fib Bulletin 65/66: Model Code 2010. Final draft, Volume 1+2, 2012.

/CEB90/ CEB-FIP: Model code for concrete structures. Bulletin D'Information, 1990.

/CEB93/ CEB-FIP fib Bulletin 217: Selected Justification Notes - based on papers originally presented to the colloquium on the final draft CEB-FIP Model Code 90 in Rio de Janeiro, August 1991, 1993.

/Che95/ CHEYREZY, M.; MARET, V.; FROUIN, L.: Microstructural analysis of RPC (reactive powder concrete). In: Cement and concrete research, 25 (7), 1995, pp. 1491–1500.

/CNR07/ National Research Council (CNR): Guide for the Design and Construction of Fiber-Reinforced Concrete Structures. Advisory Committee on Technical Recommendations for Construction. Rome, Italy, 2007.

/DAfStb08/ Deutscher Ausschuss für Stahlbeton (DAfStb): Sachstandsbericht Ultrahochfester Beton, Heft 561, 2008.

/DAfStb10/ Deutscher Ausschuss für Stahlbeton (DAfStb): Richtline Stahlfaserbeton, 2010.

/DAfStb76/ Deutscher Ausschuss für Stahlbeton: Studie zum Trag- und Verformungsverhalten von Stahlbeton, Heft 260, 1976.

/Dav01/ DAVIES, J.M.: Lightweight Sandwich Construction. Blackwell Science Ltd., on behalf of CIB Working Commission W056 Sandwich Panels, 2001.

/DBV01/ Deutscher Beton- und Bautechnik-Verein e.V. (DBV): Merkblatt Stahlfaserbeton, 2001.

/Den98/ DEN UIJL, J.: Bond modelling of prestressing strand. In: Special Publication, 180, 1998, pp. 145–170.

/DIBt80/ Deutsches Institut für Bautechnik (DIBt): Richtlinie für die Prüfung von Spannstählen auf ihre Eignung zur Verankerung durch sofortigen Verbund, 1980.

/DIN00/ DIN EN 206-1: Beton-Teil 1: Festlegung, Eigenschaften, Herstellung und Konformität, 2000.

/DIN04/ DIN EN 1992-1-1: Eurocode 2: Bemessung und Konstruktion von Stahlbeton-und Spannbetontragwerken–Teil 1-1: Allgemeine Bemessungsregeln und Regeln für den Hochbau, 2004.

/DIN05/ DIN EN 196-1: Prüfverfahren für Zement–Teil 1: Bestimmung der Festigkeit; Deutsche Fassung EN 196-1: 2005, 2005.

/DIN09/ DIN EN 12350: Prüfung von Frischbeton-Teil 2: Setzmaß. EN 12350-2: 2009-08, 2009.

/DIN10a/ DIN EN 12350: Prüfung von Frischbeton - Teil 8: Selbstverdichtender Beton - Setzfließmaß. EN 12350-8: 2009-08, 2010.

/DIN10b/ DIN EN 1990: Grundlagen der Tragwerksplanung mit DIN EN 1990/NA: 2010-12, 2010.

/DIN13a/ DIN EN 826: Thermal insulating products for building applications– determination of compression behaviour. German version EN, 2013.

/DIN13b/ DIN EN 14509: Self-supporting double skin metal faced insulating panels - Factory made products – Specifications. German version EN 14509:2013, 2013.

/DIN13c/ DIN EN 12090: Thermal insulating products for building applications-determination of shear behaviour. German version EN 12090, 2013.

/DIN13d/ DIN EN 1607: Thermal insulating products for building applications– determination of tensile strength perpendicular to faces. German version EN, 2013.

/Emp95/ EMPELMANN, M.: Zum nichtlinearen Trag- und Verformungsverhalten von Stabtragwerken aus Konstruktionsbeton unter besonderer Berücksichtigung von Betriebsbeanspruchungen. Dissertation, RWTH Aachen University, 1995.

/Fai49/ FAIRBAIRN, W.: An account of the construction of the Britannia and Conway tubular bridges. London, Richard and John E. Taylor, 1849.

/Fee96/ FEENSTRA, P.; BORST, R.: A composite plasticity model for concrete. In: International Journal of solids and structures, 33 (5), 1996, pp. 707–730.

/Feh05/ FEHLING, E.; SCHMIDT, M.; TEICHMANN, T.; BUNJE, K.; BORNEMANN, R.; MIDDENDORF, B.: Entwicklung, Dauerhaftigkeit und Berechnung ultra-hochfester Betone (UHPC) [Development, durability and design of ultra-high strength concrete (UHPC)]. Research Report, University of Kassel, Kassel, Germany, 2005.

/FHWA06a/ Federal Highway Administration: Material Property Characterization of Ultra-High Performance Concrete. FHWA-HRT-06-103. U.S. Department of Transportation, 2006.

/FHWA06b/ Federal Highway Administration: Structural Behavior of Ultra-High Performance Concrete Prestressed I-Girders. FHWA-HRT-06-115. U.S. Department of Transportation, 2006.

/Foe89/ FOERSTER, H.; RIZKALLA, S.; HEUVEL, J.: Behavior and Design of Shear Connections for Loadbearing Wall Panels. In: PCI Journal, 34 (1), 1989, pp. 102–119.

/Fos01/ FOSTER, S.: On behavior of high-strength concrete columns: cover spalling, steel fibers, and ductility. In: ACI Structural Journal, 98 (4), 2001, pp. 583–589.

/Han14/ HAN, S.-J.; LEE, D.; KIM, K.; SEO, S.-Y.: Degradation of flexural strength in reinforced concrete members caused by steel corrosion. In: Construction and Building Materials, 54, 2014, pp. 572–583.

/Han16/ HAN, S.; LEE, D.; CHO, S.; KA, S.: Estimation of transfer lengths in precast pretensioned concrete members based on a modified thick‐walled cylinder model. In: Structural Concrete, 17 (1), 2016, pp. 52‐62.

/Heg10/ HEGGER, J.; BERTRAM, G.: Verbundverhalten von vorgespannten Litzen in UHPC. Teil 1: Versuche zur Verbundfestigkeit und zur Übertragungslänge. In: Beton-und Stahlbetonbau, 105 (6), 2010, pp. 379–389.

/Hel16/ HELBIG, T.; UNTERER, K.; KULAS, C.; REMPEL, S.: Fuß ‐ und Radwegbrücke aus Carbonbeton in Albstadt ‐ Ebingen. In: Beton ‐ und Stahlbetonbau, 111 (10), 2016, pp. 676‐685.

/Her05/ HERRMANN, A.; ZAHLEN, P.; ZUARDY, I.: Sandwich structures technology in commercial aviation. In: Thomson, O. T; Bozhevolnaya, E; Lyckegaard, A. (Eds.): Sandwich structures 7: Advancing with sandwich structures and materials, Aalborg, Denmark, 2005.

/Hil76/ HILLERBORG, A.; MODÉER, M.; PETERSSON, P.-E.: Analysis of crack formation and crack growth in concrete by means of fracture mechanics and finite elements. In: Cement and concrete research, 6 (6), 1976, pp. 773–781.

/Hof50/ HOFF, N.: Bending and buckling of rectangular sandwich plates, 1950.

/Hol65/ HOLMBERG, A.; PLEM, E.: Behaviour of load-bearing sandwich-type structures. Byggforskningen, 1965.

/Hon16/ HONARVAR, E.; SRITHARAN, S.; ROUSE, J.M.; AALETI, S.: Bridge decks with precast UHPC waffle panels: a field evaluation and design optimization. In: Journal of Bridge Engineering, 21 (1), 2016, pp. 1-13.

/Hor10/ HORSTMANN, M.: Zum Tragverhalten von Sandwichkonstruktionen aus textilbewehrtem Beton. Dissertation, RWTH Aachen University, 2010.

/Jia08/ JIANG, Z.; ZHANG, H.; ZHANG, Z.; MURAYAMA, H.: Improved bonding between PAN-based carbon fibers and fullerene-modified epoxy matrix. In: Composites Part A: Applied Science and Manufacturing, 39 (11), 2008, pp. 1762–1767.

/JSCE97/ Japan Society of Civil Engineers: Recommendations for Design and Construction of Concrete Structures using Continuous Fiber Reinforcing Materials, 1997.

/Jun06/ JUNGWIRTH, J.: Zum Zugtragverhalten von zugbeanspruchten Bauteilen aus Ultra-Hochleistungs-Faserbeton. Dissertation, École polytechnique fédérale de Lusanne (EPFL), 2006.

/Jus15/ JUST, M.: Sicherheitskonzept für Textilbeton. In: Beton ‐ und Stahlbetonbau, 110 (S1), 2015, pp. 42‐46.

/Jus83/ JUST, M.: Ergebnisse experimenteller Untersuchungen zum Langzeitverhalten von PUR-Hartschaumstoff-Stützkernbauteilen und Schlussfolgerungen für die Anwendung. IfL-Mitteilung 22. Mitteilungen aus dem Institut für Leichtbau und ökonomische Verwendung von Werkstoffen, Dresden, 1983.

/Kue15/ KUERES, D.; STARK, A.; HERBRAND, M.; CLASSEN, M.: Numerische Abbildung von Beton mit einem plastischen Schädigungsmodell - Grundlegende Untersuchungen zu Normalbeton und UHPC. In: Bauingenieur, 90, 2015, pp. 252–264.

/Küh68/ KÜHN, E.; RIETHMÜLLER, R.: Entwicklung und Erprobung eines vorgespannten Faltwerkträgers als großflächiges Dachelement. In: Bauplanung - Bautechnik, 22 (2), 1968, pp. 73–77.

/Lal88/ LALDJI, S.; YOUNG, A.: Bond between steel strand and cement grout in ground anchorages. In: Magazine of concrete research, 40 (143), 1988, pp. 90–98.

/Lau14/ LAUFS, W.; DESARZENS, P.: Ductal - Fassade Louis Vuitton in Aventura/Florida. In: Bautechnik, 91 (3), 2014, pp. 186-192.

/Lee13/ LEE, C.-D.; KIM, K.-B.; CHOI, S.: Application of ultra-high performance concrete to pedestrian cable-stayed bridges. In: Journal of Engineering Science and Technology, 8 (3), 2013, pp. 296–305.

/Lee98/ LEE, J.; FENVES, G.: Plastic-damage model for cyclic loading of concrete structures. In: Journal of engineering mechanics, 124 (8), 1998, pp. 892–900.

/Leu08/ LEUTBECHER, T.: Rissbildung und Zugtragverhalten von mit Stabstahl und Fasern bewehrtem ultrahochfesten Beton (UHPC). Dissertation, Universität Kassel, 2008.

/Leu12/ LEUTBECHER, T.; FEHLING, E.: Tensile Behavior of Ultra-High-Performance Concrete Reinforced with Reinforcing Bars and Fibers: Minimizing Fiber Content. In: ACI Structural Journal, 109 (2), 2012, pp. 253–264.

/Lin96/ LIN Y.Z.: Tragverhalten von Stahlfaserbeton. Dissertation, Universität Karlsruhe, 1996.

/Lu00/ LU, Z.; BOOTHBY, T.; BAKIS, C.; NANNI, A.: Transfer and development lengths of FRP prestressing tendons. In: PCI Journal, 45 (2), 2000, pp. 84–95.

/Lub89/ LUBLINER, J.; OLIVER, J.; OLLER, S.; ONATE, E.: A plastic-damage model for concrete. In: International Journal of solids and structures, 25 (3), 1989, pp. 299–326.

/Ma09/ MA, J.: Faserfreier Ultrahochfester Beton. Dissertation. Universität Leipzig, 2009.

/Mah99/ MAHMOUD, Z.; RIZKALLA, S.; ZAGHLOUL, E.-E.: Transfer and development lengths of carbon fiber reinforced polymers prestressing reinforcement. In: ACI Structural Journal, 96, 1999, pp. 594–602.

/Maj03/ MAJEWSKI, S.: The mechanics of structural concrete in terms of elasto-plasticity. In: Wydawnictwo Politechniki Śląskiej, Gliwice, 2003.

/Mar06/ MARKOVIC, I.: High-Performance Hybrid-Fibre Concrete - Development and Utilisation, Dissertation, Delft University of Technology, 2006.

/Mik70/ MIKKOLA, M.; SCHNOBRICH, W.: Material behavior characteristics for reinforced concrete shells stressed beyond the elastic range. University of Illinois Engineering Experiment Station. College of Engineering. University of Illinois at Urbana-Champaign, 1970.

/Min51/ MINDLIN, R.: Influence of rotary inertia and shear on flexural motions of isotropic elastic plates. In: Journal of Applied Mechanics, Transactions of the ASME, 18, 1951, pp. 31-38.

/Möh56/ MÖHLER, K.: Über das Tragverhalten von Biegeträgern und Druckstäben mit zusammengesetzten Querschnitten und nachgiebigen Verbindungsmitteln. Dissertation, Universität Karlsruhe, 1956.

/Mül15/ MÜLLER, F.; KOHLMEYER, C.; SCHNELL, J.: Sandwichelemente mit Deckschichten aus Hochleistungsbeton und einem Kern aus extrudiertem Polystyrol. In: Beton ‐ und Stahlbetonbau, 110 (12), 2015, pp. 799‐810.

/Nan92/ NANNI, A.; TANIGAKI, M.; HASUO, K.: Bond anchorage of pretensioned FRP tendon at force release. In: Journal of Structural Engineering, 118 (10), 1992, pp. 2837–2854.

/Nan96/ NANNI, A.; BAKIS, C.; O'NEIL, E.; DIXON, T.: Performance of FRP tendon-anchor systems for prestressed concrete structures. In: PCI Journal, 41 (1), 1996, pp. 34–43.

/Nit01/ NITSCH, A.: Spannbetonfertigteile mit teilweiser Vorspannung aus hochfestem Beton. Dissertation, RWTH Aachen University, 2001.

/Noo96/ NOOR, A.; BURTON, W.; BERT, C.: Computational models for sandwich panels and shells. In: Applied Mechanics Reviews, 49, 1996, pp. 155-199.

/Oh06/ OH, B.; SUNG KIM, E.; CHEOL CHOI, Y.: Theoretical analysis of transfer lengths in pretensioned prestressed concrete members. In: Journal of engineering mechanics, 132 (10), 2006, pp. 1057–1066.

/Pah11/ PAHN, M.: Beitrag zur Ermittlung von Schnitt- und Verformungsgrößen bei mehrschichtigen Stahlbetonwandtafeln mit Verbindungsmitteln aus glasfaserverstärktem Kunststoff. Dissertation, University of Technology Kaiserslautern, 2011.

/Pes03/ PESSIKI, S.; MLYNARCZYK, A.: Experimental evaluation of the composite behavior of precast concrete sandwich wall panels. In: PCI Journal, 48 (2), 2003, pp. 54–71.

/Pfu07/ PFUNDSTEIN, M.; GELLERT, R.; RODOLPHI, A.; SPITZNER, M.H.; SPRENGARD, C.; ALBRECHT, W.: Dämmstoffe: Grundlagen, Materialien, Anwendungen. Institut für internationale Architekturdokumentation GmbH & Co. KG, München, 2007.

/Pfy03/ PFYL, T.: Tragverhalten von stahlfaserbeton. Disseration, ETH Zürich, 2003.

/Pla66/ PLANTEMA, F.J.: Sandwich construction. Wiley, New York, 1966.

/Pol93/ POLAK, M.; VECCHIO, F.: Nonlinear analysis of reinforced-concrete shells. In: Journal of Structural Engineering, 119 (12), 1993, pp. 3439–3462.

/Rei45/ REISSNER, E.: The effect of transverse shear deformation on the bending of elastic plates. In: Journal of Applied Mechanics, Transaction of the ASME, 12, 1945, pp. A69-A77.

/Ric95/ RICHARD, P.; CHEYREZY, M.: Composition of reactive powder concretes. In: Cement and concrete research, 25 (7), 1995, pp. 1501–1511.

/RILEM01/ International Union of Testing and Research Laboratories for Materials and Structures (RILEM): TC 162-TDF: Test and design methods for steel fibre reinforced concrete. Recommenadations. Uni-axial tension test for steel fibre reinforced concrete. In: Materials and Structures, Vol. 34, Rilem Publications, 34, 2001, pp. 3–6.

/RILEM02/ International Union of Testing and Research Laboratories for Materials and Structures (RILEM): TC 162-TDF: Test and design methods for steel fibre reinforced concrete. Bending test. Final Recommendations. In: Materials and Structures, Rilem Publications, 35, 2002, pp. 579–582.

/RILEM73/ International Union of Testing and Research Laboratories for Materials and Structures (RILEM): RC 6 TC9 ‑ RC: Bond test for reinforcement steel. 2. Pull-out test, 1973 (2nd edition 1983).

/Riz09/ RIZKALLA, S.; HASSAN, T.; LUCIER, G.: FRP shear transfer mechanism for precast, prestressed concrete sandwich load-bearing panels. In: ACI Special Publication 31, 265, 2009, pp. 603–625.

/Riz12/ RIZKALLA, S.; LUCIER, G.; DAWOOD, M.: Innovative use of FRP for the precast concrete industry. In: Advances in Structural Engineering, 15 (4), 2012, pp. 565–574.

/Rüh70/ RÜHLE, H.; KÜHN, E.; WEIßBACH, K.; ZEIDLER, D.: Räumliche Dachtragwerke: Konstruktion und Ausführung. Band 1: Beton, Holz, Keramik. Verlagsgesellschaft Rudolf Müller, 1970.

/Sal94/ SALMON, D.; TADROS, M.; CULP, T.: A new structurally and thermally efficient precast sandwich panel system. In: PCI Journal, 39 (4), 1994, pp. 90–101.

/Sal97/ SALMON, D.; EINEA, A.; TADROS, M.; CULP, T.: Full scale testing of precast concrete sandwich panels. In: ACI Structural Journal, 94, 1997, pp. 239–247.

/Sar71/ SARGIN, M.: Stress-strain relationships for concrete and the analysis of structural concrete sections, 4Solid Mechanics Division, University of Waterloo, 1971.

/Sch08/ SCHYDT, J.; HEROLD, G.; MÜLLER, H.S.: Long term behavior of ultra high performance concrete under the attack of chlorides and aggressive waters. In: Proceedings of the 2nd international symposium on ultra high performance concrete, 2008, pp. 231–238.

/See97/ SEEBER, K.; ANDREWS JR, R.; JACQUES, F.; BATY, J., et al.: State-of-the-art of precast/prestressed sandwich wall panels. PCI Committee Report, 42 (2), 1997, pp. 92-134.

/Sha13/ SHAMS, A.; STARK, A.: Untersuchungen zum Verbundverhalten von Sandwichelementen mit Betondeckschichten und geschäumten Polyurethan-Kernschichten. In: Bauingenieur, 10, 2013, pp. 412–419.

/Sha14/ SHAMS, A.; HORSTMANN, M.; HEGGER, J.: Experimental investigations on textile-reinforced concrete (TRC) sandwich sections. In: Composite Structures, 118, 2014, pp. 643–653.

/Sha15a/ SHAMS, A.; STARK, A.; HOOGEN, F.; HEGGER, J., et al.: Innovative sandwich structures made of high performance concrete and foamed polyurethane. In: Composite Structures, 121, 2015, pp. 271–279.

/Sha15b/ SHAMS, A.: A Noval Approach for the Production and Design of Load-carrying Sandwich Panels with Reinforced Concrete Facings. Dissertation, RWTH Aachen University, 2015.

/Sou97/ SOUDKI, K.; GREEN, M.; CLAPP, F.: Transfer length of carbon fiber rods in precast pretensioned concrete beams. In: PCI Journal, 42 (5), 1997, pp. 78–87.

/Spe07/ SPECK, K.: Beton unter mehraxialer Beanspruchung - Ein Materialgesetz für Hochleistungsbetone unter Kurzzeitbelastung. Dissertation, TU Dresden, 2007.

/SPP05/ SPP 1182: Schwerpunktprogramm Nachhaltig Bauen mit UHPC, Deutsche Forschungsgemeinschaft, Beginn 2005. http://www.spp1182.de.

/Sta13/ STARK, A.; HEGGER, J.: Verbundverhalten von CFK-Spannbewehrungen in UHPFRC. In: Beton- und Stahlbetonbau, 108 (10), 2013, pp. 701–710.

/Sta16a/ STARK, A.; CLASSEN, M.: Prestressed Sandwich Beams with UHPC Layers. In: First International Interactive Symposium on UHPC, 18.-20.07.2016, Des Moines, Iowa, USA, 2016.

/Sta16b/ STARK, A.; KUERES, D.; HEGGER, J.: Sandwichelemente mit UHPC-Deckschichten und geschäumten PUR-Kernschichten. In: Beton- und Stahlbetonbau, 2016.

/Sta16c/ STARK, A.; PERSE, S.; HEGGER, J.: Test on the Transfer Length of CFRP Tendons in UHPC. In: Fehling, E; Middendorf, B; Thiemicke, J. (Eds.): Ultra-High Performance Concrete and High Performance Construction Materials: Proceedings of HiPerMat 2016, 4th International Symposium on Ultra-High Performance Concrete and High Performance Materials Kassel, March 9-11, 2016.

/Sta74/ STAMM, K.; WITTE, H.: Sandwichkonstruktionen - Berechnung, Fertigung, Ausführung. Springer-Verlag, 1974.

/Stü47/ STÜSSI, F.: Zusammengesetzte Vollwandträger. In: International Association for Bridge and Structural Engineering (IABSE), 8, 1947, pp. 249–269.

/Tep79/ TEPFERS, R.: Cracking of concrete cover along anchored deformed reinforcing bars. In: Magazine of concrete research, 31 (106), 1979, pp. 3–12.

/Ter13/ TERRASI, G.: Prefabricated thin-walled structural elements made from high performance concrete prestressed with CFRP wires. In: Journal of Materials Science Research, 2 (1), 2013, pp. 1-14.

/Tim51/ TIMOSHENKO, S.; GOODIER, J.N.: Theory of Elasticity. McGraw-Hill, New York, 1951.

/Voo03/ VOO, J.Y.L.; FOSTER, S.J.: Variable Engagement Model for Fibre Reinforced Concrete in Tension. Univ. Report No. R-420, University of New South Wales, Sydney, Australia, 2003.

/Voo14/ VOO, J.Y.L.; FOSTER, S.J.; VOO, C.C.: Ultrahigh-performance concrete segmental bridge technology: Toward sustainable bridge construction. In: Journal of Bridge Engineering, 20 (8), 2014, pp. B5014001_1-12.

/Wan01/ WANG, T.; HSU, T.: Nonlinear finite element analysis of concrete structures using new constitutive models. In: Computers & structures, 79 (32), 2001, pp. 2781–2791.

/Wan04/ WANG, X.; LIU, X.: Modeling bond strength of corroded reinforcement without stirrups. In: Cement and concrete research, 34 (8), 2004, pp. 1331–1339.

/Zan13/ ZANI, G.: High Performance Cementitious Composites for sustainable roofing panels. PhD thesis. Politecnico di Milano, 2013.

/Zen95/ ZENKERT, D.: An introduction to sandwich construction. Engineering materials advisory services, 1995.

Appendix

A Bond Behaviour of CFRP Reinforcement in UHPFRC

A.1 Pull-Out Tests

Table A.1: Parameter variation of pull-out tests

Test No. [-]	CFRP type [-]	Ø [mm]	bond length [mm]	Jacking stress [MPa]	c/d_p [-]	age [d]
PO_C-1	strand	7.5	15.0	1350	9.5	1
PO_C-2	bar	5.0	10.0	1350	14.5	1
PO_C-3	strand	7.5	15.0	1350	9.5	3
PO_C-4	bar	5.0	10.0	1350	2.5	1
PO_C-5	strand	7.5	15.0	1350	2.5	1
PO_C-6	strand	7.5	15.0	1750	2.5	1
PO_S-1	strand (steel)	9.3	18.6	1350	7.6	1

Table A.2: Concrete properties of pull-out tests

Test No. [-]	$f_{cm,cyl}$ [MPa]	$f_{cm,cube}$ [MPa]	E_{cm} [MPa]	$f_{ct,flex}$ [MPa]
PO_C-1	54.0	71.8	30,500	7.3
PO_C-2	57.8	70.0	30,000	6.2
PO_C-3	109.0	122.0	39,000	7.6
PO_C-4	55.2	67.8	30,700	6.0
PO_C-5	40.0	45.0	22,300	3.0
PO_C-6	---	61.0	28,200	5.3
PO_S-1	51.8	67.2	29,100	6.0

PO-C-1: CFRP strand Ø7.5 mm, σ_p = 1350 MPa, c/d_p = 9.5, 1d

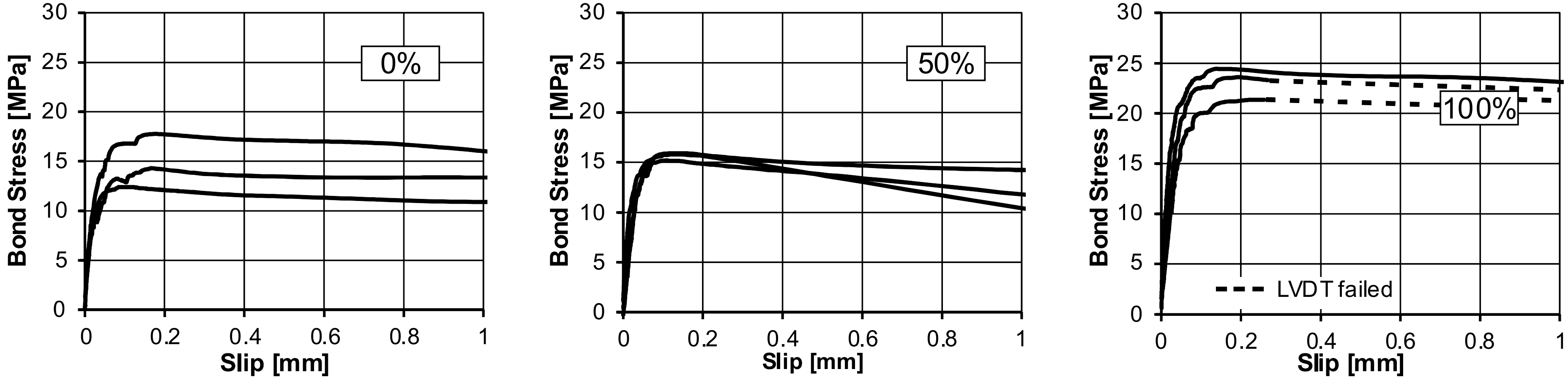

PO-C-2: CFRP bar Ø5.0 mm, σ_p = 1350 MPa, c/d_p = 14.5, 1d

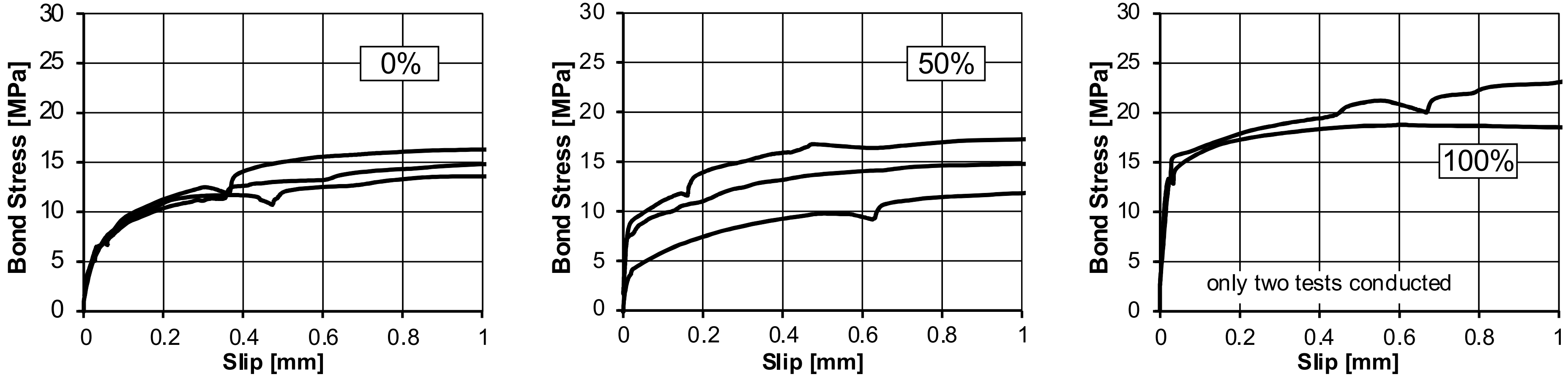

PO-C-3: CFRP strand Ø7.5 mm, $\sigma_p = 1350$ MPa, $c/d_p = 9.5$, 3d

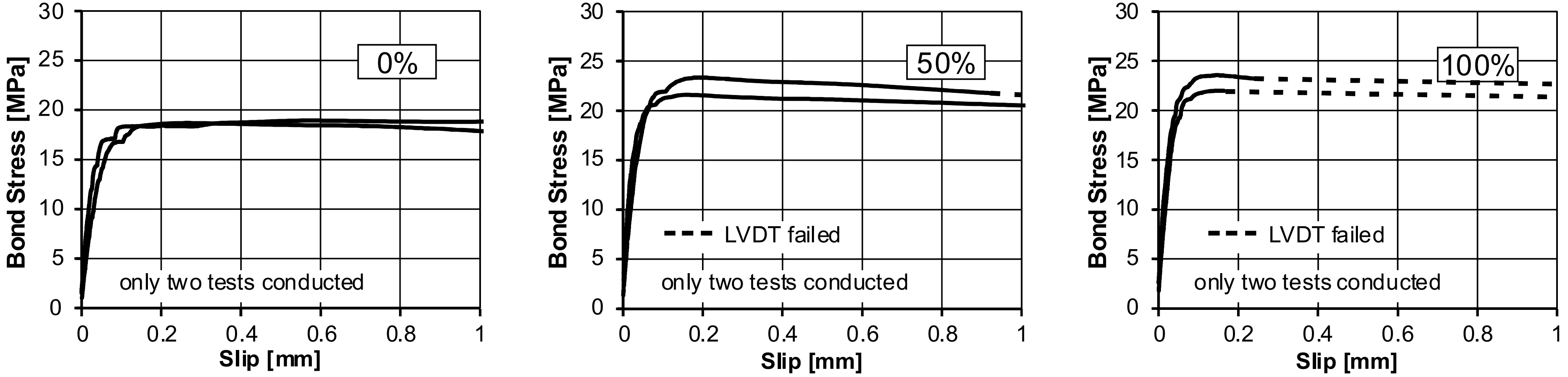

PO-C-4: CFRP bar Ø5.0 mm, $\sigma_p = 1350$ MPa, $c/d_p = 2.5$, 1d

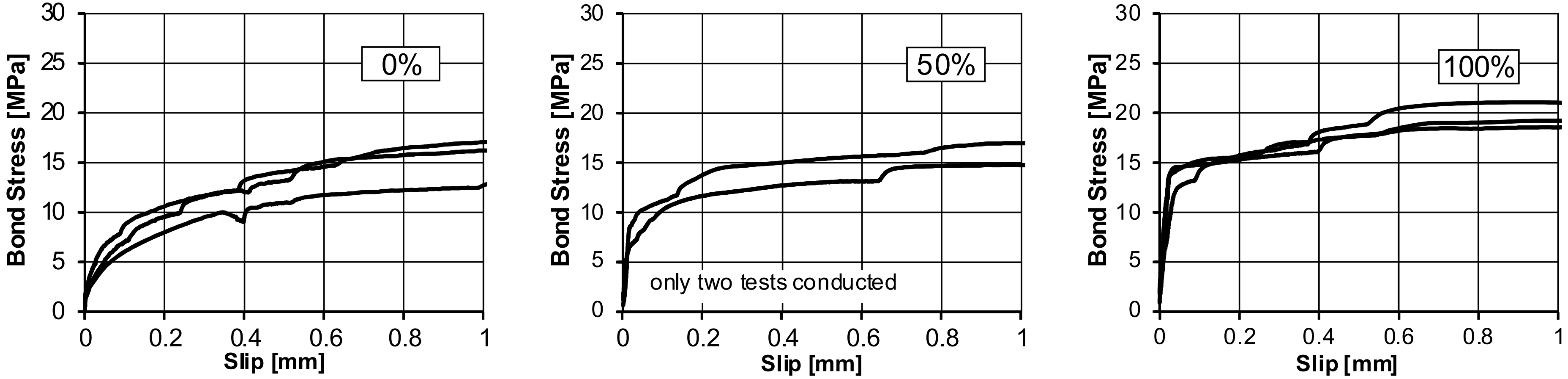

PO-C-5: CFRP strand Ø7.5 mm, σ_p = 1350 MPa, *c*/*d*$_p$ = 2.5, 1d

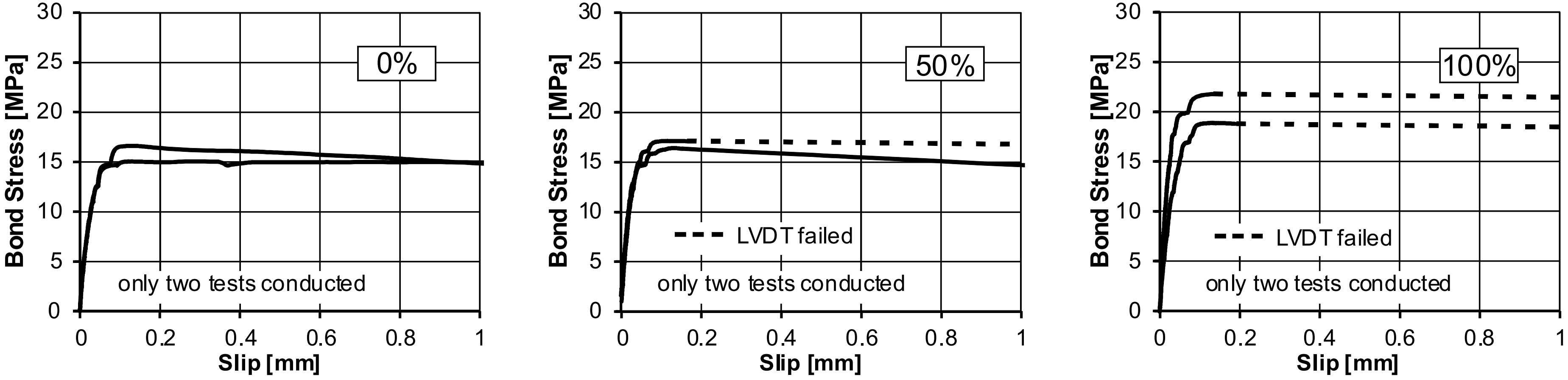

PO-C-6: CFRP strand Ø7.5 mm, σ_p = 1750 MPa, *c*/*d*$_p$ = 9.5, 1d

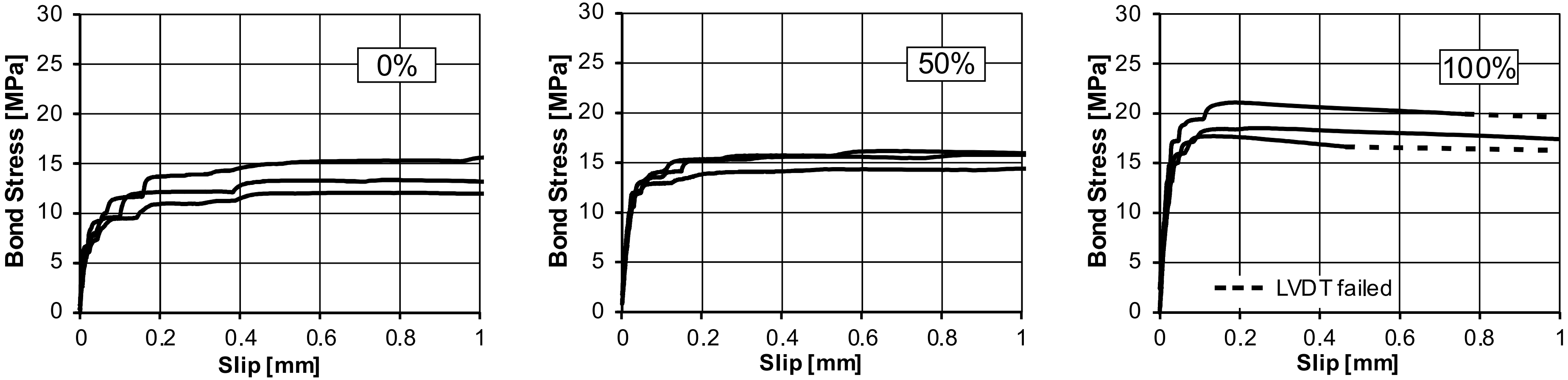

PO-S-1: steel strand Ø9.3 mm, σ_p = 1350 MPa, c/d_p = 7.6, 1d

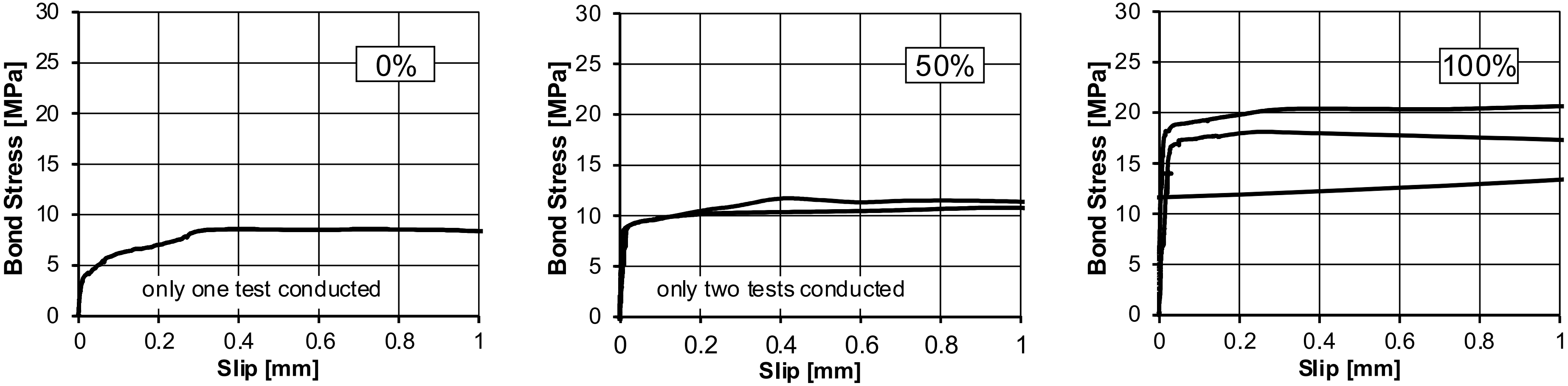

A.2 Tests on the Transfer Length

Table A.3: Parameter variation of tests on the transfer length

Test No. [-]	CFRP type [-]	Ø [mm]	Jacking stress [MPa]	c/d_p [-]	s/d_p [-]	b [mm]	h [mm]
TL-1	strand	7.5	1350	3.0	8.0	120.0	52.5
TL-2	strand	7.5	1350	2.0	8.0	105.0	37.5
TL-3	strand	7.5	1350	2.5	8.0	112.5	45.0
TL-4	strand	7.5	1350	2.5	5.0	90.0	45.0
TL-5	bar	5.0	1350	5.0	12.5	122.5	55.0
TL-6	bar	5.0	1350	4.0	12.5	112.5	45.0
TL-7	bar	5.0	1350	4.0	8.0	90.0	45.0
TL-8	bar	5.0	1350	3.0	12.5	102.5	35.0
TL-9	bar	5.0	1350	3.0	8.0	80.0	35.0
TL-10	strand	7.5	1350	2.8	8.0	117.5	50.0
TL-11	strand	7.5	1350	2.8	5.0	95.0	50.0
TL-12	strand	7.5	1750	3.5	8.0	127.5	60.0
TL-13	strand	7.5	1750	4.0	8.0	135.0	67.5
TL-14	strand	7.5	1350	3.5	5.0	105.0	60.0
TL-15	strand	7.5	1350	3.5	8.0	127.5	60.0
TL-16	strand	7.5	675	3.5	5.0	105.0	60.0
TL-17	strand	7.5	675	2.0	8.0	105.0	37.5
TL-18	strand	7.5	675	2.0	5.0	82.5	37.5
TL-19	strand	7.5	675	2.5	8.0	112.5	45.0

Table A.4: Concrete properties of tests on the transfer length

Test No. [-]	$f_{cm,cyl}$ [MPa]	$f_{cm,cube}$ [MPa]	E_{cm} [MPa]	$f_{ct,flex}$ [MPa]
TL-1/TL-2	65.9	76.6	32,500	9.0
TL-3/TL-4	61.0	68.7	30,500	5.7
TL-5/TL-6	64.2	68.0	31,200	6.2
TL-7	43.4	60.1	28,100	6.7
TL-8/TL-9	48.5	66.0	30,100	4.4
TL-10/TL-11	51.1	63.1	29,700	6.7
TL-12/TL-13	48.3	54.9	27,700	7.8
TL-14/TL-15	60.4	73.8	32,900	7.0
TL-16/TL-17	79.2	80.0	36,800	5.2
TL-18/TL-19	65.2	84.1	36,200	5.6

Concrete compression strains:

TL-1

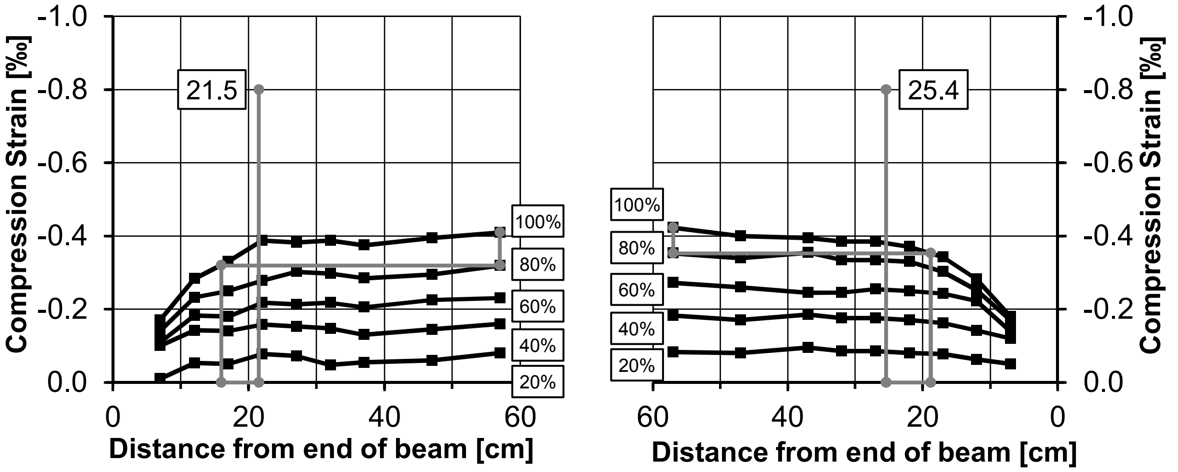

TL-2

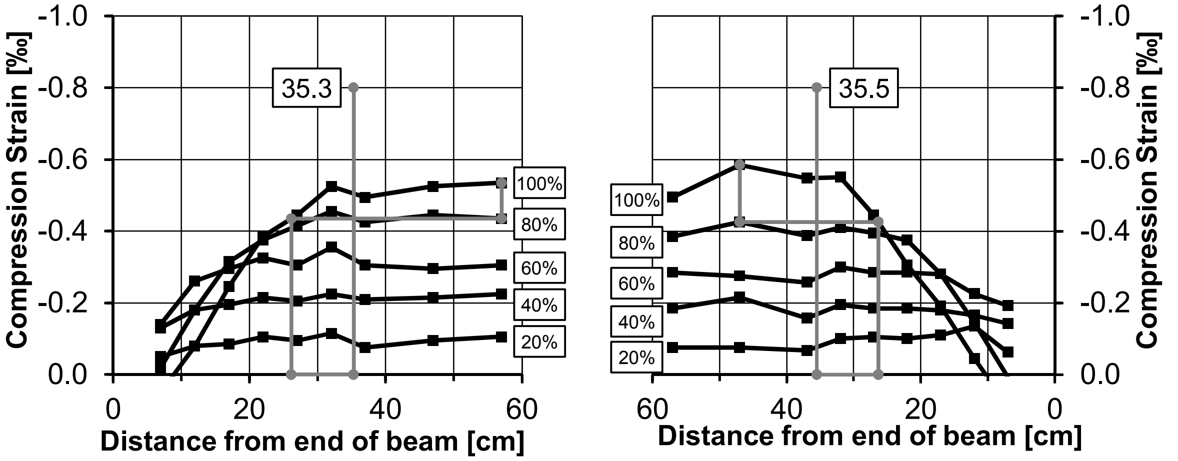

TL-3

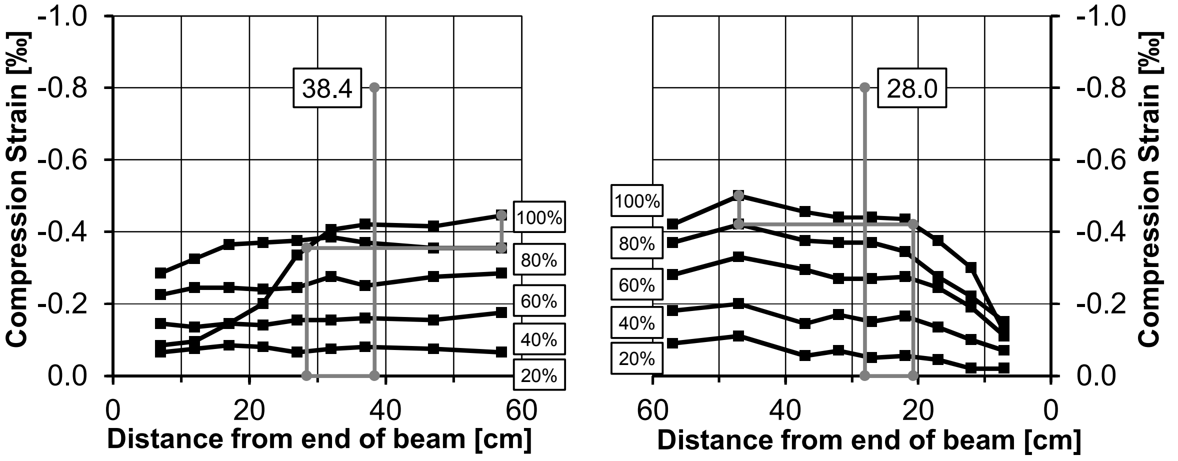

TL-4

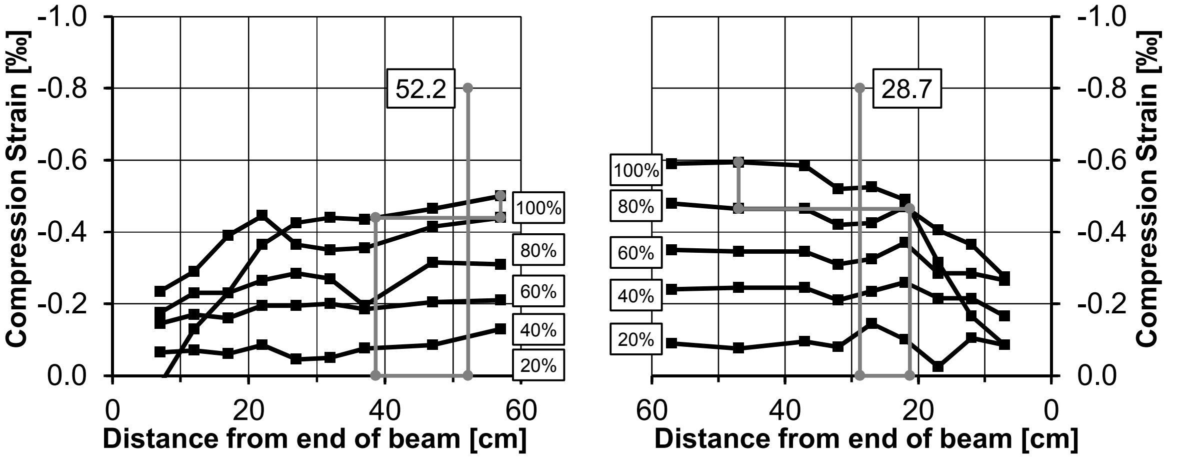
Compression Strain [‰]
-1.0
-0.8
-0.6
-0.4
-0.2
0.0
52.2
28.7
100%
80%
60%
40%
20%
0
20
40
60
Distance from end of beam [cm]

TL-5

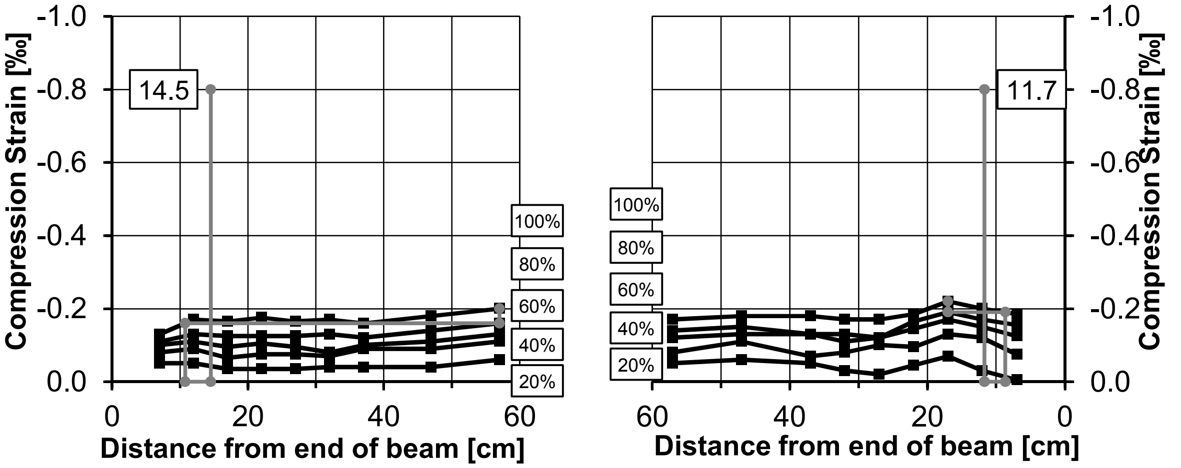
Compression Strain [‰]
-1.0
-0.8
-0.6
-0.4
-0.2
0.0
14.5
11.7
100%
80%
60%
40%
20%
0
20
40
60
Distance from end of beam [cm]

TL-6

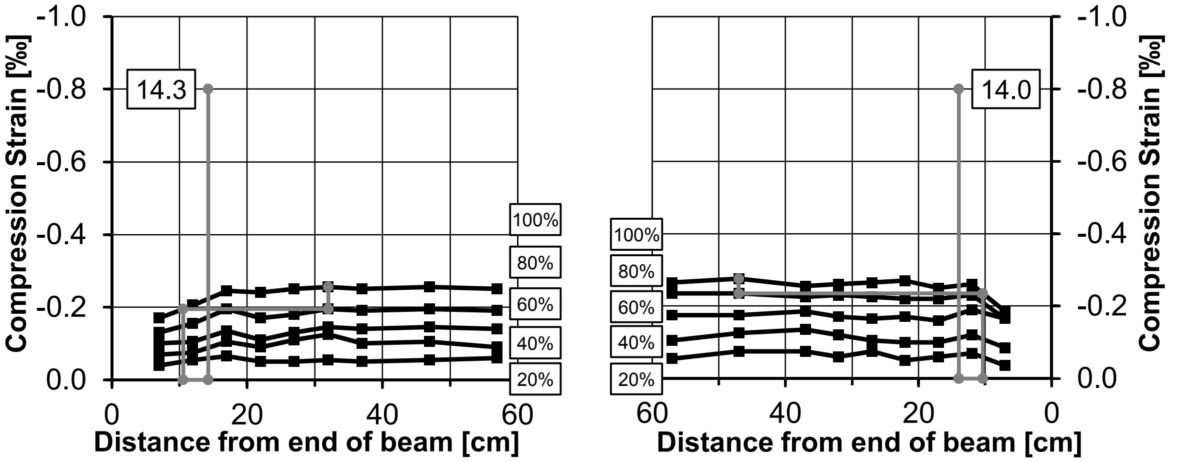
Compression Strain [‰]
-1.0
-0.8
-0.6
-0.4
-0.2
0.0
14.3
14.0
100%
80%
60%
40%
20%
0
20
40
60
Distance from end of beam [cm]

TL-7

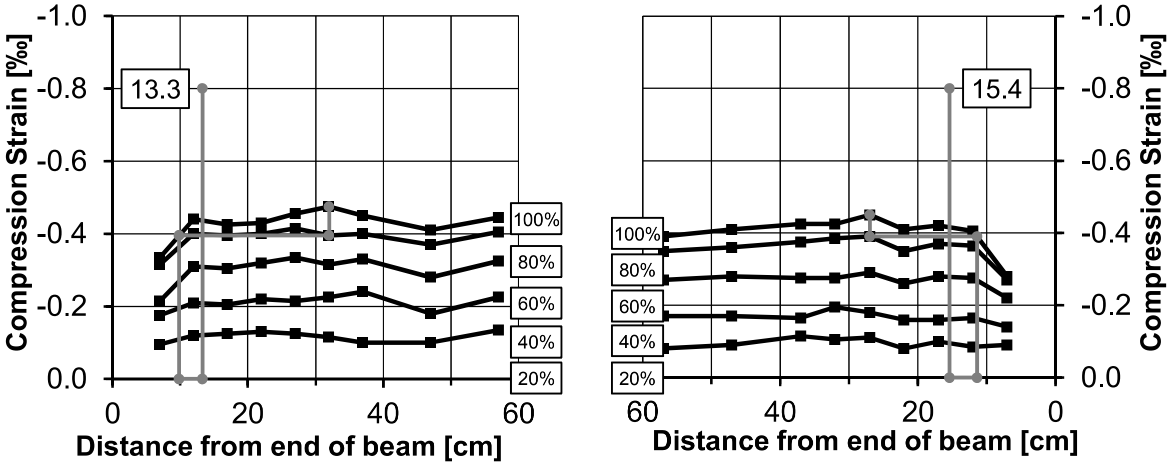
Compression Strain [‰]
-1.0
-0.8
-0.6
-0.4
-0.2
0.0
13.3
15.4
100%
80%
60%
40%
20%
0
20
40
60
Distance from end of beam [cm]

TL-8

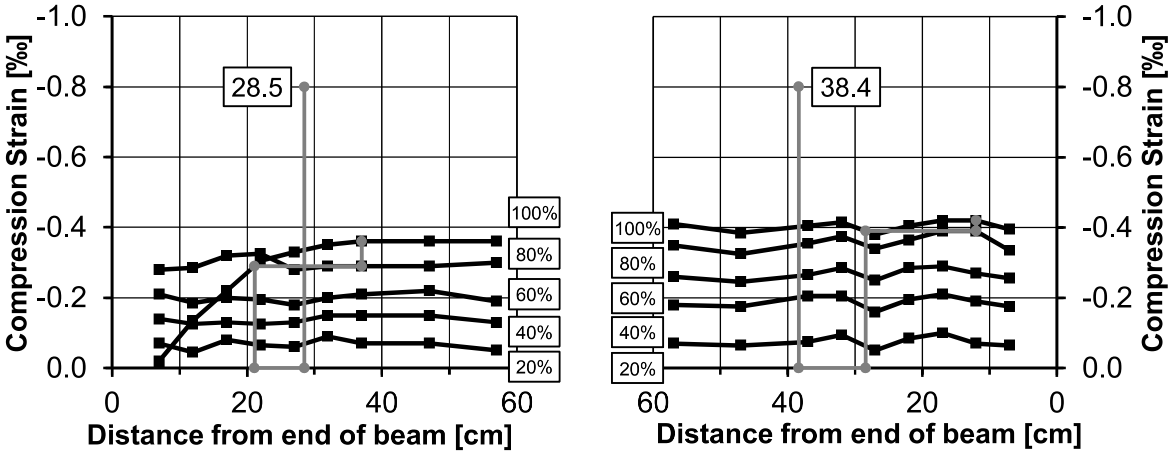
Compression Strain [‰]
-1.0
-0.8
-0.6
-0.4
-0.2
0.0
28.5
38.4
100%
80%
60%
40%
20%
0
20
40
60
Distance from end of beam [cm]

TL-9

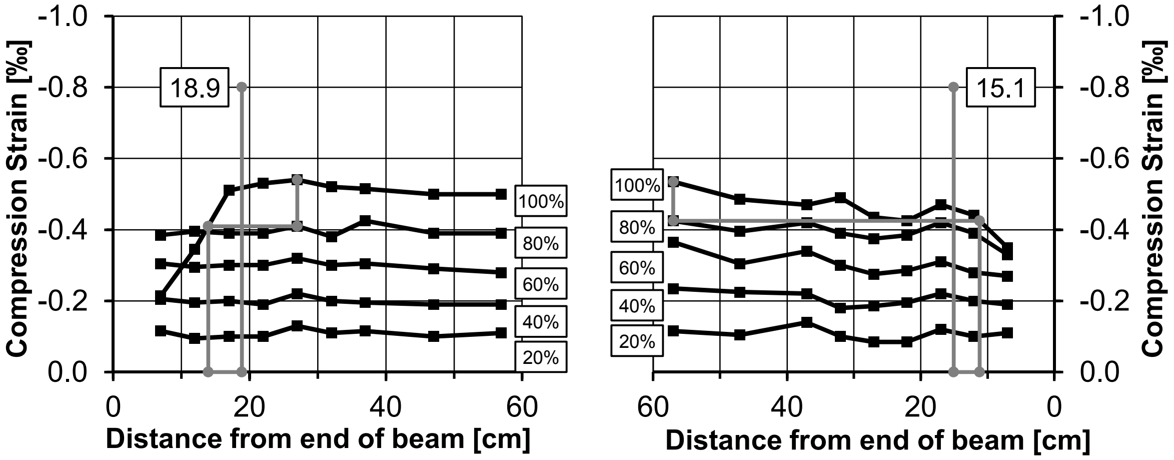
Compression Strain [‰]
-1.0
-0.8
-0.6
-0.4
-0.2
0.0
18.9
15.1
100%
80%
60%
40%
20%
0
20
40
60
Distance from end of beam [cm]

TL-10

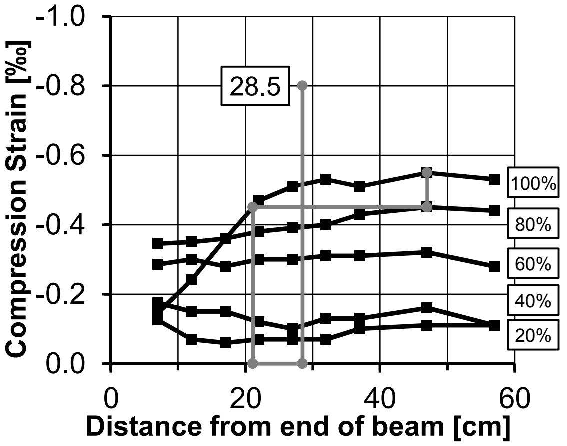

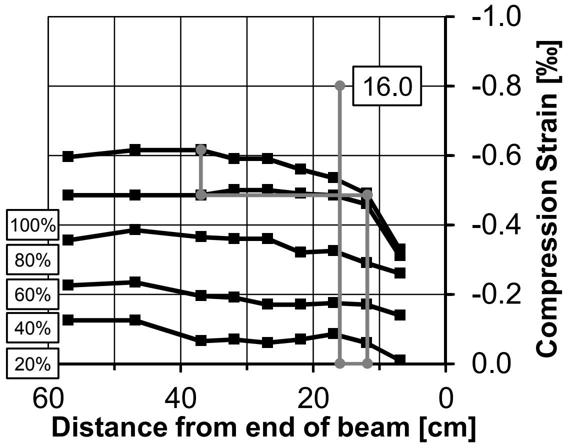

TL-11

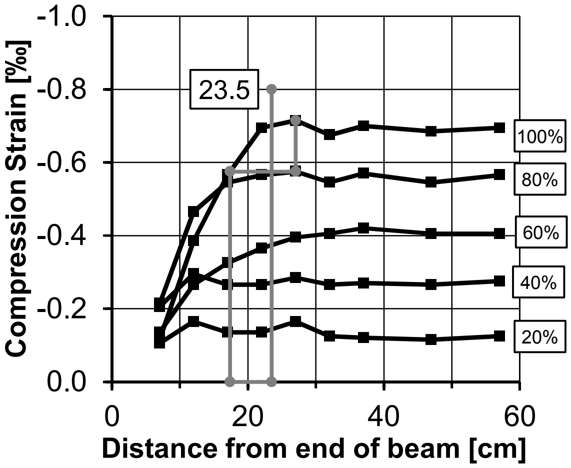

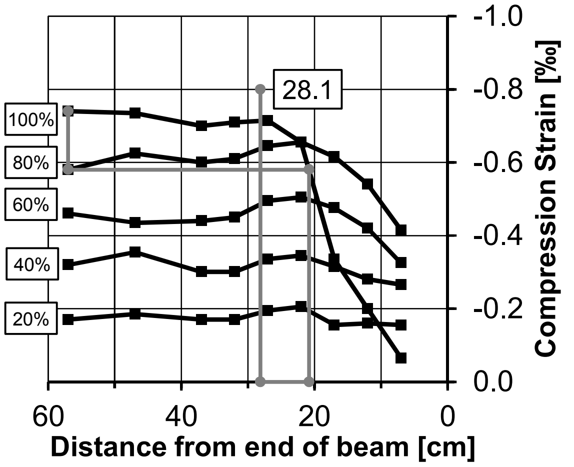

TL-12

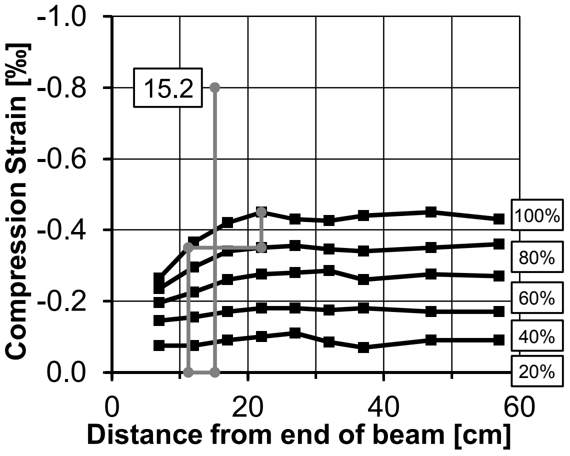

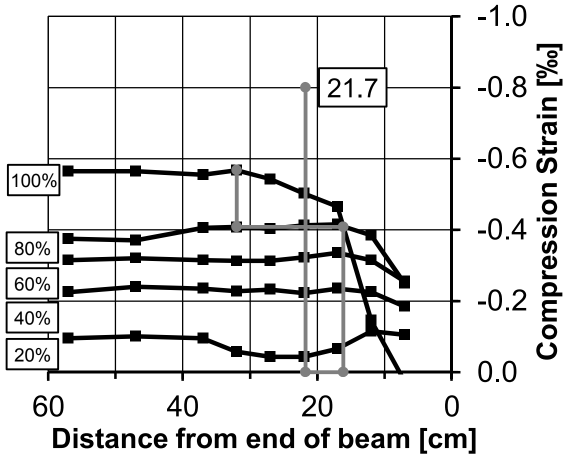

TL-13

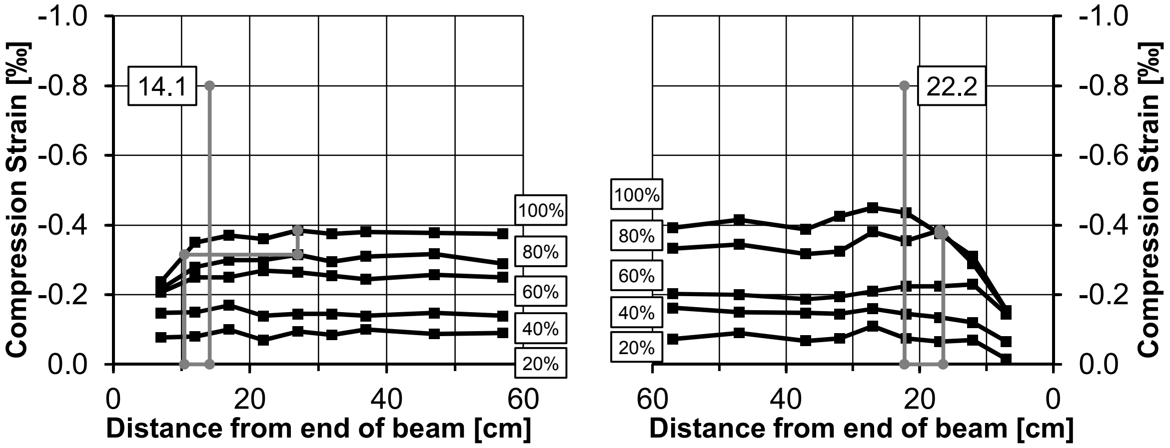

TL-14

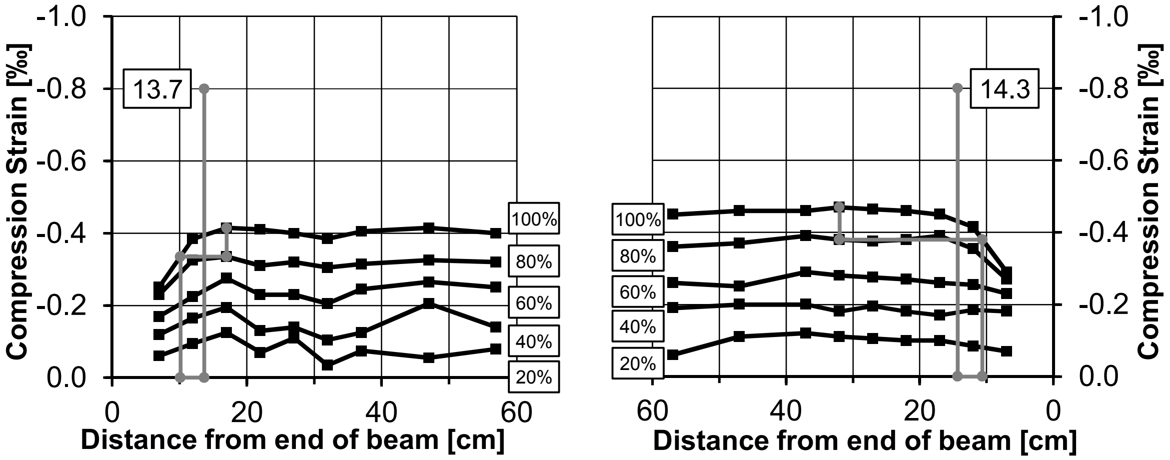

TL-15

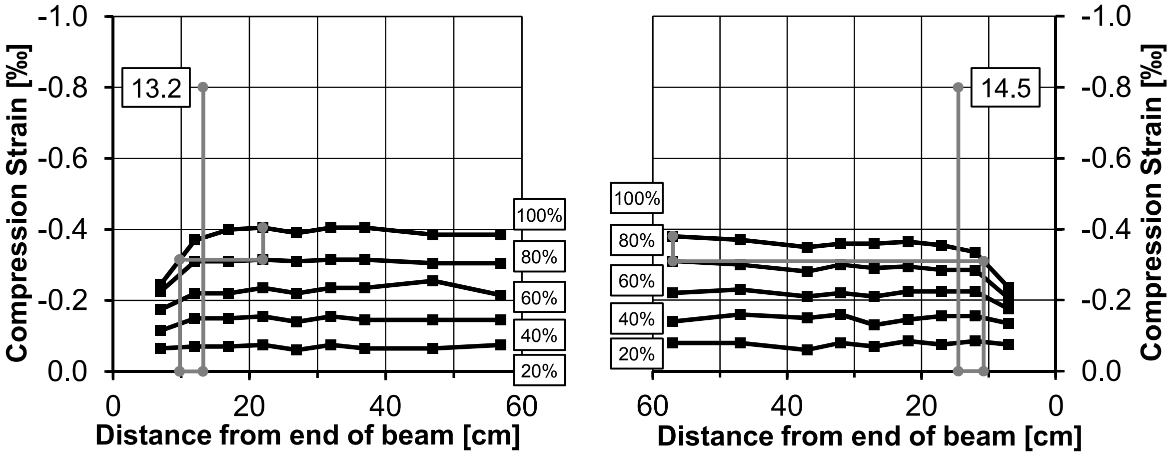

TL-16

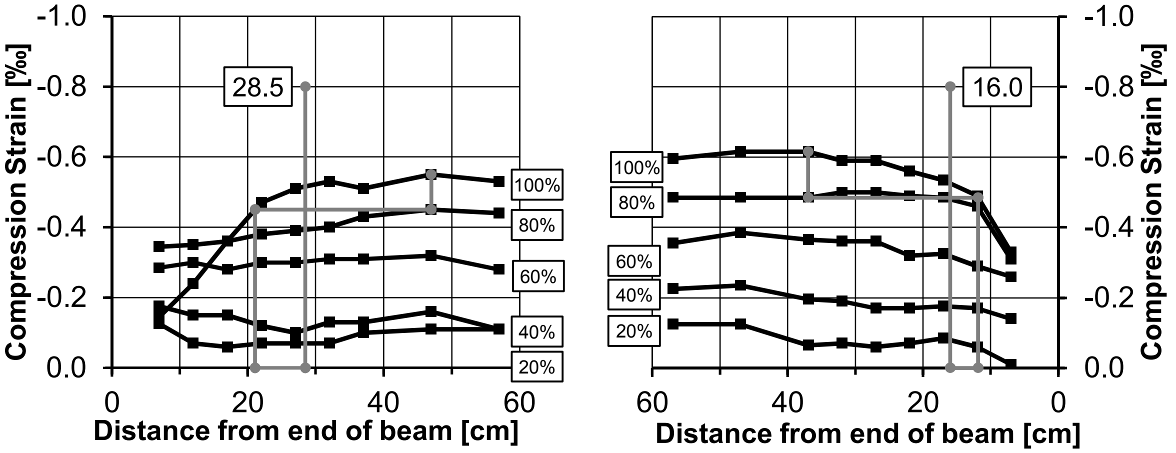

TL-17

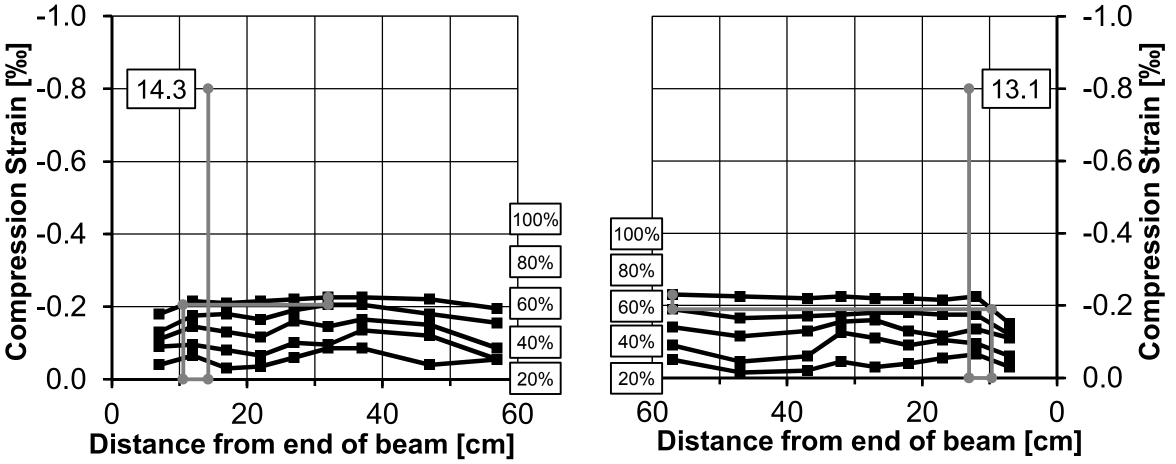

TL-18

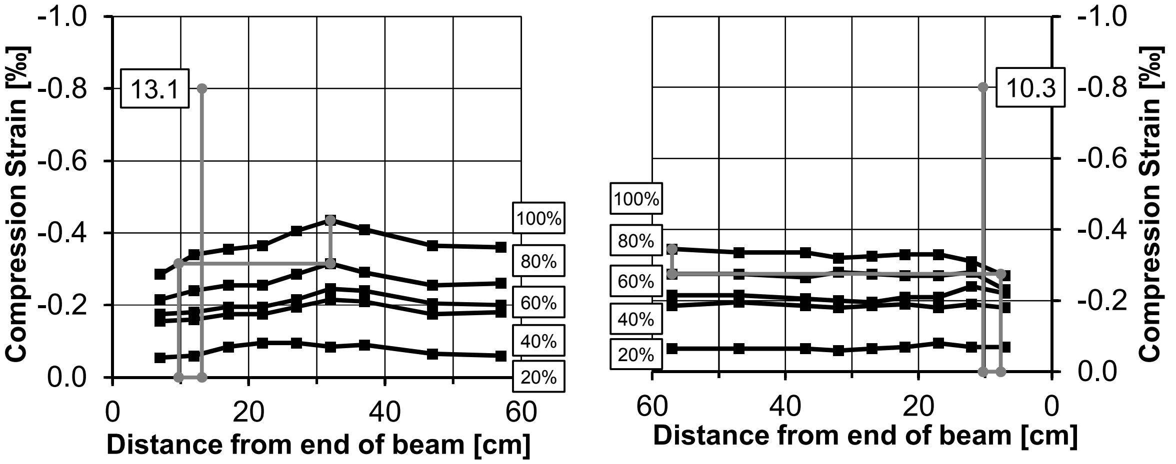

TL-19

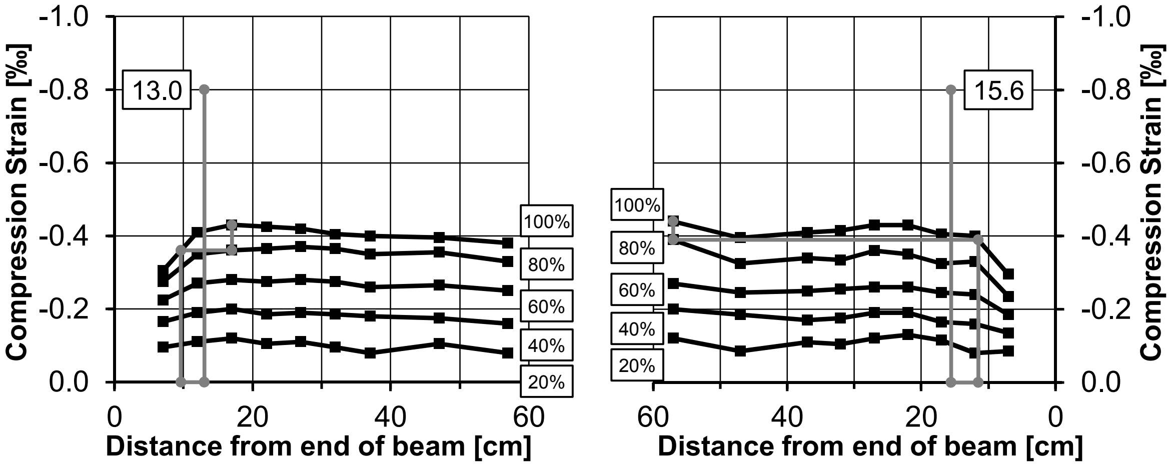

Bond slip of tendons

TL-1

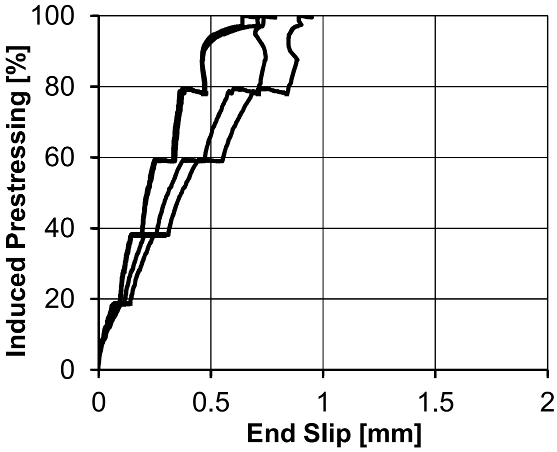

TL-2

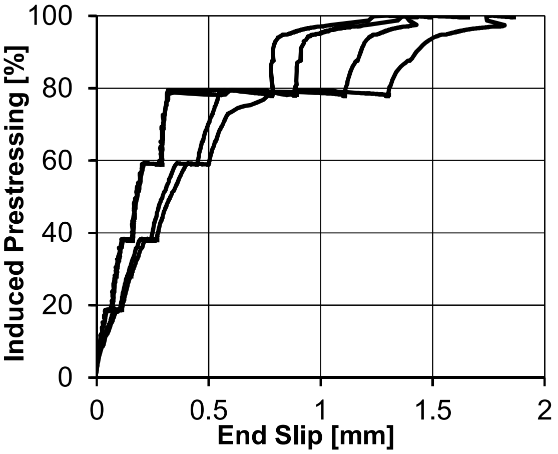

TL-3

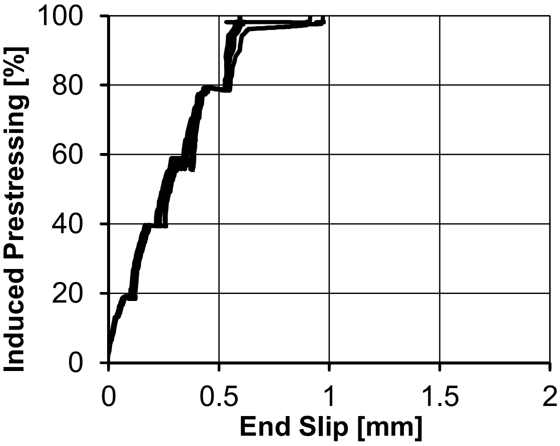

TL-4

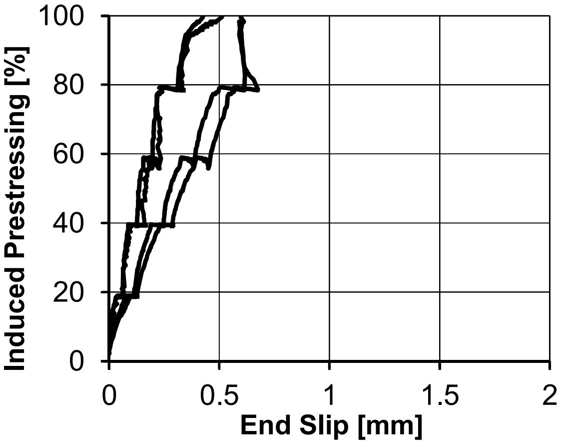

TL-5

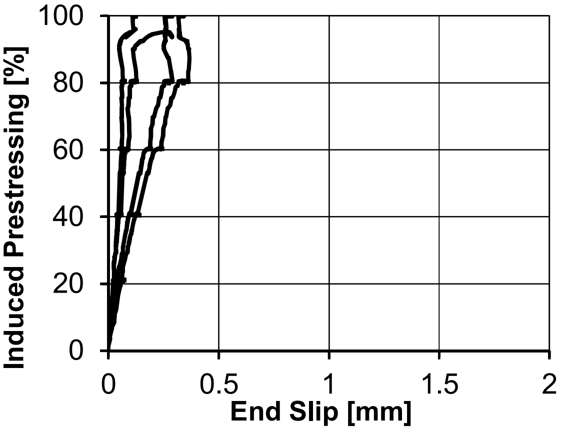

TL-6

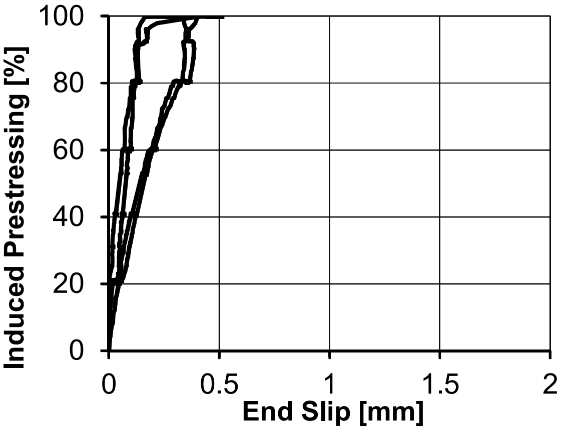

TL-7

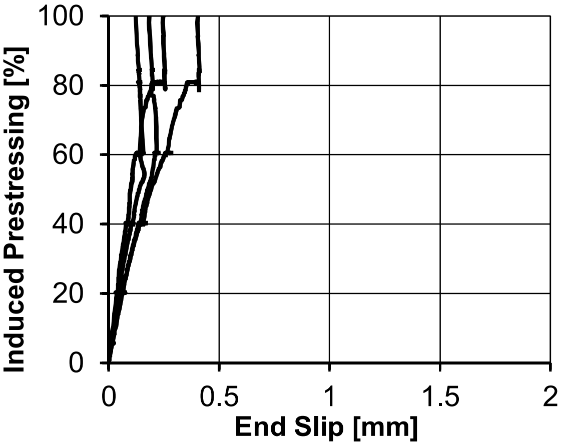

TL-8

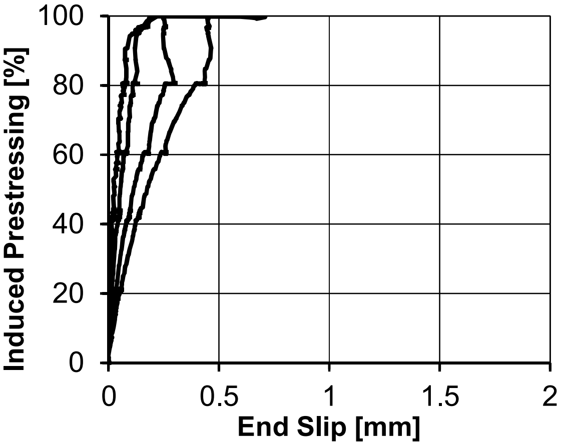

TL-9

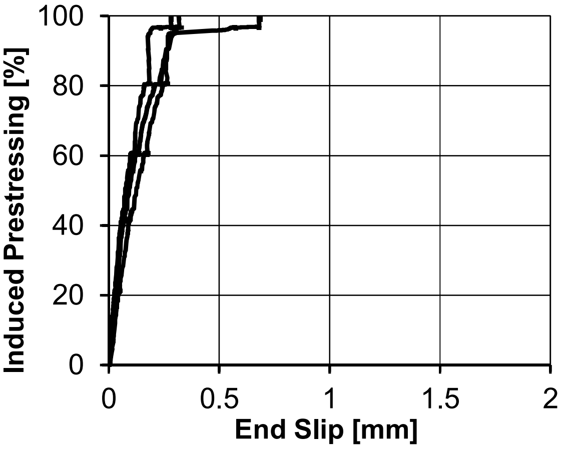

TL-10

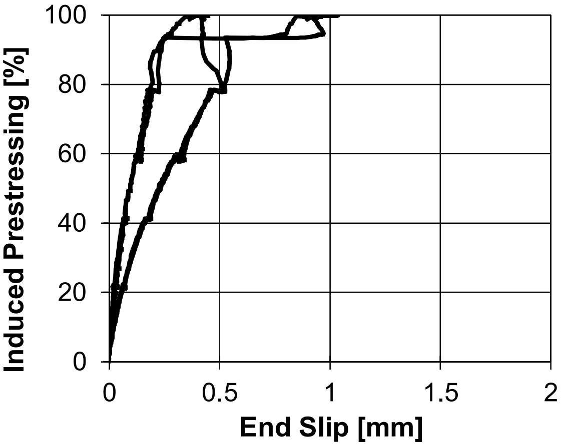

TL-11

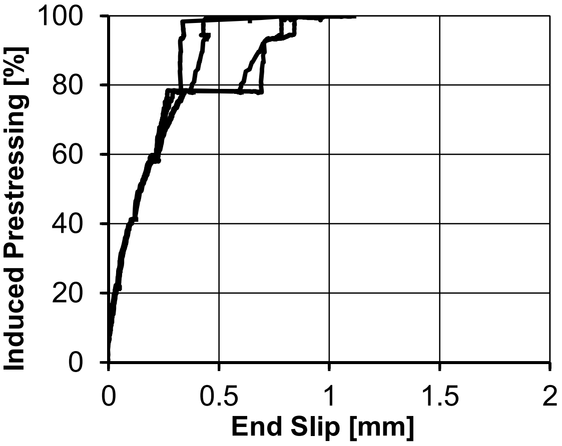

TL-12

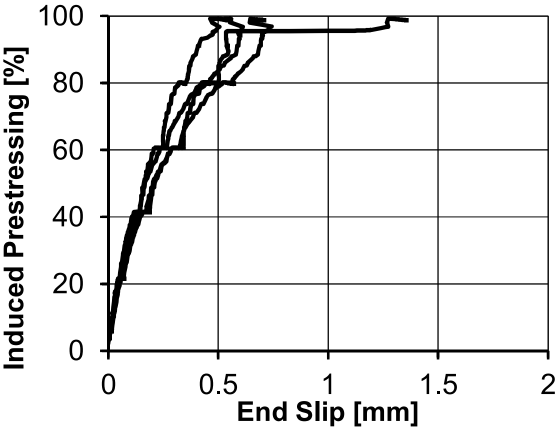

TL-13

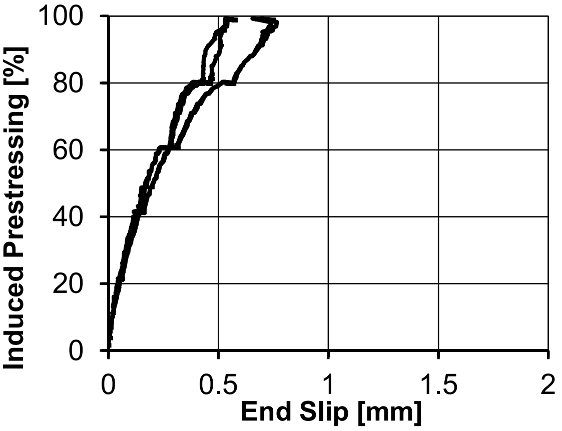

TL-14

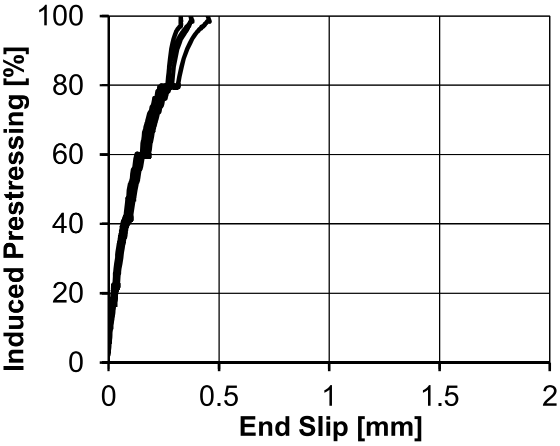

TL-15

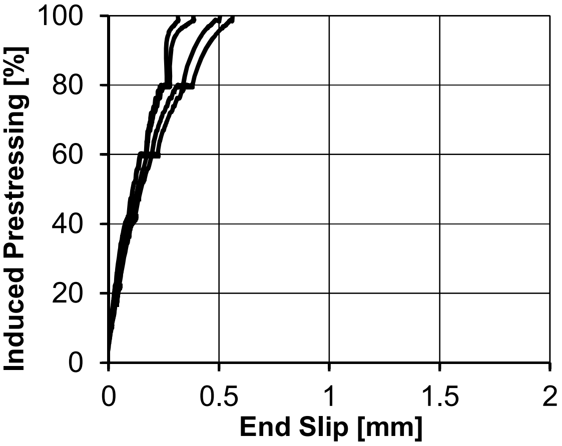

TL-16

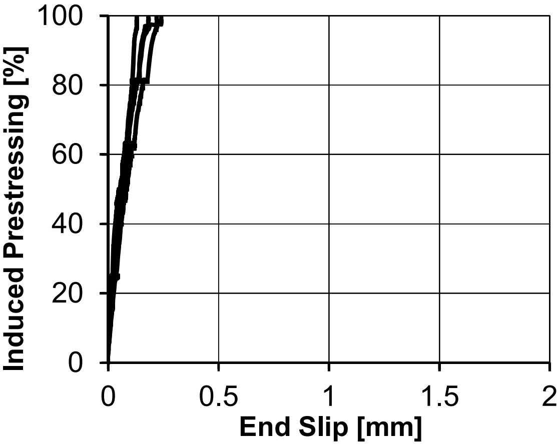

TL-17

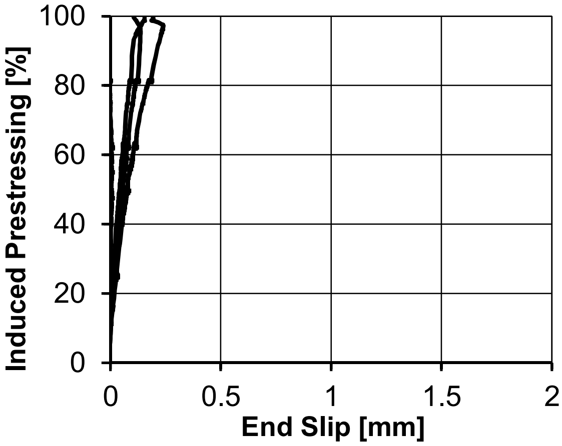

TL-18

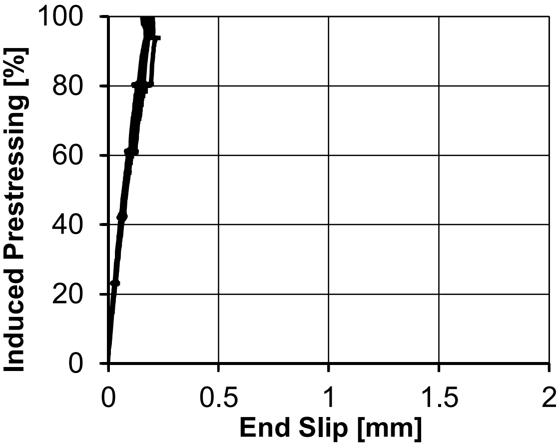

TL-19

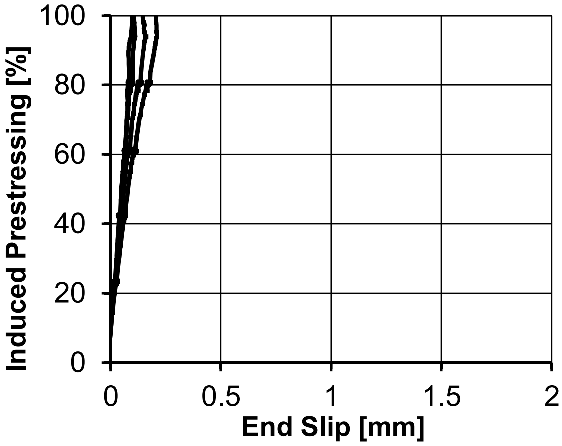

B Sandwich Sections under Tensile and Shear Loading

B.1 Tensile Tests

T-200-1 **T-200-2** **T-200-3** **T-200-4** **T-200-5**	**Core height [mm]**	**Connector [-]**	**Failure load [kN]**	**Displacement *Δv* [mm]**
	200	-	~25	~1.25

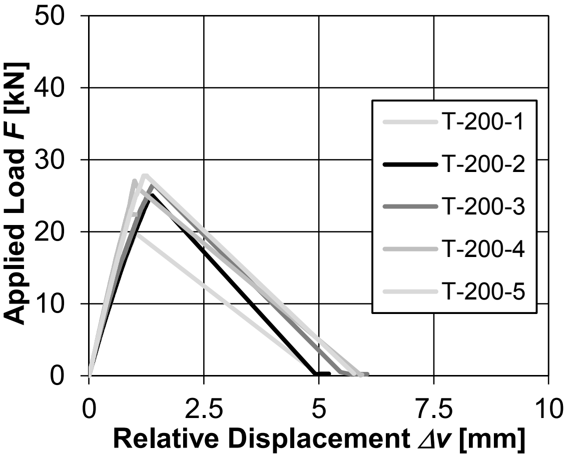

T-200-C-1 **T-200-C-2** **T-200-C-3** **T-200-C-4**	**Core height [mm]**	**Connector [-]**	**Failure load [kN]**	**Displacement *Δv* [mm]**
	200	1 x CFRP shear grid	~24	~1.1

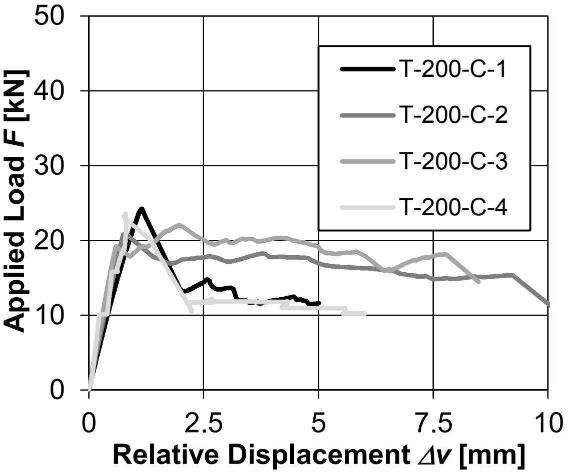

B.2 Shear Tests

S-200-1 S-200-2 S-200-3 S-200-4 S-200-5	Core height [mm]	Connector [-]	Failure load [kN]	Displacement	
				Δu [mm]	Δv [mm]
	200	-	~38	~9.0	~2.5

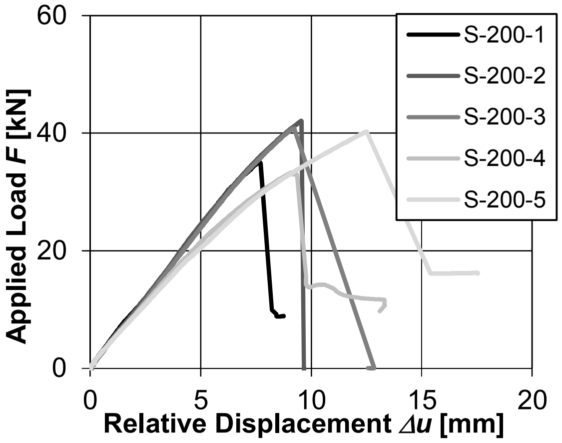

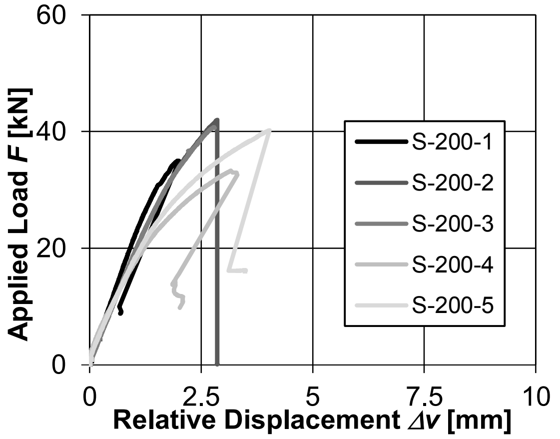

S-200-C-20-1 S-200-C-20-2	Core height [mm]	Connector [-]	Failure load [kN]	Displacement	
				Δu [mm]	Δv [mm]
	200	1x shear grid, t_R = 20 mm	~46	~8.5	~8.5

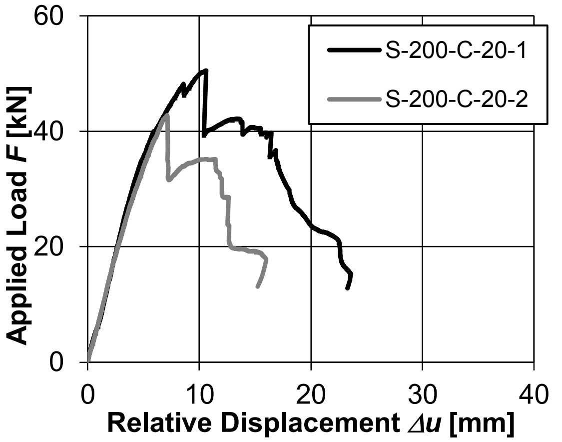

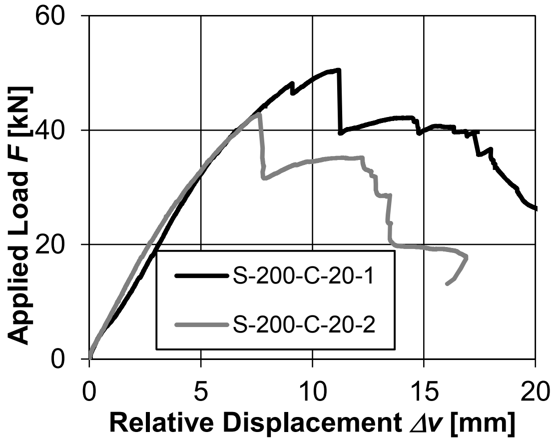

S-200-C-30-1 **S-200-C-30-2**	**Core height [mm]**	**Connector [-]**	**Failure load [kN]**	**Displacement**	
				***Δu* [mm]**	***Δv* [mm]**
	200	1 x shear grid, t_R = 30 mm	~47	~12.5	~6.5

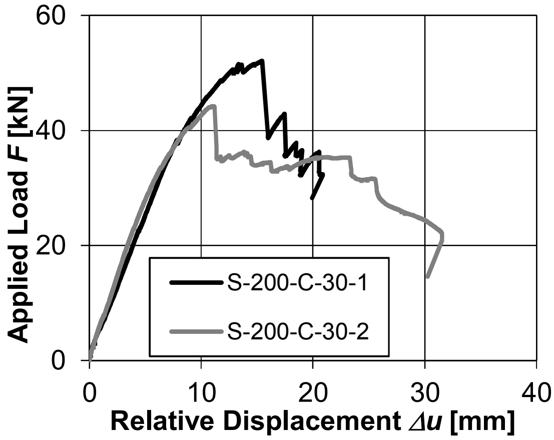

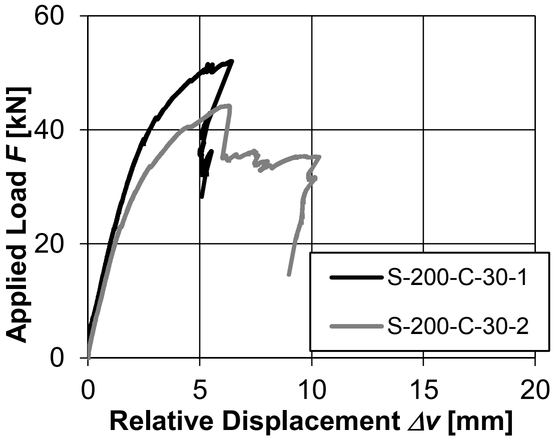

S-200-C-40-1 **S-200-C-40-2**	**Core height [mm]**	**Connector [-]**	**Failure load [kN]**	**Displacement**	
				***Δu* [mm]**	***Δv* [mm]**
	200	1 x shear grid, t_R = 40 mm	~48	~9.0	~10.0

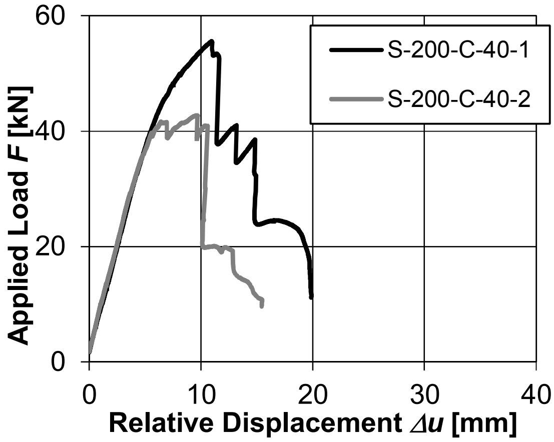

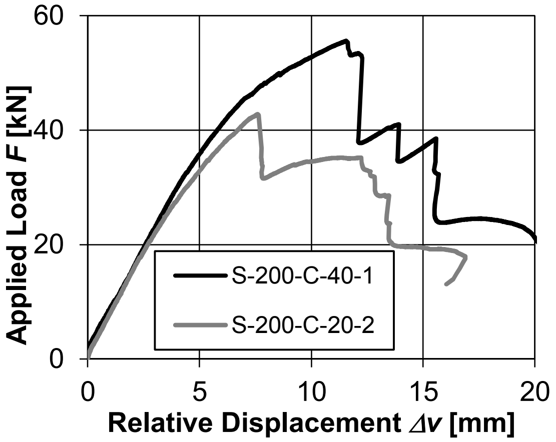

S-200-2C-30-1 S-200-2C-30-2 S-200-2C-30-3	Core height [mm]	Connector [-]	Failure load [kN]	Displacement	
				Δu [mm]	Δv [mm]
	200	2 x shear grid, t_R = 40 mm	~60	~14.0	~6.0

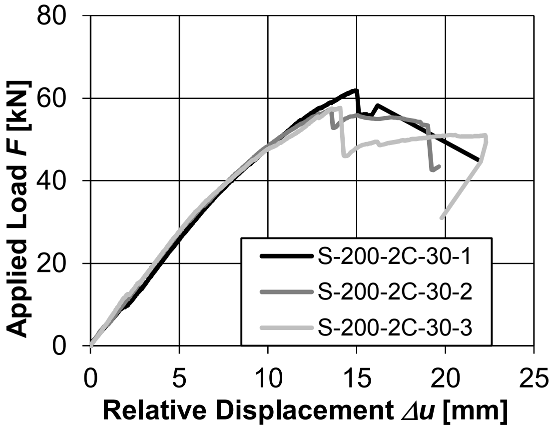

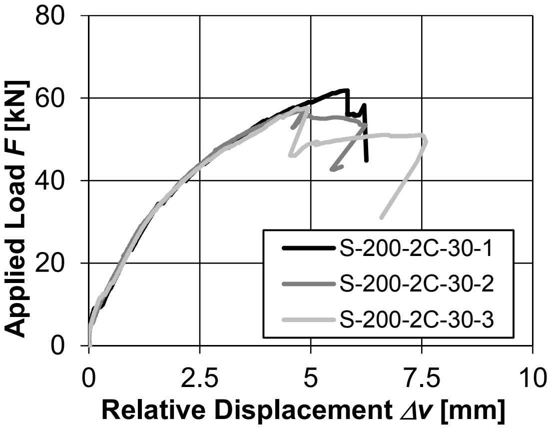

S-200-pin-15-1 S-200-pin-15-2 S-200-pin-15-3	Core height [mm]	Connector [-]	Failure load [kN]	Displacement	
				Δu [mm]	Δv [mm]
	200	4 x pin (TM), t_{pin} = 15 mm	~36	~9.0	~0.9

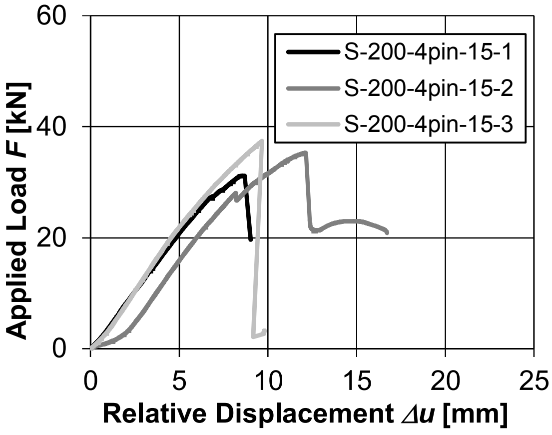

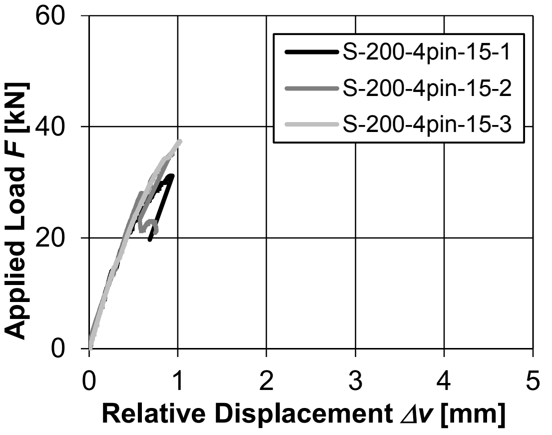

S-100-1 **S-100-2** **S-100-3**	**Core height [mm]**	**Connector [-]**	**Failure load [kN]**	**Displacement**	
				Δu [mm]	**Δv [mm]**
	100	-	~60	~10.5	~1.2

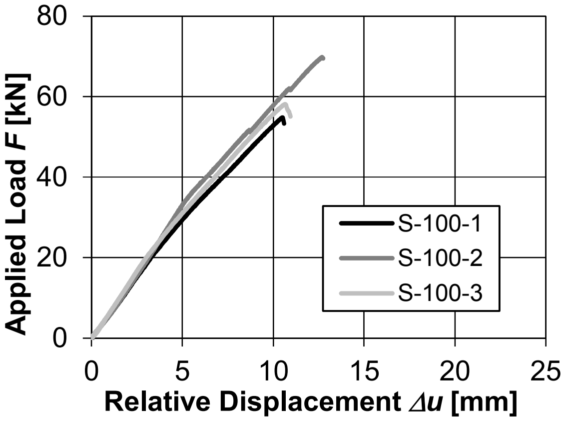

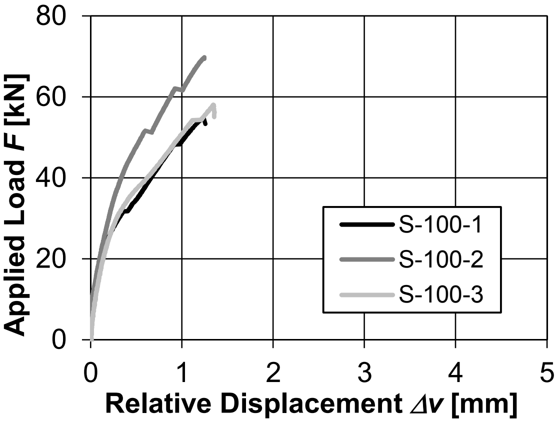

S-100-C-30-1 **S-100-C-30-2** **S-100-C-30-3**	**Core height [mm]**	**Connector [-]**	**Failure load [kN]**	**Displacement**	
				Δu [mm]	**Δv [mm]**
	100	1 x shear grid, t_R = 30 mm	~85	~16.0	~2.5

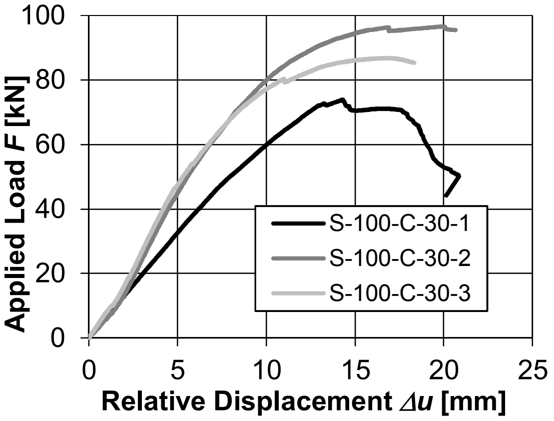

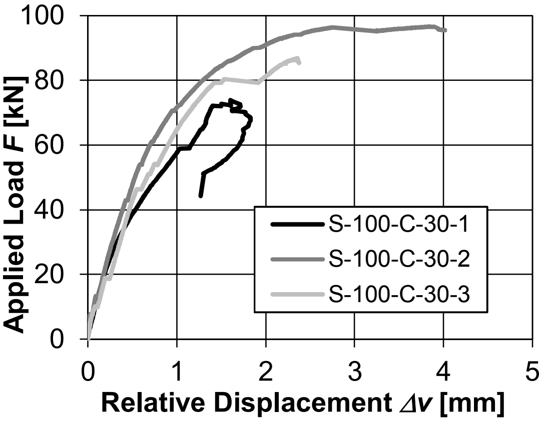

Cylindrical shear test	Core height [mm]	Connector [-]	Failure load [kN]	Displacement *Δu* [mm]	 *Δv* [mm]
	50 / 200	-	~44 / ~43	~2.5 / ~4.8	-

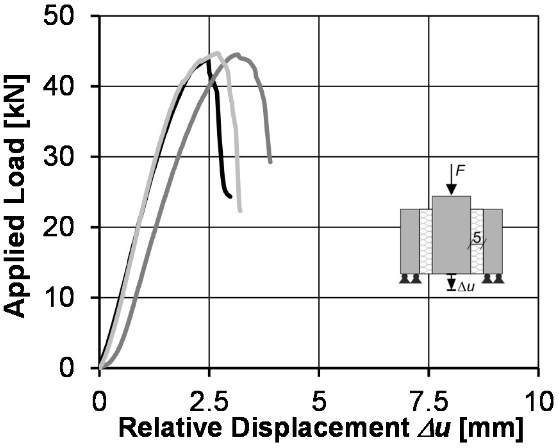

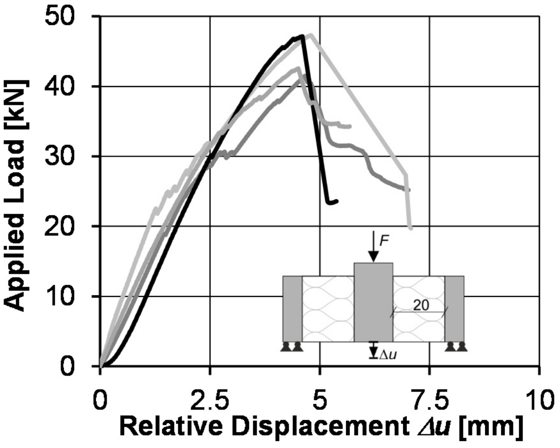

C Folded Plate and Doubly Curved Elements under Flexural Loading

C.1 Folded Plate Elements

Test setup

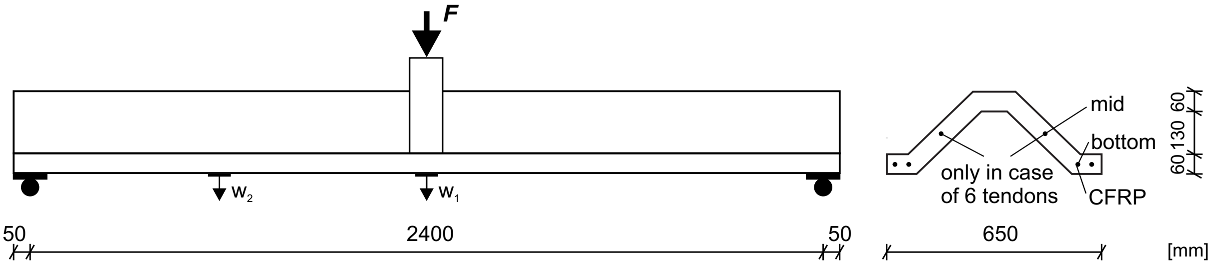

Transfer length

Concrete compressions: Extensometer in same arrangement as for tests on the transfer length at bottom flange and in case of six tendons, additionally at mid height.

End slip: Relative displacement between tendons and UHPFRC element

Table C.5: Parameter variation of flexural tests on folded plate elements

Test No. [-]	CFRP Type [-]	Number [-]	Jacking stress [MPa]
FP-1	strand	4	1350
FP-2	bar	4	1350
FP-3	strand	6	1350
FP-4	bar	6	1350
FP-5	strand	4	675
FP-6	bar	4	0
FP-7	bar	4	675
FP-8	---	---	---

Table C.6: Concrete properties of folded plate elements

Test No. [-]	$f_{cm,cyl}$ [MPa]		$f_{cm,cube}$ [MPa]		E_{cm} [MPa]		$f_{ct,flex}$ [MPa]	
	1d	**28d**	**1d**	**28d**	**1d**	**28d**	**1d**	**28d**
FP-1	67.8	149.6	---	182.4	---	45,500	10.5	19.5
FP-2	58.1	154.0	70.6	181.0	32,500	43,900	8.7	19.0
FP-3	71.8	148.9	72.6	168.8	31,700	45,400	10.4	20.6
FP-4	83.3	157.9	84.3	177.4	36,300	45,300	12.4	21.3
FP-5	70.8	151.7	79.1	189.5	32,200	44,400	8.5	13.9
FP-6	NA	150.5	NA	171.2	NA	43,800	NA	17.7
FP-7	52.2	149.6	60.8	161.2	31,900	43,700	6.9	17.5
FP-8	NA	148.9	NA	160.0	NA	45,600	NA	19.9

	CFRP Type [-]	Diameter [mm]	Jacking Stress [MPa]	Number [-]
FP-1	Strand	7.5	1350	4

Prestressing: Compression strains and end slip

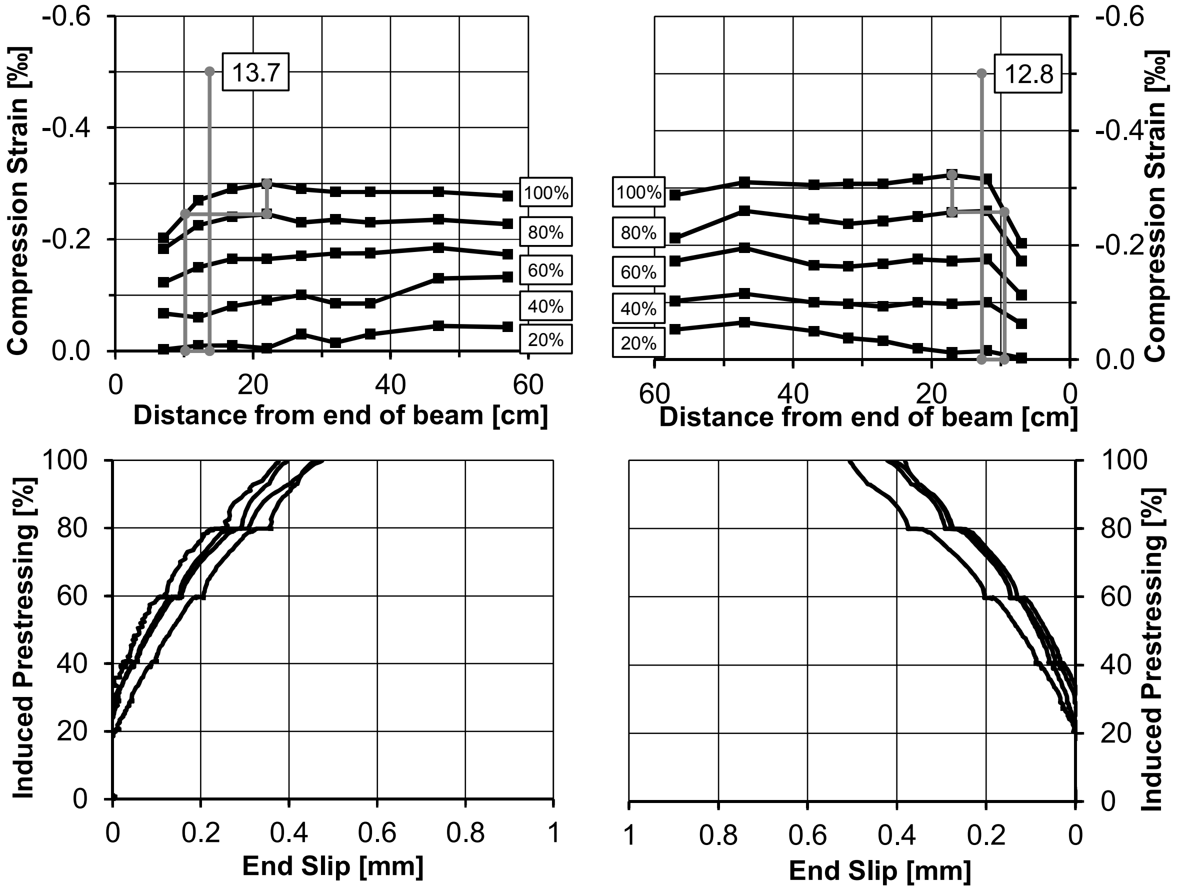

Results of three-point bending test and crack pattern

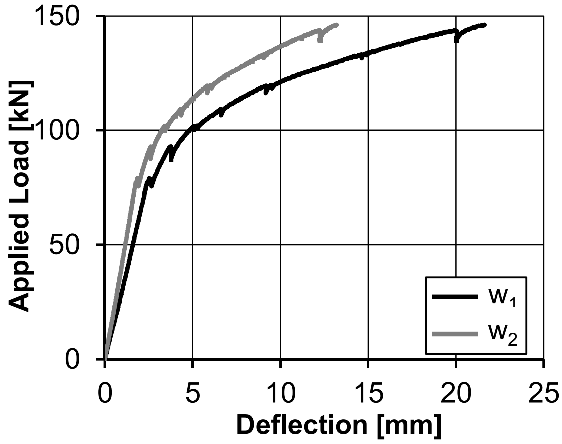

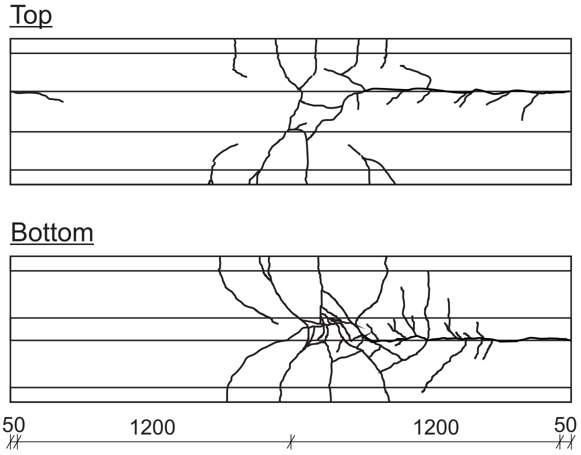

	CFRP Type [-]	Diameter [mm]	Jacking Stress [MPa]	Number [-]
FP-2	Bar	5.0	1350	4

Prestressing: Compression strains and end slip

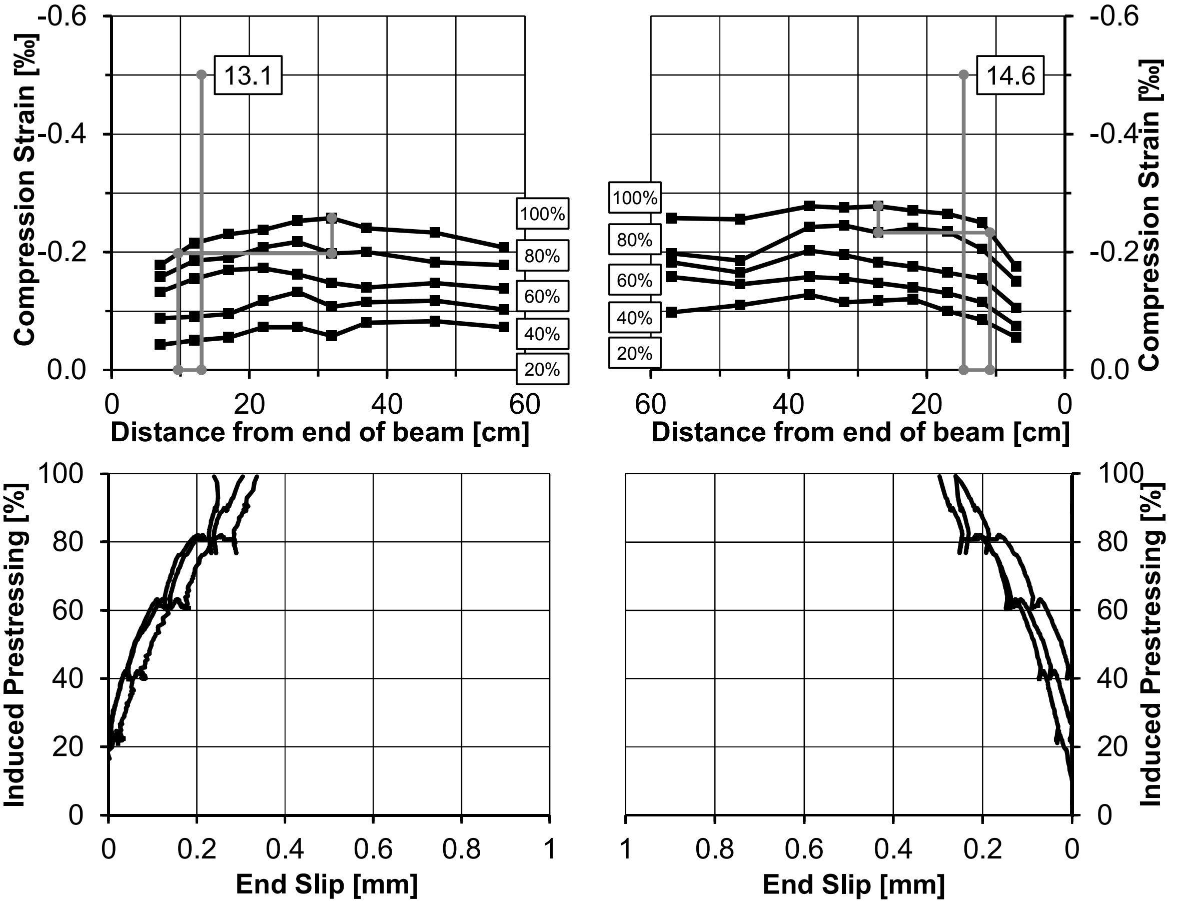

Results of three-point bending test and crack pattern

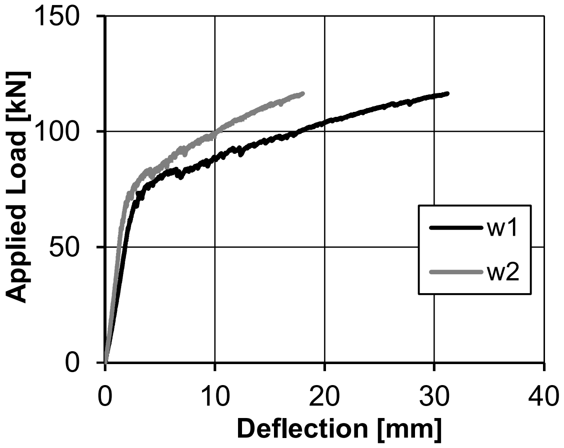

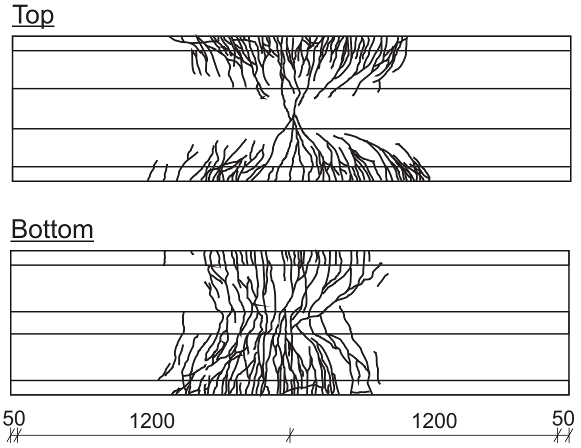

	CFRP Type [-]	Diameter [mm]	Jacking Stress [MPa]	Number [-]
FP-3	Strand	7.5	1350	6

Prestressing: Compression strains and end slip

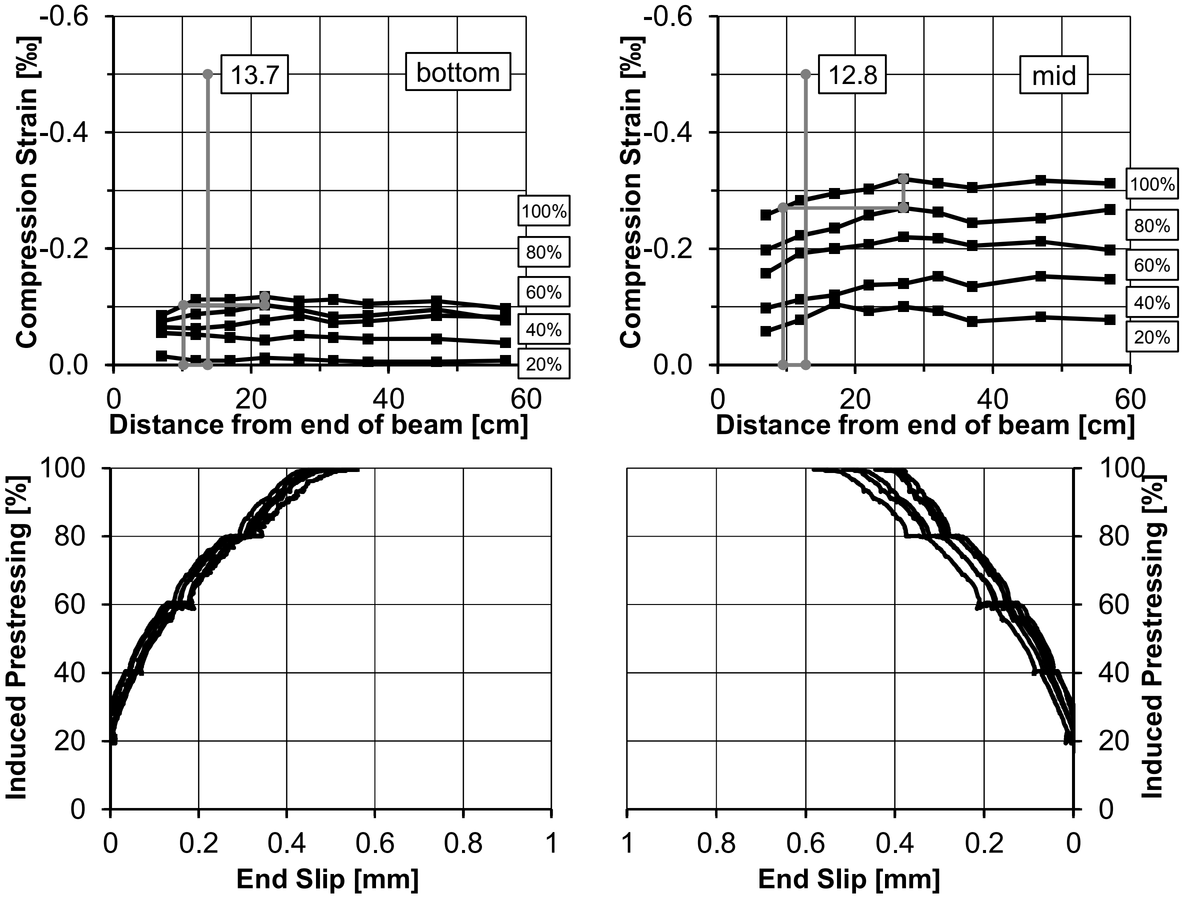

Results of three-point bending test and crack pattern

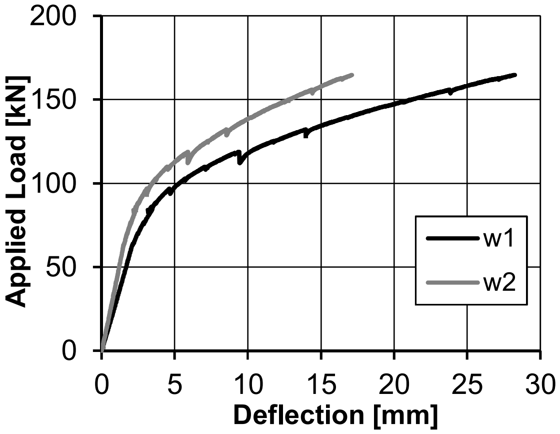

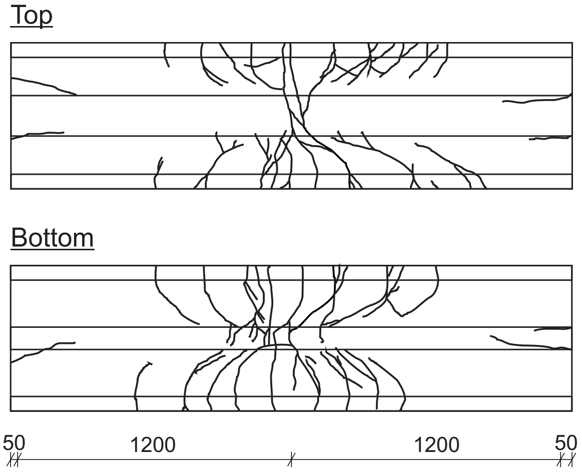

FP-4	CFRP Type [-]	Diameter [mm]	Jacking Stress [MPa]	Number [-]
	Bar	5.0	1350	6

Prestressing: Compression strains and end slip

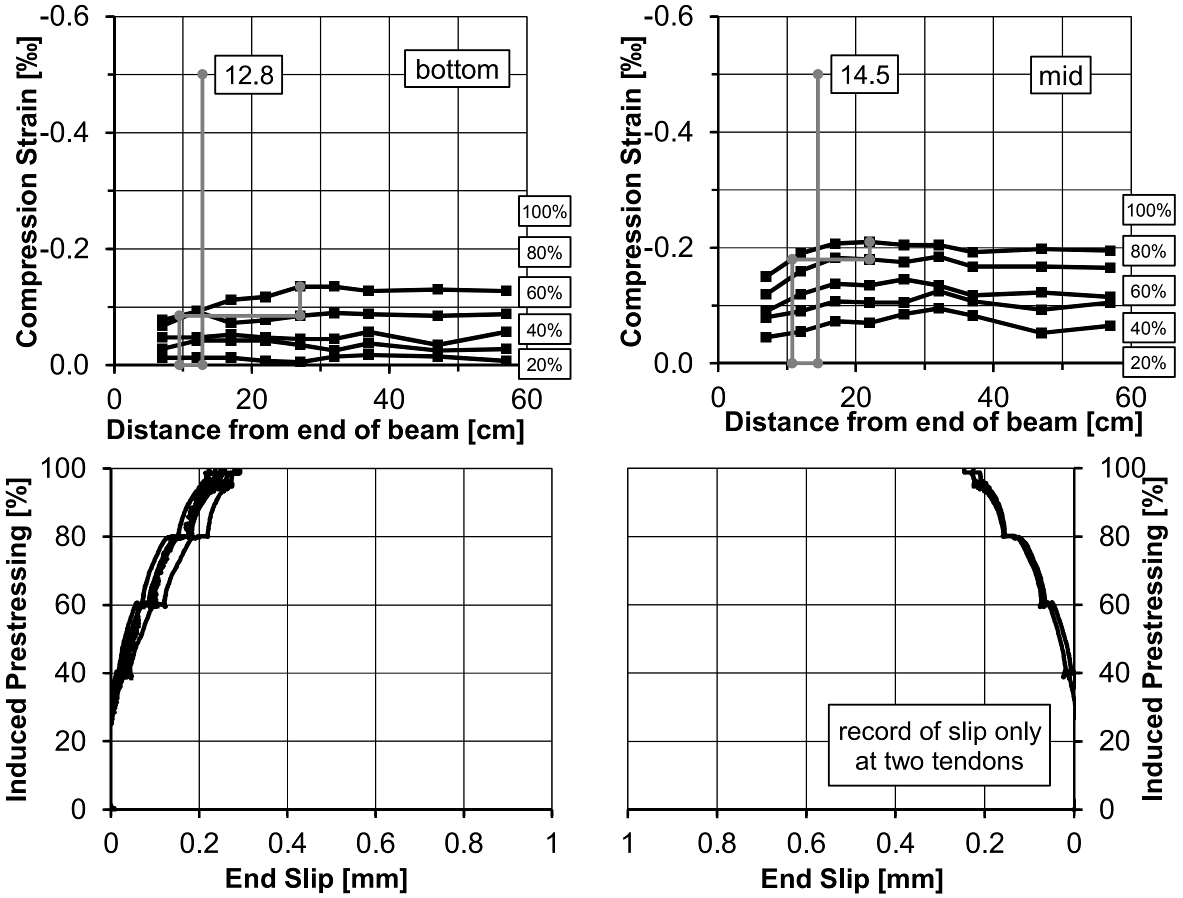

Results of three-point bending test and crack pattern

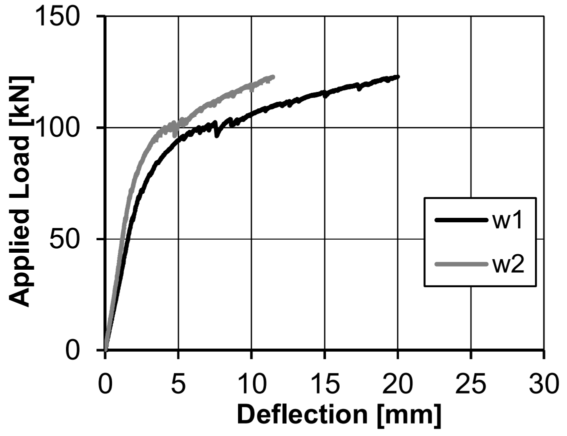

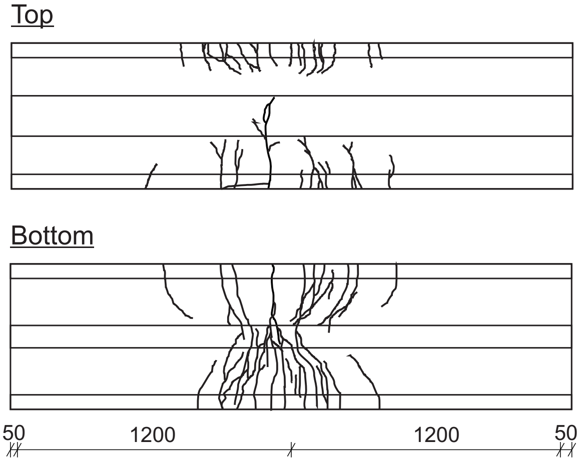

	CFRP Type [-]	Diameter [mm]	Jacking Stress [MPa]	Number [-]
FP-5	Strand	7.5	675	4

Prestressing: Compression strains and end slip

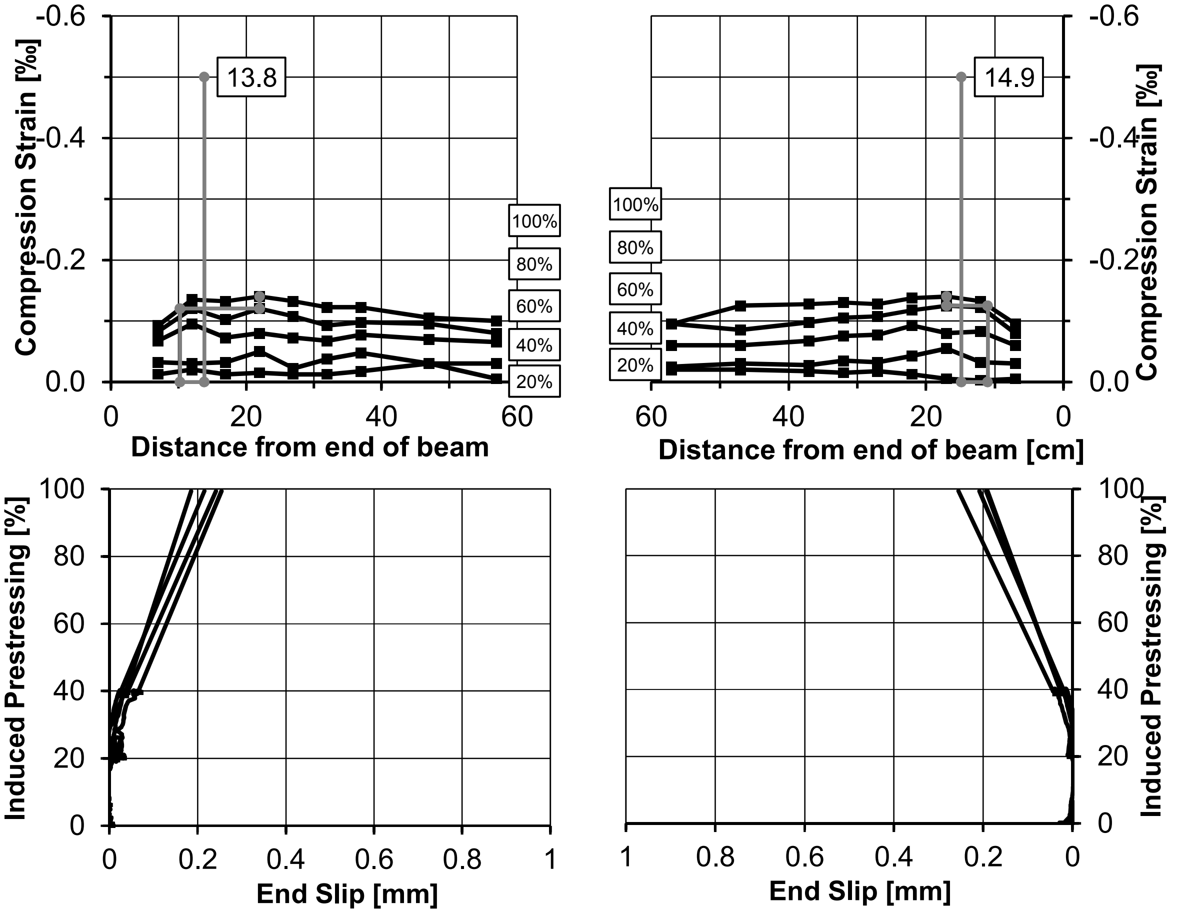

Results of three-point bending test and crack pattern

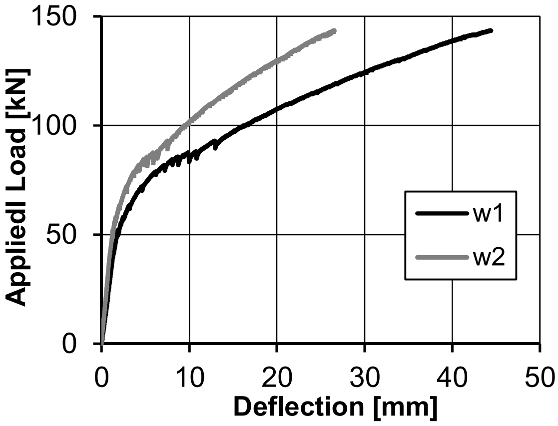

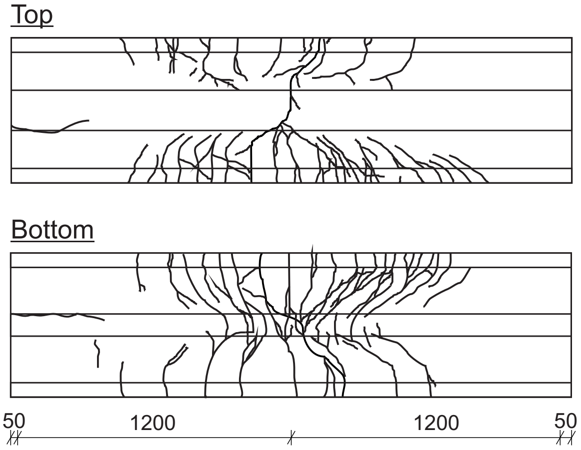

	CFRP Type [-]	Diameter [mm]	Jacking Stress [MPa]	Number [-]
FP-6	Bar	5.0	0	4

Results of three-point bending test and crack pattern

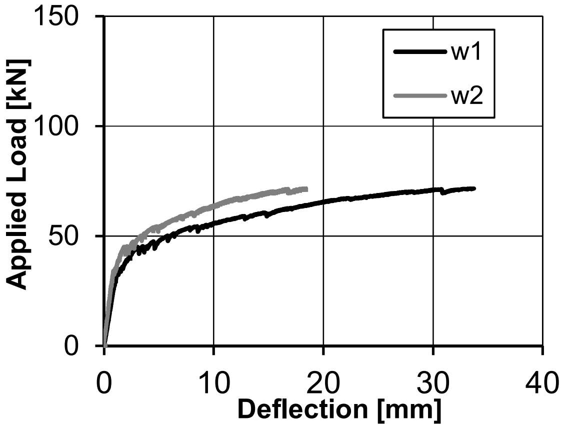

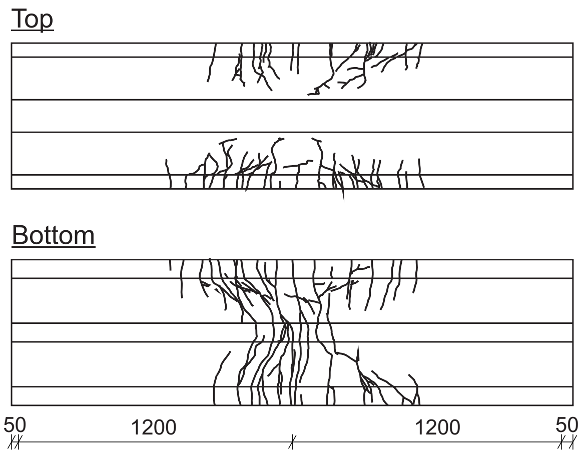

	CFRP Type [-]	Diameter [mm]	Jacking Stress [MPa]	Number [-]
FP-7	Bar	5.0	675	4

Prestressing: Compression strains and end slip

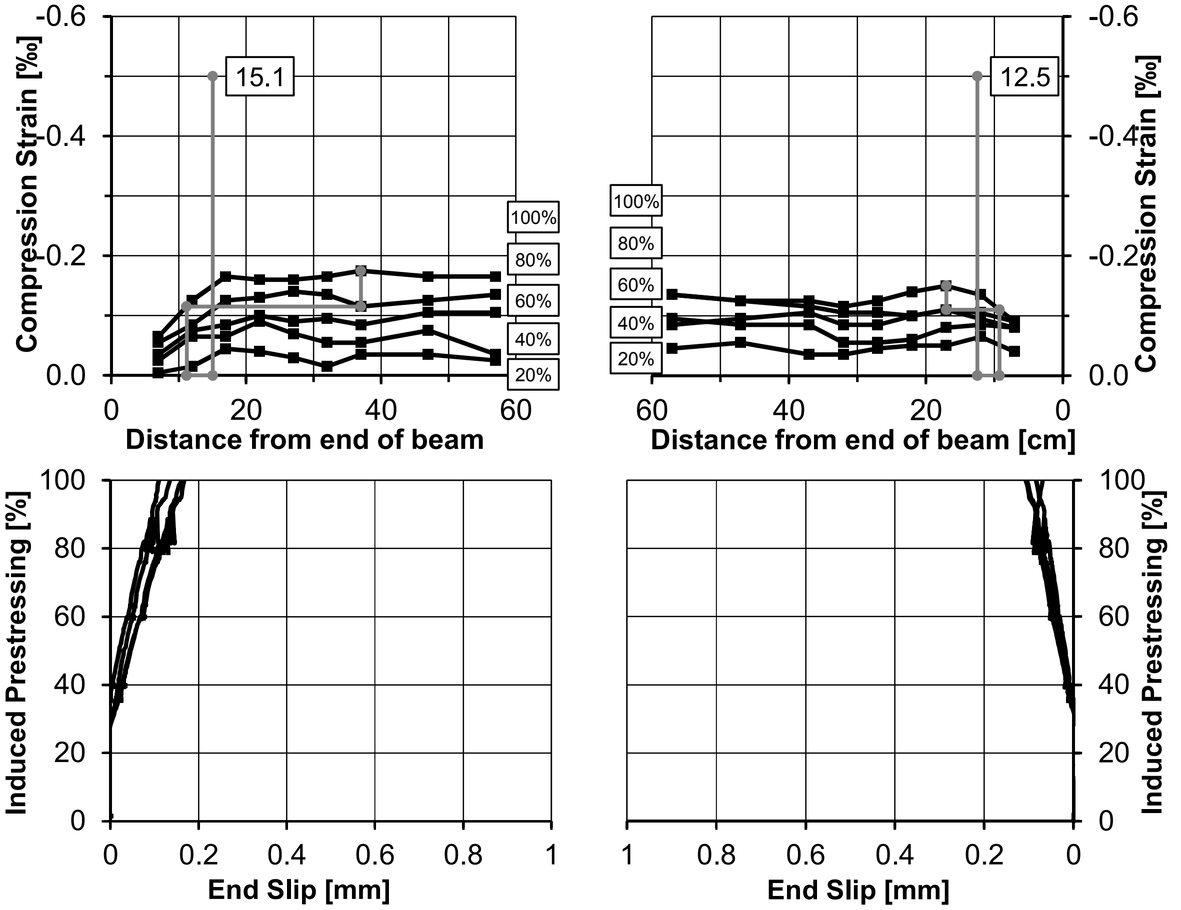

Results of three-point bending test and crack pattern

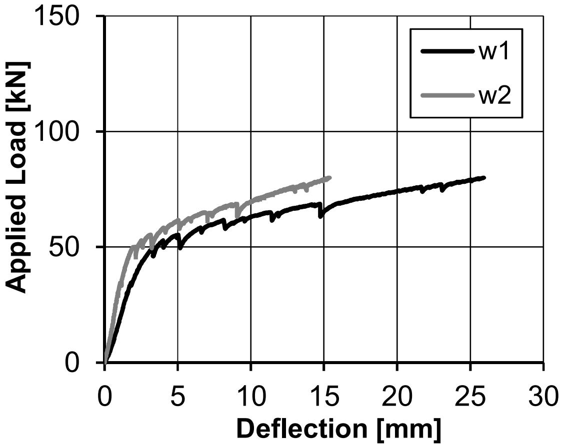

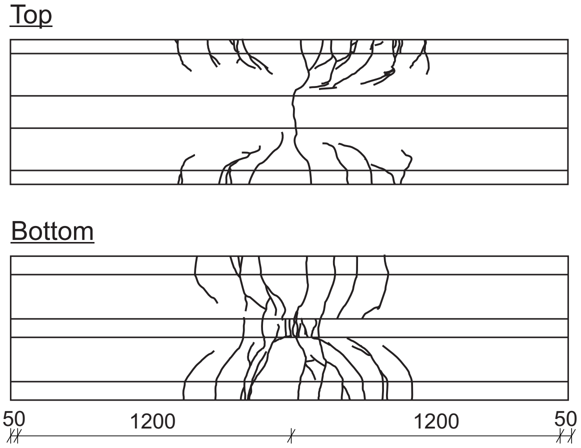

FP-8	CFRP Type [-]	Diameter [mm]	Jacking Stress [MPa]	Number [-]
	---	---	---	---

Results of three-point bending test and crack pattern

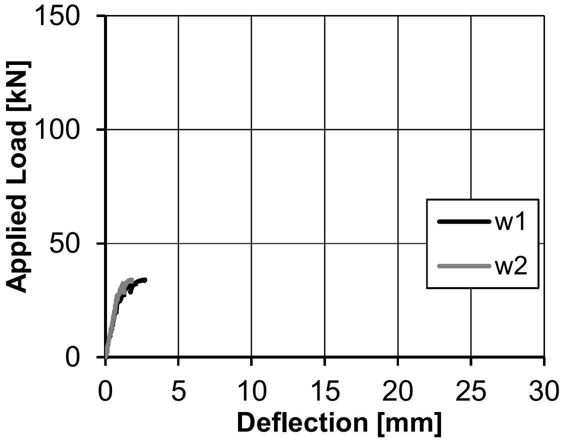

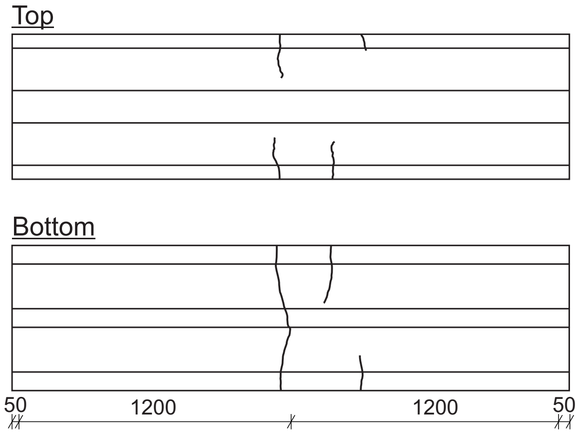

C.2 Doubly Curved Elements

Test setup

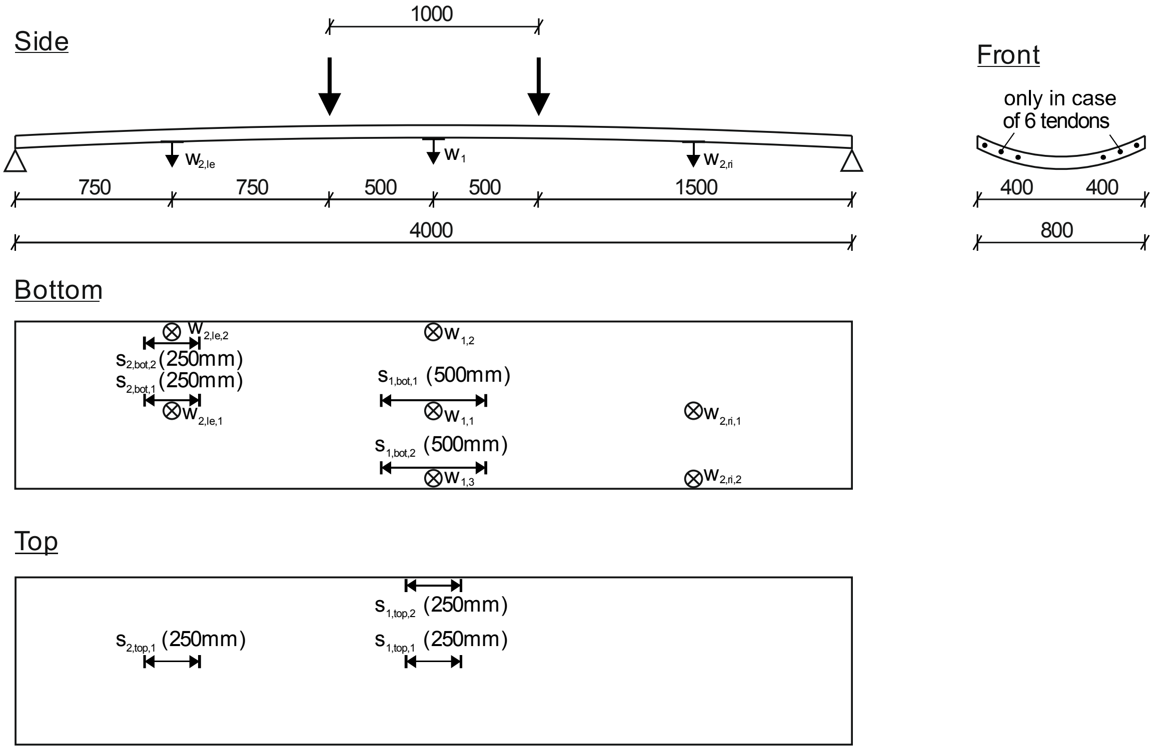

Transfer length

End slip: Relative displacement between tendons and UHPFRC element

Table C.7: Parameter variation of flexural tests on doubly curved elements

Test No. [-]	CFRP Type [-]	Number [-]	Jacking stress [MPa]
HP-1	bar	6	0
HP-2	bar	4	0
HP-3	steel strand	6	800
HP-4	strand	4	675
HP-5	strand	4	1350
HP-6	strand	6	675

Table C.8: Concrete properties of doubly curved elements

Test No. [-]	$f_{cm,cyl}$ [MPa]		$f_{cm,cube}$ [MPa]		E_{cm} [MPa]		$f_{ct,flex}$ [MPa]	
	1d	**28d**	**1d**	**28d**	**1d**	**28d**	**1d**	**28d**
HP-1	NA	137.9	NA	175.9	NA	46,600	NA	16.9
HP-2	NA	134.5	NA	174.6	NA	44,800	NA	18.1
HP-3	---	142.4	84.5	154.8	---	45,500	10.5	23.1
HP-4	78.3	141.4	100.1	184.6	40,000	46,500	12.5	19.9
HP-5	62.3	137.5	77.8	176.0	35,400	45,100	8.8	19.5
HP-6	62.5	148.6	62.5	177.6	37,400	45,700	7.7	16.7

HP-1	CFRP Type [-]	Diameter [mm]	Jacking Stress [MPa]	Number [-]
	bar	5.0	0	6

Prestressing: End slip

none

Results of four-point bending test and corresponding crack pattern

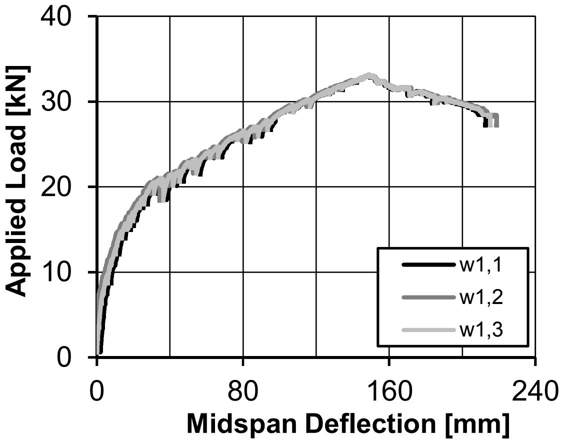

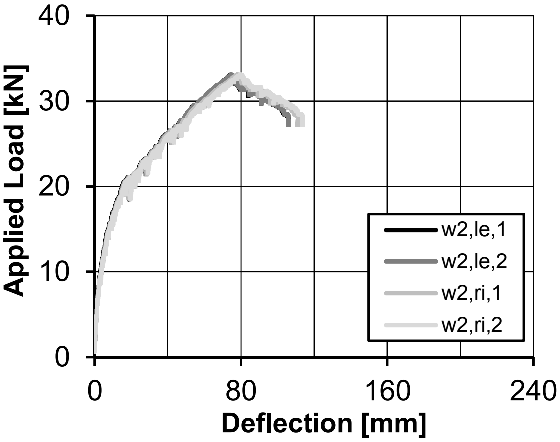

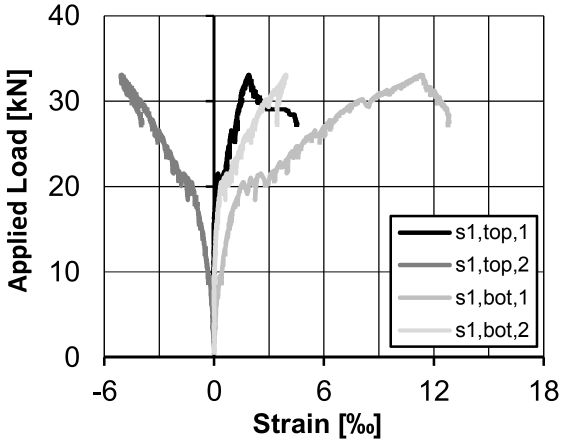

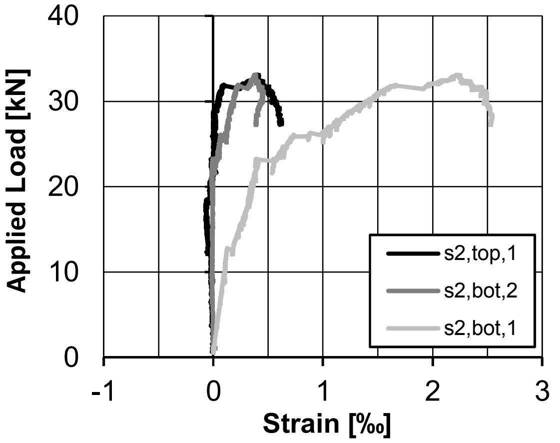

Corresponding crack pattern after testing

Top

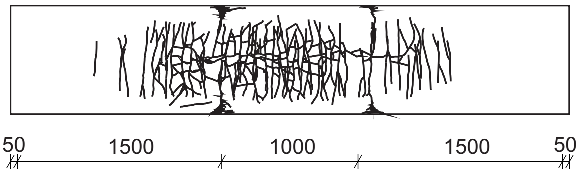

Bottom

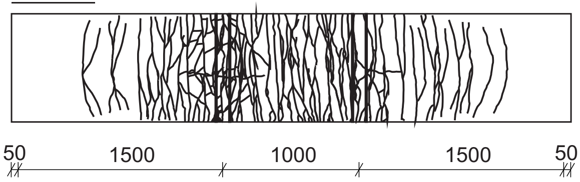

HP-2	CFRP Type [-]	Diameter [mm]	Jacking Stress [MPa]	Number [-]
	bar	5.0	0 MPa	4

Prestressing: End slip

none

Results of four-point bending test and corresponding crack pattern

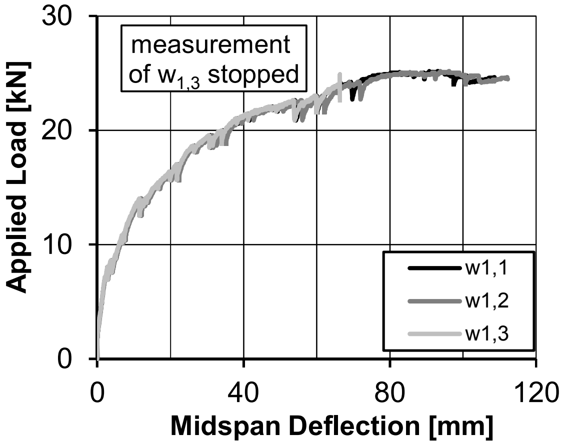

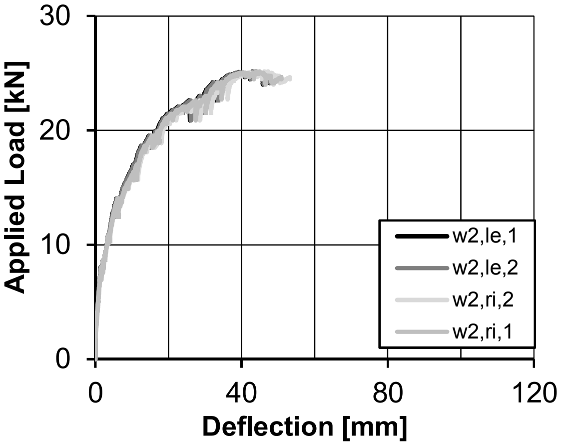

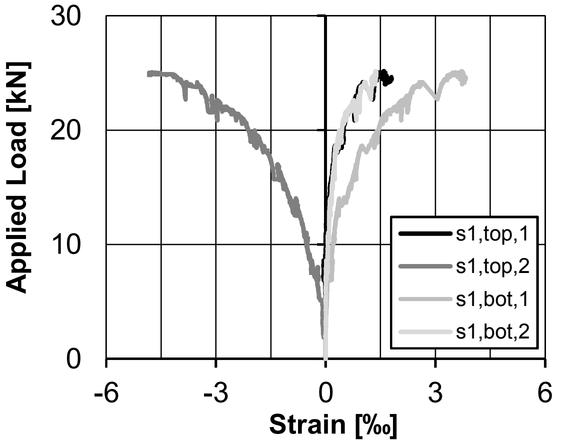

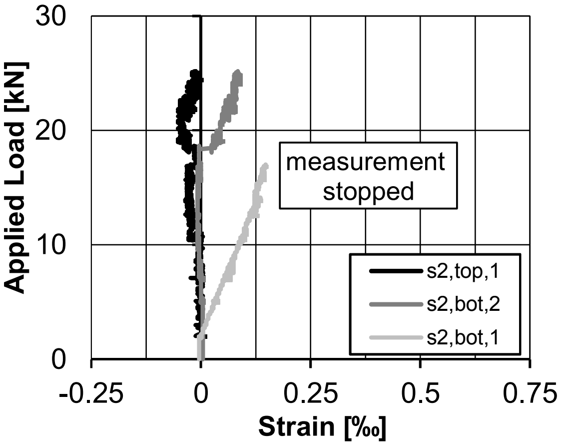

Corresponding crack pattern after testing

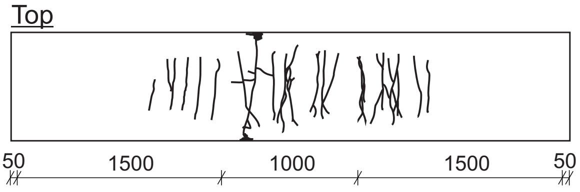

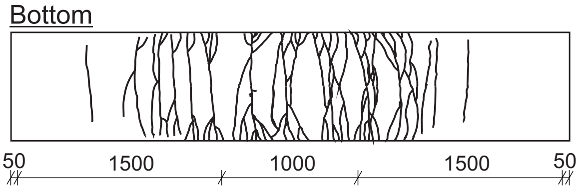

	Type [-]	Diameter [mm]	Jacking Stress [MPa]	Number [-]
HP-3	Steel strand	9.3	800 MPa	6

Results of four-point bending test and corresponding crack pattern

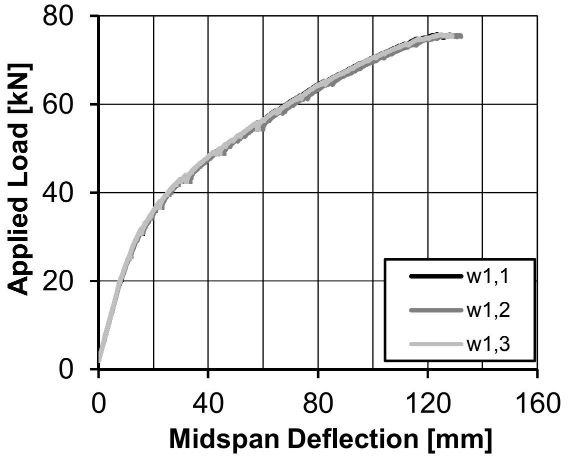

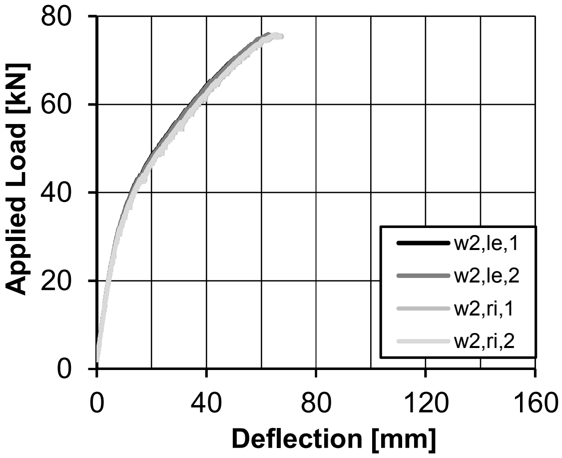

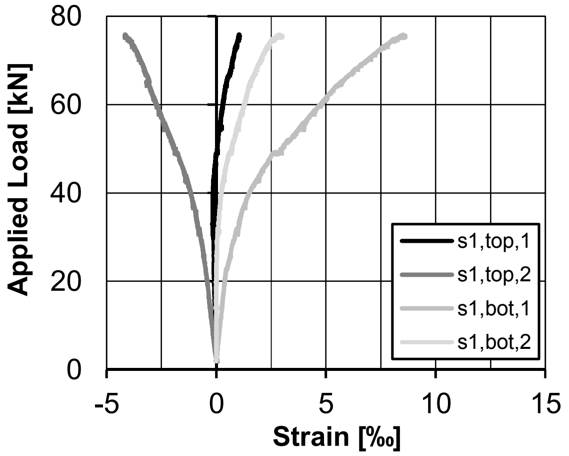

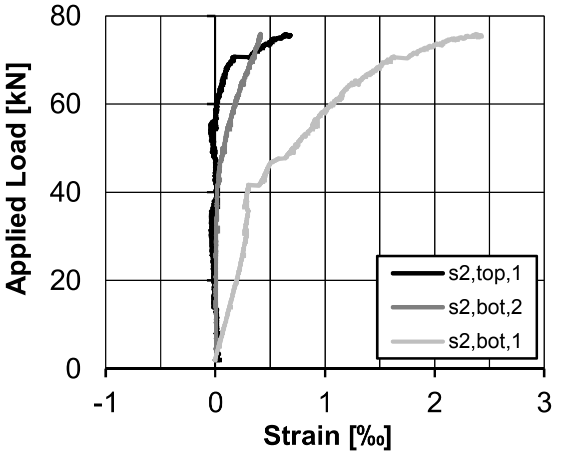

Prestressing: End slip

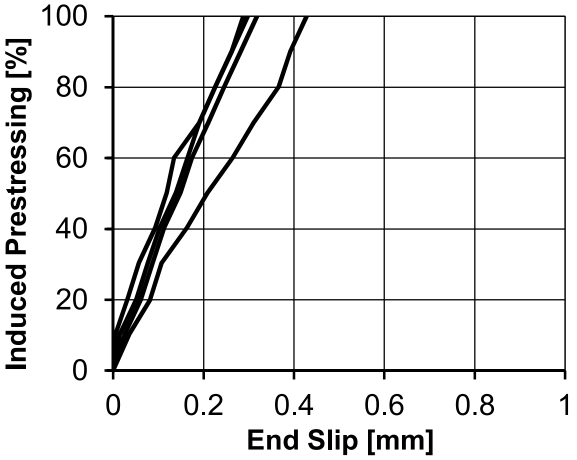

Crack pattern

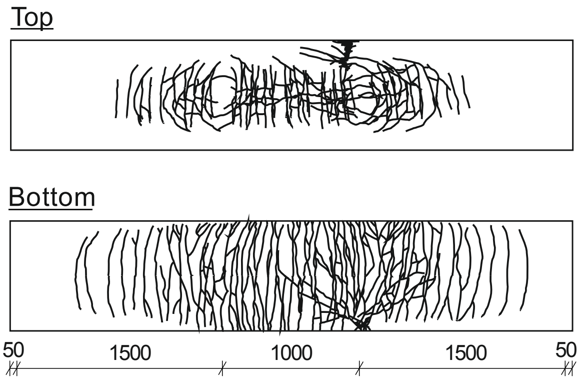

	CFRP Type [-]	Diameter [mm]	Jacking Stress [MPa]	Number [-]
Test HP-4	strand	7.5	675	4

Results of four-point bending test

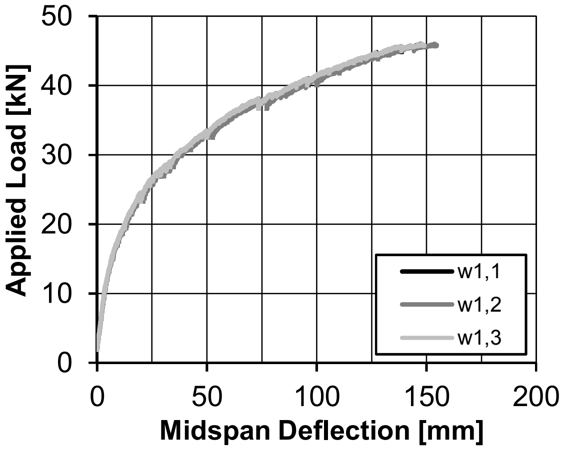

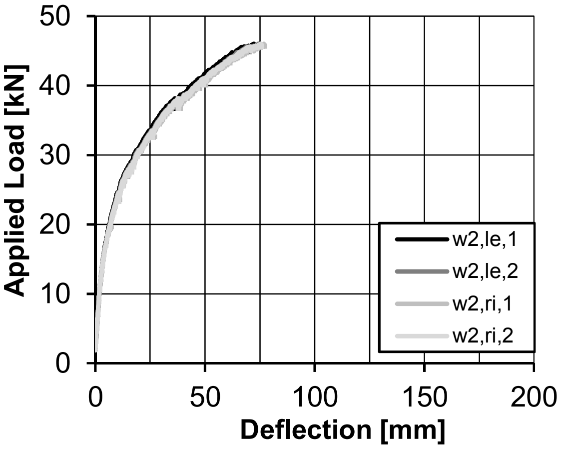

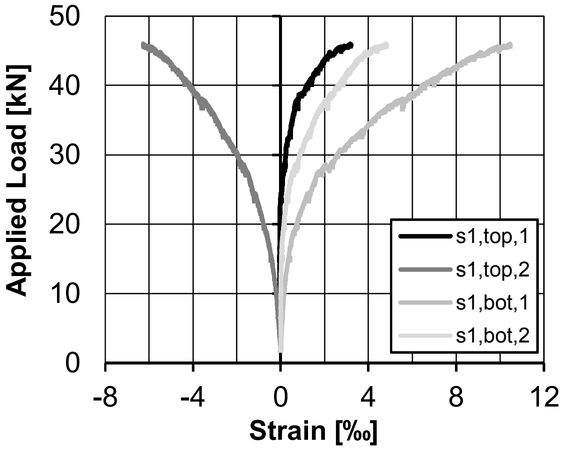

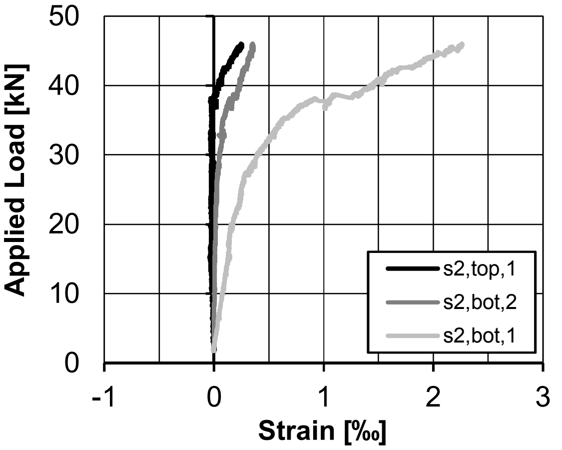

Prestressing: End slip

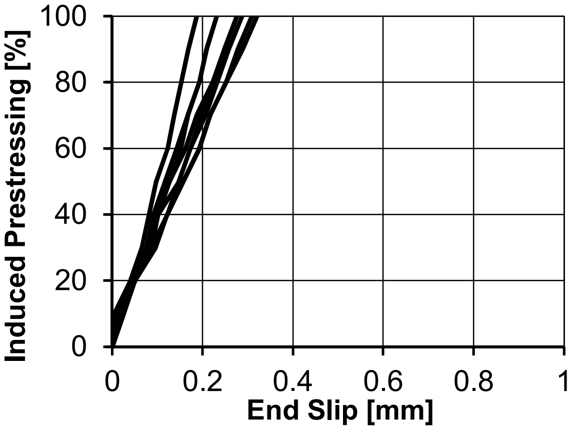

Crack pattern

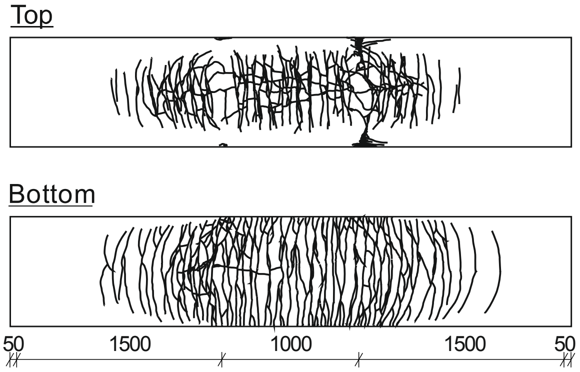

Test HP-5	CFRP Type [-]	Diameter [mm]	Jacking Stress [MPa]	Number [-]
	strand	7.5	1350	4

Results of four-point bending test

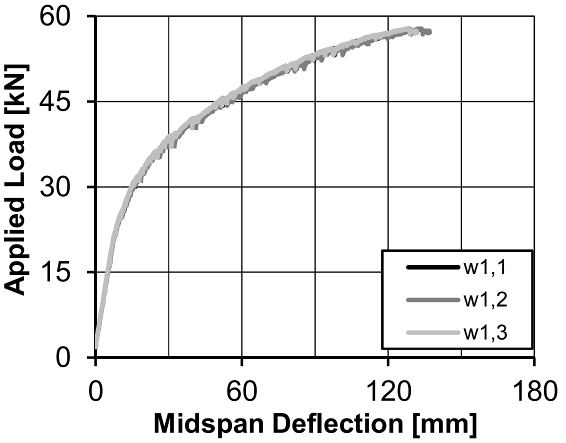

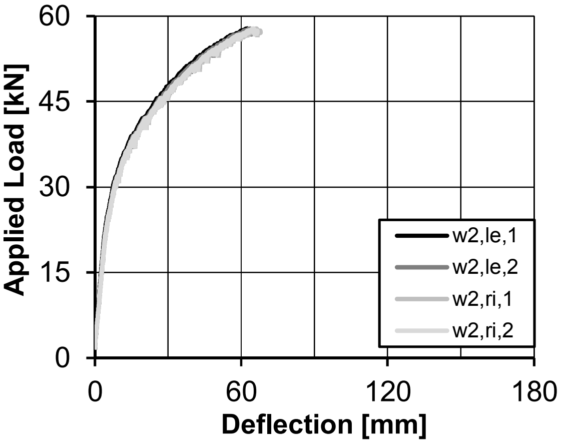

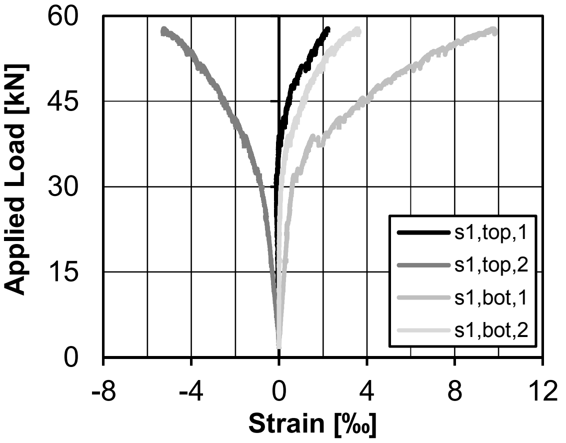

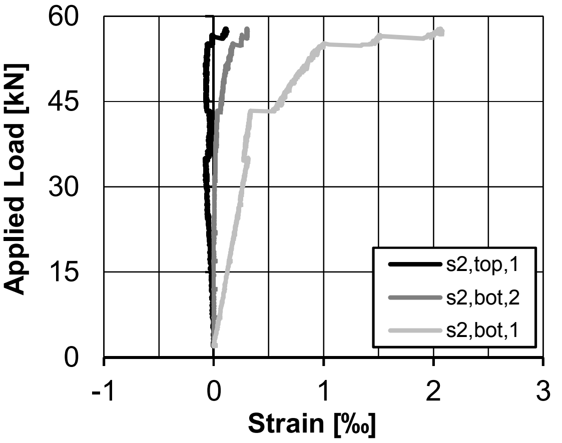

Prestressing: End slip

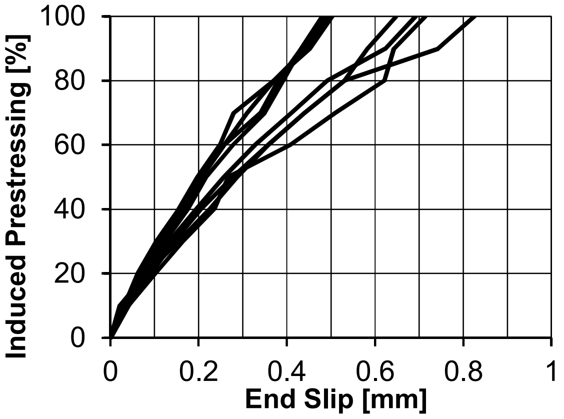

Crack pattern

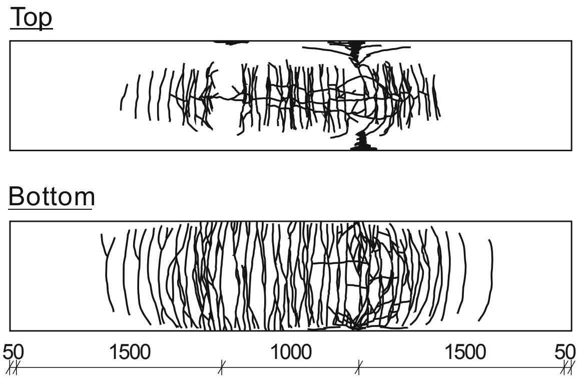

Test HP-6	CFRP Type [-]	Diameter [mm]	Jacking Stress [MPa]	Number [-]
	strand	7.5	675	6

Results of four-point bending test

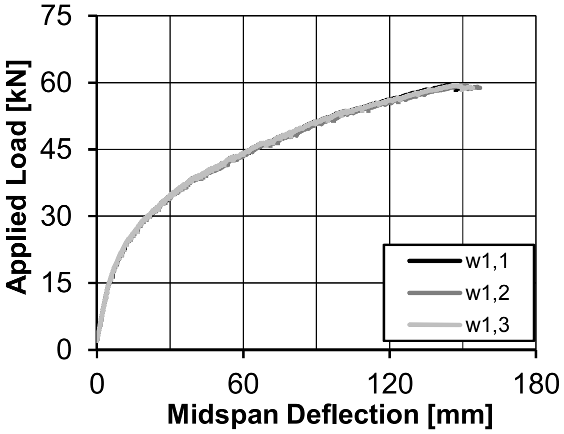

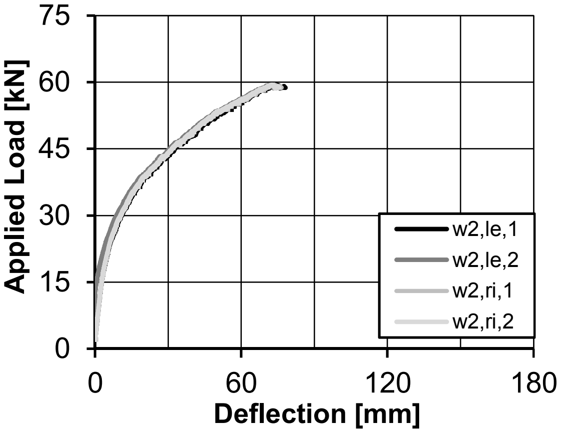

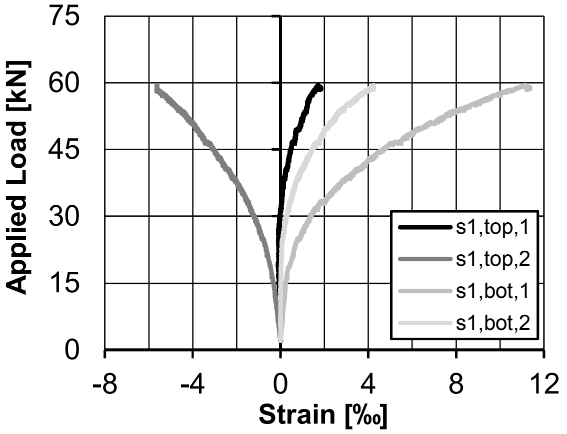

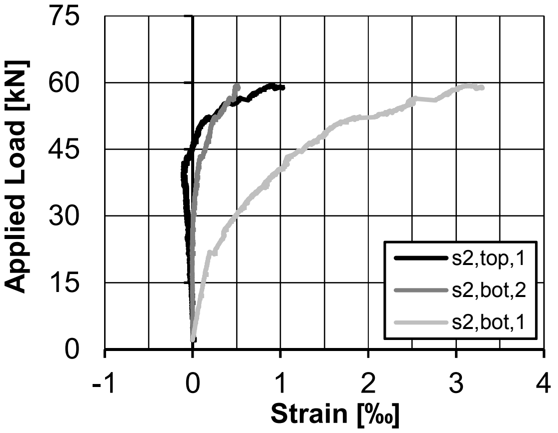

Prestressing: End slip

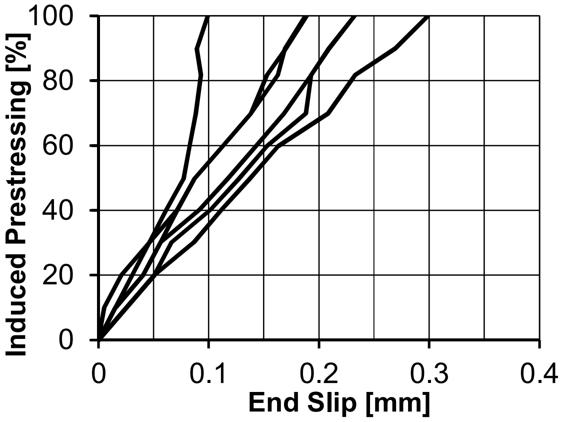

Crack pattern

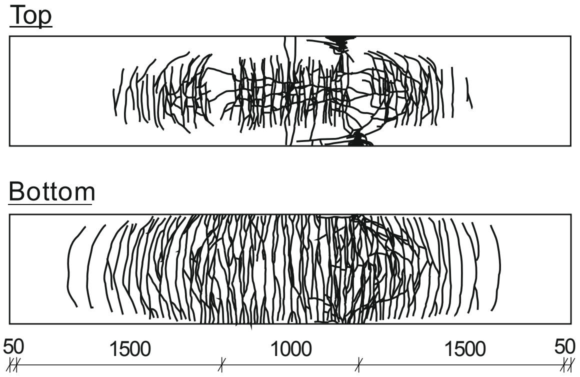

D Sandwich Panels under Flexural Loading

D.1 Flat Sandwich Panels

Test setup

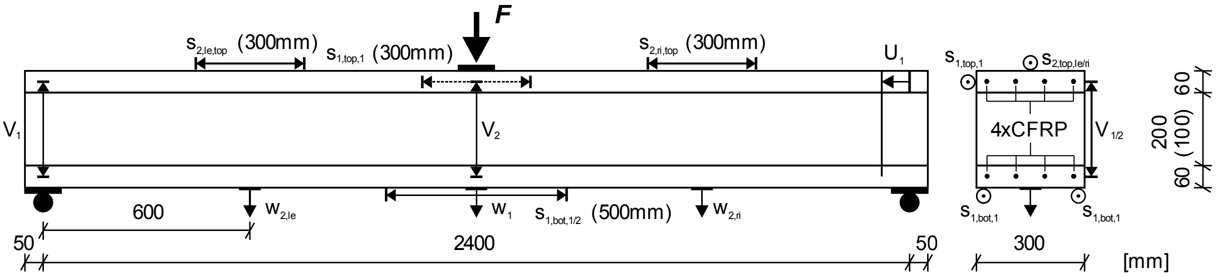

Transfer length

Concrete compressions: Extensometer in same arrangement as for tests on the transfer length. End slip: Relative displacement between tendons and UHPFRC element

Table D.1: Parameter variation of flexural tests on flat sandwich panels

Test No.	CFRP Type		Jacking stress		Shear grid
[-]	[-]		[MPa]		[-]
	bottom	top	bottom	top	
SB-1	---	---	---	---	no
SB-2	bar	bar	0	0	no
SB-3	bar	bar	0	0	yes
SB-4	strand	---	675	---	yes
SB-5	strand	bar	675	0	no
SB-6	strand	strand	675	675	yes
SB-7*	strand	bar	675	0	yes

*h_c = 100 mm

Table D.2: Concrete properties of flat sandwich panels [1d]

Test No.	$f_{cm,cyl,1d}$		$f_{cm,cube,1d}$		$E_{cm,1d}$		$f_{ct,flex,1d}$	
[-]	[MPa]		[MPa]		[MPa]		[MPa]	
	bottom	top	bottom	top	bottom	top	bottom	top
SB-1	NA	NA	NA	NA	NA	NA	NA	NA
SB-2	NA	NA	NA	NA	NA	NA	NA	NA
SB-3	NA	NA	NA	NA	NA	NA	NA	NA
SB-4	49.3	NA	50.0	NA	29,300	NA	4.6	NA
SB-5	58.6	NA	65.8	NA	31,400	NA	6.0	NA
SB-6	95.3	64.7	97.7	78.7	37,200	34,300	7.5	5.6
SB-7	54.2	NA	57.1	NA	29,400	NA	6.9	NA

Table D.3: Concrete properties of flat sandwich panels [28d]

Test No.	$f_{cm,cyl,28d}$		$f_{cm,cube,28d}$		$E_{cm,28d}$		$f_{ct,flex,28d}$	
[-]	[MPa]		[MPa]		[MPa]		[MPa]	
	bottom	top	bottom	top	bottom	top	bottom	top
SB-1	143.6	143.6	170.1	170.1	41,400	41,400	19.3	19.3
SB-2	142.0	142.0	174.6	174.6	44,700	44,700	17.7	17.7
SB-3*	137.6	145.5	166.8	164.6	46,700	46,100	21.1	19.5
SB-4*	137.6	145.5	166.8	164.6	46,700	46,100	21.1	19.5
SB-5	129.6	142.9	171.9	168.9	44,000	42,400	18.7	19.0
SB-6	152.4	142.3	170.5	168.8	43,500	43,200	17.6	19.9
SB-7	142.9	129.6	168.8	171.9	42,400	44,000	19.0	18.7

*: same concreting

	CFRP Type [-]		Diameter [mm]		Jacking Stress [MPa]		Shear grid	Core height [mm]
SB-1	**top**	**bottom**	**top**	**bottom**	**top**	**bottom**		
	Only fibres	Only fibres	Only fibres	Only fibres	---	---	no	200

Crack pattern after testing

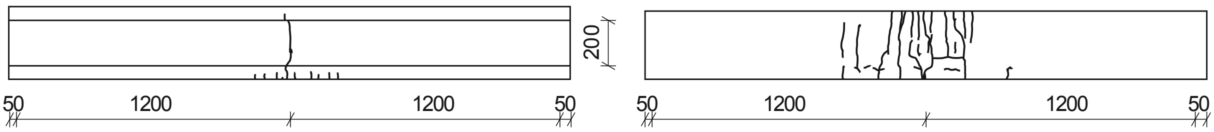

Side

Bottom

Results of three-point bending test

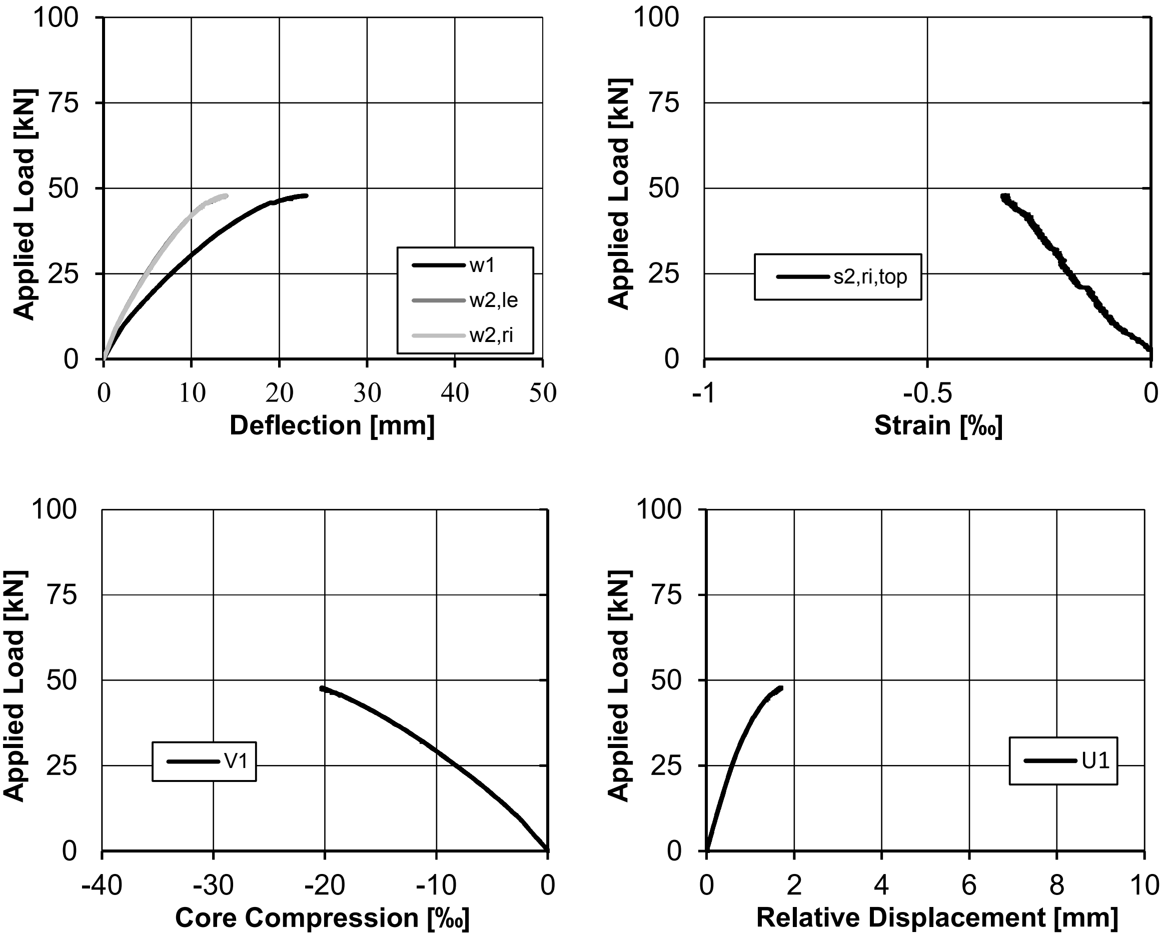

	CFRP Type [-]		Diameter [mm]		Jacking Stress [MPa]		Shear grid	Core height [mm]
SB-2	top	bottom	top	bottom	top	bottom	no	200
	Bar	Bar	5.0	5.0	---	---		

Crack pattern after testing

Side

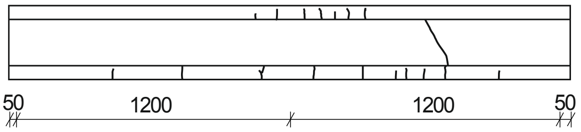

Bottom

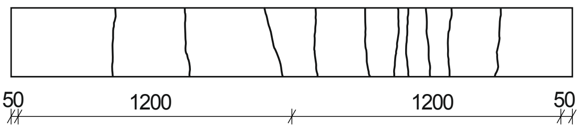

Results of three-point bending test

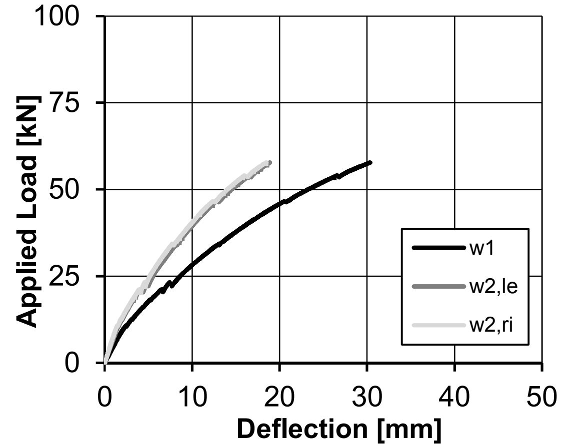

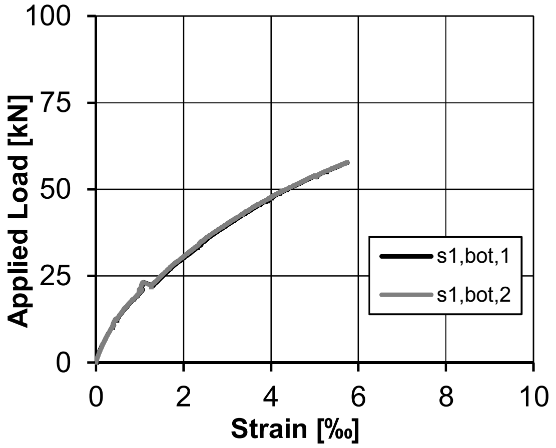

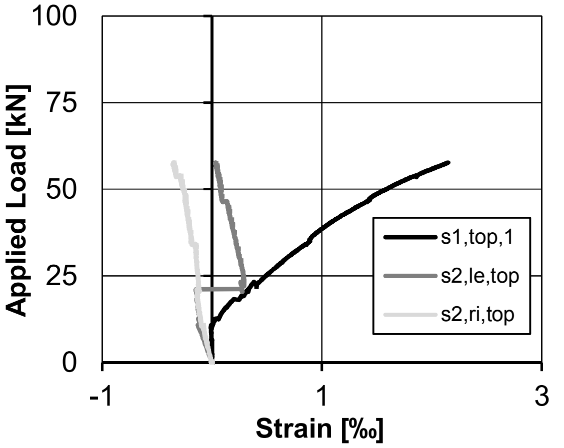

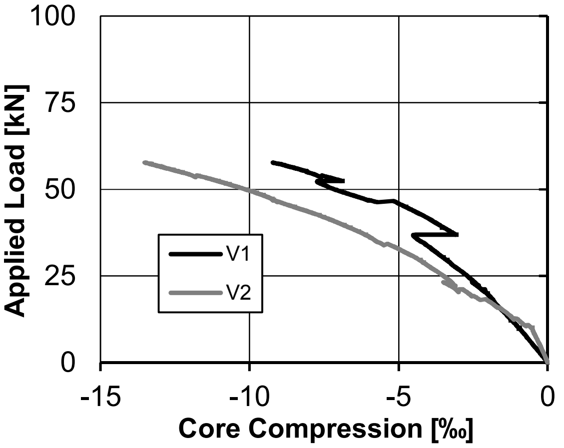

	CFRP Type [-]		Diameter [mm]		Jacking Stress [MPa]		Shear grid	Core height [mm]
SB-3	**top**	**bottom**	**top**	**bottom**	**top**	**bottom**		
	Bar	Bar	5.0	5.0	---	---	yes	200

Results of three-point bending test and crack pattern after testing

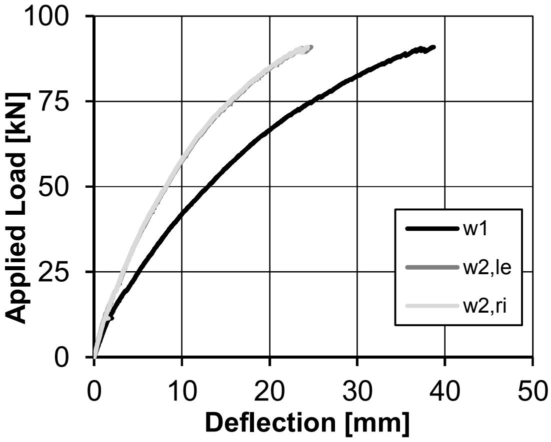

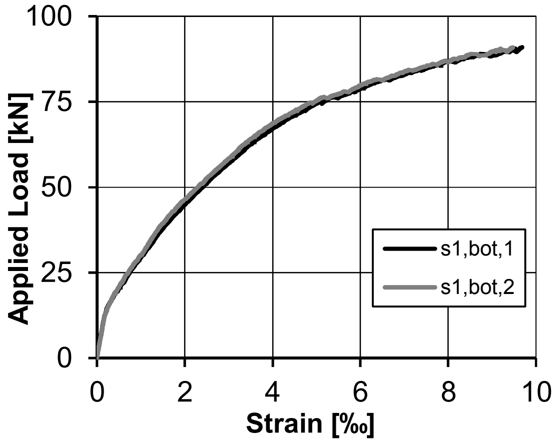

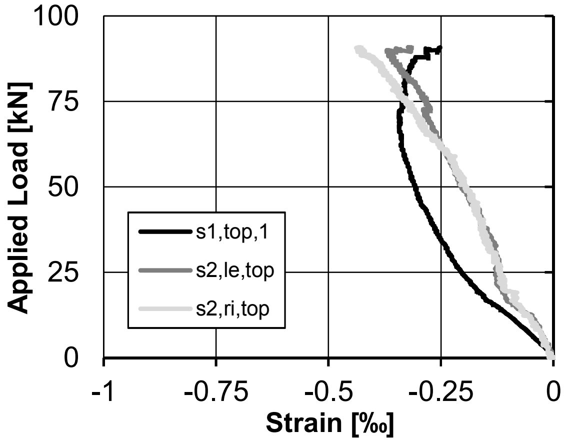

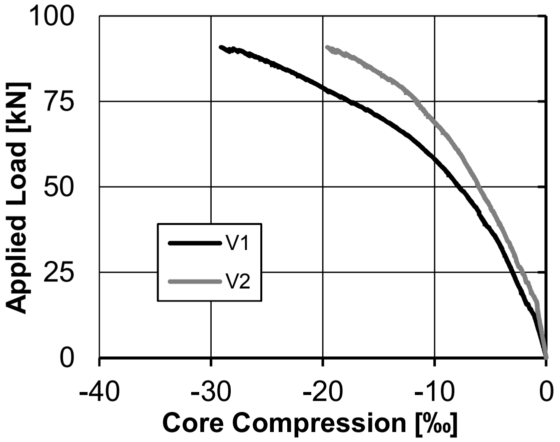

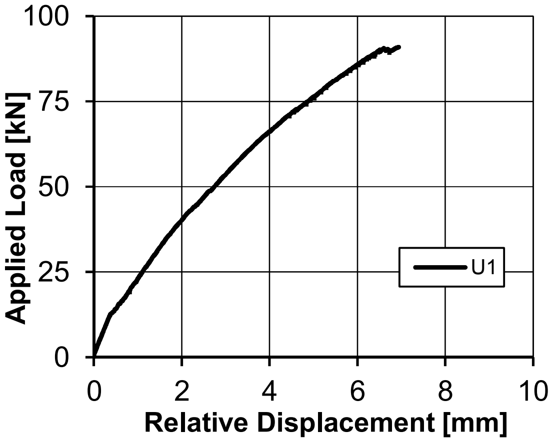

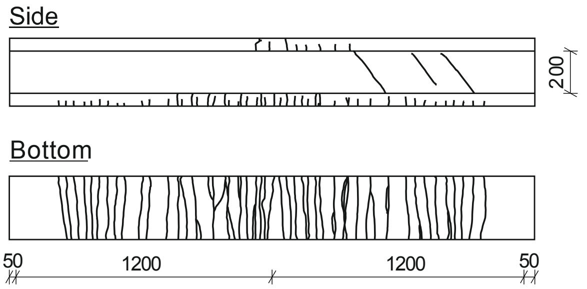

	CFRP Type [-]		Diameter [mm]		Jacking Stress [MPa]		Shear grid	Core height [mm]
SB-4	**top**	**bottom**	**top**	**bottom**	**top**	**bottom**		
	Only fibres	Strand	---	7.5	---	675	yes	200

Prestressing: Compression strains and end slip

Measurement of compression strains not possible due to production process

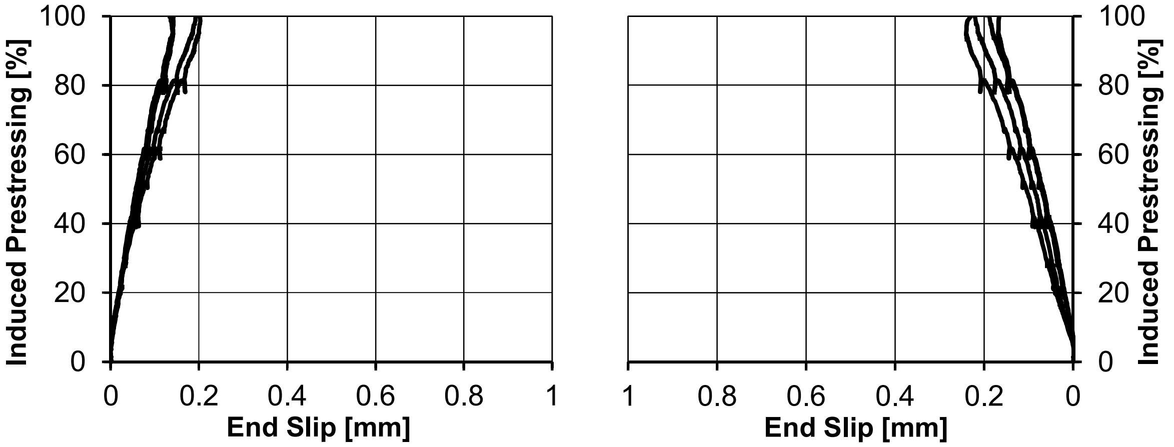

Crack pattern after testing

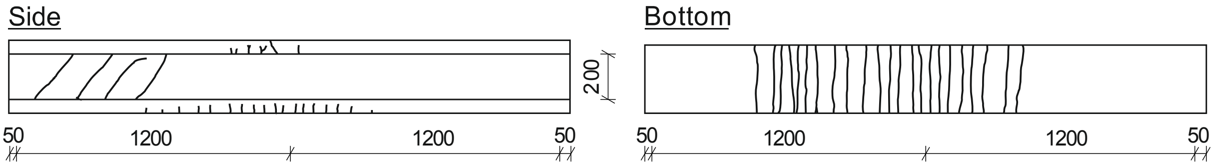

Results of three-point bending test

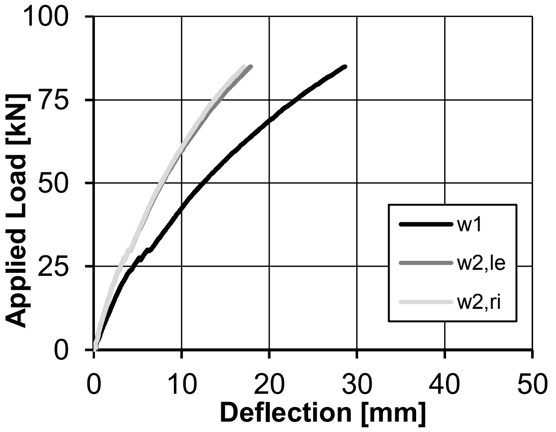

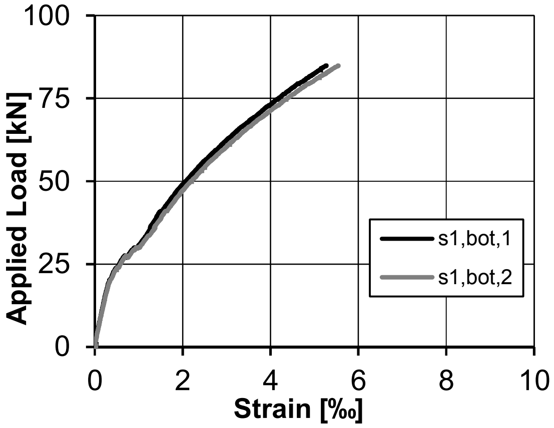

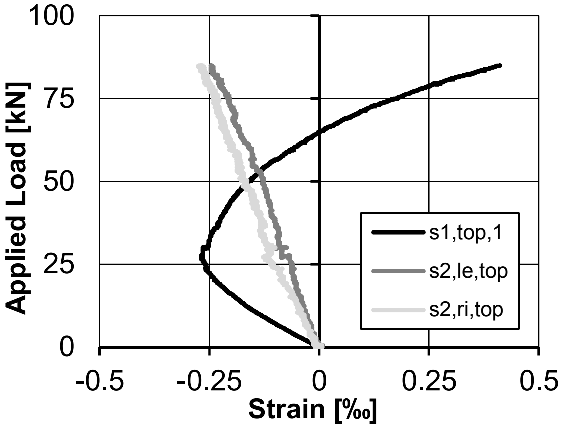

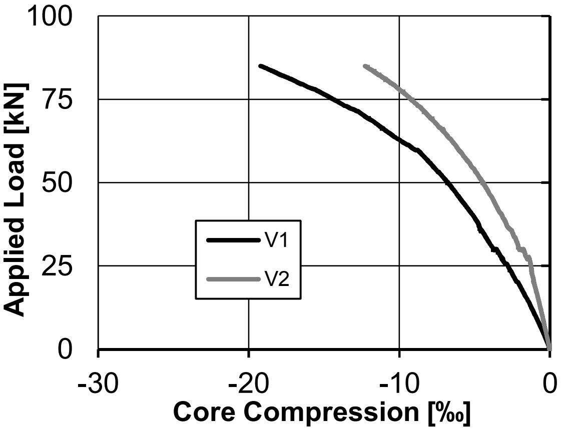

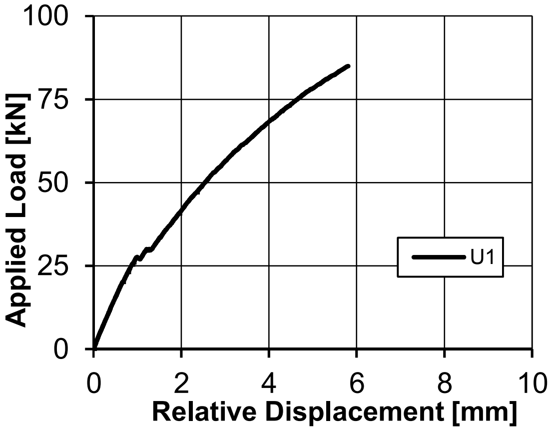

	CFRP Type [-]		Diameter [mm]		Jacking Stress [MPa]		Shear grid	Core height [mm]
SB-5	**top**	**bottom**	**top**	**bottom**	**top**	**bottom**	no	200
	Bar	Strand	5.0	7.5	---	675		

Prestressing: Compression strains and end slip

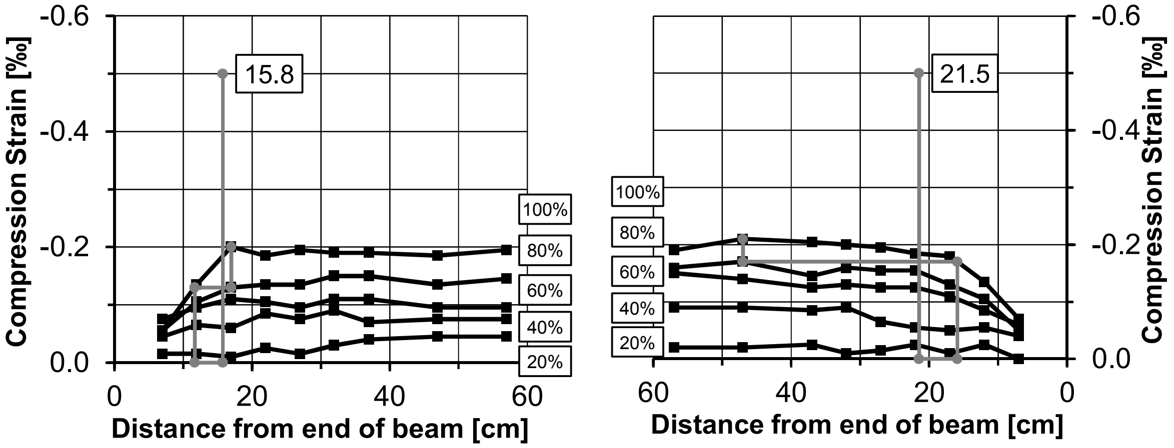

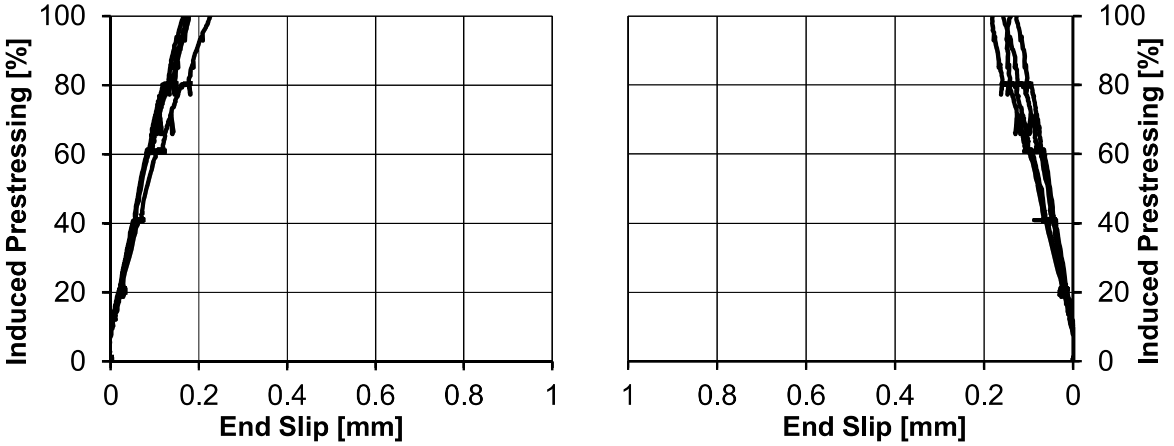

Crack pattern after testing

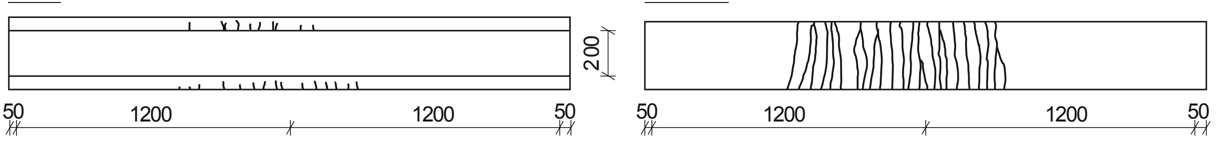

Side

Bottom

Results of three-point bending test

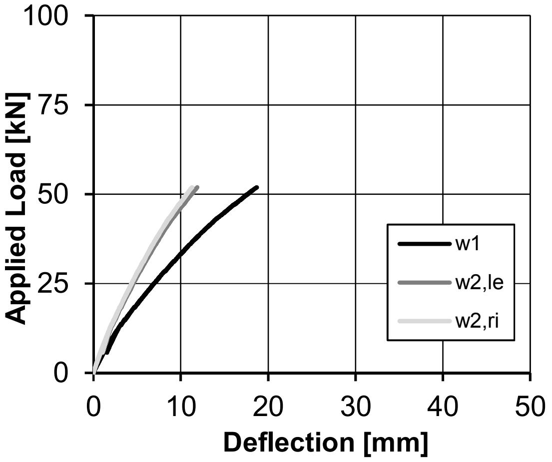

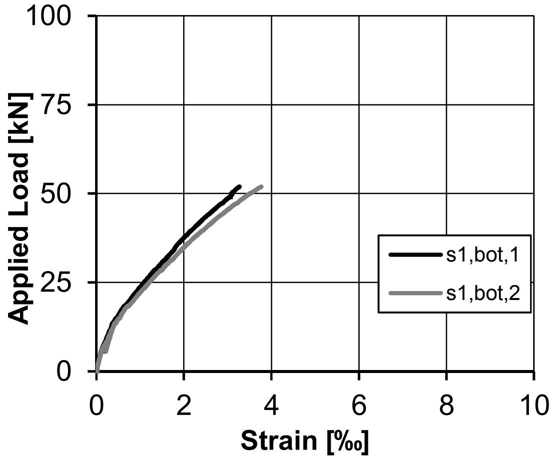

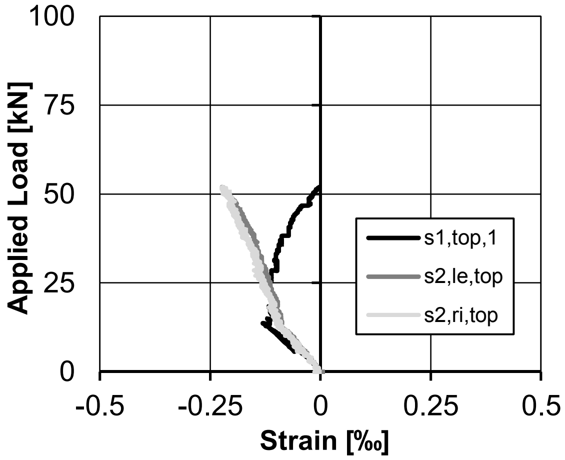

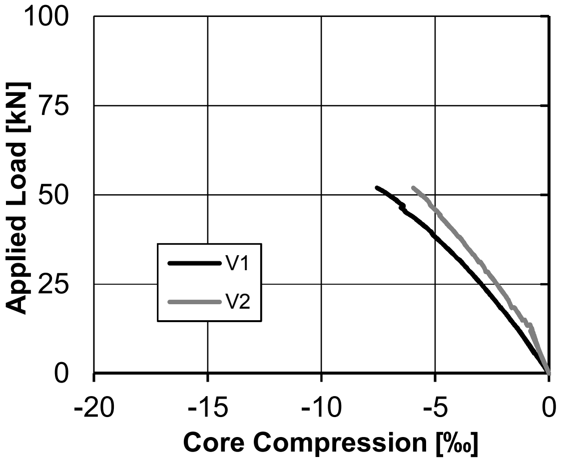

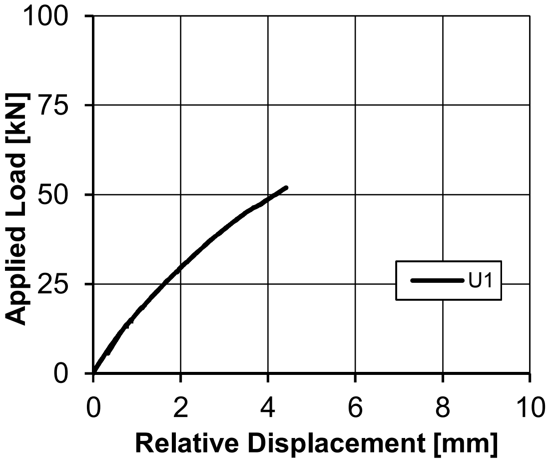

	CFRP Type [-]		Diameter [mm]		Jacking Stress [MPa]		Shear grid	Core height [mm]
SB-6	**top**	**bottom**	**top**	**bottom**	**top**	**bottom**	yes	200
	Strand	Strand	7.5	7.5	675	675		

Prestressing: Compression strains and end slip

Measurement of compression strains not possible due to production process

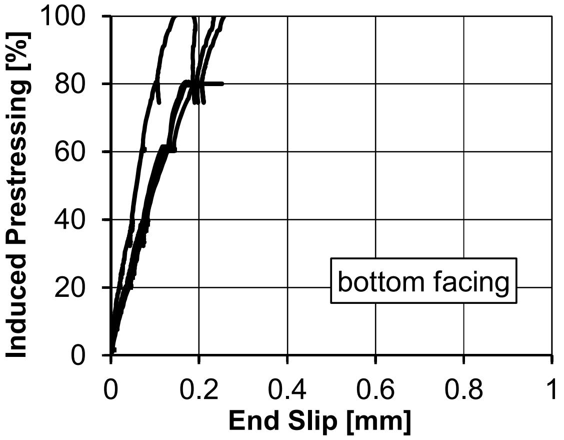

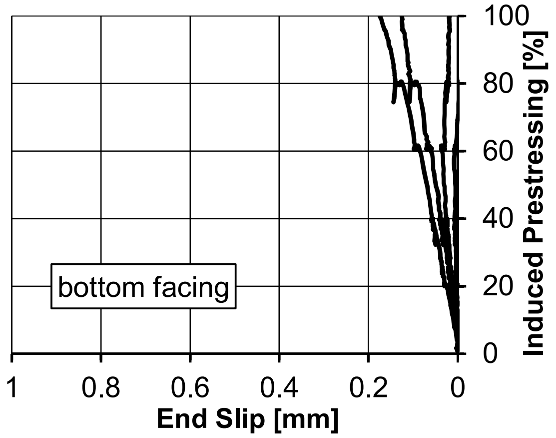

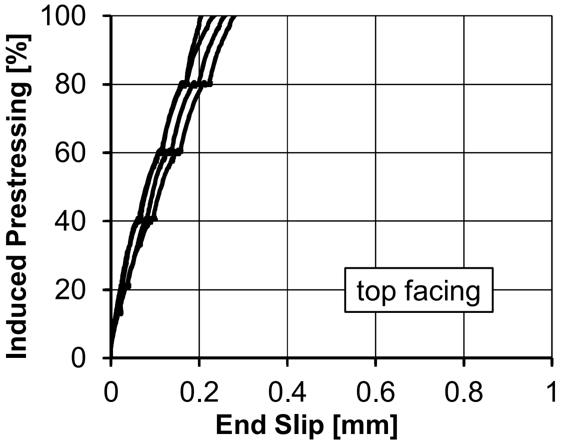

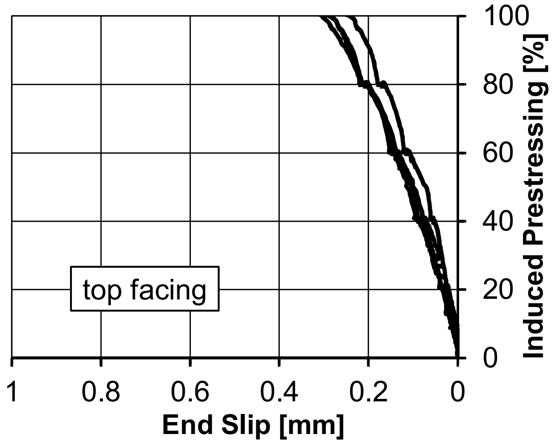

Crack pattern after testing

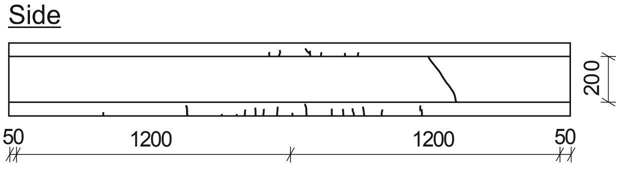

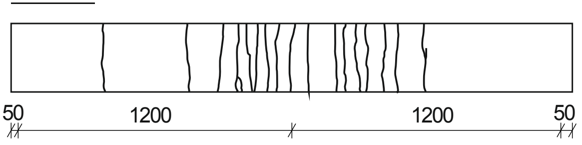

Results of three-point bending test

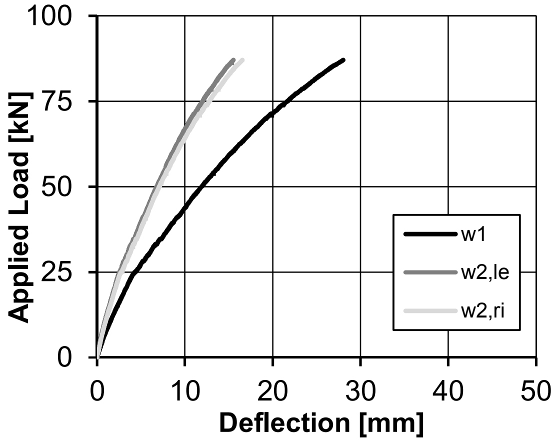

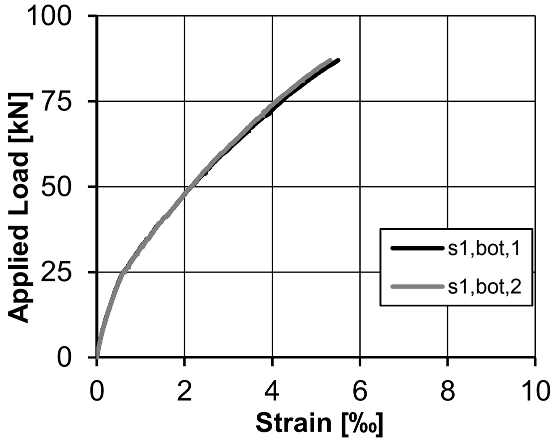

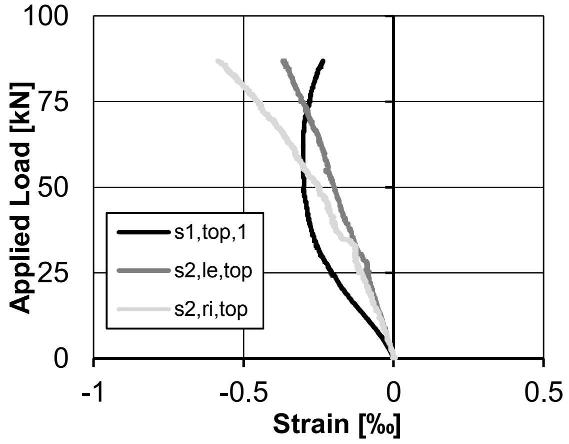

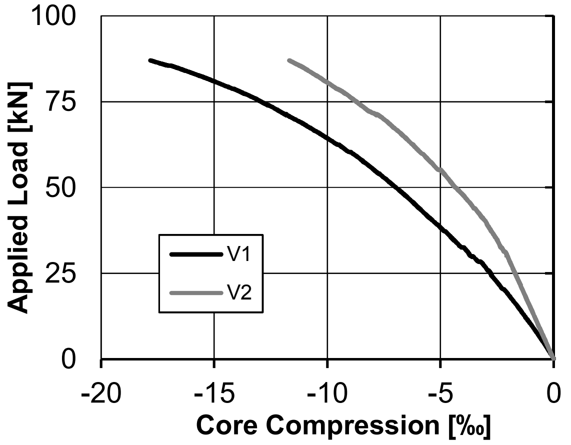

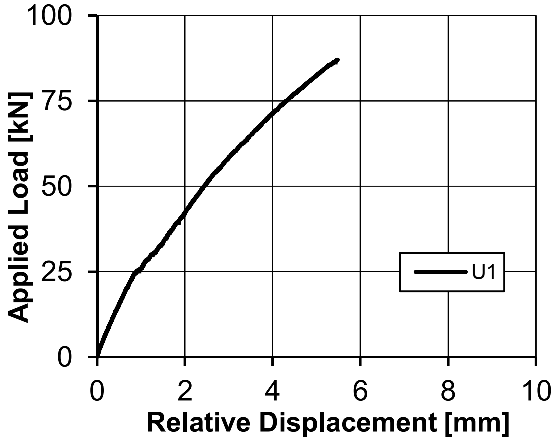

	CFRP Type [-]		Diameter [mm]		Jacking Stress [MPa]		Shear grid	Core height [mm]
SB-7	**top**	**bottom**	**top**	**bottom**	**top**	**bottom**	yes	100
	Bar	Strand	5.0	7.5	---	675		

Prestressing: Compression strains and end slip

Concrete compression strains and end slip not measured

Crack pattern after testing

Side

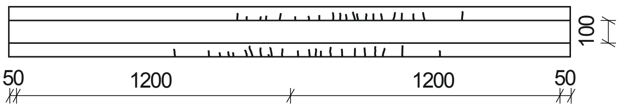

Bottom

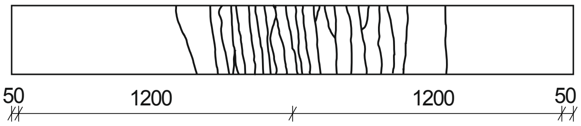

Results of three-point bending test

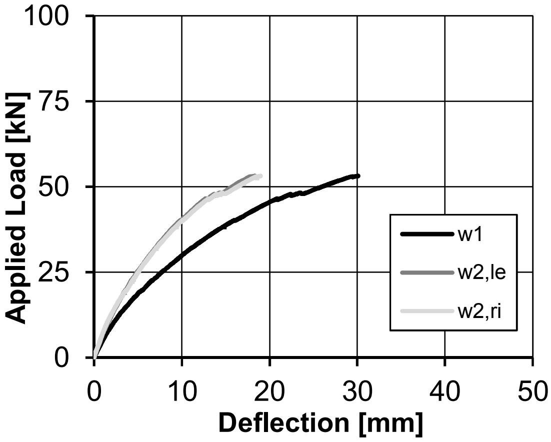

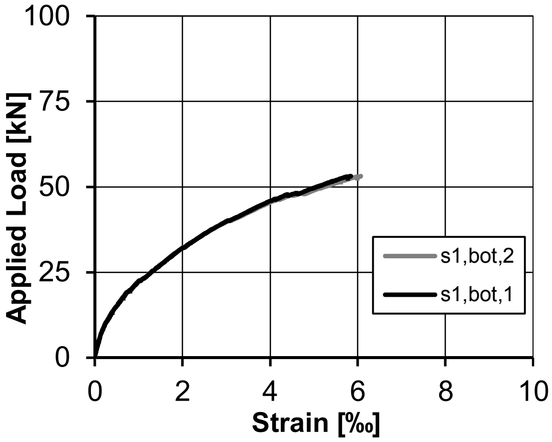

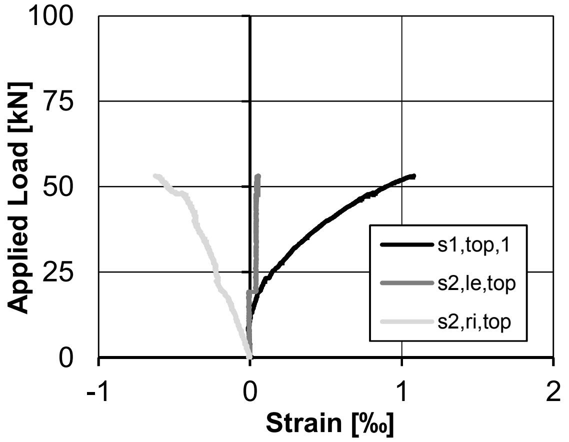

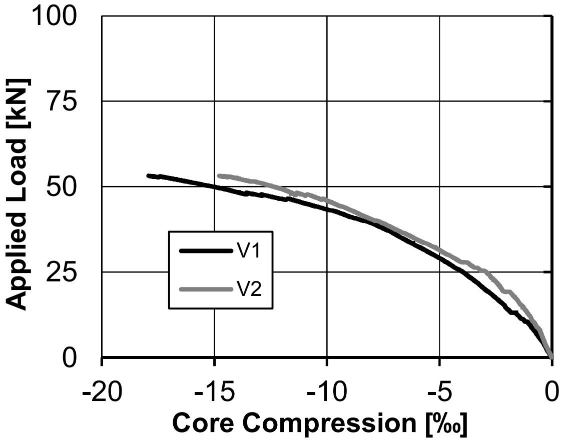

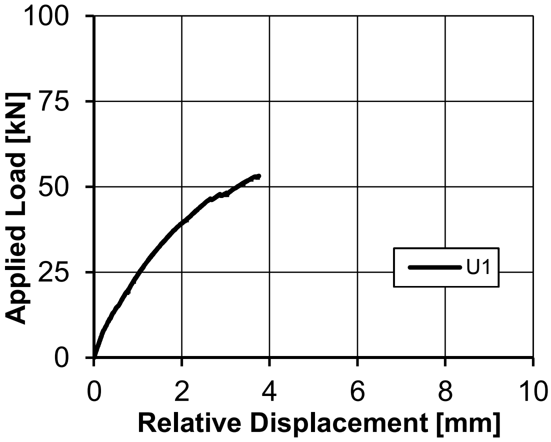

D.2 Folded Plate Sandwich Panels

Test setup

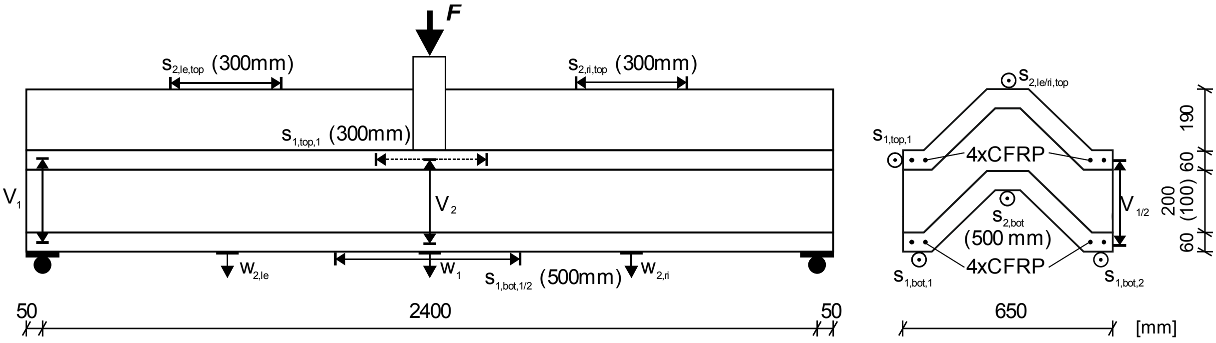

Transfer length

Concrete compressions: Extensometer in same arrangement as for tests on the transfer length at bottom flange.

End slip: Relative displacement between tendons and UHPFRC element

Table D.4: Parameter variation of flexural tests on folded plate sandwich panels

Test No.	CFRP Type		Jacking stress	
[-]	[-]		[MPa]	
	bottom	top	bottom	top
SFP-1	strand	---	675	---
SFP-2	bar	---	1,350	---
SFP-3	strand	bar	1,350	0
SFP-4	bar	bar	0	0
SFP-5	strand	strand	675	675
SFP-6	strand	strand	1,350	675
SFP-7*	strand	strand	675	675

*h_c = 100 mm

Table D.5: Concrete properties of folded plate sandwich panels [1d]

Test No.	$f_{cm,cyl,1d}$		$f_{cm,cube,1d}$		$E_{cm,1d}$		$f_{ct,flex,1d}$	
[-]	**[MPa]**		**[MPa]**		**[MPa]**		**[MPa]**	
	bottom	**top**	**bottom**	**top**	**bottom**	**top**	**bottom**	**top**
SFP-1	39.8	NA	45.0	NA	24,600	NA	6.6	NA
SFP-2	48.7	NA	66.2	NA	29,200	NA	9.1	NA
SFP-3	60.7	NA	68.9	NA	34,900	NA	8.4	NA
SFP-4	NA	NA	NA	NA	NA	NA	NA	NA
SFP-5	---	88.2	---	96.1	---	40,900	---	10.0
SFP-6	90.4	96.1	96.3	106.5	41,100	---	10.5	15.8
SFP-7	81.8	79.5	73.8	83.1	36,300	37,400	8.5	9.6

Table D.6: Concrete properties of folded plate sandwich panels [28d]

Test No.	$f_{cm,cyl,28d}$		$f_{cm,cube,28d}$		$E_{cm,28d}$		$f_{ct,flex,28d}$	
[-]	**[MPa]**		**[MPa]**		**[MPa]**		**[MPa]**	
	bottom	**top**	**bottom**	**top**	**bottom**	**top**	**bottom**	**top**
SFP-1	143.6	149.8	170.1	166.6	41,400	43,900	19.3	28.5
SFP-2	164.4	152.8	176.1	171.9	44,600	45,200	16.2	22.0
SFP-3	151.4	162.5	---	150.1	48,500	47,800	22.1	22.6
SFP-4	153.1	164.5	173.3	178.7	45,900	45,800	19.6	19.0
SFP-5	146.1	150.0	147.1	166.1	45,600	43,700	22.0	19.8
SFP-6	---	151.8	163.7	147.8	45,600	45,900	21.0	20.6
SFP-7	141.2	145.1	171.9	156.1	46,200	45,900	22.2	16.4

	CFRP Type [-]		Diameter [mm]		Jacking Stress [MPa]		Core height [mm]
SFP-1	**Top**	**Bottom**	**Top**	**Bottom**	**Top**	**Bottom**	200
	Only fibres	strand	Only Fibres	7.5	---	675	

Prestressing: Compression strains and end slip

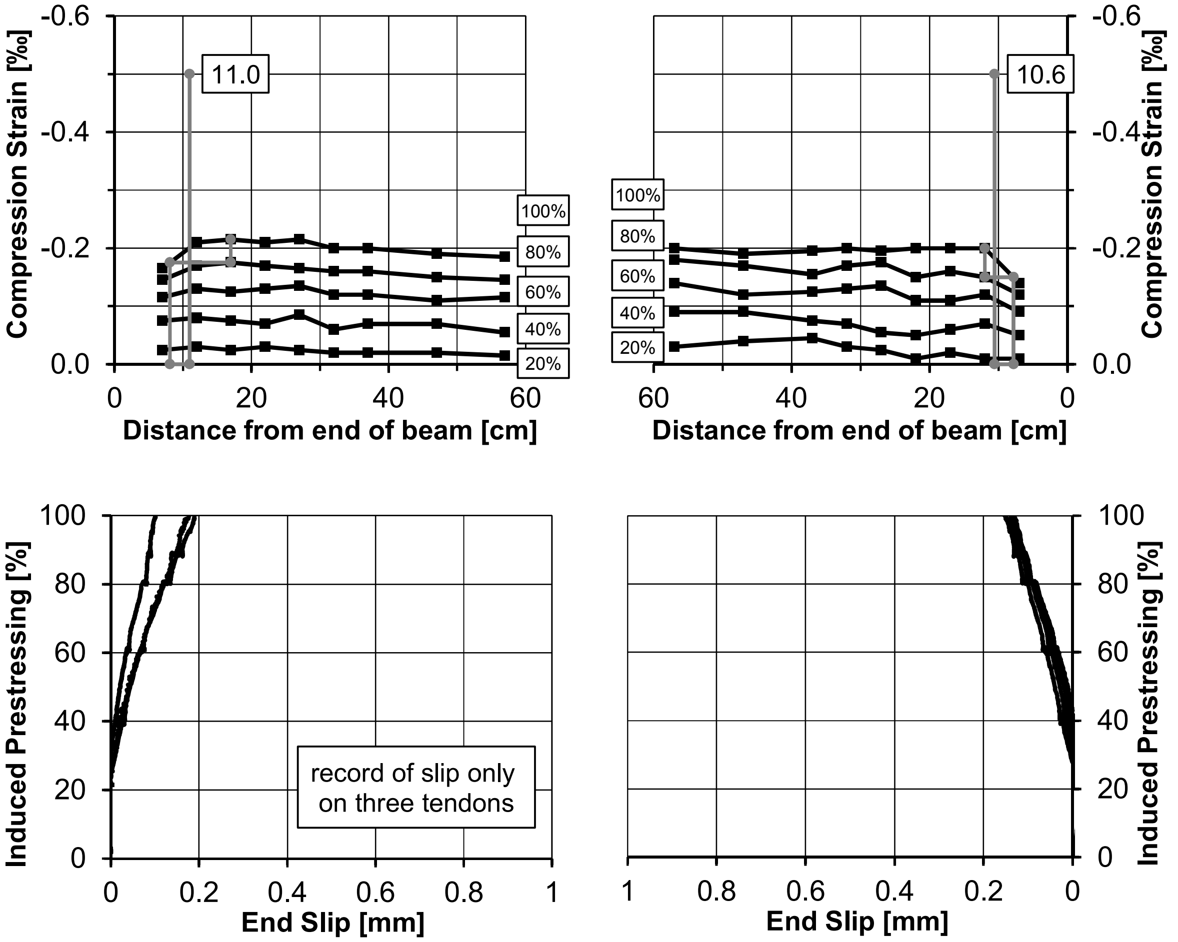

Crack pattern after testing

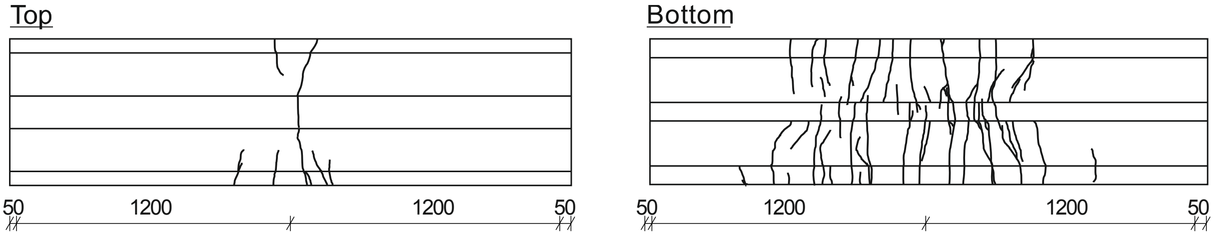

Results of three-point bending test

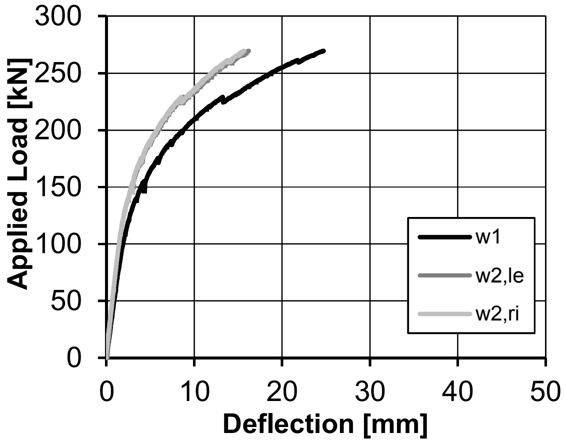

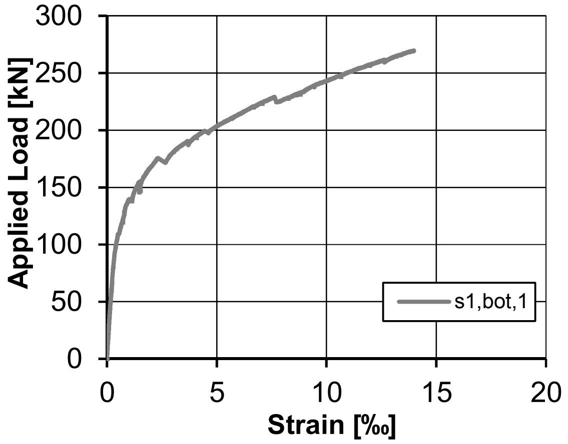

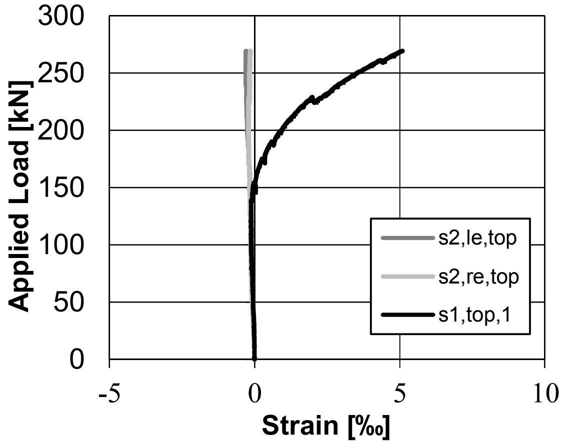

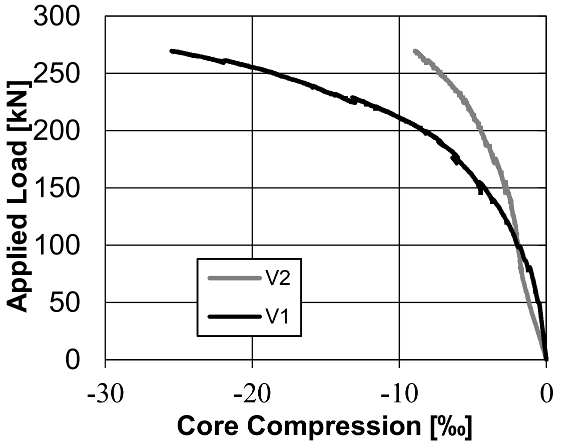

	CFRP Type [-]		Diameter [mm]		Jacking Stress [MPa]		Core height [mm]
SFP-2	**Top**	**Bottom**	**Top**	**Bottom**	**Top**	**Bottom**	200
	Only fibres	Bar	Only Fibres	5.0	---	1350	

Prestressing: Compression strains and end slip

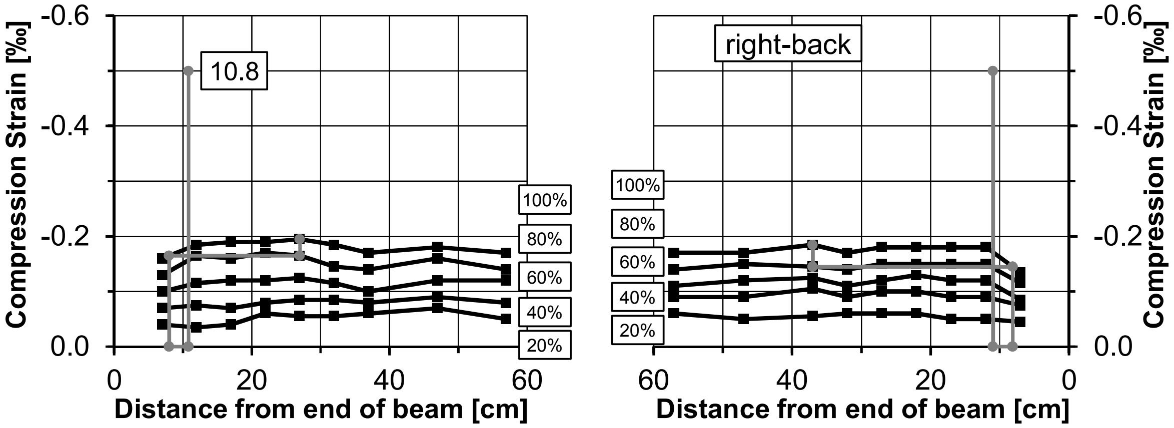

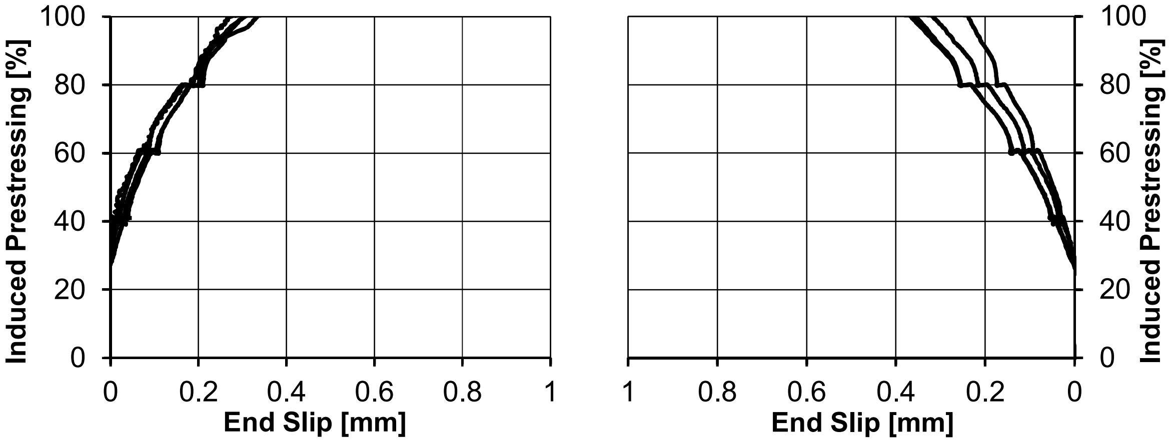

Crack pattern after testing

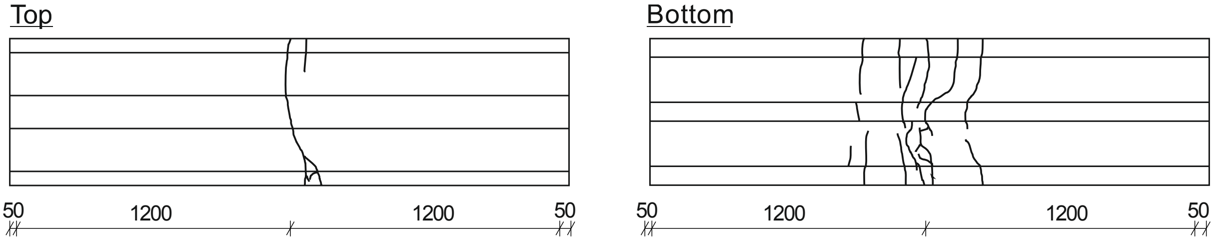

Results of three-point bending test

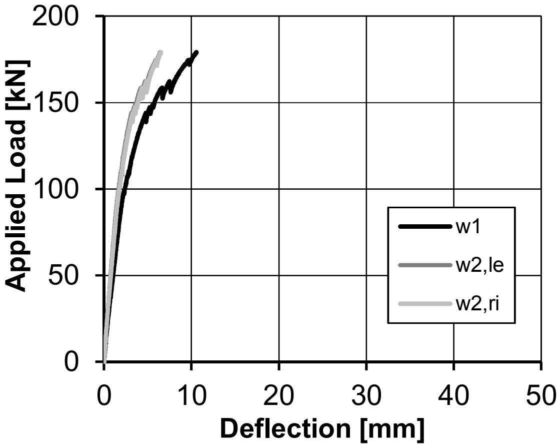

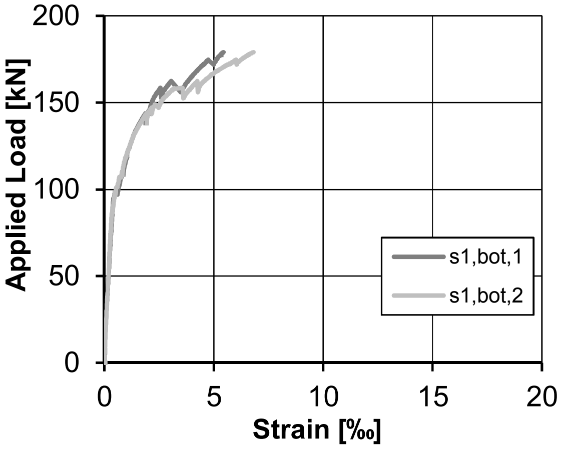

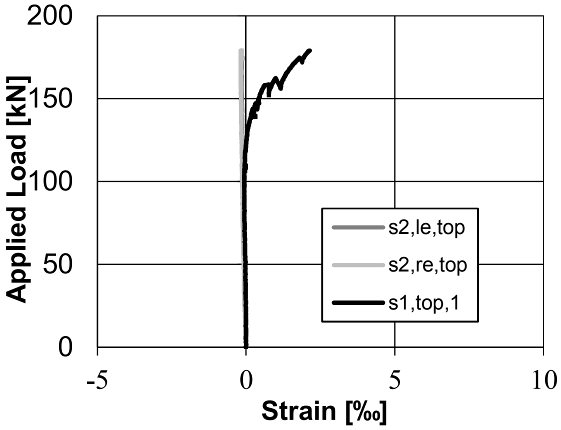

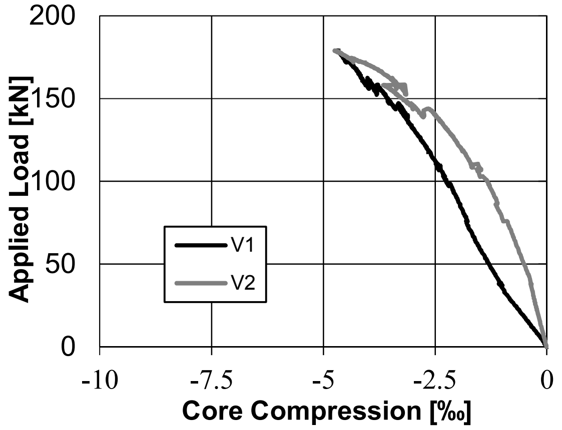

	CFRP Type [-]		Diameter [mm]		Jacking Stress [MPa]		Core height [mm]
SFP-3	**Top**	**Bottom**	**Top**	**Bottom**	**Top**	**Bottom**	200
	Bar	Strand	5.0	7.5	0	1350	

Prestressing: Compression strains and end slip

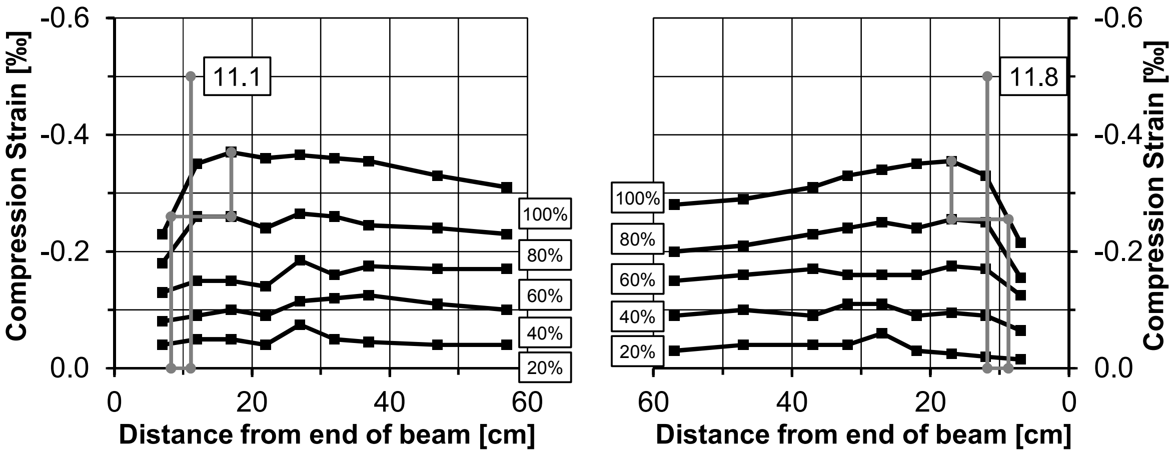

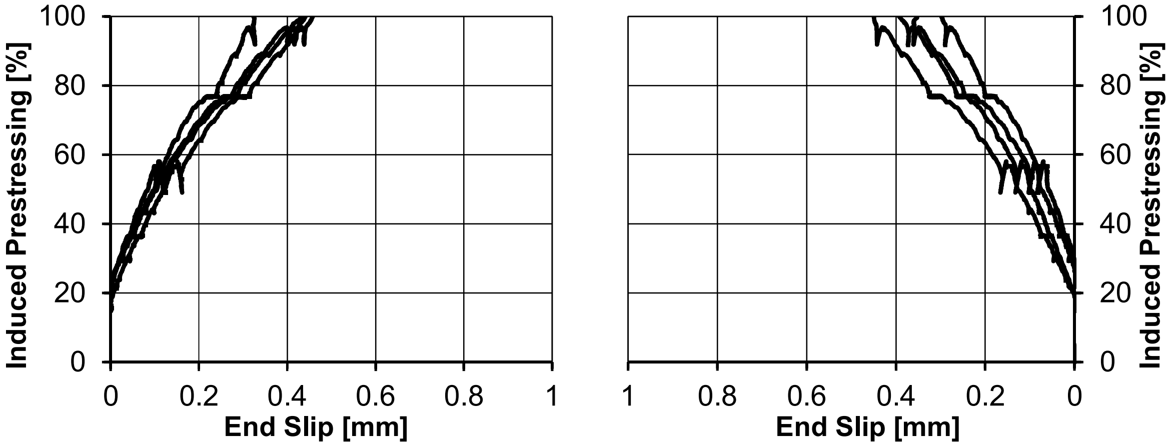

Crack pattern after testing

Top

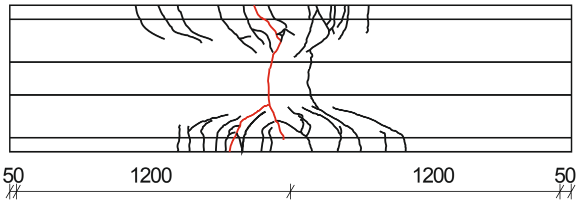

Bottom

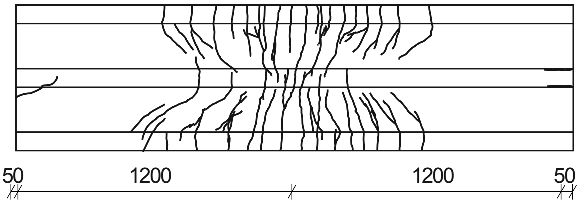

Results of three-point bending test

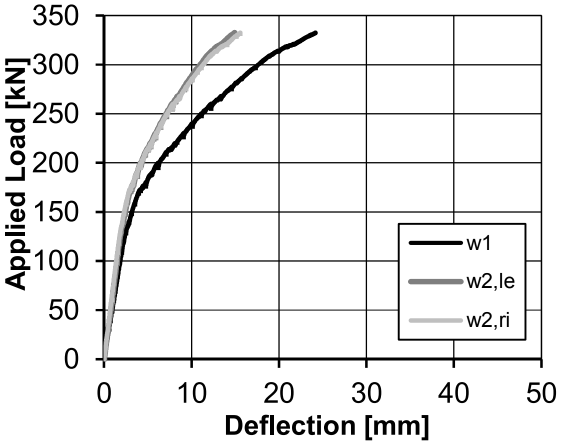

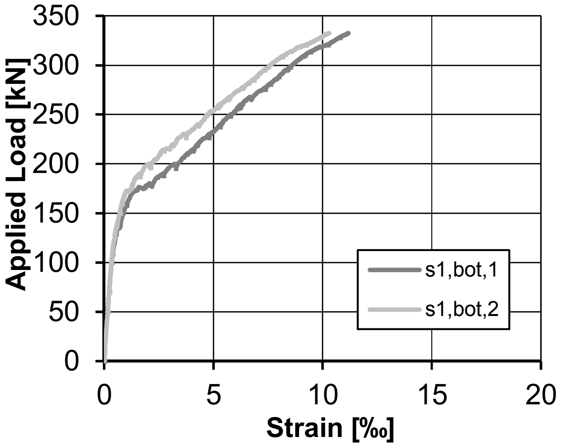

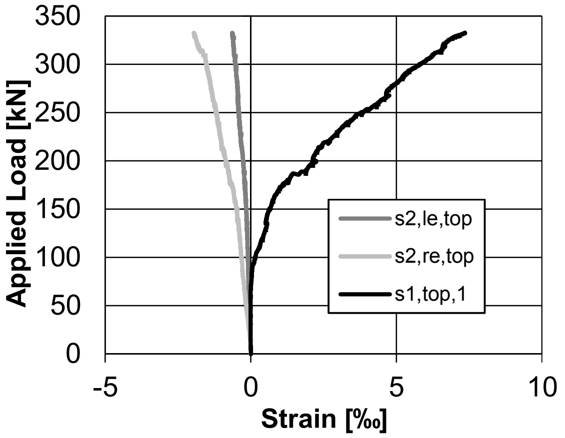

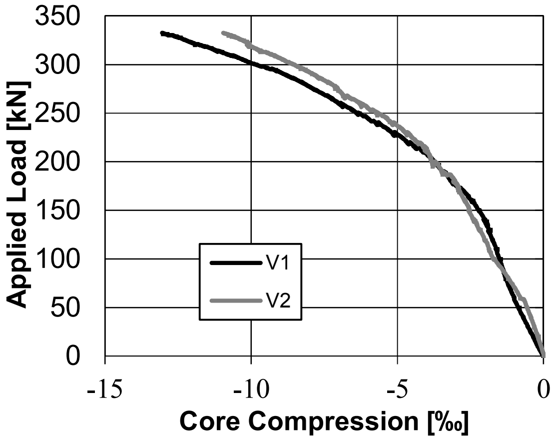

	CFRP Type [-]		Diameter [mm]		Jacking Stress [MPa]		Core height [mm]
SFP-4	**Top**	**Bottom**	**Top**	**Bottom**	**Top**	**Bottom**	200
	Bar	Bar	5.0	5.0	0	0	

Prestressing: Compression strains and end slip

NA

Crack pattern after testing

Top

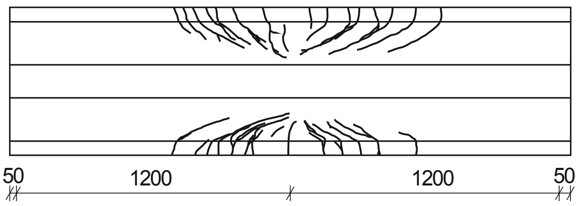

Bottom

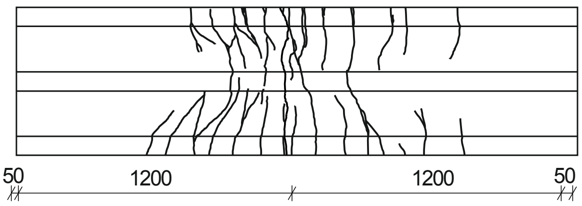

Results of three-point bending test

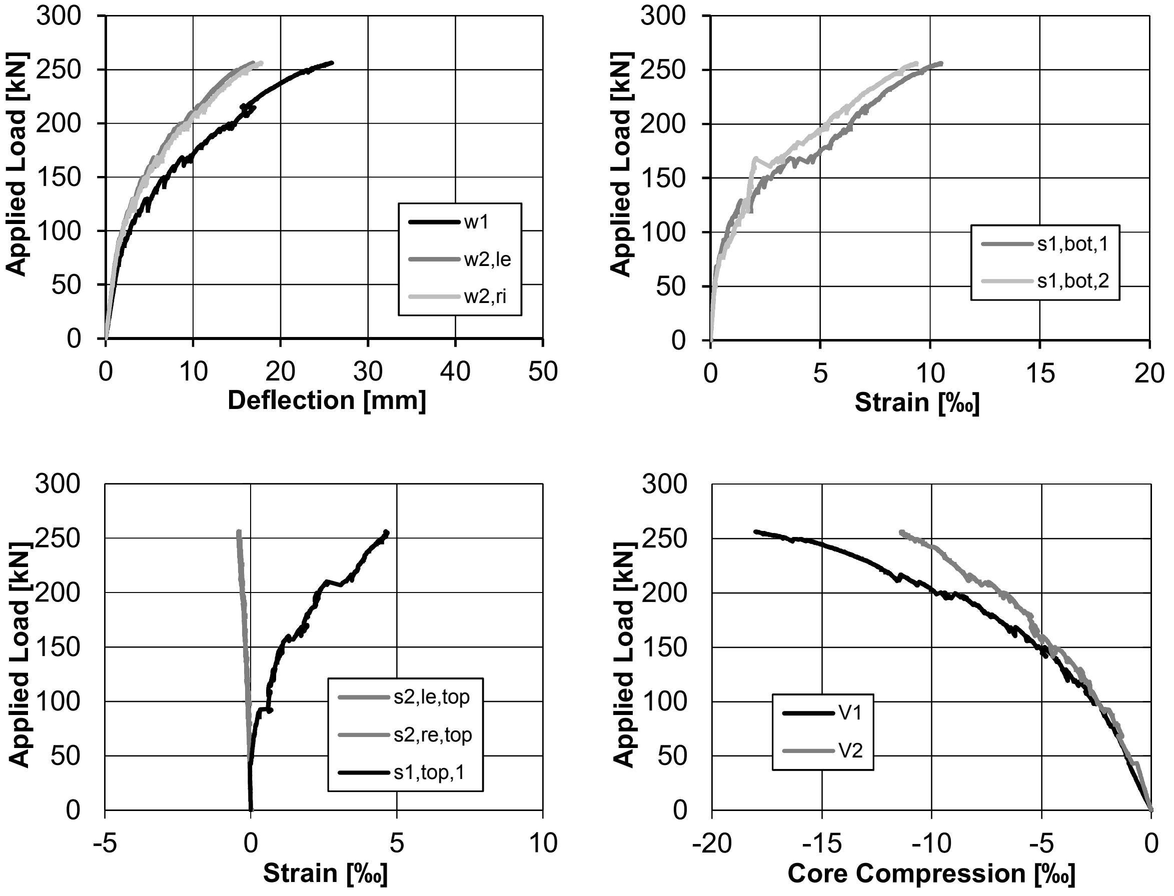

	CFRP Type [-]		Diameter [mm]		Jacking Stress [MPa]		Core height [mm]
SFP-5	**Top**	**Bottom**	**Top**	**Bottom**	**Top**	**Bottom**	200
	Strand	Strand	7.5	7.5	675	675	

Prestressing: Compression strains and end slip

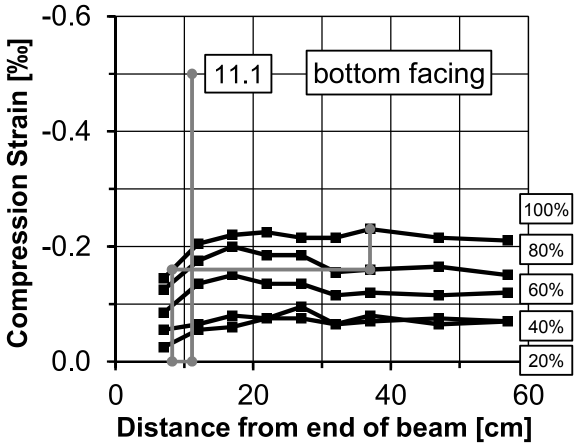

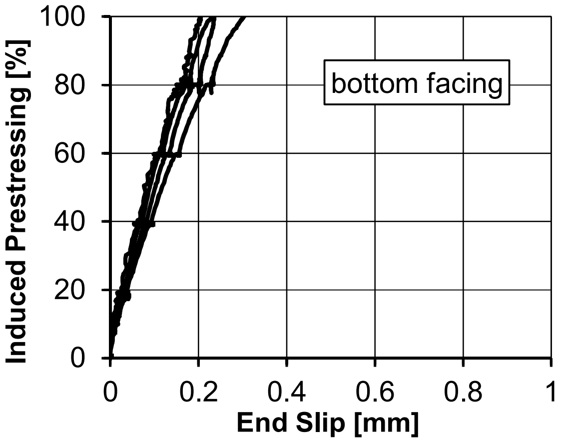

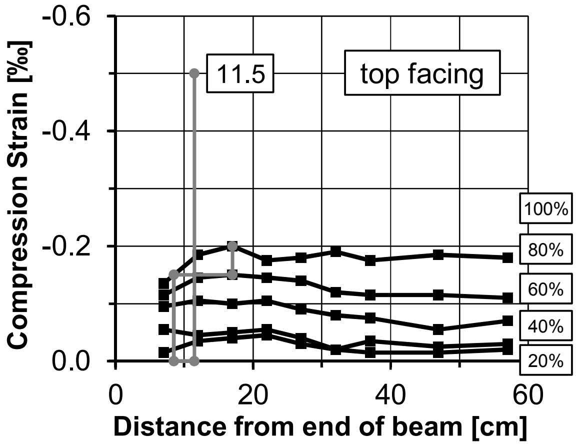

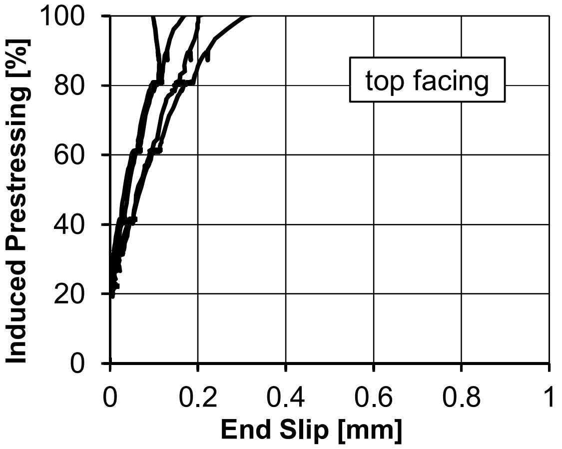

Crack pattern after testing

Top

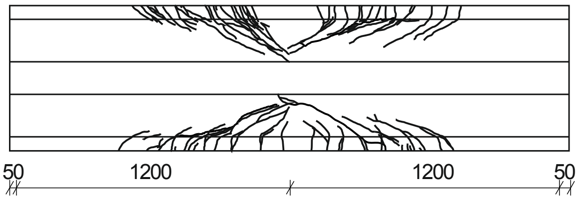

Bottom

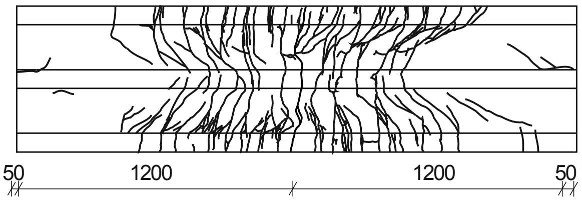

Results of three-point bending test

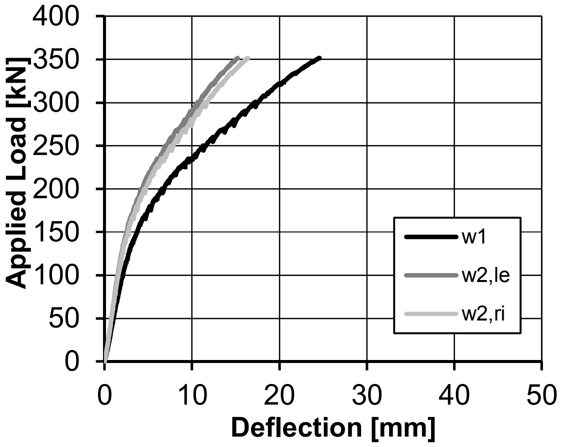

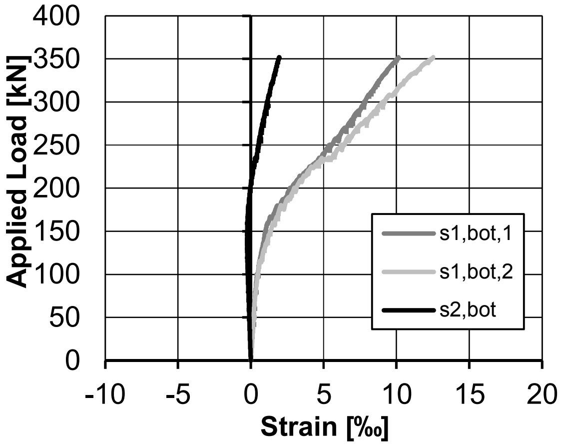

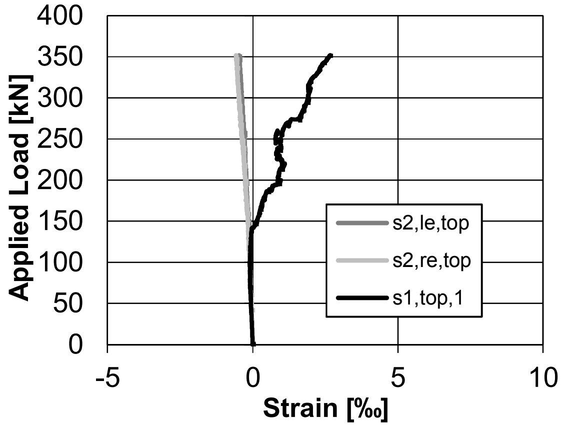

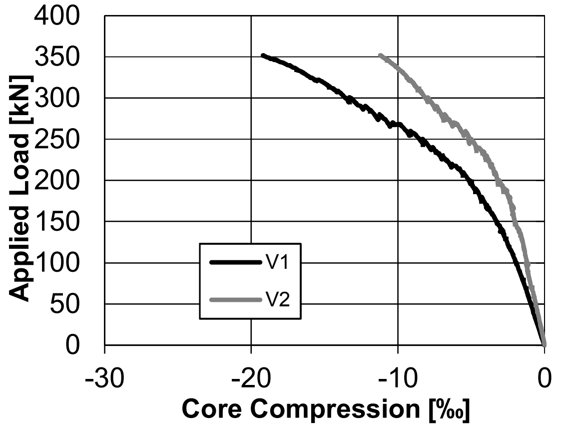

	CFRP Type [-]		Diameter [mm]		Jacking Stress [MPa]		Core height [mm]
SFP-6	**Top**	**Bottom**	**Top**	**Bottom**	**Top**	**Bottom**	200
	Strand	Strand	7.5	7.5	675	1350	

Prestressing: Compression strains and end slip

Compression strains and end slip not measured for top facing.

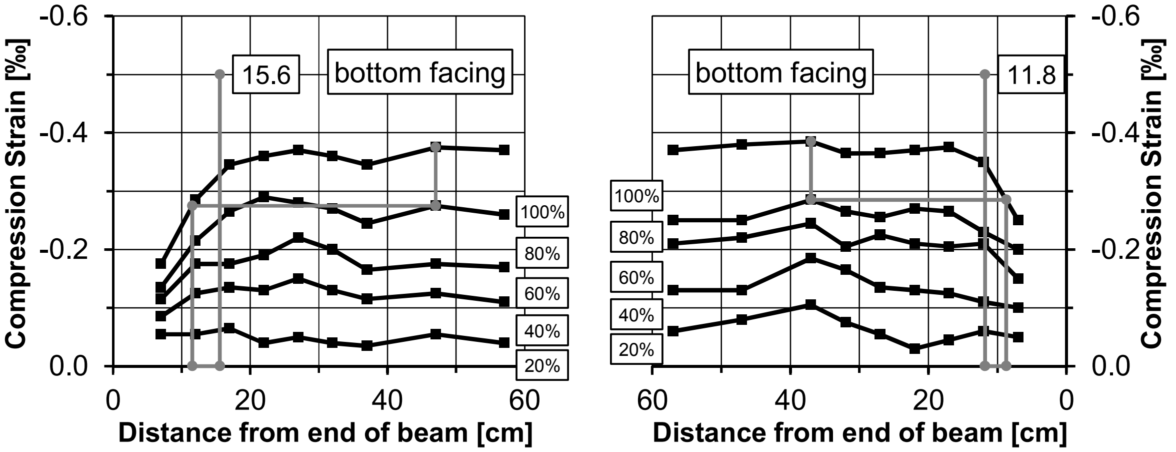

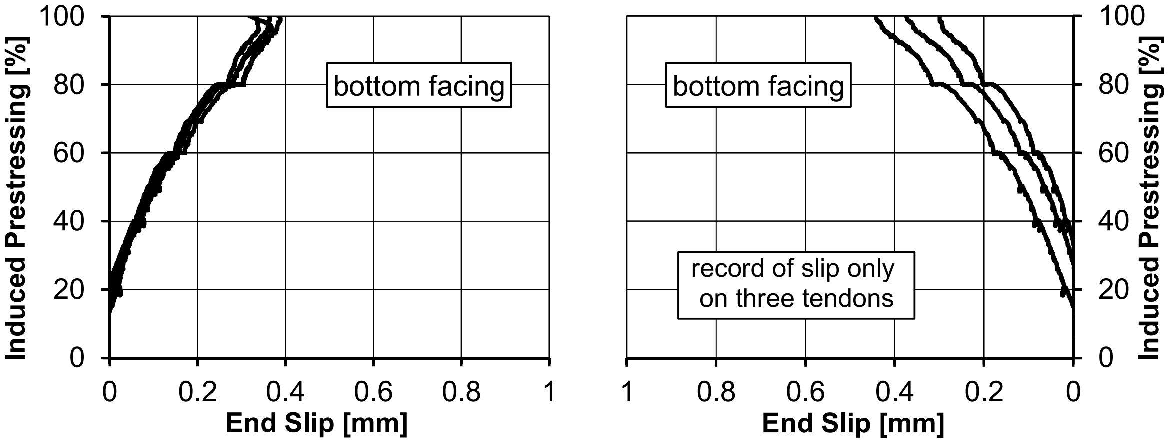

Crack pattern after testing

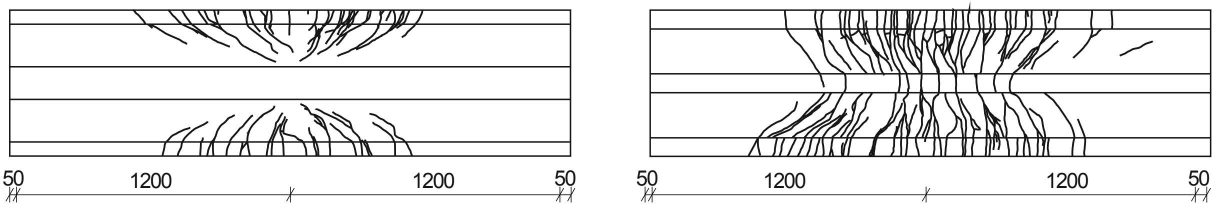

Results of three-point bending test

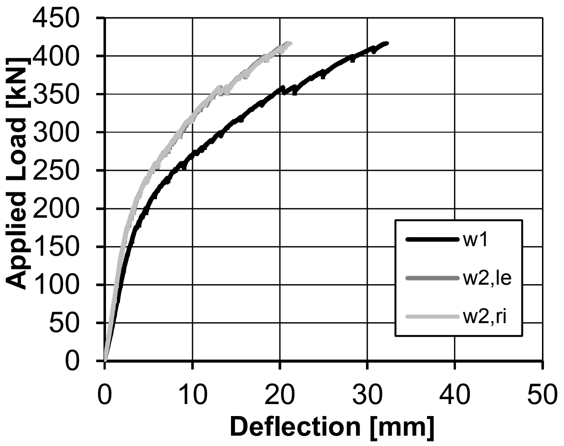

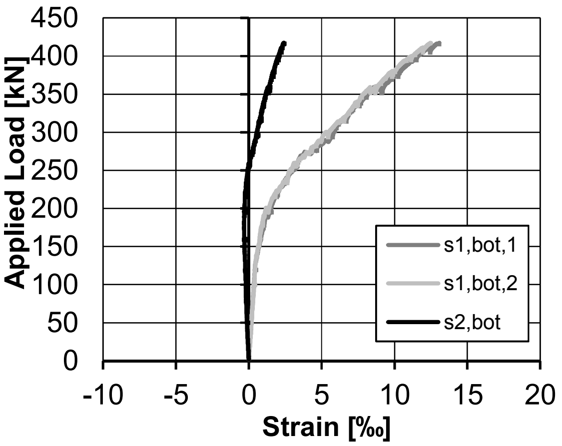

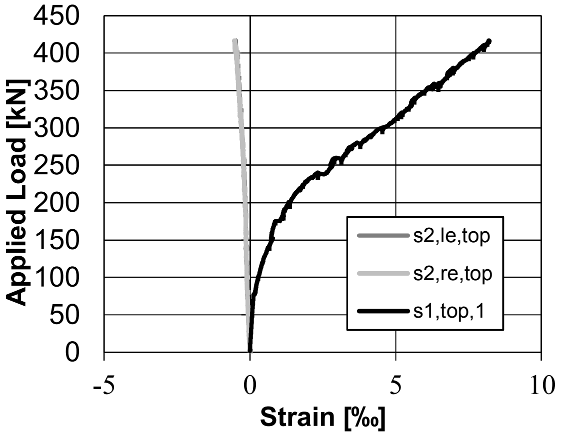

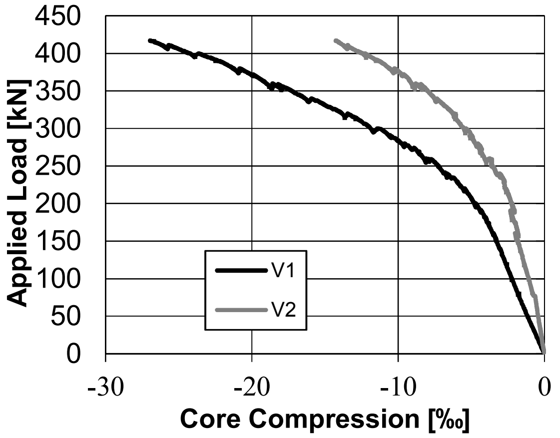

	CFRP Type [-]		Diameter [mm]		Jacking Stress [MPa]		Core height [mm]
SFP-7	**Top**	**Bottom**	**Top**	**Bottom**	**Top**	**Bottom**	100
	Bar	Strand	5.0	7.5	0	675	

Prestressing: Compression strains and end slip

Compression strains and end slip not measured for bottom facing.

Crack pattern after testing

Top

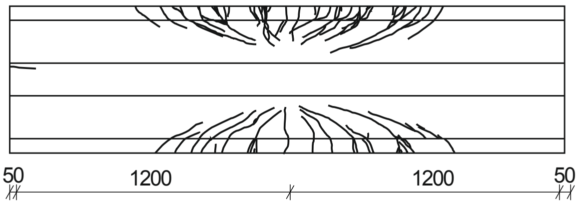

Bottom

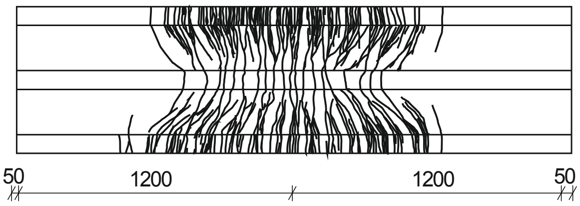

Results of three-point bending test

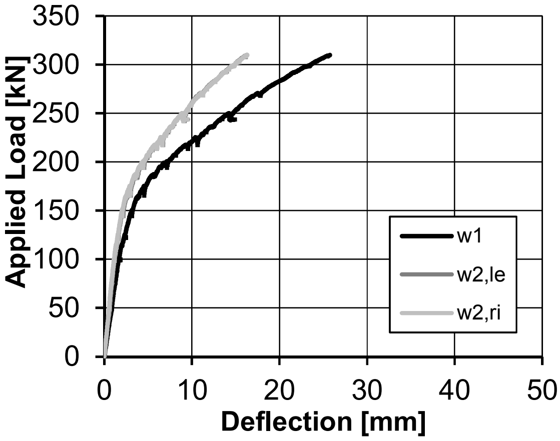

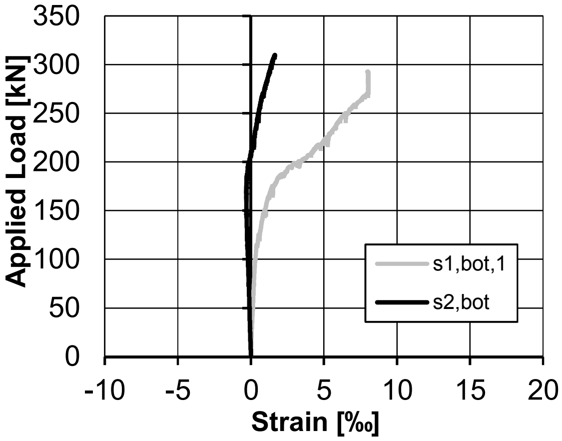

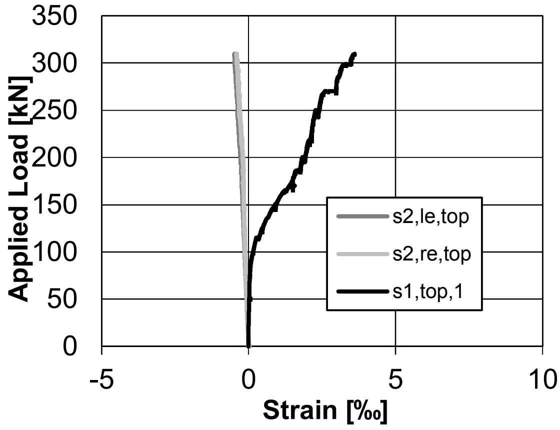

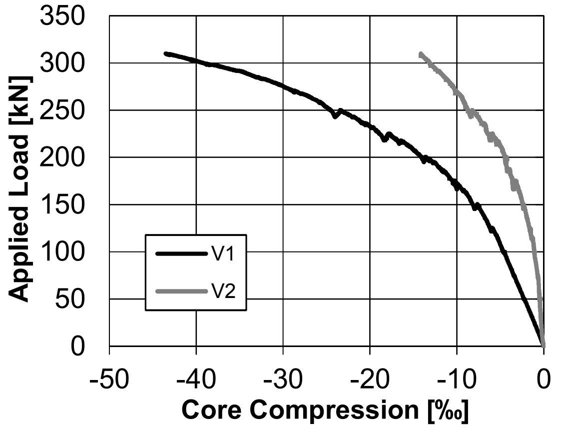

D.3 Doubly Curved Sandwich Panels

Test setup

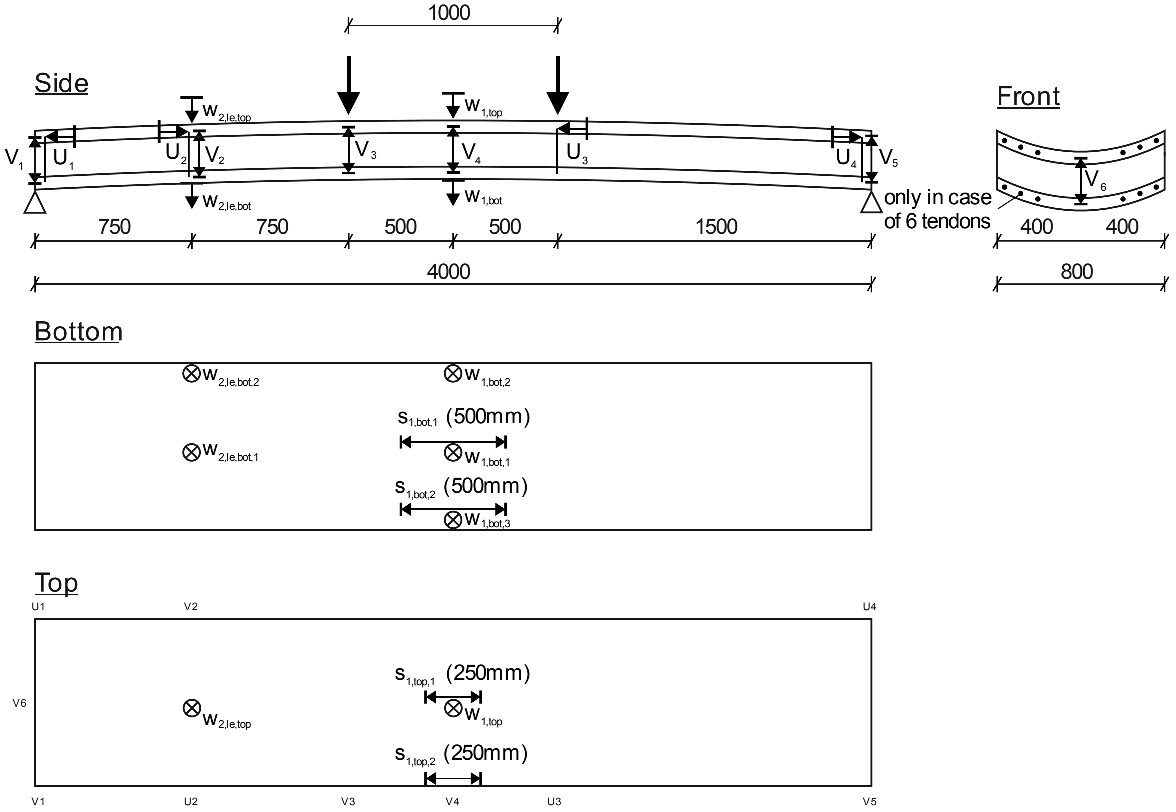

Transfer length

End slip: Relative displacement between tendons and UHPFRC element

Table D.7: Parameter variation of flexural tests on folded plate sandwich panels

Test No.	CFRP Type		Number		Jacking stress	
	[-]		[-]		[MPa]	
[-]	bottom	top	bottom	top	bottom	top
SHP-1	bar	bar	6	6	0	0
SHP-2	strand	strand	4	4	675	675
SHP-3	strand	strand	6	6	675	675
SHP-4	strand	bar	6	6	675	0
SHP-5	strand	strand	6	6	1,350	675
SHP-6*	strand	bar	6	6	675	0

*h_c = 100 mm

Table D.8: Concrete properties of doubly curved sandwich panels [1d]

Test No. [-]	$f_{cm,cyl,1d}$ [MPa]		$f_{cm,cube,1d}$ [MPa]		$E_{cm,1d}$ [MPa]		$f_{ct,flex,1d}$ [MPa]	
	bottom	top	bottom	top	bottom	top	bottom	top
SHP-1	NA	NA	NA	NA	NA	NA	NA	NA
SHP-2	64.4	53.2	83.6	92.5	36,100	29,100	8.9	9.3
SHP-3	81.2	38.0	86.3	59.6	40,200	23,500	9.0	6.7
SHP-4	63.9	NA	87.2	NA	29,400	NA	10.5	NA
SHP-5	58.0	55.9	77.8	84.7	29,400	27,400	9.9	8.2
SHP-6	30.0	NA	50.8	NA	18,800	NA	3.8	NA

Table D.9: Concrete properties of doubly sandwich panels [28d]

Test No. [-]	$f_{cm,cyl,28d}$ [MPa]		$f_{cm,cube,28d}$ [MPa]		$E_{cm,28d}$ [MPa]		$f_{ct,flex,28d}$ [MPa]	
	bottom	top	bottom	top	bottom	top	bottom	top
SHP-1	159.8	151.2	173.7	173.5	45,200	44,700	16.6	11.4
SHP-2	153.1	157.8	180.3	176.2	45,100	46,900	18.3	15.1
SHP-3	162.6	148.8	172.2	166.7	45,700	44,000	24.1	19.4
SHP-4	155.1	157.7	162.3	173.9	45,500	46,000	22.8	18.7
SHP-5	143.7	155.7	163.9	176.7	45,500	45,400	18.6	19.8
SHP-6	141.2	139.2	177.4	154.9	44,600	45,000	14.6	19.3

	CFRP Type [-]		**Diameter [mm]**		**Number [-]**		**Jacking Stress [MPa]**		**Core height [mm]**
SHP-1	**top**	**bottom**	**top**	**bottom**	**top**	**bottom**	**top**	**bottom**	200
	Bar	Bar	5.0	5.0	6	6	0	0	

Prestressing: End slip

NA

Corresponding crack pattern after testing

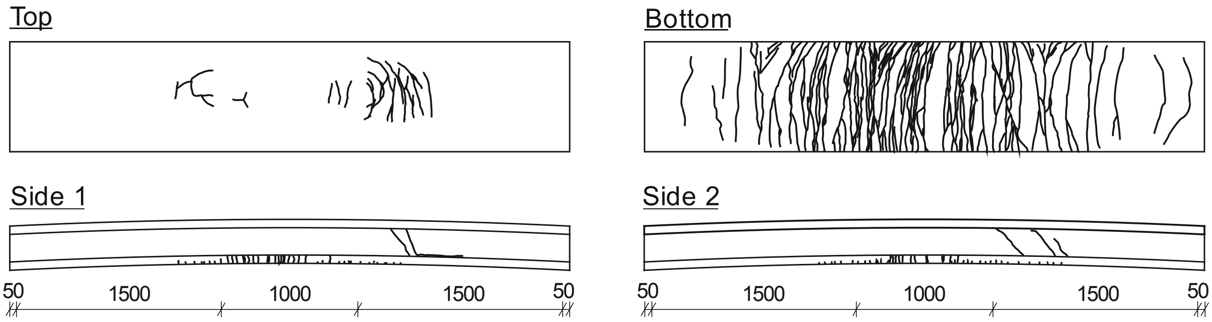

Results of four-point bending test

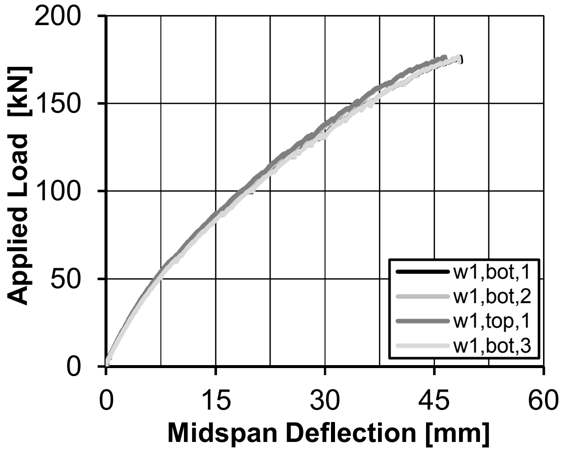

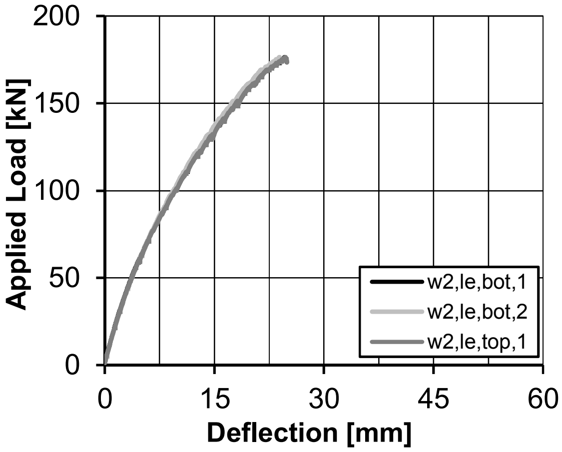

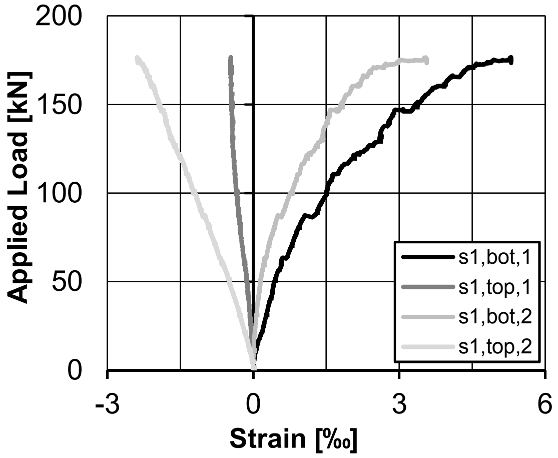

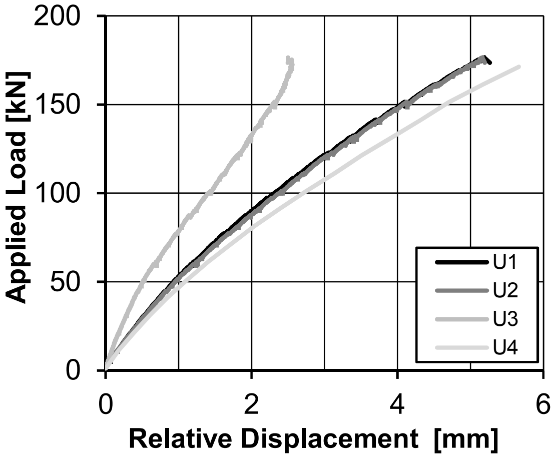

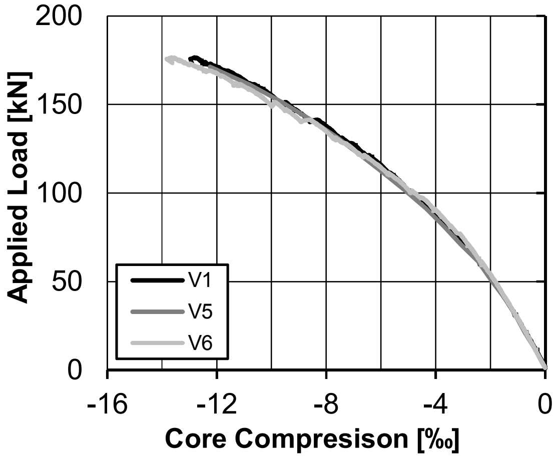

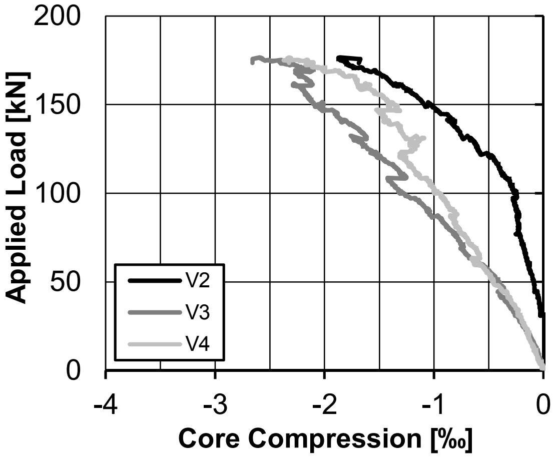

	CFRP Type [-]		Diameter [mm]		Number [-]		Jacking Stress [MPa]		Core height [mm]
SHP-2	**top**	**bottom**	**top**	**bottom**	**top**	**bottom**	**top**	**bottom**	200
	Strand	Strand	7.5	7.5	4	4	675	675	

Prestressing: End slip

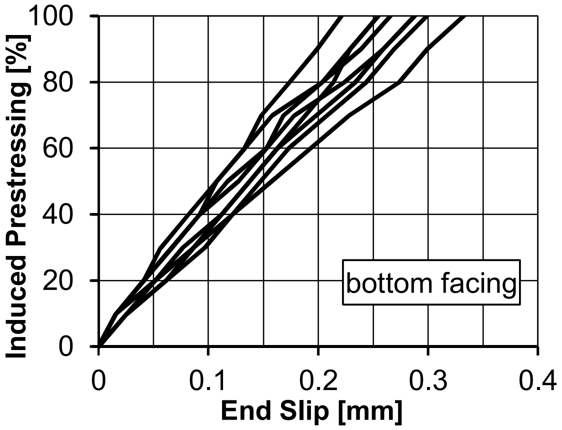

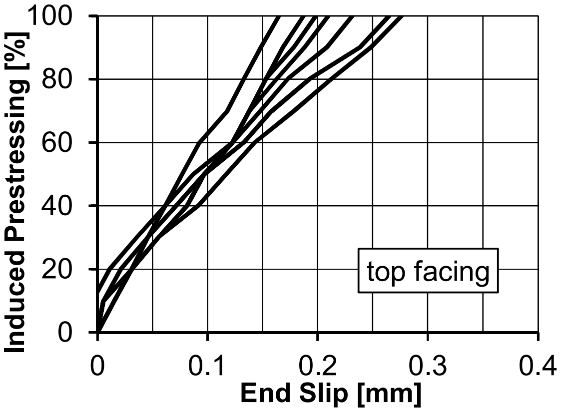

Corresponding crack pattern after testing

Top

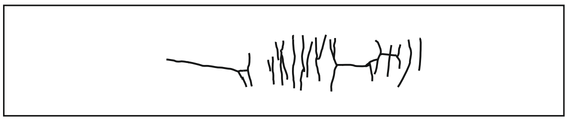

Bottom

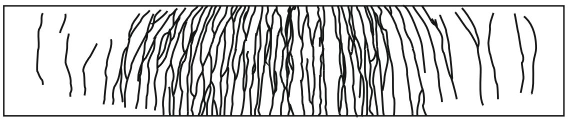

Side 1

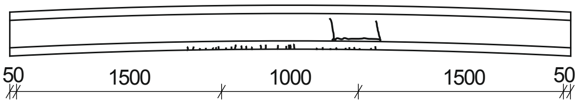

Side 2

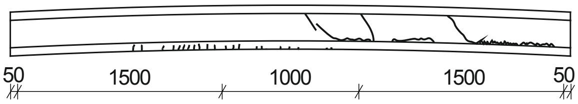

Results of four-point bending test

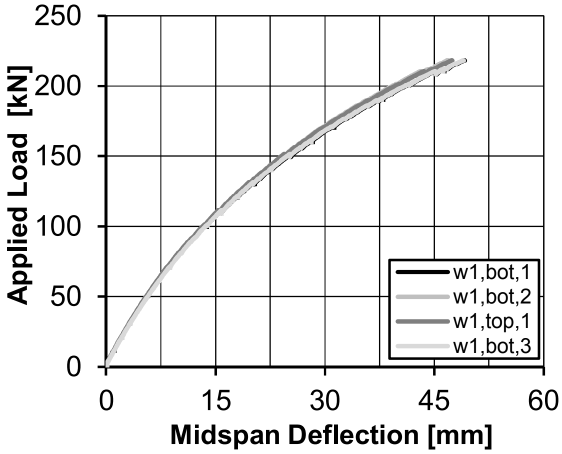

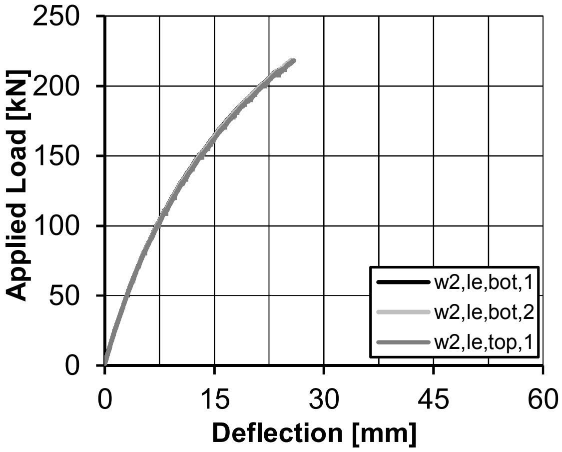

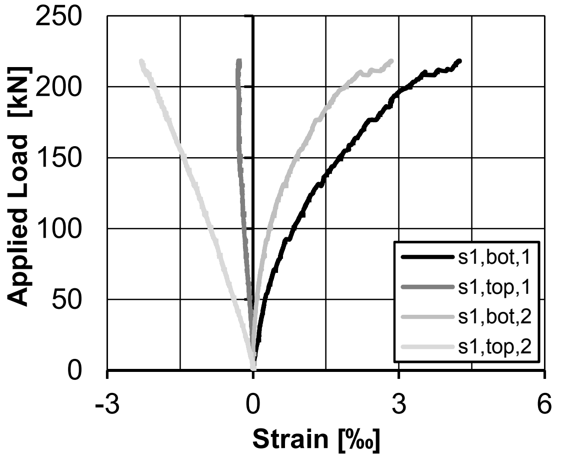

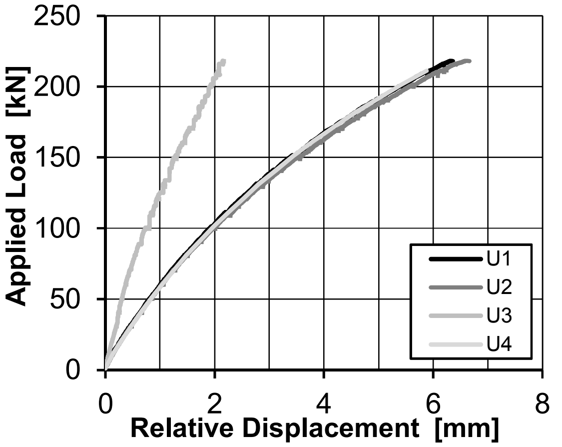

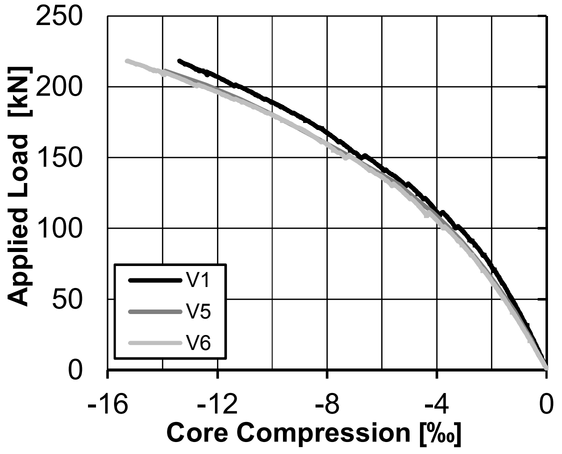

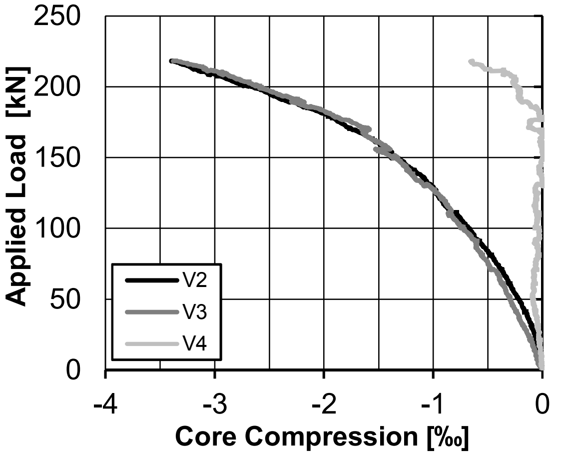

	CFRP Type [-]		Diameter [mm]		Number [-]		Jacking Stress [MPa]		Core height [mm]
SHP-3	**top**	**bottom**	**top**	**bottom**	**top**	**bottom**	**top**	**bottom**	200
	Strand	Strand	7.5	7.5	6	6	675	675	

Prestressing: End slip

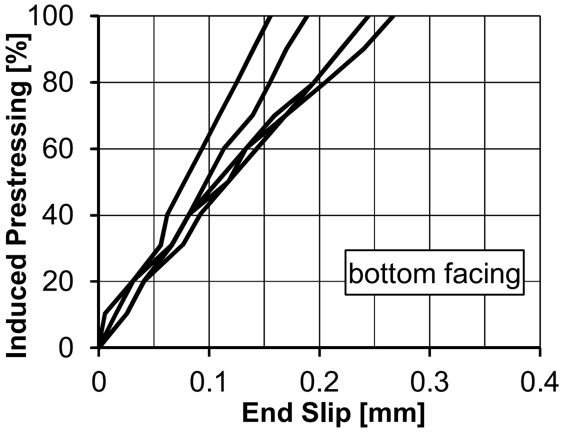

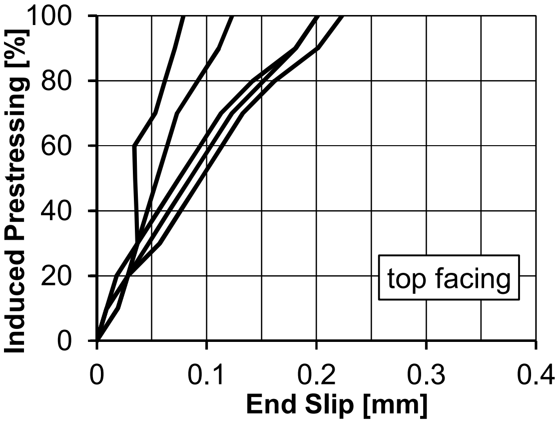

Corresponding crack pattern after testing

Top

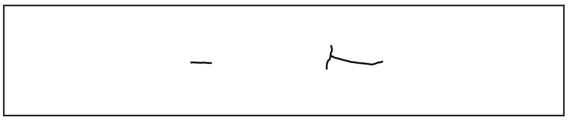

Bottom

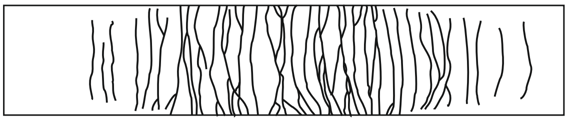

Side 1

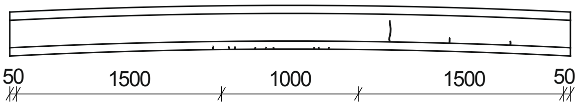

Side 2

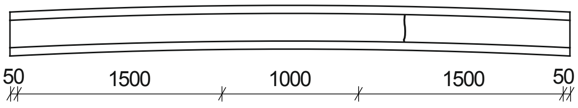

Results of four-point bending test

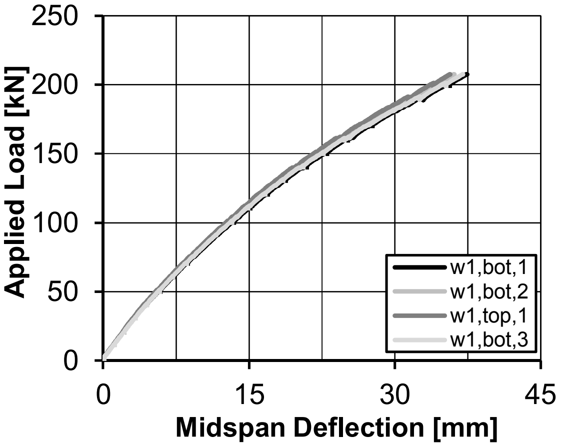

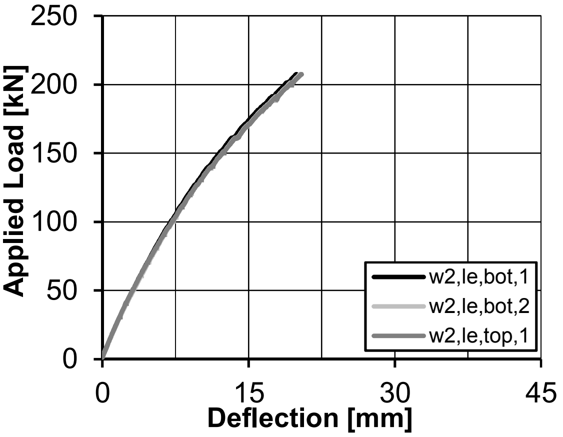

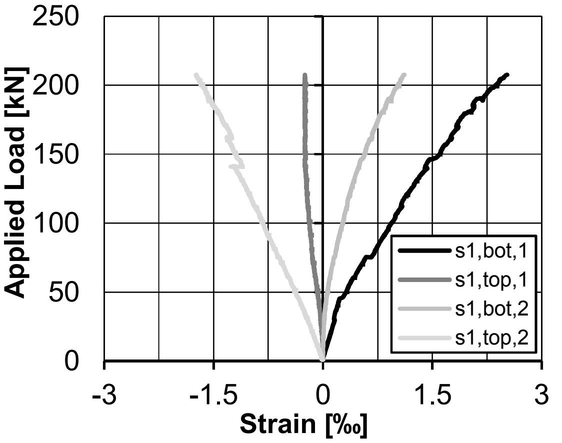

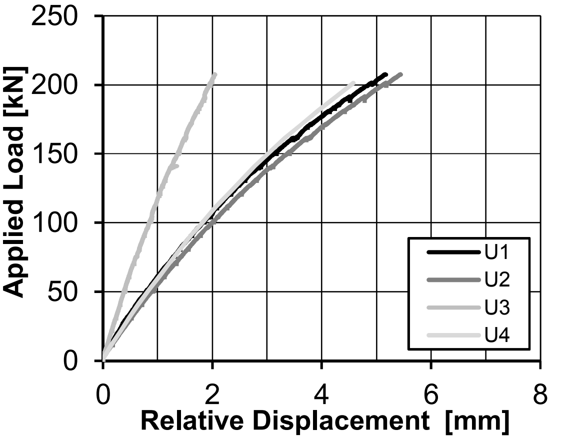

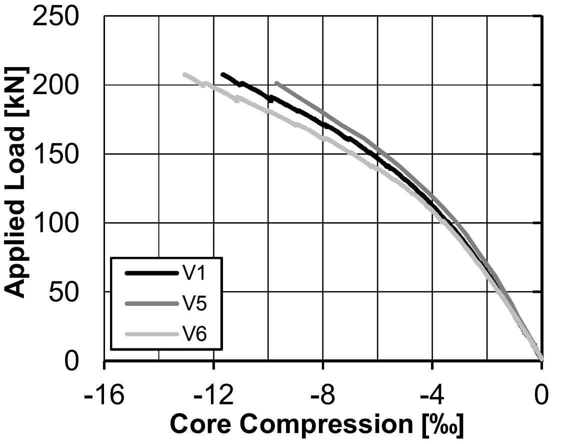

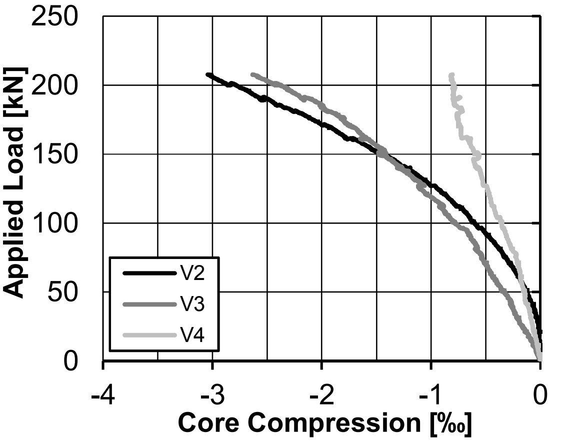

	CFRP Type [-]		Diameter [mm]		Number [-]		Jacking Stress [MPa]		Core height [mm]
SHP-4	**top**	**bottom**	**top**	**bottom**	**top**	**bottom**	**top**	**bottom**	200
	Bar	Strand	5.0	7.5	6	6	0	675	

Prestressing: End slip

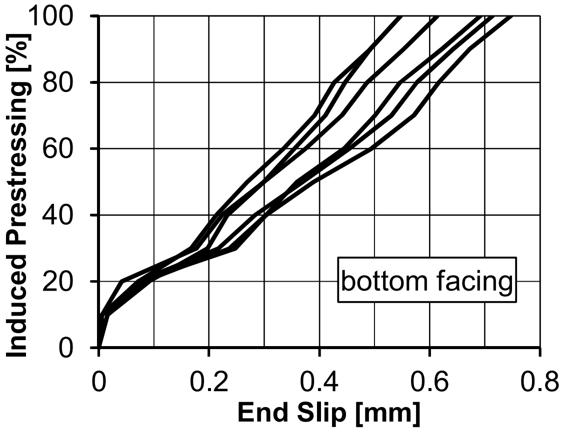

Corresponding crack pattern after testing

Top

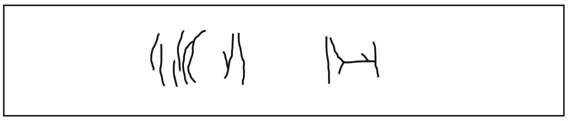

Bottom

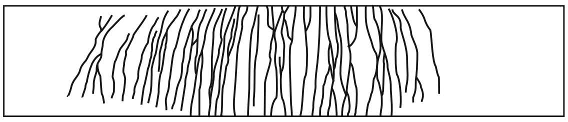

Side 1

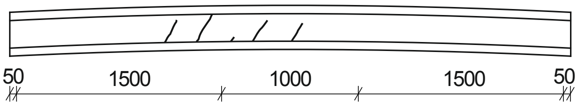

Side 2

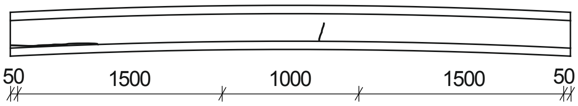

Results of four-point bending test

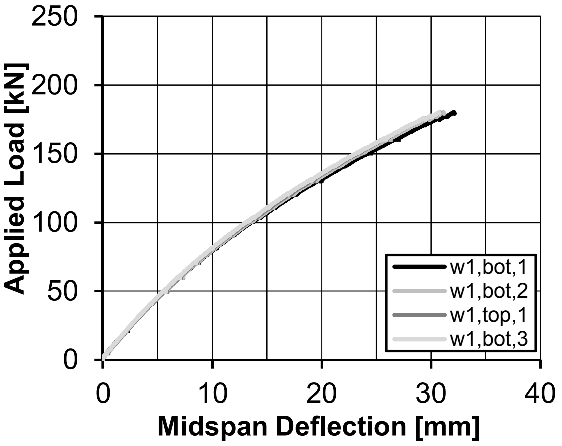

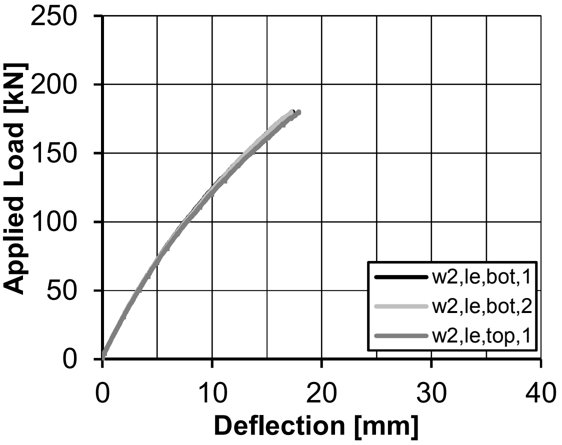

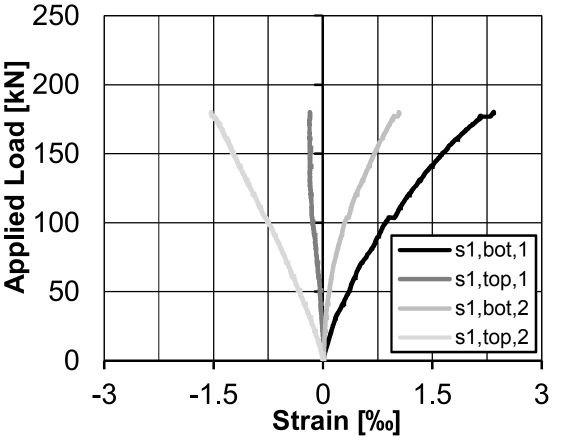

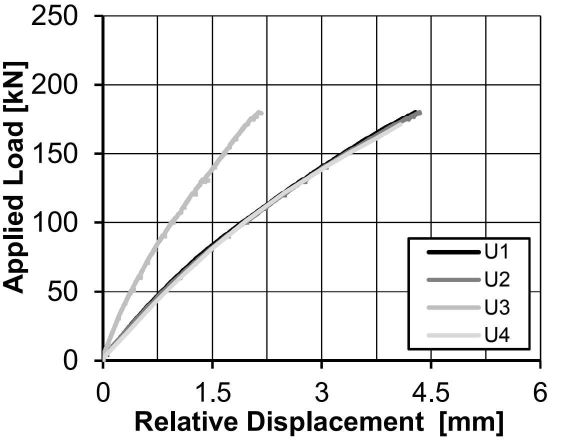

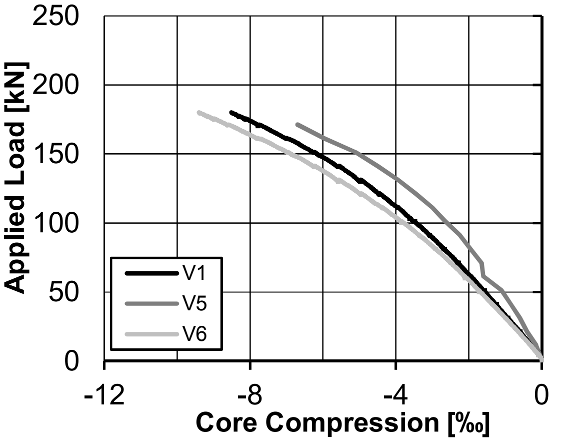

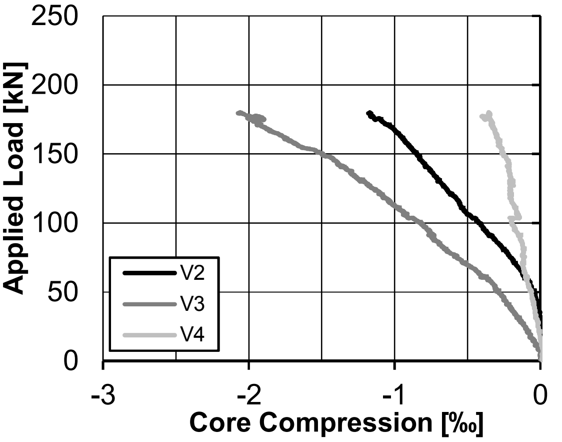

	CFRP Type [-]		Diameter [mm]		Number [-]		Jacking Stress [MPa]		Core height [mm]
SHP-5	**top**	**bottom**	**top**	**bottom**	**top**	**bottom**	**top**	**bottom**	200
	Strand	Strand	7.5	7.5	6	6	675	1350	

Prestressing: End slip

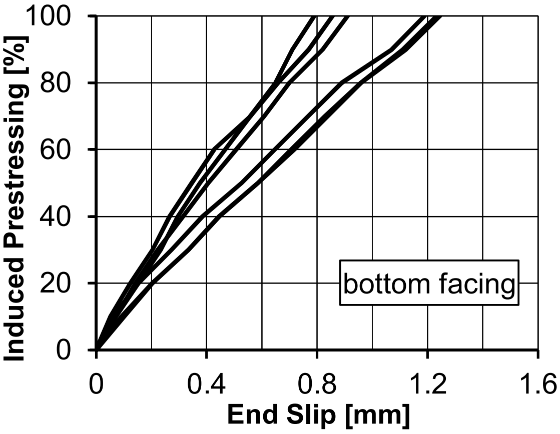

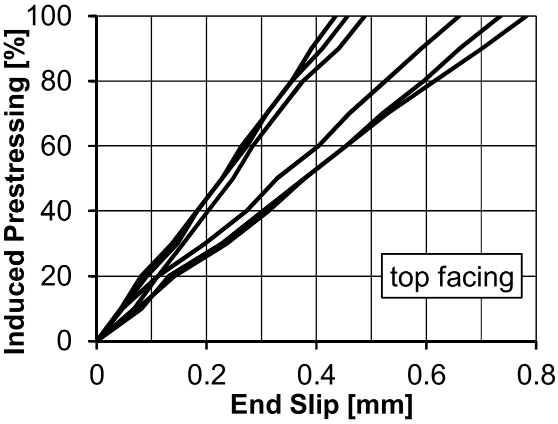

Corresponding crack pattern after testing

Top

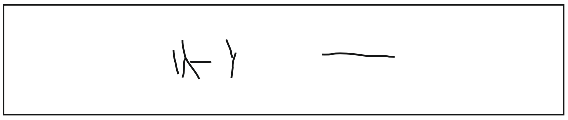

Bottom

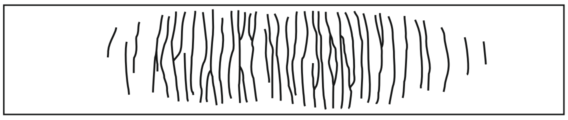

Side 1

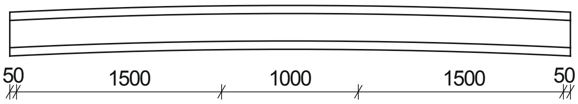

Side 2

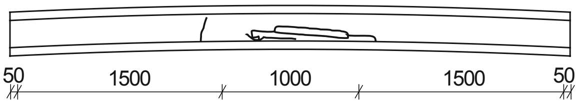

Results of four-point bending test

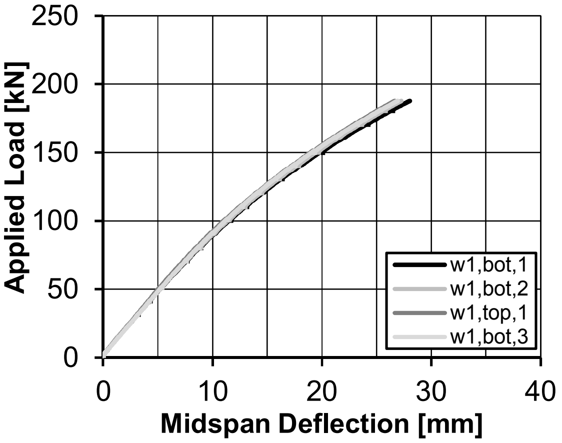

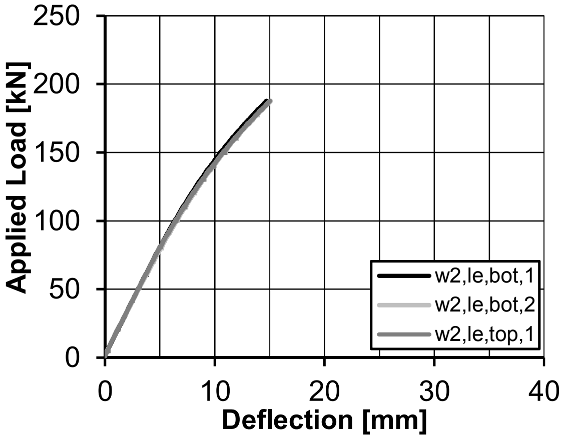

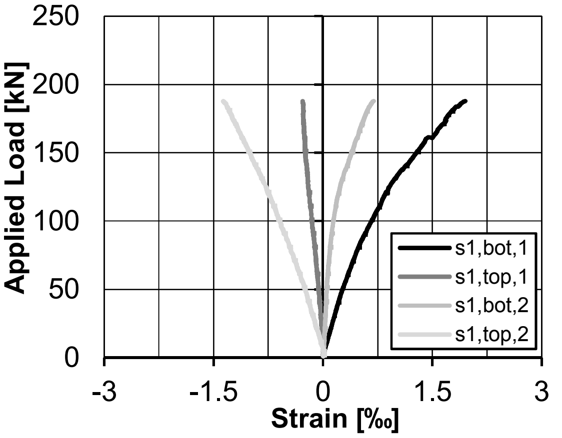

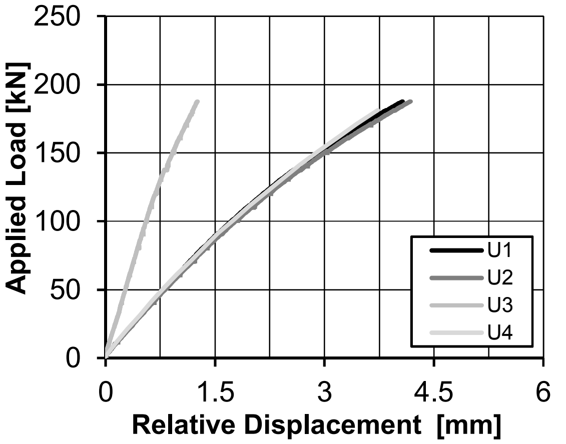

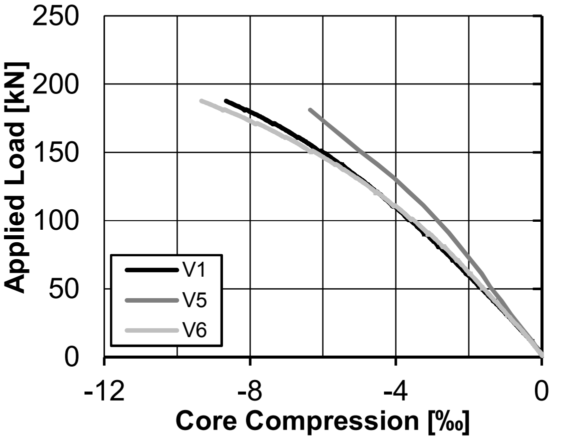

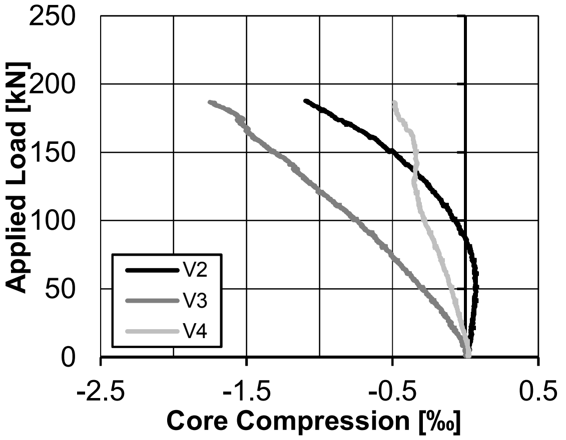

	CFRP Type [-]		Diameter [mm]		Number [-]		Jacking Stress [MPa]		Core height [mm]
SHP-6	**top**	**bottom**	**top**	**bottom**	**top**	**bottom**	**top**	**bottom**	100
	Bar	Strand	5.0	7.5	6	6	0	675	

Prestressing: End slip

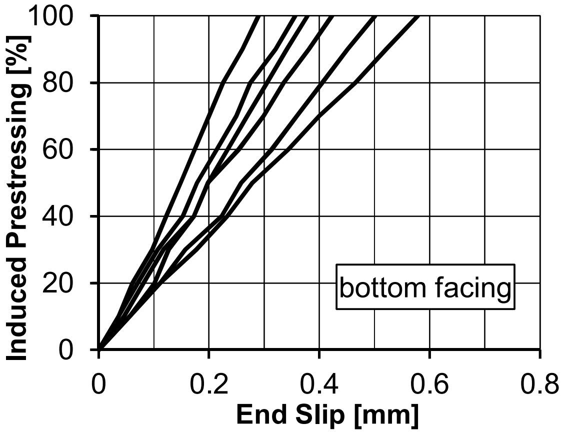

Corresponding crack pattern after testing

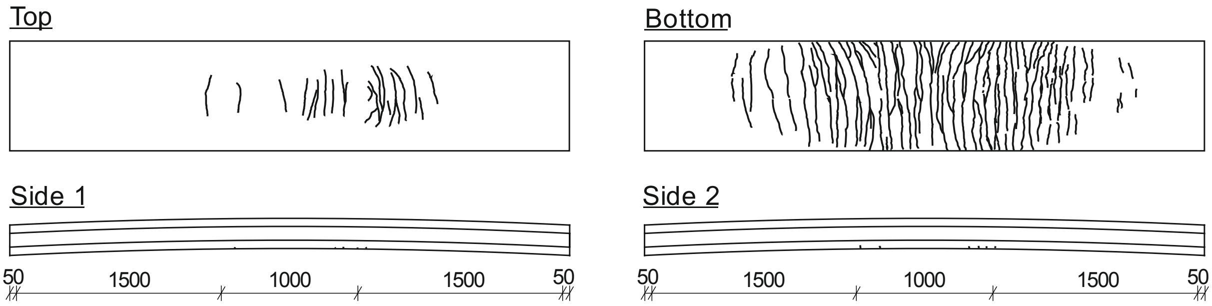

Results of four-point bending test

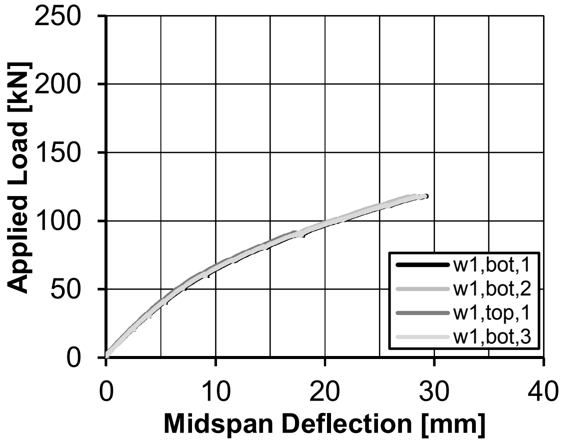

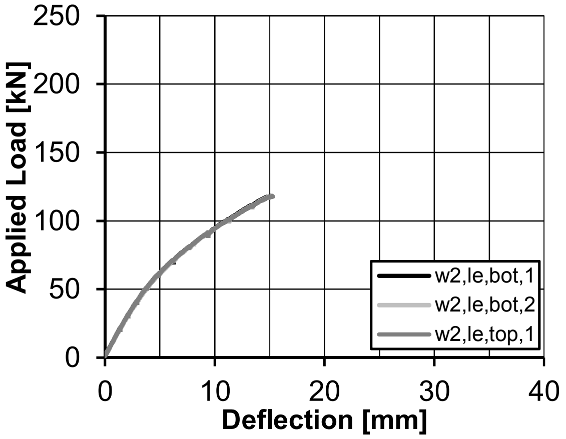

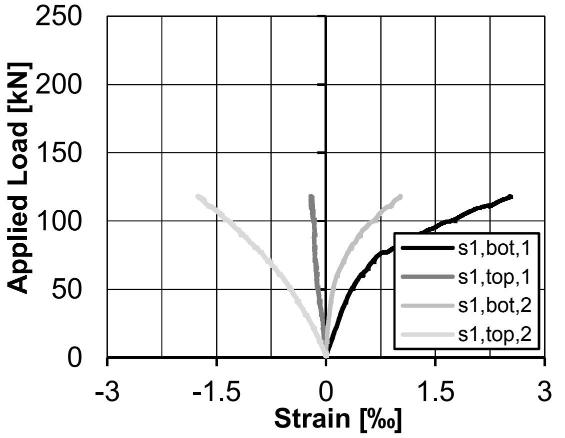

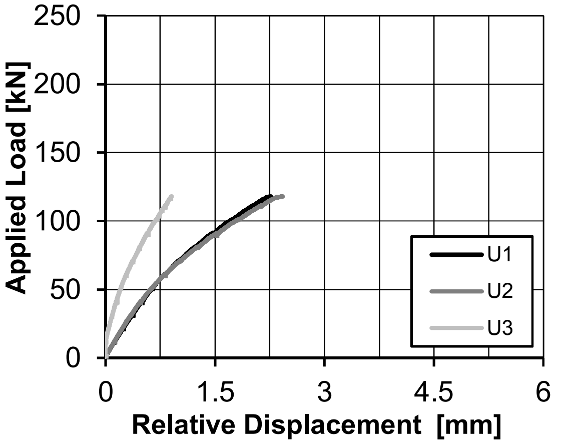

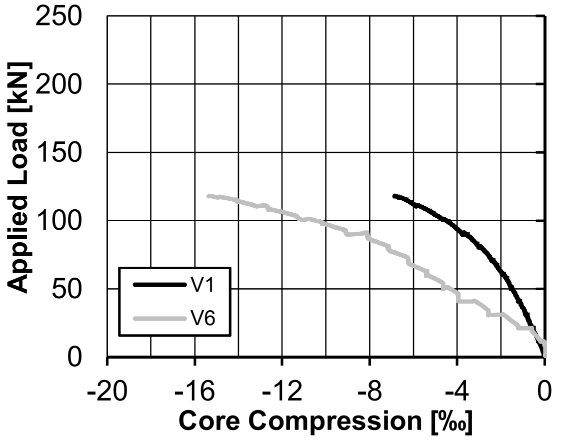

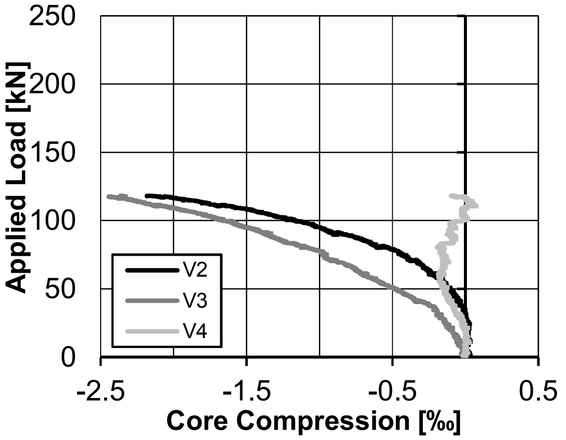

E Sandwich Theory: Analytical Model

E.1 Constitutive equations based on /Sta74/

The following derivations can be found in /Sta74/ and are based on Fig. 7.24 (chapter 7).

Core shear strain γ_c:

$$\gamma_c = \gamma_1 + \gamma_{2c} \tag{E.1}$$

Shear strain γ_1 from deflection *w*:

$$\gamma_1 = \frac{dw}{dx} = w' \tag{E.2}$$

Shear strain γ corresponding to central axis of top and bottom facing:

$$\gamma = \gamma_1 + \gamma_2 = w' + \gamma_2 \tag{E.3}$$

Relative displacement ΔU of top and bottom facing:

$$\Delta U = a \cdot \gamma = h_c \cdot \gamma_c \tag{E.4}$$

Relationship of γ and γ_c:

$$\gamma = \frac{h_c}{a} \gamma_c \tag{E.5}$$

Partial core shear strains γ_2 and γ_{2c}:

$$\gamma_2 = \frac{h_c}{a} \gamma_c - w', \qquad \gamma_{2c} = \frac{a}{h_c} \gamma - w' \tag{E.6}$$

Strains of top and bottom facings:

$$\varepsilon_{top} = \frac{\mathrm{d}u_{top}}{\mathrm{d}x}, \quad \varepsilon_{bot} = \frac{\mathrm{d}u_{bot}}{\mathrm{d}x} \tag{E.7}$$

Axial displacements of top and bottom facings:

$$u_{top} = \overline{u} - a_{top}\gamma_2 - z_{top}\gamma_1, \qquad u_{bot} = \overline{u} + a_{bot}\gamma_2 - z_{bot}\gamma_1 \tag{E.8}$$

Strains of top and bottom facings:

$$\varepsilon_{top} = \bar{u}' - a_{top}\gamma'_2 - z_{top}\gamma'_1 , \qquad \varepsilon_{bot} = \bar{u}' + a_{bot}\gamma'_2 - z_{bot}\gamma'_1 \tag{E.9}$$

Stresses of top and bottom facings:

$$\sigma_{top} = E_{top}(\bar{u}' - a_{top}\gamma'_2 - z_{top}\gamma'_1), \qquad \sigma_{bot} = E_{bot}(\bar{u}' + a_{bot}\gamma'_2 - z_{bot}\gamma'_1) \tag{E.10}$$

Shear stress τ:

$$\tau = G\gamma_{\mathrm{c}} \tag{E.11}$$

Internal forces:

$$N = \int_{(A)} \sigma \,\mathrm{d}A, \quad M = \int_{(A)} \sigma z \,\mathrm{d}A, \quad V = \int_{(A)} \tau \,\mathrm{d}A, \tag{E.12}$$

$$\begin{aligned} N &= (D_{bot}a_{bot} - D_{top}a_{top})\gamma_2' + D\bar{u}' \\ M &= (D_{bot}a_{bot} - D_{top}a_{top})\bar{u}' + B_s\gamma_2' - (B_{bot} + B_{top})\gamma_1' \end{aligned} \tag{E.13}$$

Relationship of axial stiffnesses D_{i} and distances a_{i}:

$$D_{bot}a_{bot} - D_{top}a_{top} = 0, \qquad a_{bot} + a_{top} = a \tag{E.14}$$

Distance from centre line of sandwich to centre lines of facings:

$$a_{bot} = \frac{D_{top}}{D}a, \; a_{top} = \frac{D_{bot}}{D}a \tag{E.15}$$

Axial stiffness of bottom and top facing as well as total stiffness:

$$D_{bot} = E_{bot}bt_{bot} = E_{bot}A_{bot}, \quad D_{top} = E_{top}bt_{top} = E_{top}A_{top}, D = D_{bot} + D_{top} \tag{E.16}$$

Flexural rigidities of bottom and top facings:

$$\begin{aligned} B_{bot} &= E_{bot}\int_{A_{bot}} z_{bot}z \; dA = E_{bot}\int_{A_{bot}} z_{bot}(z_{bot} + a_{bot}) \; dA \\ B_{top} &= E_{top}\int_{A_{top}} z_{top}z \; dA = E_{top}\int_{A_{top}} z_{top}(z_{top} - a_{top}) \; dA \end{aligned} \tag{E.17}$$

Flexural rigidities of flat bottom and top facings:

$$B_{bot} = E_{bot} \frac{bt_{bot}^3}{12} = E_{bot} I_{bot}, \ B_{top} = E_{top} \frac{bt_{top}^3}{12} = E_{top} I_{top} \tag{E.18}$$

Flexural rigidity from sandwich action:

$$B_s = D_{bot} a_{bot}^2 + D_{top} a_{top}^2 = \frac{D_{bot} D_{top}}{D} a^2 \tag{E.19}$$

Total flexural rigidity:

$$B = B_s + B_{bot} + B_{top} \tag{E.20}$$

Total bending moment:

$$M = M_s + M_{bot} + M_{top} \tag{E.21}$$

Bending moment from sandwich action:

$$M_s = (D_{bot} a_{bot} - D_{top} a_{top}) \bar{u}' + B_s \gamma_2' \tag{E.22}$$

Bending moment of bottom and top facing:

$$M_{bot} = -B_{bot} \gamma_1', \qquad M_{top} = -B_{top} \gamma_1' \tag{E.23}$$

Shear force of core material and shear stiffness:

$$V_s = A\gamma, \qquad A = G \frac{ba^2}{h_c} \tag{E.24}$$

Shear forces of bottom and top facings:

$$V_{bot} = M_{bot}' = -B_{bot} \gamma_1'', \qquad V_{top} = M_{top}' = -B_{top} \gamma_1'' \tag{E.25}$$

Total shear forces:

$$V = A\gamma - (B_{bot} + B_{top}) \gamma_1'' \tag{E.26}$$

Resulting internal forces:

$$\begin{aligned} N &= D\bar{u}' \\ M &= B_s\gamma' - Bw'' \\ V &= A\gamma - (B_{bot} + B_{top})w''' \end{aligned} \tag{E.27}$$

Relationships for internal forces M, N_x and V_z:

$$\left.\begin{aligned} \frac{\mathrm{d}M}{\mathrm{d}x} - V_z + N_x w' = 0 \\ \frac{\mathrm{d}Vz}{\mathrm{d}x} + q = 0 \end{aligned}\right\} \tag{E.28}$$

Relationships of N_x and V_z to N and V:

$$N_x = N + V\gamma_2, \qquad V_z = V + N\gamma_1 \tag{E.29}$$

Neglecting γ_2, since $N >> V$:

$$N_x = N, \qquad V_z = V + N\gamma_1 \tag{E.30}$$

Relationships for internal forces M, N and V:

$$\left.\begin{aligned} \frac{\mathrm{d}M}{\mathrm{d}x} - V = 0 \\ \frac{\mathrm{d}V}{\mathrm{d}x} + q + Nw'' = 0 \end{aligned}\right\} \tag{E.31}$$

Relationships of shear angle γ and deflection w for constant B_s and constant A (applying eq. (E.28) to eq. (E.31)):

$$B_s(\gamma'' - w''') - A\gamma = 0, \; A\gamma' + Nw'' - (B_{bot} + B_{top})w^{\mathrm{IV}} = -q \tag{E.32}$$

Decoupled differential equation for deflection w and shear angle γ:

$$\left.\begin{aligned} -\frac{B_{bot} + B_{top}}{A} w^{\mathrm{VI}} + \left(\frac{B}{B_s} + \frac{N}{A}\right) w^{\mathrm{IV}} - \frac{N}{B_s} w'' = \frac{q}{B_s} - \frac{q''}{A} \\ -\frac{B_{bot} + B_{top}}{A} \gamma^{\mathrm{IV}} + \left(\frac{B}{B_s} + \frac{N}{A}\right) \gamma'' - \frac{N}{B_s} \gamma = -\frac{q'}{A} \end{aligned}\right\} \tag{E.33}$$

Decoupled differential equation for deflection w and shear angle γ for simply supported beam:

$$-\frac{B_{bot}+B_{top}}{A}w^{\mathrm{IV}}+\frac{B}{B_s}w''=-\frac{M}{B_s}-\frac{q}{A} \tag{E.34}$$

$$\gamma=\frac{B_s}{A^2}\left[\left(B_{bot}+B_{top}\right)w^{\mathrm{V}}-\left(N+A\right)w'''-q'\right] \tag{E.35}$$

E.2 Simply Supported Sandwich Beam with One Point Load *F* Based on /Sta74/

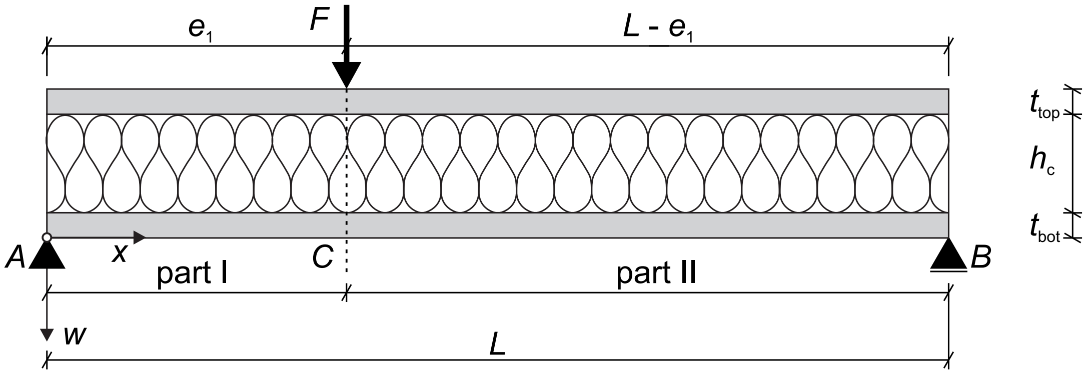

Abbreviation:

$$\alpha=\frac{B_{top}+B_{bot}}{B_s},\qquad \beta=\frac{B_s}{A\cdot L^2},\qquad \lambda^2=\frac{1+\alpha}{\alpha\cdot\beta} \tag{E.36}$$

Bending moments:

$$\begin{aligned}&\text{Part I}\,(\xi\le\varepsilon): && M_I=F\cdot L\cdot(1-\varepsilon)\cdot\xi\\ &\text{Part II}\,(\xi\ge\varepsilon): && M_{II}=F\cdot L\cdot\varepsilon\cdot(1-\xi)\end{aligned} \tag{E.37}$$

Ratios of distances:

$$\begin{aligned}\varepsilon&=\frac{e_1}{L}\\ \xi&=\frac{x}{L}\end{aligned} \tag{E.38}$$

Deflection:

$$\begin{aligned} w_I &= \frac{FL^3}{B}\left[\frac{1}{6}(1-\varepsilon)\xi\left(2\varepsilon-\varepsilon^2-\xi^2\right)+\frac{1}{\alpha\lambda^2}(1-\varepsilon)\xi-\frac{1}{\alpha\lambda^3}\frac{\sinh\lambda(1-\varepsilon)}{\sinh\lambda}\sinh\lambda\xi\right] \\ w_{II} &= \frac{FL^3}{B}\left[\frac{1}{6}\varepsilon(1-\xi)\left(-\varepsilon^2+2\xi-\xi^2\right)+\frac{1}{\alpha\lambda^2}\varepsilon(1-\xi)-\frac{1}{\alpha\lambda^3}\frac{\sinh\lambda\varepsilon}{\sinh\lambda}\sinh\lambda(1-\xi)\right] \end{aligned} \tag{E.39}$$

Shear angle:

$$\begin{aligned} \gamma_I &= \frac{FL^2}{B}\beta\left[1-\varepsilon-\frac{\sinh\lambda(1-\varepsilon)}{\sinh\lambda}\cosh\lambda\xi\right] \\ \gamma_{II} &= \frac{FL^2}{B}\left[-\varepsilon+\frac{\sinh\lambda\varepsilon}{\sinh\lambda}\cosh\lambda(1-\xi)\right] \end{aligned} \tag{E.40}$$

Bending moments:

$$\begin{aligned} M_{bot/top,I} &= FL\frac{\alpha_{bot/top}}{1+\alpha}\left[(1-\varepsilon)\xi+\frac{\sinh\lambda(1-\varepsilon)}{\alpha\lambda\sinh\lambda}\sinh\lambda\xi\right] \\ M_{bot/top,II} &= FL\frac{\alpha_{bot/top}}{1+\alpha}\left[\varepsilon(1-\xi)+\frac{\sinh\lambda\varepsilon}{\alpha\lambda\sinh\lambda}\sinh\lambda(1-\xi)\right] \end{aligned} \tag{E.41}$$

$$\begin{aligned} M_{s,I} &= FL\frac{1}{1+\alpha}\left[(1-\varepsilon)\xi-\frac{\sinh\lambda(1-\varepsilon)}{\lambda\sinh\lambda}\sinh\lambda\xi\right] \\ M_{s,II} &= FL\frac{1}{1+\alpha}\left[\varepsilon(1-\xi)-\frac{\sinh\lambda\varepsilon}{\lambda\sinh\lambda}\sinh\lambda(1-\xi)\right] \end{aligned} \tag{E.42}$$

Shear forces:

$$\begin{aligned} V_{top/bot,I} &= F\frac{\alpha_{top/bot}}{1+\alpha}\left[1-\varepsilon+\frac{\sinh\lambda(1-\varepsilon)}{\alpha\sinh\lambda}\cosh\lambda\xi\right] \\ V_{top/bot,II} &= F\frac{\alpha_{top/bot}}{1+\alpha}\left[-\varepsilon-\frac{\sinh\lambda\varepsilon}{\alpha\sinh\lambda}\cosh\lambda(1-\xi)\right] \end{aligned} \tag{E.43}$$

$$\begin{aligned} V_{S,I} &= F\frac{1}{1+\alpha}\left[1-\varepsilon-\frac{\sinh\lambda(1-\varepsilon)}{\sinh\lambda}\cosh\lambda\xi\right] \\ V_{S,II} &= F\frac{1}{1+\alpha}\left[-\varepsilon+\frac{\sinh\lambda\varepsilon}{\sinh\lambda}\cosh\lambda(1-\xi)\right] \end{aligned} \tag{E.44}$$

E.3 Simply Supported Sandwich Beam with Two Equal Point Loads *F*/2

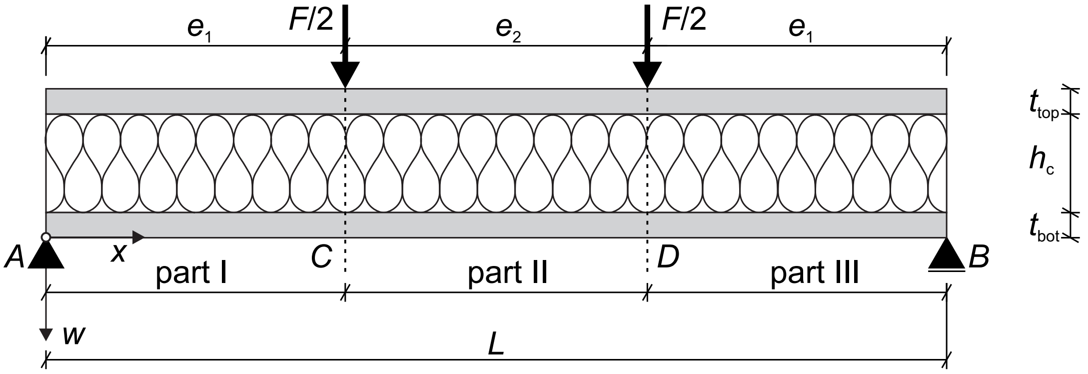

Bending moments:

$$\text{Part I } (\xi < \varepsilon): \qquad M_I = \frac{F \cdot L}{2} \cdot \left(2 - 2 \cdot \varepsilon - \chi\right) \cdot \xi$$

$$\text{Part II } (\varepsilon \le \xi \le \varepsilon + \chi): \qquad M_{II} = \frac{F \cdot L}{2} \cdot \varepsilon \qquad \text{(E.45)}$$

$$\text{Part III } (\xi > \varepsilon + \chi): \qquad M_{III} = \frac{F \cdot L}{2} \cdot \left(-\left(\varepsilon + \chi\right) \cdot \xi + 2 \cdot \varepsilon + \chi\right)$$

Ratio of distances:

$$\varepsilon = \frac{e_1}{L}, \chi = \frac{e_2}{L}, \qquad \xi = \frac{x}{L} \qquad \text{(E.46)}$$

Deflection:

$$\begin{aligned} w_I = \frac{FL^3}{2B}\Bigg[& \frac{1}{6}(2\varepsilon + \chi - 2)\xi^3 + \frac{1}{6}\left(2\varepsilon^3 - 6\varepsilon^2 + 4\varepsilon + 3\varepsilon^2\chi + 3\varepsilon\chi^2 - 6\varepsilon\chi + \chi^3 - 3\chi^2 + 2\chi\right)\xi \\ & - \frac{1}{\alpha\lambda^2}(2\varepsilon + \chi - 2)\xi - \frac{1}{\alpha\lambda^3}\frac{\sinh\lambda(1-\varepsilon) + \sinh\lambda(1-\varepsilon-\chi)}{\sinh\lambda}\sinh\lambda\xi \Bigg] \\ w_{II} = \frac{FL^3}{2B}\Bigg[& \frac{1}{6}(2\varepsilon + \chi - 1)\xi^3 + \frac{1}{6}\left(2\varepsilon^3 - 3\varepsilon^2 + 4\varepsilon + 3\varepsilon^2\chi + 3\varepsilon\chi^2 - 6\varepsilon\chi + \chi^3 - 3\chi^2 + 2\chi\right)\xi \\ & - \frac{1}{2}\varepsilon\xi^2 - \frac{1}{\alpha\lambda^2}(2\varepsilon + \chi - 1)\xi - \frac{1}{6}\varepsilon^3 + \frac{1}{\alpha\lambda^2}\varepsilon + \frac{\sinh\lambda(\xi - \varepsilon)}{\alpha\lambda^3} \\ & - \frac{1}{\alpha\lambda^3}\frac{\sinh\lambda(1-\varepsilon) + \sinh\lambda(1-\varepsilon-\chi)}{\sinh\lambda}\sinh\lambda\xi \Bigg] \qquad \text{(E.47)} \\ w_{III} = \frac{FL^3}{2B}\Bigg[& \frac{1}{6}(2\varepsilon + \chi)\xi^3 - \frac{1}{2}(2\varepsilon + \chi)\xi^2 + \frac{1}{6}\left(2\varepsilon^3 + 4\varepsilon + 3\varepsilon^2\chi + 3\varepsilon\chi^2 + \chi^3 + 2\chi\right)\xi \\ & - \frac{1}{\alpha\lambda^2}(2\varepsilon + \chi)\xi - \frac{1}{6}\left(2\varepsilon^3 + 3\varepsilon^2\chi + 3\varepsilon\chi^2 + \chi^3\right) + \frac{1}{\alpha\lambda^2}(2\varepsilon + \chi) \\ & - \frac{1}{\alpha\lambda^3}\frac{\sinh\lambda\varepsilon + \sinh\lambda(\varepsilon + \chi)}{\sinh\lambda}\sinh\lambda(1-\xi) \Bigg] \end{aligned}$$

Shear angle:

$$\begin{aligned}
\gamma_I &= \frac{FL^2}{2B}\beta\left[2-2\varepsilon-\chi-\frac{\sinh\lambda(1-\varepsilon)+\sinh\lambda(1-\varepsilon-\chi)}{\sinh\lambda}\cosh\lambda\xi\right]\\
\gamma_{II} &= \frac{FL^2}{2B}\beta\left[1-2\varepsilon-\chi+\cosh\lambda(\xi-\varepsilon)-\frac{\sinh\lambda(1-\varepsilon)+\sinh\lambda(1-\varepsilon-\chi)}{\sinh\lambda}\cosh\lambda\xi\right]\\
\gamma_{III} &= \frac{FL^2}{2B}\beta\left[-2\varepsilon-\chi+\frac{\sinh\lambda\varepsilon+\sinh\lambda(\varepsilon+\chi)}{\sinh\lambda}\cosh\lambda(1-\xi)\right]
\end{aligned}\tag{E.48}$$

Bending moments:

$$\begin{aligned}
M_{bot/top,I} &= \frac{FL}{2}\frac{\alpha_{bot/top}}{1+\alpha}\left[(2-2\varepsilon-\chi)\xi+\frac{\sinh(\lambda(1-\varepsilon))+\sinh(\lambda(1-\varepsilon-\chi))}{\alpha\lambda\sinh(\lambda)}\sinh(\lambda\xi)\right]\\
M_{bot/top,II} &= \frac{FL}{2}\frac{\alpha_{bot/top}}{1+\alpha}\left[(1-2\varepsilon-\chi)\xi+\varepsilon-\frac{\sinh(\lambda(\xi-\varepsilon))}{\alpha\lambda}\ldots\right.\\
&\qquad\left.\ldots+\frac{\sinh(\lambda(1-\varepsilon))+\sinh(\lambda(1-\varepsilon-\chi))}{\alpha\lambda\sinh(\lambda)}\sinh(\lambda\xi)\right]\\
M_{bot/top,III} &= \frac{FL}{2}\frac{\alpha_{bot/top}}{1+\alpha}\left[-(2\varepsilon+\chi)\xi+2\varepsilon+\chi+\frac{\sinh(\lambda\varepsilon)+\sinh(\lambda(\varepsilon+\chi))}{\alpha\lambda\sinh(\lambda)}\sinh(\lambda(1-\xi))\right]
\end{aligned}\tag{E.49}$$

$$\begin{aligned}
M_{s,I} &= \frac{FL}{2}\frac{1}{1+\alpha}\left[(2-2\varepsilon-\chi)\xi-\frac{\sinh(\lambda(1-\varepsilon))+\sinh(\lambda(1-\varepsilon-\chi))}{\lambda\sinh(\lambda)}\sinh(\lambda\xi)\right]\\
M_{s,II} &= \frac{FL}{2}\frac{1}{1+\alpha}\left[(1-2\varepsilon-\chi)\xi+\varepsilon+\frac{\sinh(\lambda(\xi-\varepsilon))}{\lambda}\ldots\right.\\
&\qquad\left.\ldots-\frac{\sinh(\lambda(1-\varepsilon))+\sinh(\lambda(1-\varepsilon-\chi))}{\lambda\sinh(\lambda)}\sinh(\lambda\xi)\right]\\
M_{s,III} &= \frac{FL}{2}\frac{1}{1+\alpha}\left[-(2\varepsilon+\chi)\xi+2\varepsilon+\chi-\frac{\sinh(\lambda\varepsilon)+\sinh(\lambda(\varepsilon+\chi))}{\lambda\sinh(\lambda)}\sinh(\lambda(1-\xi))\right]
\end{aligned}\tag{E.50}$$

Shear forces:

$$\begin{aligned}
V_{top/bot,I} &= \frac{F}{2}\frac{\alpha_{top/bot}}{1+\alpha}\left[2-2\varepsilon-\chi+\frac{\sinh(\lambda(1-\varepsilon))+\sinh(\lambda(1-\varepsilon-\chi))}{\alpha\sinh(\lambda)}\cosh(\lambda\xi)\right]\\
V_{top/bot,II} &= \frac{F}{2}\frac{\alpha_{top/bot}}{1+\alpha}\left[1-2\varepsilon-\chi-\frac{\cosh(\lambda(\xi-\varepsilon))}{\alpha}\ldots\right.\\
&\qquad\left.\ldots+\frac{\sinh(\lambda(1-\varepsilon))+\sinh(\lambda(1-\varepsilon-\chi))}{\alpha\sinh(\lambda)}\cosh(\lambda\xi)\right]\\
V_{top/bot,III} &= \frac{F}{2}\frac{\alpha_{top/bot}}{1+\alpha}\left[-2\varepsilon-\chi+\frac{\sinh(\lambda\varepsilon)+\sinh(\lambda(\varepsilon+\chi))}{\alpha\sinh(\lambda)}\cosh(\lambda(1-\xi))\right]
\end{aligned}\tag{E.51}$$

$$
\begin{aligned}
V_{s,I} &= \frac{F}{2}\frac{1}{1+\alpha}\left[2-2\varepsilon-\chi-\frac{\sinh(\lambda(1-\varepsilon))+\sinh(\lambda(1-\varepsilon-\chi))}{\sinh(\lambda)}\cosh(\lambda\xi)\right] \\
V_{s,II} &= \frac{F}{2}\frac{1}{1+\alpha}\left[1-2\varepsilon-\chi+\cosh(\lambda(\xi-\varepsilon))\ldots\right. \\
&\qquad \left.\ldots-\frac{\sinh(\lambda(1-\varepsilon))+\sinh(\lambda(1-\varepsilon-\chi))}{\sinh(\lambda)}\cosh(\lambda\xi)\right] \\
V_{s,III} &= \frac{F}{2}\frac{1}{1+\alpha}\left[-2\varepsilon-\chi-\frac{\sinh(\lambda\varepsilon)+\sinh(\lambda(\varepsilon+\chi))}{\sinh(\lambda)}\cosh(\lambda(1-\xi))\right]
\end{aligned}
\tag{E.52}
$$

E.4 Simply Supported Sandwich Beam with Uniformly Distributed Loading Based on /Sta74/

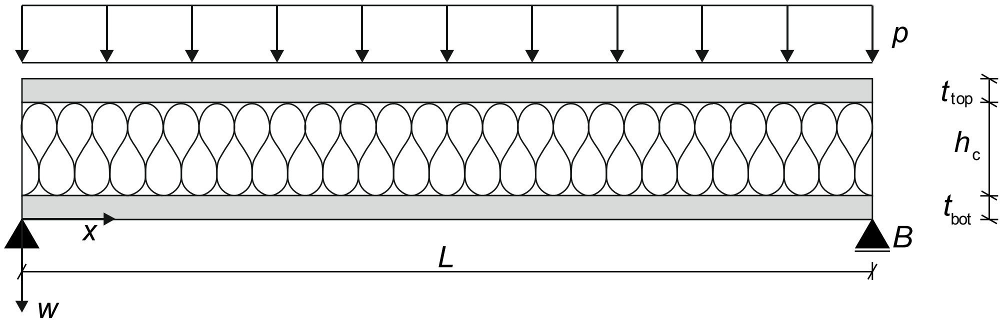

Ratio of distances:

$$\xi = \frac{x}{L} \tag{E.53}$$

Deflection:

$$w = \frac{pL^4}{B}\left[\frac{1}{24}\xi\left(1-2\xi^2+\xi^3\right)+\frac{1}{2\alpha\lambda^2}\xi(1-\xi)-\frac{1}{\alpha\lambda^4}\frac{\cosh\lambda/2-\cosh\lambda(1-2\xi)/2}{\cosh\lambda/2}\right] \tag{E.54}$$

Shear angle:

$$\gamma = \frac{pL^3}{B}\beta\left[\frac{1}{2}(1-2\xi)-\frac{1}{\lambda}\frac{\sinh\lambda(1-2\xi)/2}{\cosh\lambda/2}\right] \tag{E.55}$$

Bending moments:

$$M_{bot/top} = pL^2\frac{\alpha_{bot/top}}{1+\alpha}\left[\frac{1}{2}\xi(1-\xi)-\frac{1}{\alpha\lambda^2}\left(\frac{\cosh\lambda/2-\cosh\lambda(1-2\xi)/2}{\cosh\lambda/2}\right)\right] \tag{E.56}$$

$$M_S = pL^2 \frac{1}{1+\alpha}\left[\frac{1}{2}\xi(1-\xi) - \frac{1}{\lambda^2}\left(\frac{\cosh\lambda/2 - \cosh\lambda(1-2\xi)/2}{\cosh\lambda/2}\right)\right] \tag{E.57}$$

Shear forces:

$$V_{top/bot} = pL\frac{\alpha_{top/bot}}{1+\alpha}\left[\frac{1}{2}(1-2\xi) + \frac{1}{\alpha\lambda}\frac{\sinh\lambda(1-2\xi)/2}{\cosh\lambda/2}\right] \tag{E.58}$$

$$V_S = pL\frac{1}{1+\alpha}\left[\frac{1}{2}(1-2\xi) - \frac{1}{\lambda}\frac{\sinh\lambda(1-2\xi)/2}{\cosh\lambda/2}\right] \tag{E.59}$$